TRACING CHEMICAL WEATHERING USING LITHIUM AND POTASSIUM ISOTOPES

Wenshuai Li

A dissertation submitted to the faculty at the University of North Carolina, Chapel Hill, in partial fulfillment of the requirements for the degree of Doctor of Philosophy in the Department of Geological Sciences in the School of Arts & Sciences

Chapel Hill
2021

Approved by:

Xiao-Ming Liu

Fang-Zhen Teng

Laura Wasylenki

Larry Benninger

Julia Barzyk

ABSTRACT

Wenshuai Li: Tracing Chemical Weathering Using Lithium and Potassium Isotopes
(Under the direction of Xiao-Ming Liu)

Silicate weathering is one of the driving forces of element cycling between atmosphere, hydrosphere, lithosphere, modulating habitats on Earth's surface for the biosphere. Lithium (Li) and potassium (K) isotope ratios (expressed as $\delta^{7}Li$ and $\delta^{41}K$) have potentials to trace weathering processes as the isotopes are highly fractionated by fluid-mineral interactions. This dissertation focuses on Li and K isotope fractionations during chemical weathering based on experiments and field observations and their links to element cycles. Chapter 2 develops an improved protocol for chromatographic isolation of Li, enabling reliable Li isotope analysis. Chapter 3 provides a novel view on Li isotope behavior during clay adsorption, following a Rayleigh-type model in a closed system. Chapter 4 investigates K isotope fractionation during clay adsorption. Combined with synchrotron radiation, I highlight opposite K isotope fractionations during clay adsorption and incorporation. Chapter 5 investigates Li and K isotope fractionations during silicate dissolution, thus providing supplementary knowledge of weathering-driven isotope fractionation. Chapter 6 assesses the Li isotope composition in Hawaiian regoliths forming on distinct climate zones and addresses comparative contributions of external additions, native sources, and biogeochemical cycles. Chapter 7 evaluates the K isotope composition in Hawaiian regoliths on distinct climate zones and highlight the use of K isotopes for climate tracing. Chapter 8 leverages the use of K isotope in soils and plants to trace biological K utilization. In sum, this dissertation emphasizes and explains similarity and difference between Li and K isotope fractionation during weathering.

PERFACE

This dissertation is dedicated to my parents, mentor, and friends, who provide consistent inspiration and love. Thank you for all of your support along the way.

ACKNOWLEDGEMENTS

I want to express my gratitude to many people for their kindness, patience, and support during my Ph.D. career in the last five years. First of all, I sincerely thank my parents for their unconditional love. Their only requirement is that I could enjoy a long and happy life. I never wish for a splendid life, and my biggest wish is to be a good son and stay with them forever.

I would like to express my deepest appreciation to my advisor: Xiao-Ming Liu, who accepted my application when I plunged into misery during my gap year. She exhausted her ability to provide all necessaries for my research and never set limits on my research interests. We have been through a lot together, including but not limited to travels to Hawai‘i and Canada, proposal writing, and exploring collaborations with numerous research groups. She never blamed me when I messed things up and think highly of my research ability and achievements. Although I am so ordinary, I am extremely fortunate to have a respectable advisor and a lifelong friend.

I want to thank Fang-Zhen Teng on my committee for his support of K isotope analysis and contribution to manuscript writing, and thanks to Yan Hu for her help day and night in the MC-ICP-MS lab to ensure high-quality data for my project. I appreciate Laura Wasylenki, Larry Benninger, and Julia Barzyk for serving on my Ph.D. committee and great help with my thesis.

I want to thank Oliver A. Chadwick, who devotes his life to soil science. Thanks to his kindness, carefulness and guidance, my knowledge, research strategies, and writing skills have been improved a lot. I thank Yongfeng Hu and Mengqiang Zhu so much, who are patient and knowledgeable scientists and educators, and opens the door to synchrotron radiation for me.

I want to thank my best friends in UNC-CH for our happy time and precious friendships: Can Liu, Chenyun Dai, Jun Hu, and Chang Liu.

I would like to recognize the assistance I received from our group members Cheng Cao, Xikai Wang, Heather Hanna, and Clement Bataille for fruitful discussion and joyful moments of life. I thank visiting scholars in our group who brought knowledge and happiness to me: Xiaodan Wang, Qixin Wu, Liqiang Xu, Xiaofeng Liu, and Yiwen Cao. People in our group provided tremendous help academically and personally. We got through memorable graduate school time, and I will always remember our friendship and happy moment.

I am grateful for the help of the Geology faculty, staff members, and graduate colleagues that overlapped with me at UNC-CH. Especially, thanks to Drew S. Coleman, Allen F. Glazner, Joel W. Hudley, Larry K. Benninger, Jonathan M. Lees, Donna Surge, Ryan Mills, Deborah J. Harris, Deltra Tate, Xiao Yang, and Chao Wang.

I sincerely acknowledge people for help with field work: James McManus and Brian A. Haley, for their kind guidance and assistance during the cruise to the Pacific Ocean. I also thank people for their help in the lab: Carrie Donley, Amar S. Kumbhar, and Josh Chen for XPS, electron microscope, and XRD analysis in CHANL. I would like to thank Pengfei Yu in Tongji University, Qiaohui Song in GIG-CAS and Yibo Yang in CETES-CAS for their help with Nd-Sr isotope analysis. I thank Ming Li in CUG-Wuhan for help with Ca isotope measurement. I am grateful to Mohsen Shakouri and Qunfeng Xiao in CLS, Bruce Rave in NSLS-II, Matthew Latimer in SSRL and Alpha N'Diaye in ALS for their help with XAS analysis. I am also grateful to Mengqiang Zhu for his help with access to synchrotron facilities and sharing spectral data.

Last but not least, the completion of my dissertation would not have been possible without the support of my parents for their love, encouragement, and inspiration

TABLE OF CONTENTS

LIST OF TABLES

LIST OF FIGURES

CHAPTER 1: INTRODUCTION

Chemical weathering of silicate rocks is one of the primary drivers for various geological processes on Earth's surface, such as (i) shaping planetary topography, (ii) promoting soil formation, (iii) controlling terrestrial nutrient supplies to the oceans, and (iv) regulating changes in atmospheric CO_2 and global carbon cycles (Royer et al., 2007; Berner and Berner, 2012). Silicate weathering supports element cycling between the atmosphere, hydrosphere, lithosphere, and biosphere (Goldich et al., 1938; Liu et al., 2011). Therefore, constraining the intensity (the level of alteration and decomposition of rocks/minerals) and rate (the amount of change in weathered materials per unit time) of chemical weathering by established proxies is vital to trace climate change on geologic times (Berner and Berner, 2012; Vigier and Godderis, 2015). Chemical weathering controls the fractionation of stable isotopes on Earth's surface and helps to constrain the rate and intensity of chemical release of specific mineral components (Anbar and Rouxel, 2007; Liu et al., 2013). Particularly, basalt makes up ~8% of aerially exposed silicate rocks and basalt weathering is responsible for over ~30% of global CO_2 consumption (Gaillardet et al., 1999; Dessert et al., 2003). In addition, basalt weathering is critical in the formation of economic ore deposits and ecological sustainment (White and Brantley, 1995). To advance the understanding of silicate (basalt) weathering, applicable isotope tracers for weathering processes include $^{7}Li/^{6}Li$ and $^{41}K/^{39}K$ have potentials for tracing chemical weathering over geological time (e.g., Liu et al., 2013; Dellinger et al., 2017; Chen et al., 2020; Teng et al., 2020)

Lithium (Li) is a water-soluble trace element, which can be readily solubilized from parent rocks and incorporated into secondary clay minerals during continental weathering.

Lithium has two stable isotopes, ^{7}Li and ^{6}Li, with abundances of 92.41% and 7.59%, respectively, and ~17% mass difference and considerable isotope fractionation potential. Due to low-temperature fluid-mineral exchange reactions, there is ~30‰ difference in $\delta^{41}Li$ between the Upper Continental Crust (an average of 0±2‰, Teng et al., 2004; or a loess-constrained value of 0.6±0.6‰, Sauzéat et al., 2015) with modern seawater (~31‰, Hathorne and James, 2006). Lithium stable isotopes have multiple advantages as a weathering tracer. First, neither silicate dissolution nor metamorphic dehydration appears to fractionate Li isotopes (Marschall et al., 2007; Pistiner and Henderson, 2003; Teng et al., 2007; Wimpenny et al., 2010). Nevertheless, Li isotopes have been shown to fractionate substantially by weathering, likely due to the equilibrium partitioning between secondary minerals and surrounding waters (Huh et al., 1998; Liu et al., 2013; 2015; Millot et al., 2010; Pogge von Strandmann et al., 2010; Teng et al., 2004; Dellinger et al., 2017). In general, isotopically light Li is preferentially scavenged by secondary silicate minerals and iron or aluminum oxides (Pistiner and Henderson, 2003; Hindshaw et al., 2019). Moreover, Li has only one redox state (+1 charge) and is thus insensitive to redox variations (cf., Fe, Mo, U, etc.). In addition, Li is not a nutrient involved in the biosphere. Therefore, biological activities probably do not directly affect its elemental and isotopic behaviors (Lemarchand et al., 2010). Moreover, Li isotopes are important in terms of tracing silicate weathering because of the low abundance of Li in carbonate rocks relative to silicate rocks (Penniston-Dorland et al., 2017). Numerous studies showed that Li isotopes are a useful proxy to solely trace silicate weathering processes that are used to describe weathering intensity/rate/congruency, or weathering regime integrating over most dependencies (Huh et al., 1998, 2001; 2004; Kisakürek et al., 2005; Liu et al., 2013; Dellinger et al., 2015, 2017; Henchiri et al., 2016; Ma et al., 2020; Pogge von Strangmann et al., 2017; Li et al., 2020a, 2020b).

Potassium (K) is a major element on Earth, including the continental crust, river waters, and oceans, which is water-soluble and can be leached out from host rocks and then incorporated into secondary minerals through continental weathering. Potassium has two stable isotopes, ^{39}K (93.258%) and ^{41}K (6.730%), and one naturally occurring radioactive isotope ^{40}K (0.012%) with a long half-life ($t_{1/2}$=1.248×10^9 years). The recent development of Multiple-Collector Inductively-Coupled-Plasma Mass-Spectrometry (MC-ICP-MS) has made it possible to obtain high-precision K isotopes measurement (Chen et al., 2019; Hu et al., 2018; Li et al., 2016; Morgan et al., 2018; Wang and Jacobsen 2016; X. Li et al., 2020). Because of the similarities between Li and K, the existing knowledge of Li isotope behavior in weathering settings will help to understand the less known K isotopic fractionation on Earth's surfaces. Due to weathering alteration over time, there is ~0.6‰ difference of $\delta^{41}K$ between the Bulk Silicate Earth (~ -0.48‰, Wang and Jacobsen, 2016) and the Upper Continental Crust (an average of -0.44±0.05‰, Huang et al., 2020) with the modern seawater (~0.12‰, Wang et al., 2020). There are many advantages that enable using K isotopes for tracing silicate weathering processes. First, K is a major element, and its isotopic variations may be closely coupled with the cycling of alkali elements, thus complementing the isotopic systems of trace elements of Li. Igneous processes fractionate K isotopes in a narrow range relative to chemical weathering (Tuller-Ross et al., 2019a; Tuller-Ross et al., 2019b). In comparison, the K isotope composition of weathering products reflects the chemical composition of the weathered material and K releases from bedrock (having low $\delta^{41}K$) to K scavenging by secondary minerals (driving waters to high $\delta^{41}K$) (Chen et al., 2020; Huang et al., 2020; Li et al., 2019; Teng et al., 2020; Wang et al., 2021). Although K is one of the macronutrients and its isotopes can be strongly fractionated by psychophysiological processes, ~90% of K in riverine dissolved loads is derived from silicate

weathering as reported in literatures (Berner and Berner, 2012; Meybeck, 1987). Similar to Li, K has only one redox state (+1 charge) and is indiscernible to variations in oxygen fugacity, and K is almost exclusively hosted in silicate rocks, which makes it unique to trace silicate weathering. Several studies investigated terrestrial weathering archives to use K isotopes as a promising weathering proxy (e.g., S. Li et al., 2019; Chen et al., 2020; Teng et al., 2020), and more systematic experimental and field investigations on K isotope behavior are warranted.

The following eight chapters are presented six independent papers that have either been published, or have been submitted to peer-review journals. Chapter 2 introduces an efficient chromatographic method of Li purification for isotope analysis using MC-ICP-MS. Chapters 3, 4, and 5 experimentally investigate the isotope behavior of Li and K during clay adsorption and rock dissolution to explain field observation in weathering systems. The following three chapters (6, 7, and 8) examine Li and K isotopic fractionation along with element cycles during chemical weathering of the Hawaiian basalt in contrasting weathering regimes. The final chapter 9 summarizes the dissertation.

Chapter two establishes a new dual-column system for Li purification to achieve the accurate and precise measurement of Li isotopic compositions using MC-ICP-MS. Compared with single-column systems, our dual-column system yields a consistent elution range of the Li-bearing fraction (7–16 mL) for samples with a wide range of Li loads and matrix compositions, so that column re-calibration is not required. Besides, this efficient method achieves complete Li recovery (~100%) and low matrix interference (i.e., Na/Li$\lesssim$1) in a short elution time (~6 h). This work has been published as an article titled “Optimisation of Lithium Chromatography for Isotopic Analysis in Geological Reference Materials by MC-ICP-MS” in *Geostandards and Geoanalytical Research* by Wenshuai Li, Xiao-Ming Liu, and Linda V. Godfrey.

Chapter three reports the result of closed-system batch experiments to determine the mechanisms and quantify the magnitudes of Li isotope fractionations during adsorption onto kaolinite under constrained laboratory conditions. The isotope fractionation in all experiments sets can be best described by Rayleigh distillation models. Significant Li isotope fractionation occurs following a kinetic law in closed systems during adsorption on kaolinite. Adsorption-driven Li isotope fractionation conforms to a kinetic solid-liquid isotope fractionation factor ~0.992. This study reveals a vital kinetic role of clay uptake in Li isotope fractionation during chemical weathering, and the dominance of the kinetic mechanism explains field observations on rivers worldwide. This work has been published as an article titled "Experimental investigation of lithium isotope fractionation during kaolinite adsorption: Implications for chemical weathering" in *Geochimica et Cosmochimica Acta* by Wenshuai Li and Xiao-Ming Liu.

Chapter four reports the result of closed-system batch experiments to determine the mechanisms and quantify the magnitudes of K isotope fractionations during adsorption onto kaolinite and smectite under constrained laboratory conditions. Absolute isotope fractionations between adsorbed and aqueous phases remained near-constant, regardless of variations in solute pH, ionic strength, and initial KCl. Observed isotope fractionation can be best described by an equilibrium isotopic law with a constant solid-liquid fractionation factor ~1.00075. To reconcile distinct behaviors of K isotope fractionation in experiments and weathering environments, I confirm that differences in atomic coordination on clay surfaces and in structures and highlight the dominance of clay incorporation rather than adsorption controlling K isotope behavior during chemical weathering. This work has been published as an article titled "Potassium Isotope Fractionation during Clay Adsorption" in *Geochimica et Cosmochimica Acta* with the authorship of Wenshuai Li, Xiao-Ming Liu, Yan Hu, Fang-Zhen Teng, and Yongfeng Hu.

Chapter five experimentally investigates the isotopic behaviors of Li and K during the dissolution of silicate rocks, including basalt and granite. I provide a time-series interpretation of Li and K isotope fractionation during silicate dissolution in ultra-acidic (unidirectional) and near-natural (organic ligand-involved) environments. In the experiments, the Li and K isotopic pattern could be divided into two-to-three stages. The initial enrichment of light isotopes in the liquids can be ascribed to the kinetic isotope effect, confounded by ionic diffusion and ion solvation. A later transition towards no isotope fractionation of Li and K may be explained by (i) the masking effect from dissolution and (ii) an imprint from the destruction of $^{7}Li/^{41}K$-enriched surface layers. Lateral resorption of solute Li (not for K) after ~100 h reaction could be facilitated by the electrostatic attraction from increasing surface negative charges and active hydroxyls with increasing pH. Therefore, the presence of organic ligands impacts dissolution stoichiometry and potentially modifies Li isotope fractionation in weathering environments. In comparison, K isotope fractionation driven by rock dissolution stops immediately (within days) after starting the experiments. This research helps to understand the mechanisms of Li and K isotope fractionation during chemical weathering and trace long-term climate change using geological records. This work has been published as an article titled "Lithium and potassium isotope fractionation during silicate rock dissolution: An experimental approach" in *Chemical Geology* with the authorship of Wenshuai Li, Xiao-Ming Liu, Kun Wang, and Piers Koefoed.

Chapter six examines Li geochemistry of the humid and arid regolith profiles formed on the Pololū lavas, the Kohala Mountain, Hawai'i to understand the influence of terrestrial soil-atmosphere-biosphere exchanges on Li geochemical behaviors. I found decoupling of Li element and isotopic composition in the shallow regolith from those of the deep regolith, which implies different regolith controls on Li chemistry at vertical locations. The main finding of this study is

that the Li geochemistry in the regolith has been substantially influenced by (i) atmospheric deposition, (ii) plant cycling, and (iii) secondary mineral formation. The outcome emphasizes climate-regulated and long-neglected biological controls on terrestrial Li cycling during chemical weathering. This work has been published as an article titled "Lithium Isotope Behavior in Hawaiian Regoliths: Soil-Atmosphere-Biosphere Exchanges" in *Geochimica et Cosmochimica Acta* with the authorship of Wenshuai Li, Xiao-Ming Liu, and Oliver A. Chadwick.

Chapter seven examines K geochemistry in the regolith profiles developed at the humid and arid sides of Kohala Mountain, Hawai'i. I conclude that K derived from eolian accretion over time is critical, especially the humid regolith receiving heavy rainfall. This conclusion is supported by increased crustal K imprint, enriched quartz and illite-K phases, and more radiogenic Nd-Sr isotopic compositions towards the surface. Light K isotopic composition in the humid regolith relative to basaltic $\delta^{41}K$ value is principally caused by preferential incorporation of isotopically light K into kaolin minerals. In comparison, heavier K isotopic values in the arid regolith than basaltic δ41K reflect an interplay between clay adsorption of isotopically heavier K under more alkaline condition and better preservation of marine aerosol K imprints. Biological activities contribute to soil K enrichment, but exert negligible influences on K isotopic variations due to rapid leaching and the masking effects of exogenous sources. The outcome supports that K isotopic composition in the regolith depends on climate, making terrestrial K isotopic records a potential tracer of weathering processes and paleo-climate. This work has been submitted as an article titled "Potassium isotopic fractionation during chemical weathering in humid and arid Hawaiian regoliths" to *Geochimica et Cosmochimica Acta* with the authorship of Wenshuai Li, Xiao-Ming Liu, Yan Hu, Fang-Zhen Teng, Yongfeng Hu, and Oliver A. Chadwick.

Chapter eight focuses on K isotopic fractionation within a humid and an arid soil-plant system sampled on the windward and leeward sides of Kohala Mountain, Hawai‘i. I studied soils and individual tissue samples such as roots, stems, barks, shoots (a sum of stems and fresh leaves), leaves (fresh and dead), seeds, and flowers of trees and grasses. I conclude that two dominant processes are responsible for plant-mediated K isotopic fractionation, including (1) K redistribution during intra-plant circulation and (2) uptake at the root-soil interface. For intra-plant circulation of K, there is a high affinity of isotopically lighter K to organic complexes as K-pectate, and K-pectate is particularly enriched in roots and fresh leaves. For K uptake at root-soil interface, isotopically lighter K is preferentially taken by roots from soil bioavailable pools following a low-affinity (passive) transport path. Soil K budget in two sites reflects strong source mixing effects with limited plant imprints. This work provides exploratory data on the biogeochemical fractionation of K isotopes in the soil-plant system. This work has been published as an article titled “Potassium Isotopic Fractionation in A Humid and An Arid Soil-Plant System in Hawai‘i” in *Geoderma* with the authorship of Wenshuai Li, Xiao-Ming Liu, Yan Hu, Fang-Zhen Teng, Yongfeng Hu, and Oliver A. Chadwick.

Conclusions and future directions are presented in Chapter nine.

CHAPTER 2: OPTIMISATION OF LITHIUM CHROMATOGRAPHY FOR ISOTOPIC ANALYSIS IN GEOLOGICAL REFERENCE MATERIALS

This chapter is published as: Li, W., Liu, X. M. and Godfrey, L. V. (2019). Optimisation of lithium chromatography for isotopic analysis in geological reference materials by MC-ICP-MS. Geostandards and Geoanalytical Research, 43(2), 261-276.

1. Introduction

Chemical weathering of silicate rocks significantly impacts Earth's carbon cycle and therefore has long been considered as a key long-term climate control through geological time (e.g., Liu et al., 2015; Liu and Rudnick, 2011; Misra and Froelich, 2012; Pogge von Strandmann et al., 2017). Compared to other isotope systems, lithium (Li) isotopes are unique because they trace only silicate weathering but are insensitive to carbonate weathering fluctuation (Kisakurek et al., 2005; Millot et al., 2010b). The use of Li isotope system as a reliable weathering tracer requires analytical protocols for a broad range of geological samples with varying Li content and matrix/ Li ratios (Van Hoecke et al., 2015). MC-ICP-MS (Bryant et al., 2003; Tomascak et al., 1999) has increasingly been adopted for precise and accurate Li isotopic analysis. However, Li isotope measurements are extremely sensitive to interferences, and incomplete recovery of Li during columns causes a high degree of isotope fractionation (Huang et al., 2010). High resolution, high-yield chemical separation of Li from the matrix prior to measurement (James and Palmer, 2000; Magna et al., 2004; Millot et al., 2004; Misra and Froelich, 2009) is necessary because matrix elements may cause significant instrumental mass-dependent isotope fractionation due to the space-charge effect from ionization of non-analytes (Bryant et al., 2003; Košler et al., 2001).

Early attempts to isolate Li from geological materials required three or four separate column procedures (James and Palmer, 2000; Liu and Rudnick, 2011; Moriguti and Nakamura, 1998; Rudnick et al., 2004; Teng et al., 2006). These approaches are time-consuming and generally require a large volume of eluents, and thus increasing the risk of high blanks. Moreover, nonquantitative Li recovery contributes to artificial on-column isotopic fractionation (Misra and Froelich, 2009). Refined single- and dual-column cation-exchange chromatography has been described in the literature (Choi et al., 2013; Gao and Casey, 2012; Huang et al., 2010; Jeffcoate et al., 2004; Lin et al., 2016; Nishio and Nakai, 2002; Rosner et al., 2007; Tomascak et al., 1999; Van Hoecke et al., 2015). Inorganic acids with (Choi et al., 2013; Huang et al., 2010; Jeffcoate et al., 2004; Lin et al., 2016; Nishio and Nakai, 2002; Phan et al., 2016; Rosner et al., 2007; Tomascak et al., 1999) or without (Gao and Casey, 2012; Misra and Froelich, 2009; Van Hoecke et al., 2015) an organic solvent (i.e., methanol) are usually adopted as the eluent.

However, the application of single-column quantitative separation of Li could be limited by high cumulative procedural blanks, the tailing of Li peaks, and incomplete Li recovery, and subsequent column-induced isotope fractionation (Misra and Froelich, 2009). To achieve satisfactory Li/matrix elements separation, relatively large resin loads and high aspect ratios, and eluent volumes are required. Therefore, the single-column system elution rates are significantly slowed, resulting in 7~10 h separation procedures (Lin et al., 2016; Phan et al., 2016; Tomascak et al., 1999; Van Hoecke et al., 2015). Thus, the efficiency of one-column systems must also be reconsidered. The majority of previous studies used standards with limited lithology, most common igneous rocks. Different amounts of Li loading and different sample matrixes (i.e., Na, Mg of Li elution curves) (Chan et al., 2002, 1999; Moriguti and Nakamura, 1998; Tomascak et al., 2016; Van Hoecke et al., 2015) require column re-calibration (Bohlin et al., 2018). Therefore,

the use of single-column separation methods is limited for diverse geological materials. In some cases, the single-column method may not be sufficient, and therefore individually calibrated separation protocols are required to achieve complete removal of matrix elements and full recovery of Li during chromatography (Phan et al., 2016; Tomascak et al., 2016; Van Hoecke et al., 2015). For example, Von Hoecke et al. (2015) developed separate single-column systems for carbonates and clays, respectively.

In this study, we have revisited multiple single-column systems and examined the features of both inorganic acids and acids/organics mixture eluents. In comparison with single-column systems, an efficient dual-column system has been developed to achieve consistent Li elution for various geological materials. In addition, the newly developed chromatography has been examined with a wide range of geological materials within the context of paleoclimatological research. The accuracy and precision of our isotopic measurements are evaluated. Finally, we provide a rigorous test of the separation methodologies to establish an optimized Li chromatography for the community.

2. Materials and Methods

This section presents a full description of the proposed protocols and analysis methods.

2.1. Chemicals and reference materials

Ultrapure water (18.2 MΩ·cm) was acquired using a Milli-Q Element system (Direct-Q® 3 UV). Commercially available nitric acid (HNO_3), hydrochloric acid (HCl), and hydrofluoric acid (HF) were purified in-house with double distillation in a Teflon™ sub-boiling still and gravimetrically diluted to the required molarities as necessary with Milli-Q water. The molarities of hydrochloric acids (6 / 0.5 / 0.2 $mol \cdot L^{-1}$) were used for column separation. Optima-grade methanol (CH_3OH, >99.99% metal basis) was purchased from Fisher Scientific™. Lithium carbonate

isotopic reference material IRMM-016 (Flesch et al. 1973), available from the Institute for Reference Materials and Measurements (IRMM), was employed for evaluation of the isolation procedure and for calibration of Li isotopic analysis.

For optimization of the isolation of Li from various geological samples, eight certified international reference materials and two synthetic fluids with different Li contents and matrix/ Li ratios are adopted in this study to evaluate the matrix effect on column chemistry. Lithium isotopic ratios for international reference materials are necessary for method validation (Kane, 2001). Geological reference materials analyzed in this study are listed here. A limestone standard (NIST-SRM-1d) was purchased from the National Institute of Standards and Technology (NIST). A coral standard (JCP-1) was acquired from the Geological Survey of Japan (GSJ). A granodiorite (GSP-2), a continental flood basalt (BCR-2), an ocean island basalt (BHVO-2, purchased in 2016), and a marine manganese nodule (NOD-A-1) were obtained from United States Geological Survey (USGS). Another ocean island basalt (BHVO-2, purchased in 2010) was generously provided by Prof. Allen F. Glazner (UNC-CH) for comparison. A basalt standard (JB-2) and a granite standard (JG-2) were purchased from the Geological Survey of Japan GSJ. A clay standard (kaolinite, KGa-2) was gained from the Clay Mineral Society (SMC). Seawater (NASS-7) was purchased from the National Research Council Canada (NRCC). One in-house synthetic fluid (Syn-1) was made from Li (aq)-clay adsorption experiments in a high-Na system, in analogy to pore water. Another synthetic fluid (Syn-2) was prepared with 50 ppb Li (IRMM-016), doped with 10 ppm K, Fe, and 100 ppm Ca, Mg, Al, Na, to emulate the behavior of the matrix in the ion exchange separation experiments.

2.2. Sample preparation

Sample preparation was performed at the Plasma Mass Spectrometry Laboratory (PMS) at the University of North Carolina at Chapel Hill (UNC-CH), and aqueous samples were directly diluted with 2% nitric acid. Clay (10 mg), manganese nodule (50 mg), and the remaining solid samples were weighed (100 mg). Samples were digested with a HF-HNO_3 (3:1 v/v) mixture and put on a hotplate at ~120 ºC until total dissolution was achieved. Next, the samples were dried down, refluxed with *aqua regia,* and put on a hotplate at ~120 ºC overnight. The drying operation was repeated, using the same amount of HCl and with at least 24 h on the hotplate until the solution was clear). The solutions were then evaporated to dryness again at ~120 ºC. Finally, the residues were dissolved in 10 mL 2% nitric acid in preparation for ion-exchange separation. All prepared samples were kept in 10 mL Savillex® Teflon beakers and stored in class 100 laminar flow exhaust hoods (AirClean® 600 PCR workstation, AirClean System).

2.3. Chromatography

Four single-column and one dual-column separation methods were evaluated in this study. The purification of Li was evaluated via single-column systems modified from Von Hoecke et al. (2015) and Phan et al. (2016). Our designed dual-column system was also evaluated, in which the AG50W-X8 (BioRad™) cation exchange resin (200~400 mesh) was used, as is common in Li separation. The BioRad™ short (0.8 x 4 cm, 10 mL reservoir) and a custom-made long (0.6 x 9 cm, 10 mL reservoir) acid-cleaned polypropylene columns were prepared for resin loading. All operations were performed in class 100 laminar flow hoods (AirClean® 600 PCR workstation) following all general precautions to reduce contamination. We have developed and tested the single-/dual-column systems using inorganic (0.2/0.5 M HCl) or mixed (1.5 M HNO_3 + 70% Methanol) eluents for Li separation efficiency. The details of the experiment design and chromatographic procedure for Li isolation displayed in Table 1.

Resin and empty polypropylene chromatography columns were alternately acid-cleaned with 6 M HCl, 4 M HNO_3, and Milli-Q water multiple times and carefully filled with 2.0 or 2.5 mL resin bed volumes (in 0.2 M HCl) to prevent bubble formation. Prior to usage, the resin-packed columns were washed by rinsing sequentially with 10 mL 6 M HCl and 15 mL Milli-Q water to further remove possible impurities. Blank checks with 30 mL Milli-Q water eliminated any possible contaminations. If the resin is not cleaned before the usage, a tailing of the Na background will step into the Li fraction. The columns need to be backwashed after resin loading by 10 mL 6 M HCl and 15 mL Milli-Q water to exclude impurities. If the resin is not cleaned before the Li separation procedure, tailing of the Na background in the Li elution range can occur.

Tomascak et al. (2016) have suggested that HNO_3+methanol mixtures provide a better separation of Li/Na than inorganic eluents, while HCl has a better separation factor for Li/Na than HNO_3. The separation factor of Li from Na in 0.2 M HCl is approximately 1.5 (Gao and Casey, 2012), which is sufficient to achieve negligible spectral interferences and blanks relative to the amount of Li processed. To test the extraction ability of eluents, a set of parallel investigations were conducted in this study. For chromatography preparation, 1–2 mL (10–20 mg solids, a wide [Li] range of 7.2–325.1 ng) prepared samples were dried down and digested in 1 mL 1.5 M HNO_3+70 % methanol mixture, 0.5 M HCl, and 0.2 M HCl respectively for the short column and in 2ml 0.2 M HCl for the long column. After sample loading, 1 and 2 mL eluents for the short and long columns were collected for each step.

In the dual-column system, the first column with 2.5 mL total resin volume is used to separate Li from the majority of the sample matrix, and the second column is used to further purify Li. The column yields should achieve nearly 100% Li recovery. Prepared samples were

dried down and digested in 1 mL 0.2 M HCl for the first long column. We collected the 0.2 M HCl fraction between 19 mL and 44 mL by 50 mL Savillex® Teflon beakers, see details in the discussion part. The collected solution was dried down at 120 ºC overnight and re-dissolved in 0.2 M HCl and was then loaded in the short second column. Next, most of the matrix cations (i.e., Mg, Al, K, and Ca) are effectively removed from the resin within the first 3 mL 0.2 M HCl elution. In addition, using 0.2 M HCl can prevent possible early elution of Li. We then switched to 0.5 M HCl, which has stronger extraction ability, to ensure an early elution and a restricted elution range of Li fractions with a relatively small volume. The Li-bearing fraction was collected in the following 4–16 mL 0.5 M HCl. After the entire chromatographic isolation process, a minimum of 40 mL 6 M HCl is adopted to sufficiently regenerate the resin prior to the next usage (Van Hoecke et al., 2015). The collected solution was dried and then diluted to appropriate concentrations in 2% HNO_3 prior to analysis by mass spectrometry. The procedural blanks were less than 0.004 ng Li (<< total Li mass load, 7~325 ng) as routinely measured, which is considered negligible and allows for the acquisition of precise and accurate isotope compositions.

Table 1. Chemical separation procedures for various column systems.

Details	Single-column A (modified from Phan et al., 2016)	Single-column B (modified from Von Hoccke et al., 2015)	Single-column C (modified from Von Hoccke et al., 2015)	Single-column D (this study)	Dual-column E (this study)
Para-meter	Short column with 2 mL resin (H: 4	Short column with 2 mL resin (H: 4 cm)	Short column with 2 mL resin (H: 4 cm)	Long column with 2.5 mL resin (H: 9 cm)	1st long column with 2.5 mL resin (H: 9 cm) 2nd short column with 2 mL resin (H: 4 cm)
Sample loading	1 mL sample (10-20 mg) digest in 1.5 M HNO_3 +	1 mL sample (10-20 mg) digest in 0.2 M HCl	1 mL sample (10-20 mg) digest in 0.5 M HCl	2 mL sample (10-20 mg) digest in 0.2 M HCl	1st long column 2 mL sample (10-20mg) digest in 0.2 M HCl 2nd long column dried collection digest in 0.2 M HCl
Collect	21 mL 1.5 M HNO_3 + 70% methanol	30 mL 0.2 M HCl	30 mL 0.5 M HCl	60 mL 0.2 M HCl	1st long column (0.2 M HCl; 18~44 mL collected) 2nd short column (0.2 M HCl, 1~3 mL; 0.5 M HCl, 4~16 mL; 7~16 mL collected)
Post column check	2 mL 1.5 M HNO_3 + 70% methanol	2 mL 0.2 M HCl	2 mL 0.5 M HCl	2 mL 0.2 M HCl	1st long column 2 mL 0.2 M HCl 2nd short column 2 mL 0.5 M HCl
Resin cleaning	20 ml 6 M HCl + 15 mL Milli-Q	20 mL 6 M HCl + 15 mL Milli-Q	20 mL 6 M HCl + 15 mL Milli-Q	40 mL 6 M HCl + 15 mL Milli-Q	1st long column: 40 mL 6 M HCl + 15 mL Milli-Q 2nd short column: 20 mL 6 M HCl + 15 mL Milli-Q

2.4. Mass spectrometry instrumentation

The details of the instrument settings and data acquisition parameters of Q-ICP-MS and MC-ICP-MS are summarized in Table 2. To determine the elution curves for both of the columns, the column cuts were analyzed for possible matrix elements using an Agilent Technologies™ 7900 quadrupole ICP-MS at the PMS Lab of the University of North Carolina at Chapel Hill. The Q-ICP-MS is equipped with a concentric nebulizer, mounted onto a quartz impact bead spray chamber cooled to 2°C. The sample solution in 2% (v/v) nitric acid was introduced via a peristaltic pump. The nuclides monitored were ^{7}Li, ^{23}Na, ^{24}Mg, ^{27}Al, ^{39}K, ^{43}Ca, ^{44}Ca, ^{56}Fe, and ^{57}Fe. One measurement requires almost 6 min, including washing time.

A Thermo Scientific™ Neptune Plus MC-ICP-MS in the Dept. of Earth and Planetary Sciences at Rutgers University was used to determine Li isotopic compositions. Sample introduction was accomplished using a micro-concentric PFA nebulizer (nominal uptake rate of 70 μL/min) with a Cetac Aridus II (Teledyne Instruments Inc, Omaha NE, USA) desolvating system. External correction in a standard/sample/standard normalization approach was adopted for the correction for instrumental mass discrimination using a 20 ppb solution of L-SVEC. Signal intensity on ^{7}Li ranged between 16 and 22V during the course of this study. Sample signal intensity was matched to within 95% of the standards. Each measurement requires almost 8 min, including sample uptake (during which time baselines were measured) and rinse times.

Hereafter, the Li isotopic composition is expressed as δ^{7}Li, which is the per mil deviation from the NIST L-SVEC standard, expressed as $\delta^{7}\text{Li}\ (‰, \text{L-SVEC}) = [(^{7}\text{Li}/^{6}\text{Li})_{\text{Sample}} / (^{7}\text{Li}/^{6}\text{Li})_{\text{L-SVEC}} - 1] \times 1000$. Isotopic compositions were determined by the standard–sample–standard bracketing protocol. The average value of the two bracketing standards was used to internally correct for instrumental mass bias (IMB) for the isotope ratio determination.

Table 2. Instrumental operating conditions and data acquisition parameters.

Parameters	Agilent Technologies™ 7900	Thermo Scientific™ Neptune Plus
	Instrumental operating conditions	
RF power (W)	1550	1200
RF matching (V)	1.2-1.8	<5
Ion lens settings	Optimized daily for maximum sensitivity and signal stability	
Guard electrode	On	
Cool Ar gas flow rate ($L \cdot min^{-1}$)	15	16
Auxiliary Ar gas flow rate ($L \cdot min^{-1}$)	0.8-1.0	0.81
Nebulizer Ar gas flow rate ($L \cdot min^{-1}$)	1.09	0.94
Argon sweep gas / N_2 gas ($L \cdot min^{-1}$)	/	6.90 / 0.001
Sampler and skimmer cone	Ni 7700 / Ni 7900X	Ni / Ni X-cone
Matrix	2% HNO_3	2% HNO_3
	Data acquisition parameters	
Resolution setting	/	low
Integration time (s)	0.1	4
Cycles/Blocks	/	20/2
Sample uptake time (s)	60	80
Stabilize time (s)	40	30
Measurement time (s)	50	85
Wash-out time (s)	150	150
	Neptune cup configuration	
Cup	Masses/nuclides	Amplifer resistance (Ω)
L4	^{6}Li	10^{11}
H4	^{7}Li	10^{11}

3. Results and Discussion

We addressed and evaluated several column separation methods for Li isotopic analysis in the following sections. These methods include reported single-column and our dual-column systems with elution solvents of methanol + HCl or HCl-only. Additionally, we evaluated the memory effects, matrix effects, and loading capacity. Long-term accuracy and precision of isotope analysis on the MC-ICP-MS are reported as well. The Li isotope values of 12 geological references are reported.

3.1. Evaluation of short single-column system for Li isolation

The elution profiles from all of the single-column calibration experiments are summarized in Table 2 and shown in Figs. 1-3. The first single-column system was established according to the protocol reported in Phan et al. (2016) and applied on reference samples including NIST-SRM-1d, JCP-1, BHVO-2 (2016), and KGa-2. Using the 1.5 M HNO_3+70% methanol mixture eluent, we observed an early breakthrough of Na into Li fractions, unable to separate Li from Na effectively for these particular samples adopted here (Fig. 1). The Na/Li ratios in Li fractions varied between 1050 and 4180 and would definitely result in erroneous isotopic analysis. The Li elution curves show a clear difference between carbonates (1~14 mL) and Mg/Al-silicates (5~16 mL), possibly caused by the different matrix effects of Ca and Mg/Al with methanol. Mineral acid/organic solvent mixtures can increase the peak resolution of the cation exchange column and thereby improve the separation factors to effectively remove the majority of the cations and high field strength elements (Huang et al., 2010; Korkisch et al., 1967; Tomascak et al., 2016). However, the 1.5 M HNO_3+70% methanol mixture has the following disadvantages: (1) Fast volatilization of methanol decreases the eluent composition during leaching (Ai et al., 2014), likely leading to drifting elution curves and cross-contamination of Li between columns. (2) Rapid evaporation of methanol decreases air solubility

(Swann et al., 1983), and the mesogenic air bubbles may destroy the compact resin structure. (3) The degradation of resin stimulated by organic solvent can cause significant drifts of Li/Na peaks (Jeffcoate et al., 2004); therefore, columns must be reset and calibrated periodically. (4) It has also been reported that the residual Ca content in methanol could induce poor reproducibility of Li isotope measurements (Marschall et al., 2007). Mineral acid/menthol mixtures containing a high level of impurities may exacerbate instrumental baseline shifts (Gao and Casey, 2012). (5) The presence of organics in the final elution disturbs isotopic measurements in a non-spectral way (Chernonozhkin et al., 2015). (6) Organic matter can induce complexation with target cations, making subsequent ion-exchange separation steps ineffective.

Single inorganic acid (HCl) eluents can prevent the problems associated with an organic solvent and balance the blanks introduced from the multiple reagents (Gao and Casey, 2012). Upon switching to 0.5 M and 0.2 M eluents, however, the tailing of Li/Na peaks (Figs. 2-3) demonstrates that the single short column with 2.0 mL resin cannot completely separate Li from Na. The considerable amount of Na in the Li elution fractions gives rise to Na/Li ratios in range of 2 ~7,860. Notably, 0.5 M HCl has a higher extraction ability than 0.2 M HCl, which results in advanced elution of Li and the narrow elution ranges of the Li fraction. We have been able to replicate the unusual Na leaching curve in limestone (NIST-SRM-1d) with a 0.2 M HCl eluent, though the reason for these results remains unclear and requires further study. One possible cause may be the sample size exceeding the capacity of the resin, resulting in unsymmetrical leaching curves.

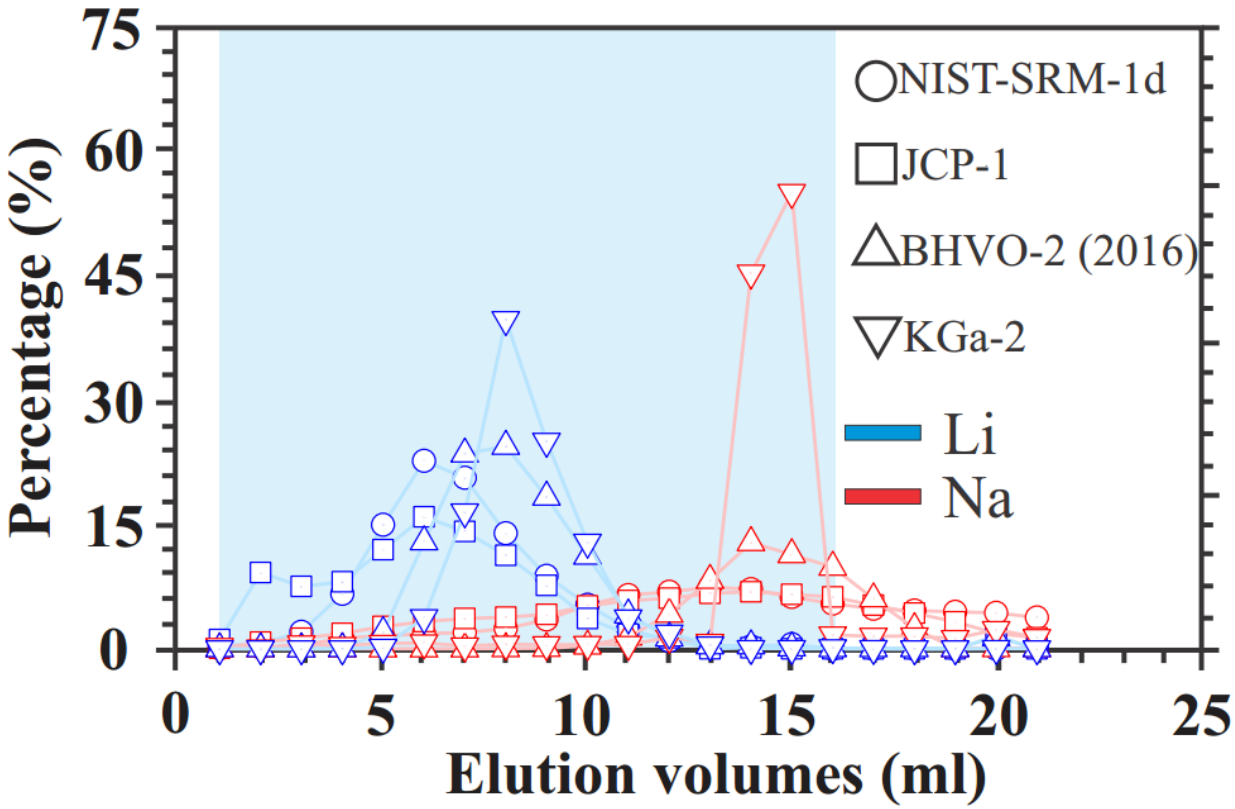

Figure 1. Lithium and Na elution curves of four reference materials via the single-column separation using 1.5 mol·L^{-1} HNO^{3} + 70% methanol.

The Li elution range (blue shaded region) is 1–16 mL. The curves exhibit significant shifts in Li peaks and incomplete Li separation from Na.

3.2. Evaluation of long single-column system for lithium isolation

The preferred elution scheme utilizes a high aspect ratio column set-up to improve separation characteristics (Sossi et al., 2015). Chromatography experiments with a single long column (ID: 0.6 cm and H: 9 cm) packed with 2.4 mL resin do not show any tails of the Li elution peaks, and complete separation of Li from Na was achieved for all geological samples studied here. Commonly, the elution curves of the element fractions become wider with higher matrix loading. There are 0–6 mL separation intervals observed between Li and Na peaks for materials with different element concentrations (Fig. 4), and the majority of Na is held by the resin. However, consistent with the conclusion of Tomascak et al. (2016), the significant shifts in Li elution curves are unavoidable for samples with a range of Li contents and matrix/Li ratios, especially for carbonate materials. After our one step column, the total amount of Na in the Li elution fractions varied from 20 to 94 ng, leading to Na/Li ratios between 0.2 and 8.9, and most Na persisted in the collected solution likely comes from inefficient separation. In addition, other matrix elements, such as Mg, Al, K, and Ca, could not be thoroughly eliminated during the one-step column. The presence of matrices with only several times the intensity of Li can cause remarkable shifts in δ^7Li of up to 3% (Magna et al., 2004; Nishio and Nakai, 2002; Tomascak et al., 1999), calling for further purification.

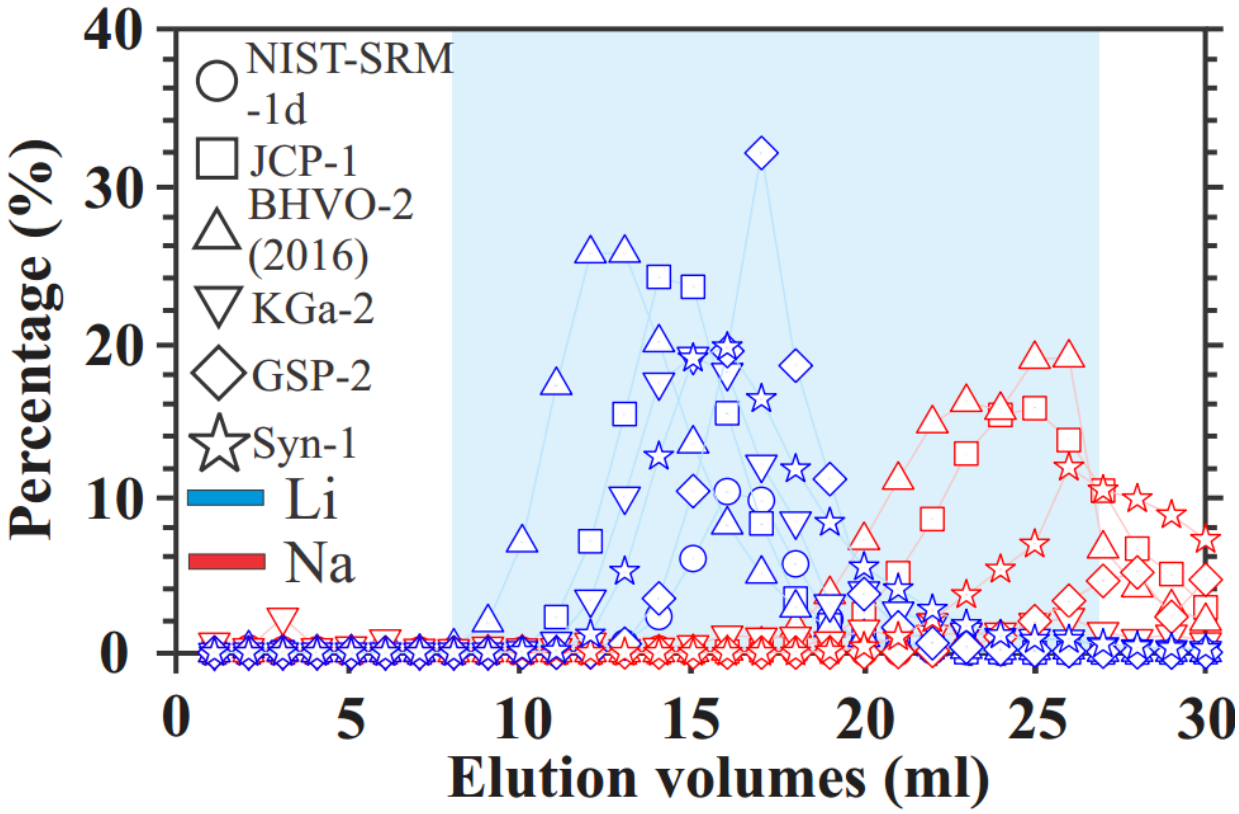

Figure 2. Lithium and Na elution curves of five reference materials and one synergistic fluid via the single-column separation using 0.2 mol·L^{-1} HCl.

The figure shows significant shifts in Li peaks and incomplete Li separation from Na. The Li elution range (blue shaded region) is 8–27 mL.

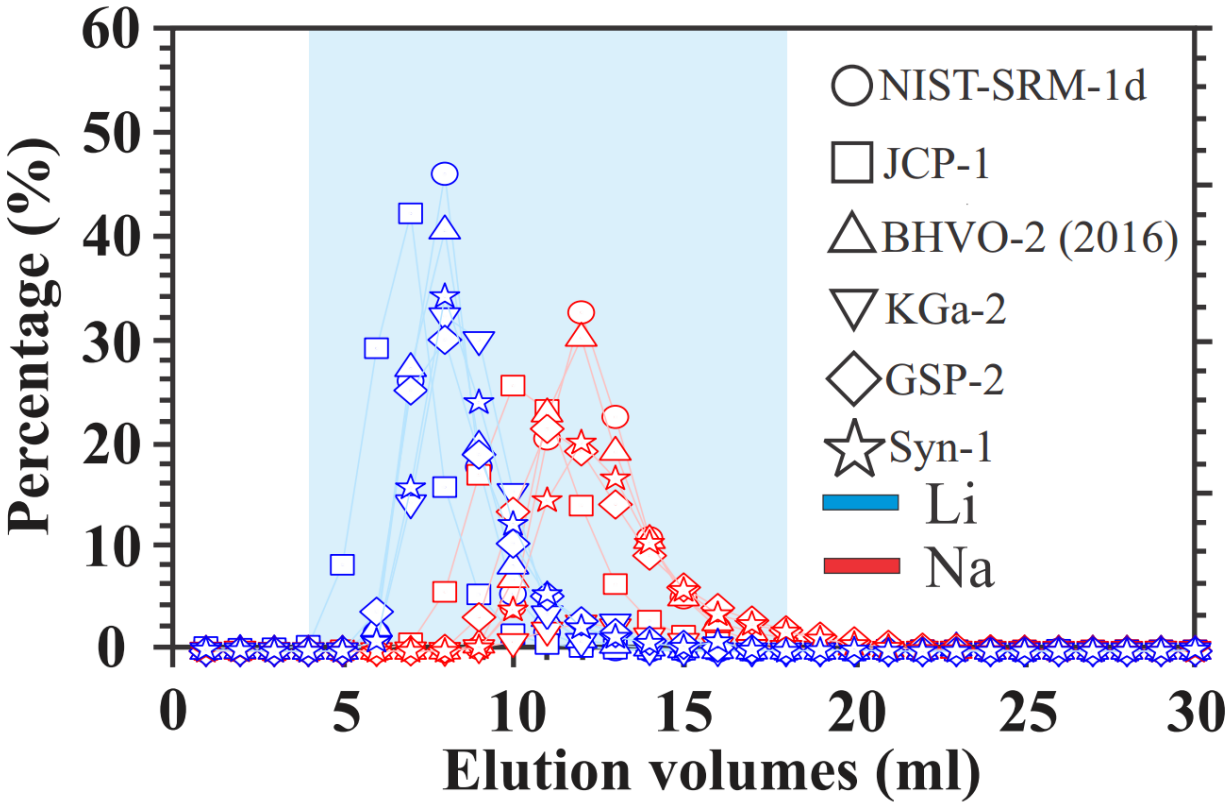

Figure 3. Lithium and Na elution curves of five reference materials and one synergistic fluid via the single-column separation using 0.5 mol·L^{-1} HCl.

The figure shows significant shifts in Li peaks and incomplete Li separation from Na. The Li elution range (blue shaded region) is 4–18 mL.

3.3. Evaluation of dual-column system for lithium isolation

The detailed information of the reported single-column methodology is listed in Table 3. The failure of the above tested single-column systems could be attributed to the bubble formation as discussed above. Moreover, the relatively short elution range and large inter diameters which is unable to separate Li form matrixes sufficiently (Tomascak et al., 2016). Previous one-column chromatographic separation methods are able to reach 100% Li recovery and separate Li from other matrixes. However, varying degrees of shifts in Li peaks in chromatography are generally unavoidable only by the single-column methodology when dealing with diverse geological samples of different compositions (Chan et al., 2002; Tomascak et al., 2016; Van Hoecke et al., 2015). Such effects may contribute to column-induced isotopic fractionation without proper re-calibrations. Therefore, special care is needed to eliminate potential isotope fractionation during the chemical separation process and to decrease the effects of matrix elements, as well as to avoid elution curve drifting. Therefore, a second short column has been designed and added after purification by the first long column, as shown in Table 4. The elution time of the dual-column systems is around 6h (the elution rate of the short column: ~3 min/mL; the elution rate of the short column ~2 min/mL). In comparison with one-column systems, the most significant advantage of this dual-column system is the consistent elution range of the Li-bearing fraction (7–16 mL) for materials with various matrix compositions (Fig. 5), eliminating the need for column re-establishment and elution curve calibration with respect to lithology/mineralogy variability. Furthermore, Na/Li ratios in Li elution fractions are consistently $\lesssim$1, and other matrix elements were readily expelled by the first 3 mL 0.2 M HCl eluent of the second column. Therefore, our dual-column system can effectively eliminate the matrix effects for later MC-ICP-MS analysis. Besides the effective separation from matrix effects and consistent elution range for

Li fractions, the method (Table 4) enables satisfactory Li recovery close to 100%, and the total elution time is only ~6 h (excluding evaporation) and is therefore even more efficient than some single-column systems (i.e., Lin et al., 2016). The whole process generally takes 1.5 days, including the evaporation step. The Li fraction can be fully recovered based on the elution curves and ICP-MS check. Clearly, this purification method yielded a closely complete recovery for Li. The calculated maximum recovery uncertainties of 6 % are mainly caused by the analytical errors (~2 to 5%) reported on Q-ICP-MS measurement, which is acceptable. Therefore, the routine Li isotope analysis of IRMM-016 on our MC-ICP-MS instrument is satisfactory for precision and accuracy check.

Table 3. Chromatographic setup for Li purification in literatures.

References	Magna et al. (2004)	Choi et al. (2013)	Phan et al. (2016)
Resin	BioRad® AG 50W-X8 (200-400 mesh)	BioRad® AG 50W-X8 (200-400 mesh)	BioRad® AG 50W-X8 (200-400 mesh)
Column material	/	Bio-Rad® poly-prep	Bio-Rad® poly-prep
Column dimension	ID: 5 mm	ID: 8 mm	ID: 8 mm
	/	H: 4 cm	H: 4 cm
Resin volume	2.1 mL	1.8 mL	2.0 mL
Eluent	1 M HNO_3 in 80%methanol	1.2 M HNO_3 + 80% methanol	1.5 M HNO_3 in 70% methanol
References	Huang et al. (2010)	Lin et al. (2016)	Bohlin et al. (2018)
Resin	BioRad® AG 50W-X8 (200-400 mesh)	BioRad® AG 50W-X8 (100-200 mesh)	BioRad® AGMP-50
Column material	Polypropylene	Boron-silicate glass	Savillex® Teflon™
Column dimension	ID: 7 mm	ID: 6 mm	ID: 4 mm
	H: 5.5 cm	H: 21.5 cm	H: 2 5cm
Resin volume	2.1 mL	2.0 mL	3.0 mL
Eluent	1 M HNO_3 in 80% methanol	1 M HNO_3 in 80% methanol	0.7 M HCl

Table 4. Lithium recovery and matrix/lithium ratios before and after isolation of reference.

Separation method	Column	Eluent	Sample	Sample load	Ave. elution	Li mass	Li mass	Li recovery	Li elution	Na/Li ratio in	Na/Li ratio in
Single-column	2 ml resin volume (height 4 cm)	21 ml (1.5 M HNO_3 + 70%	NIST-SRM-	1 ml	~1.8	21.0	21.0	99.8	1~14	3557.6	2779.2
			JCP-1			7.2	6.6	91.1	1~14	10134.1	3625.6
			BHVO-2			33.0	32.4	98.1	5~16	3798.8	234.5
			KGa-2			165.1	172.5	104.5	5~15	22.9	1.3
		30 ml 0.5 M HCl	NIST	1 ml	~2	21.0	20.8	99.1	6~13	3557.6	2871.3
			JCP-1			7.2	7.5	104.1	4~16	10134.1	5452.4
			GSP-2			325.1	324.7	99.9	5~18	603.5	578.6
			BHVO-2			33.0	33.9	102.6	5~13	3798.8	3331.9
			KGa-2			165.1	164.6	99.7	6~14	22.9	2.3
			Syn-1			7.2	7.0	97.8	5~11	16439.8	7858.9
		30 ml 0.2M HCl	NIST-SRM-	1 ml	~2	21.0	20.6	98.1	13~20	3557.6	43.2
			JCP-1			7.2	7.4	102.7	10~22	10134.1	1756.8
			GSP-2			325.1	325.4	100.1	12~26	603.5	81.9
			BHVO-2			33.0	31.7	96.1	8~22	3798.8	1131.2
			KGa-2			165.1	169.8	102.9	11~27	22.9	3.7
			Syn-1			7.2	7.0	97.2	13~22	16439.8	794.3
	2.5 ml resin volume[b] (height 9 cm)	60 ml 0.2 M HCl	NIST-SRM-	2 ml	~3	21.0	20.2	96.0	18~32	3557.6	5.2
			JCP-1			7.2	7.2	100.0	22~38	10134.1	8.9
			GSP-2			325.1	325.8	100.2	28~44	603.5	0.3
			BHVO-2			31.5	30.8	97.8	28~44	5434.3	1.2
			BHVO-2			33.0	34.6	104.8	30~42	3798.8	1.9
			BCR-2			36.6	35.5	97.0	28~44	4097.0	2.2
			JB-2			45.4	44.3	97.6	28~42	2859.4	1.3
			JG-2			208.1	206.2	99.1	26~44	998.5	0.2
			KGa-2			165.1	165.8	100.5	30~44	22.9	0.5
			SBC-1			243.7	246.4	101.1	30~44	186.7	0.0
			Syn-1			7.2	7.3	101.6	30~42	16439.8	0.8
			Syn-2			50.0	48.8	97.6	30~44	2000.0	1.6
			NASS-7			8.8	8.8	100.5	28~42	59450.0	3.6
			NOD-A-1			158.0	162.0	102.5	28~40	105.2	0.2
Dual-column[a]	2 ml resin volume[c] (height 4 cm)	1~3 ml: 0.2 M HCl 4~30 ml: 0.5M HCl	NIST-SRM-	1 ml	~2	21.0	21.1	100.5	7~16	5.2	1.1
			JCP-1			7.2	7.3	101.1		8.9	1.2
			GSP-2			325.1	323.0	99.4		0.3	0.3
			BHVO-2			31.5	30.5	96.8		1.2	0.8
			BHVO-2			33.0	34.7	105.1		1.9	1.1
			BCR-2			36.6	36.2	98.9		2.2	0.2
			JB-2			45.4	46.7	102.8		1.3	0.3
			JG-2			208.1	205.3	98.7		0.2	0.1
			KGa-2			165.1	163.1	98.8		0.5	0.4
			SBC-1			243.7	242.7	99.6		0.2	0.0
			Syn-1			7.2	7.6	105.1		0.8	0.4
			Syn-2			50.5	53.3	105.5		1.6	0.8
			NASS-7			8.8	8.7	99.6		3.6	0.8
			NOD-A-1			158.0	156.4	99.0		0.2	0.2

[a]The separation procedure of dual-column system takes about 6 h in all (excluding drying processes); [b]the first column of the dual-column system (18~44 mL will be collected for the second column); [c]the second column of the dual-column system; [d]uncertainty (2 S.D.) of 3%; e range of lithium elution peak in the optimized methods.

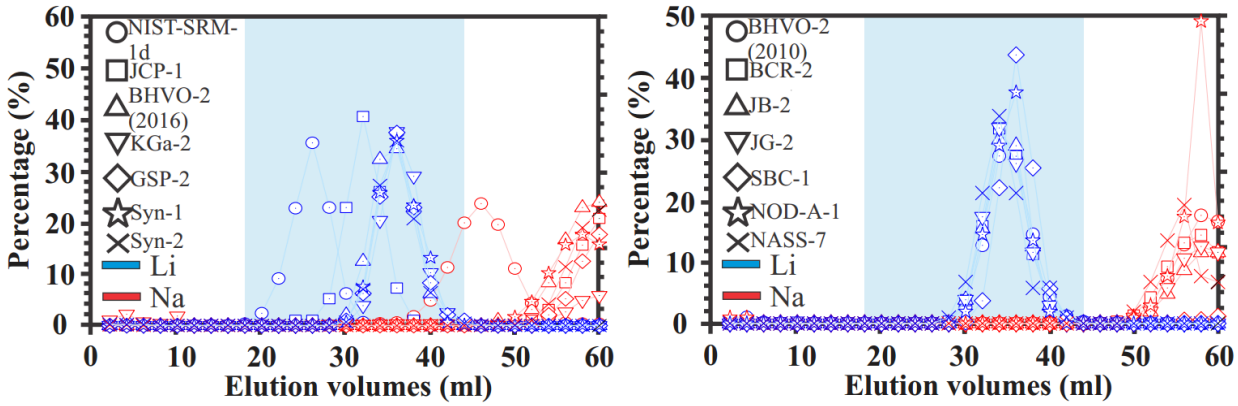

Figure 4. Lithium and Na elution curves of twelve reference materials and two synergistic fluids via the first long column separation in the dual-column system.

The Li elution range (blue shaded region) is 18–44 mL. The curves exhibit significant shifts in Li peaks and incomplete Li separation from Na.

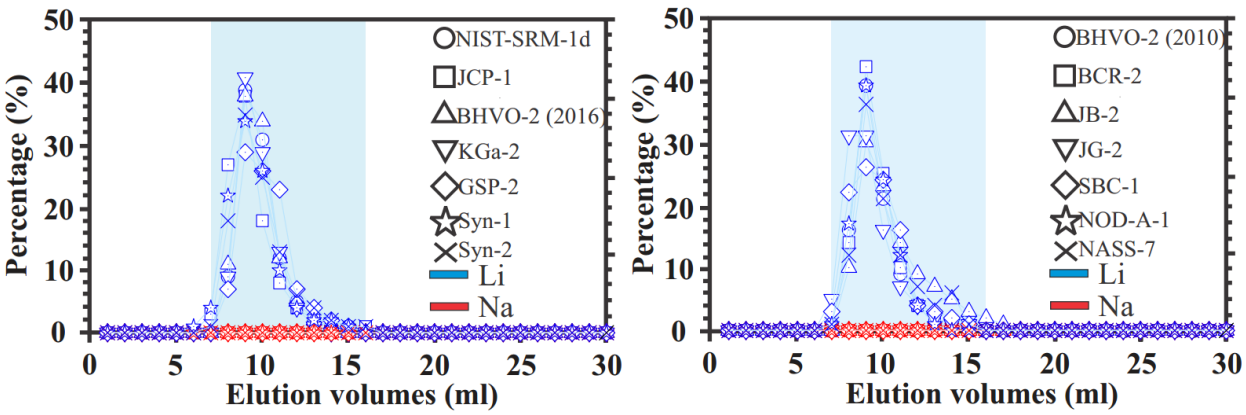

Figure 5. Lithium and Na elution curves of twelve reference materials and two synergistic fluids via the second short column separation in the dual-column system.

The Li elution range (blue shaded region) is 7–16 mL. Consistent Li elution peaks and satisfactory purification were achieved.

3.4. Evaluation of matrix effects

Elimination of the memory effect is essential for the Li isotopic analysis. Li background can be derived from (1) the introduction part (desolvator and spray chamber) and (2) the instrument (sampler and skimmer cones). An Aridus desolvating system is adopted, which allows for small amount of Li for isotopic analysis and high sensitivity. We run at 20 ppb, and the signal exceeds 0.9V/ppb on ^{7}Li (i.e., >18 V) with a memory <0.150 mV. Because of the low sample size and long washing time, memory effects could be avoided. The impact of matrices requires interference monitoring and potential correction for Li isotopic analysis. Na, especially because of its abundance in natural samples and hard separation from Li during chromatography, has long been a problematic contaminant resulting in unsatisfactory accuracy and precision, thus causing a bias as noted in previous studies (Misra and Froelich, 2009). To ensure an accurate Li isotopic analysis, the interference of Na is investigated here by measuring standard solutions IRMM-016 doped with Na at widely varying levels (Fig. 6). The plot indicates that Li isotopic analysis on our instrument at certain conditions reported above is sensitive to the presence of Na. To achieve satisfactory measurement of Li isotopes, the ratio of Na/Li for sample analysis should be less than 100% after chemical purification.

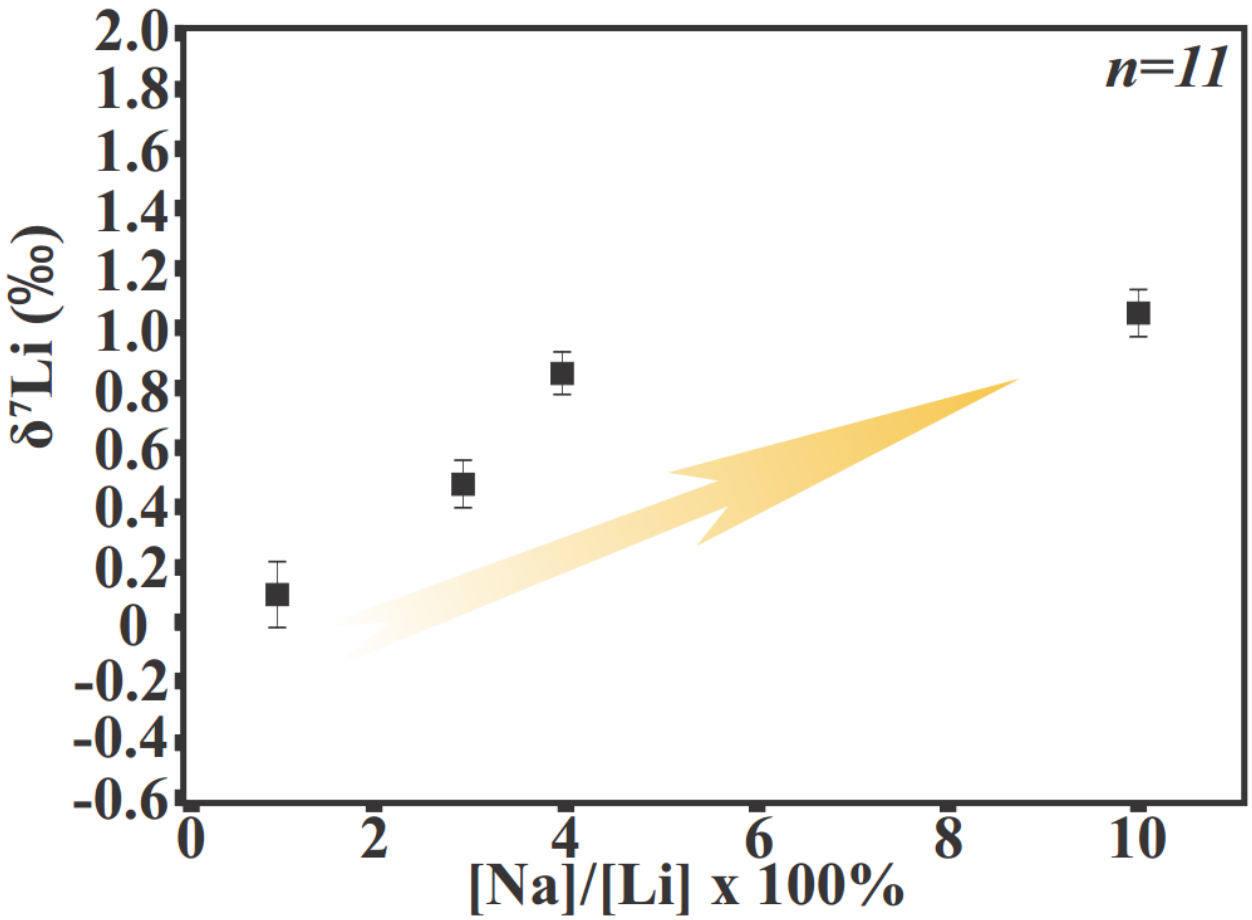

Figure 6. Lithium isotopic variations of IRMM-016 Li spiked with different amounts of Na relative to the unspiked Li solution.

3.5. Evaluation of Li loadings

Considering most of natural rocks/fluids have relative low Li mass fraction, it is necessary to evaluate any possible influence of the amount of loaded Li and other matrix cations on the separation ability of Li using the new dual-column method. Total capacity of the wet resin (AG50W resin X8, 200–400 mesh, 1.74 meq·mL^{-1}) is 4.2 meq for the long column and 3.4 meq for the short column (meq = mg × valence / molar mass). The load is less than 5% of the total resin capacity. The capacity to load ratio is within the range required for the quantitative separation of Li. The success in Li purification is generally limited by the separation of Li from Na (Misra and Froelich, 2009). The selected geostandards at a certain amount (see Sample Preparation section) amount have a large range of Na/Li (22.9–59,450.0) and [Li] (7.2–325.1 ng). The results yielded satisfactory Li recovery, which is good enough to avoid inner-column fractionation.

3.6. Lithium isotopic composition in geological reference materials

We report Li isotope compositions in a range of geological standards to evaluate the entire procedural accuracy and reproducibility for the newly developed dual-column separation method. All geostandards used here were replicated 2–4 times from digestion to isotopic analysis. Lithium contents and matrix/ Li ratios in these 12 geostandards and 2 synthetic fluids (Syn-1 and Syn-2) before and after column separation are reported in Table 4. The Li fraction in each sample was separated following the dual-column method described above (see Chromatography section), and Li isotope ratios were measured using the Neptune MC-ICP-MS as described previously.

The Li isotopic compositions of samples analyzed in this study fall within the range of reported values selected literature data reported. We listed the values measured in this study in Table 5 as references for future inter-laboratory comparison. The results from the BHVO-2 (2010) (BHVO-2

standard purchased in 2010, 4.63±0.29‰, n=3), BCR-2 (3.02±1.11‰, n=7), JB-2 (4.71±0.23‰, n=13), are consistent with published data within the analytical error. However, the standard basalt BHVO-2 (2016) (BHVO-2 standard purchased in 2016, 5.68±0.14‰, n=7) show an increase of ~1 per mill compared to that of BHVO-2 (2010). The reported values after multiple replicates indicate the heterogeneity of BHVO-2 in terms of Li isotope composition. In addition, we observed a negligible variance of [Li] in the elemental compositions of the two BHVO-2 references. In this case, we speculate that the heterogeneity of Li isotope composition in BHVO-2. The results demonstrate that the basalt materials of BHVO-2 should be treated with caution for inter-laboratory comparisons. The average δ^7Li values measured for two granite standards JG-2 (0.42±1.01‰, n=12) and GSP-2 (-0.56±0.55‰, n=3) are in agreement with published data (-0.7 to 0.42‰, James and Palmer, 2000; Jeffcoate et al., 2004; Lin et al., 2016; Phan et al., 2016; Pistiner and Henderson, 2003). The seawater standard NASS-7 has a δ^7Li value of 31.4 ‰ (30.42±0.97‰, n=3), which is consistent with the published NASS-5 and NASS-6 values (29.6 to 30.87‰, Choi et al., 2013; Huang et al., 2010; Lin et al., 2016; Pfister et al., 2017; Rosner et al., 2007). The carbonate standard JCP-1 shows δ^7Li of 19.6 ‰, which is slightly lower than the reported data (20.16-20.27‰, Bohlin et al., 2018; Huang et al., 2010), but the difference is within our two standard derivations. Clay standard KGa-2 (kaolinite) presents δ^7Li of 0.15±0.14‰ (n=3), close to reported data of 0.1 ‰ (Tsai et al., 2014). The first-published Li isotopic values in three sedimentary geostandards, carbonate standard NIST-SRM-1d, manganese nodule standard NOD-A-1, and shale standard SBC-1 are 5.63±0.48‰ (n=4), 26.31±0.97‰ (n=7), and 0.29±0.23‰ (n=3) respectively, allowing for inter-laboratory data comparison. We consider the relatively low value of NIST-SRM-Id is mainly induced by the mixed clay fraction.

Table 5. Summary of measured δ^7Li isotope values and reported data in studied reference materials.

Reference	Reference	δ^7Li (‰)	2S.D.	Reference	Reference	δ^7Li (‰)	2S.D.
BHVO-1	James and Palmer (2000)	5.8	/	JG-2	Lin et al (2016)	0.15	0.15
BHVO-1	Thermo Finnigan Report	4.61	/	JG-2	Phan et al (2016)	0	0.2
BHVO-1	Chan and Frey (2003)	5.2	/	JG-2	Jeffcoate et al (2004)	0.24	0.2
BHVO-1	Pistiner and Henderson (2003)	5.5	0.6	JG-2	Pistiner and Henderson (2003)	-0.7	0.4
BHVO-1	Pistiner and Henderson (2003)	4.7	0.4	JG-2	James and Palmer (2000)	0.4	0.1
BHVO-1	Bouman et al (2004)	5	1.5	JG-2	This study (n=12)	0.32	0.31
BHVO-1	Rudnick et al (2004)	4.3	/				
BHVO-2	Rosner et al (2007)	4.68	0.16	GSP-2	Lin et al (2016)	-0.78	0.25
BHVO-2	Lin et al (2016)	4.5	0.24	GSP-2	Sun et al (2016)	-0.8	0.3
BHVO-2	Choi et al (2013)	4.46	0.37	GSP-2	This study (n=3)	-0.56	0.55
BHVO-2	Jeffcoate et al (2004)	4.66	0.22				
BHVO-2	Gao and Casey (2012)	4.29	0.23	IRMM-016	Lin et al (2016)	0	0.16
BHVO-2	Huang et al (2010)	4.63	0.16	IRMM-016	Pfister et al (2017)	0.2	0.3
BHVO-2	Elliott et al (2006)	4.8	0.3	IRMM-016	Macpherson et al (2014)	0.1	0.4
BHVO-2	Pogge von Strandmann et al	4.9	0.8	IRMM-016	Phan et al (2016)	0.2	0.2
BHVO-2	This study (n=3)	4.63	0.29	IRMM-016	Millot et al (2004)	0.2	0.24
BHVO-2	This study (n=7)	5.68	0.14	IRMM-016	Jeffcoate et al (2004)	0.14	0.04
				Syn-IRMM-	This study (n=3)	0.19	0.22
BCR-1	Phan et al (2016)	2.5	0.5				
BCR-1	Magna et al (2004)	2.38	0.52	NASS-5	Choi et al (2013)	30.55	0.45
BCR-1	Teng et al (2006)	2	0.7	NASS-5	Choi et al (2010)	30.29	0.65
BCR-2	Choi et al (2013)	2.84	0.45	NASS-5	Rosner et al (2007)	30.64	0.44
BCR-2	Rosner et al (2007)	2.87	0.39	NASS-5	Huang et al (2010)	30.72	0.17
BCR-2	Huang et al (2010)	2.6	0.3	NASS-6	Lin et al (2016)	30.87	0.15
BCR-2	Bohlin et al (2018)	2.82	0.13	NASS-6	Pfister et al (2017)	29.6	2.2
BCR-2	This study (n=7)	3.02	0.51	NASS-6	Pogge von Strandmann et al	31.3	0.9
				NASS-7	This study (n=3)	30.42	0.97
JB-2	Moriguti and Nakamura (1998)	4.9	0.7				
JB-2	Tomascak et al (1999)	5.1	1.2	NIST-SRM-	This study (n=4)	5.63	0.48
JB-2	James and Palmer (2000)	6.8	/				
JB-2	Nishio and Nakai (2002)	4.3	0.3	JCP-1	Huang et al (2010)	20.16	0.2
JB-2	Pistiner and Henderson (2003)	3.9	0.4	JCP-1	Bohlin et al (2018)	20.27	0.41
JB-2	Zack et al (2003)	4.7	/	JCP-1	This study (n=3)	19.56	0.53
JB-2	Jeffcoate et al (2004)	4.3	0.26				
JB-2	Magna et al (2004)	4.7	0.29	NOD-A-1	This study (n=7)	26.31	0.97
JB-2	Rudnick et al (2004)	4	/				
JB-2	Seitz et al (2004)	5.2	/	SBC-1	This study (n=3)	0.29	0.03
JB-2	Huang et al (2010)	4.31	0.69				
JB-2	Chan et al (2002)	5.1	0.4	KGa-2	Tsai et al (2014)	0.1	/
JB-2	This study (n=13)	4.71	0.23	KGa-2	This study (n=3)	0.15	0.04

4. Conclusions

We investigated multiple Li purification protocols in the literature and demonstrated that satisfactory Li separation in various geological materials could not be achieved by the dual-column methods tested in this study. Instead, we developed a new dual-column separation method using long (8 cm) and short (4 cm) chromatographic columns loaded with 2.5 mL and 2.0 mL AG 50W-X8 resin, respectively. Compared to one-column systems, this dual-column system has two distinct advantages: (1) It enables the efficient (~6 h, excluding evaporation time) Li elution and satisfactory Li recovery, with negligible matrix residues (i.e. Na/Li$\lesssim$1, as well as Ca, Mg, Al, K). (2) The dual-column isolation routinely achieves a consistent elution curve for Li fractions (7–16 mL), avoiding re-calibration of columns with respect to compositional variations. Our columns can generally be used for chemically diverse geological samples, eliminating potential bias caused by compositional variations and facilitating further geochemical and paleoclimatological research. The δ^7Li values in the range of geological materials studied here agree well with published data. We reported accurate and reproducible Li isotope measurements in various geostandards, including seawater (NASS-7), igneous rocks (BHVO-2, BCR-2, JG-2, JB-2, and GSP-2), biogenetic/abiogenic carbonates (IRMM-016, JCP-1, and NIST-SRM-1d), manganese nodules (NOD-A-1) and shale/clay (SBC-1 and KGa-2). These results could serve as reference values for quality control and inter-laboratory calibration for future research. The significant Li isotopic variances (~1‰) in BHVO-2 from different batches suggested that heterogeneity in this standard and isotopic studies using this standard should be treated with caution.

CHAPTER 3: EXPERIMENTAL INVESTIGATION OF LITHIUM ISOTOPE FRACTIONATION DURING KAOLINITE ADSORPTION: IMPLICATIONS FOR CHEMICAL WEATHERING

This chapter is published as: Li, W. and Liu, X. M. (2020). Experimental investigation of lithium isotope fractionation during kaolinite adsorption: Implications for chemical weathering. Geochimica et Cosmochimica Acta, 284, 156-172.

1. Introduction

Chemical weathering, defined as the chemical dissolution of rocks and minerals on Earth's surface, transfers essential nutrients from the source region into the oceans, eventually modulating global climate over geological time scales (e.g., Kump et al., 2000; Tabor et al., 2002; John et al., 2003; Willenbring and Von Blanckenburg, 2010; Heimsath et al., 2012). Lithium (Li) isotope fractionations have been used to examine long-term chemical weathering, which contributes to the transfer of terrestrial nutrients to oceans, and is known to modulate the global carbon cycle and climate change by carbonate mineral formation (e.g., Dosseto et al., 2015; Tomascak et al., 2016; Penniston-Dorland et al., 2017). As chemical weathering is typically incongruent, soil formation serves as a critical Li sink and is accompanied by significant Li isotope fractionations. Because the Li isotopic system is less sensitive to carbonate weathering and biological activities, it is a unique weathering tracer whose behavior is dominantly regulated by the changes in silicate weathering intensity (e.g., Huh et al., 1998, 2001; Pistiner and Henderson, 2003; Hathorne and James, 2006). Stable Li isotopic compositions (reported as per-mil variations from the stable isotopic composition of an international Li standard by the notation of δ^7Li [‰] = $\{[(^7Li/^6Li)_{sample}/(^7Li/^6Li)_{standard}] - 1\}\times 1000‰$) preserved

in sedimentary records such as carbonate sediments thus provide insights into long-term feedbacks between climate and weathering (Penniston-Dorland et al., 2017; Pogge von Strandmann et al., 2017a). Marine δ^7Li records have been examined to interpret changes in weathering, such as (i) Li budget balances between riverine and submarine reverse weathering fluxes during the Cenozoic (e.g., Misra and Froelich, 2012; Vigier and Goddéris, 2015), (ii) considerable changes in denudation regimes as influenced by temperature (climate)-controlled oceanic sinks during the Cenozoic (Li and West, 2014), (iii) variations in river and hydrothermal fluxes during the Jurassic Oceanic Anoxic Events (e.g., Pogge von Strandmann et al., 2013; Lechler et al., 2015), and (iv) dramatic changes in Li inputs from continental weathering during the period of the Hirnantian glaciation (Pogge von Strandmann et al., 2017b).

Numerous studies have focused on Li isotope geochemistry within riverine systems to understand weathering processes, and possible links between Li isotope fractionation and chemical weathering has been vigorously debated. Pioneering research (Huh et al., 1998) suggested the substantial correlation between river Li isotope fractionation and weathering intensity. Following this notion, Li fluxes have been positively correlated to weathering rates, whereas riverine δ^7Li values have been shown to reflect "weathering intensity" (Kisakürek et al., 2004), "weathering congruency" (Pogge von Strandmann et al., 2008), and "weathering efficiency" (Pogge von Strandmann and Henderson, 2015). A study on Icelandic rivers suggested that silicate weathering mass fluxes and rates are difficult to infer based on the δ^7Li values of riverine sediments derived from multiple sources (Vigier et al., 2009). In comparison, studies of the Orinoco River (Huh et al., 2001), Mackenzie River (Millot et al., 2010b), and the Amazon River (Dellinger et al., 2015; 2017) have shown close relationships between river Li isotopic composition and physicochemical indexes defined as "weathering regimes", which depend on

interrelated factors including weathering rates, temperature, and climate (Pogge von Strandmann et al., 2010; Wang et al., 2015; Weynell et al., 2017; Gou et al., 2019; Bohlin and Bickle, 2019). Riverine Li isotopic ratios could be controlled by the water-rock interaction time in both subsurface and river (e.g., Wanner et al., 2014; Liu et al., 2015). Specifically, studies on the Lena River imply that riverine δ^7Li depends on the balance between rock dissolution and soil formation rather than climatic and weathering regimes (Murphy et al., 2019). No apparent correlation was found between riverine δ^7Li values and traditional weathering proxies such as Si content in streams draining mono-lithology (Liu et al., 2015). It is expected since dissolved Si is not conservative in the riverine system, while Li is largely conservative (Bencala et al., 1990; Wilke and Dayal, 1982). Investigations on the Ganges-Brahmaputra River and the high relief areas of the Yangtze River indicated that Li isotopes reflect weathering congruency and intensity (Pogge von Strandmann et al., 2017b; Ma et al., 2020). However, there is no universal correlation between riverine dissolved δ^7Li and weathering rates, and a second weathering step resulting in high dissolved δ^7Li has been found within floodplain sediments compared with mountainous regions (e.g., Bagard et al., 2015; Pogge von Strandmann et al., 2017b; Bohlin and Bickle, 2019; Ma et al., 2020).

Using Li isotopes to trace chemical weathering and climate relies on our ability to link isotope fractionations to soil formation. The processes may affect riverine Li isotopic ratios and can be addressed by well-constrained laboratory experiments: (i) how Li isotope fractionation between clays and its surrounding solutions responds to climate and corresponding tectonic controls, and (ii) which mechanism (kinetic vs. equilibrium) regulates Li isotope behavior during clay uptake during chemical weathering. Commonly, the equilibrium fractionation mechanism verified for metal isotopes (e.g., Zn, Guinoiseau et al., 2016; Ca, Brazier et al., 2019) has been

applied for Li isotopes in low-temperature fluid-clay interactions. The Li isotope fractionation, along with clay formation, is critical as ^{6}Li is preferentially hosted into octahedral sites in clay structures. All else being equal, the Li incorporation into high coordination number environments such as lattice octahedrons prefers the lighter isotope, suggested by the equilibrium stable isotope fractionation theory (Schauble, 2004). Supportively, it agrees with the result from the theoretical prediction, revealing that ^{7}Li is preferentially left in the aquo-complex (Bogatko et al., 2013; Yamaji et al., 2001).

Previous sorption experiments have indicated that Li isotope fractionations vary due to differences in clay mineralogy, i.e., >10‰ for gibbsite, 1–3‰ for ferrihydrite and chlorite, ~7‰ for kaolinite, and close to 0‰ for smectite and illite (Millot and Girard, 2007; Pistiner and Henderson, 2003). At starting Li concentrations ([Li] of 1 to 12 M) far in excess of natural concentrations, the intercalation of Li into gibbsite results in isotope fractionation between dissolved (aqueous, 'aq') and adsorbed ('ad') phases ($\Delta^{7}Li_{aq\text{-}ad} = \delta^{7}Li_{aq} - \delta^{7}Li_{ad}$) (Wimpenny et al., 2015). The magnitude of isotope fractionation depends on the availability of octahedral sites in gibbsite structure and aqueous anion speciation. Synthesis of smectite at temperatures ranging from 90 ºC to 250 ºC produces substantial variations in Li isotope fractionations (Vigier et al., 2008), which has been interpreted as the equilibrium isotope fractionation dependent on bond stiffness, temperature, and aqueous chemistry (e.g., pH and anionic composition). Based on ^{7}Li-NMR, Hindshaw et al. (2019) synthesized Mg-rich layer silicates and calculated site-specific $\delta^{7}Li$ of -21.5±1.1‰, -0.2±1.9‰ and 15.0±12.3‰ for clay octahedral, outer-sphere, and pseudo-hexagonal sites, respectively. To date, field studies and corresponding quantitative models assumed different equilibrium fractionation factors in a wide range of 13 ‰ to 30‰ between clays and water (e.g., Hathorne and James, 2006; Misra and Froelich, 2012; Bouchez et al., 2013;

Wanner et al., 2014; Bohlin and Bickle, 2019; Gou et al., 2019). Notably, recent batch basalt alternation experiments in ambient conditions by Pogge von Strandmann et al. (2019) produced Li isotope data that can be fitted by Rayleigh models, hinting a possible kinetic control. In addition, theoretical calculations have recognized the kinetic controls on Li isotope fractionations during cation mineral exchange (Hofmann et al., 2012). Clay synthesis experiments indicated a potential rate-dependent kinetic isotope effect superimposed on the equilibrium Li isotope fractionation at high pH and ambient temperatures (Hindshaw et al., 2019). Here, we performed closed-system batch experiments at room temperature to assess the mechanisms and quantify the magnitudes of Li isotope fractionations during adsorption onto a common clay mineral kaolinite under constrained laboratory conditions.

2. Materials and Experimental Setup

2.1. Materials preparation

We produced deionized water (18.2 MΩ·cm) from a Milli-Q element system (Direct-Q 3UV) for experimental preparations and used analytical-grade (>99.9% purity) LiCl, $FeCl_3$, NaCl, NaOH, and sodium hexametaphosphate (NaHMP) from Acros Organic™. Commercially available hydrochloric acid (HCl) was purified in-house by double distillation in a Teflon® sub-boiling still (Savillex™, NC, USA) and diluted to the required molarities. Our study focuses on Li adsorption onto one common secondary clay kaolinite to reach the first-order analogy to weathering environments. Here, we used the well-characterized high-defect kaolinite (KGa-2) reference material obtained from the Clay Mineral Society (www.clays.org, VA, USA). After immediate water cooling at 30 ºC, the solid product was recovered and separated by centrifugation (30 min, 12,000 rpm), and dried in an oven at 60 ºC for over two days. The N_2-BET specific surface area of kaolinite (KGa-2) (0.1–1 μm size) has been reported in a previous

study (Brazier et al., 2019), where the BET-N_2 value of kaolinite is 21.1 m^2/g. It is comparable to the certified value (the Clay Mineral Society, http://www.clays.org/), where the BET-N_2 value of KGa-2 is 23.5 m^2/g.

Critically, samples were processed to extract clay-sized fractions (0.1–1 μm), and removed surface impurity or labile components to avoid possible errors in chemical analysis. Here, we employed the washing protocol modified from Guinoiseau et al. (2016) and Brazier et al. (2019). Clay samples were immersed overnight in a mixture of NaHMP (dispersant, 10 mM) and Milli-Q water, and the clay fractions (0.1–1 μm size) were recovered based on Stokes' law. In brief, the NaHMP-extracted clay slurry was introduced into acid-cleaned centrifuge tubes using a pipette, then centrifuged at 10,000 rpm for 0.5 h, and the supernatant was discarded. A 0.5 M NaCl solution was then added to the slurry, centrifuged at 10,000 rpm for 0.5 h, and the supernatant discarded. After that, Milli-Q water was added, centrifuged at 10,000 rpm for 0.5 h, and the supernatant discarded. The water rinse process was repeated to remove excess salts and NaHMP until the concentrations of Na and P in eluent were below the detection limits of the ICP-MS instrument at sub-ppb levels to ensure that the clay was thoroughly clean to perform adsorption experiments. Finally, recovered clays were dried in a vacuum oven at 60 ºC, powdered in an agate mortar, and stored at 4 ºC for experiments. Before the experiments, we examined the possible influence of Li released from the clay structure using control groups to which no Li was added. We found the total Li release from the clay under the studied conditions to be negligible (less than 0.1 $ng \cdot mL^{-1}$), comparing to total Li loads of 14–7,000 $ng \cdot mL^{-1}$ used in these experiments.

2.2. Experiment setup

To evaluate the influence of common environmental factors on the isotope fractionation between aqueous and adsorbed Li, we designed three individual sets of kaolinite adsorption experiments under ambient temperature conditions: (i) the time-series experiments, in which we tracked aqueous chemistry as a function of reaction time for up to 15 days at pH of 7 with the constant starting Li concentration of 10 and 75 $\mu mol \cdot L^{-1}$; (ii) the pH-dependent experiments, in which we varied the solute pH from 3 to 10 with the constant starting Li concentration of 75 $\mu mol \cdot L^{-1}$; and (iii) the concentration-control experiments, in which we varied the starting Li concentration from 2 to 1,000 $\mu mol \cdot L^{-1}$at a pH range of 3 to 10. We note that KGa-2 kaolinite displays negative surface charges over the studied pH range of 3-10, leading to the electrostatic attraction to dissolved cations. Batch experiments were performed in 50 mL centrifuge tubes filled with the clay slurry (10 $g \cdot L^{-1}$) and continuously stirred at 150 rpm in a temperature-controlled water bath shaker (Thermo Scientific^{TM}). LiCl solutions were prepared with pre-set background electrolyte (NaCl) to evaluate the effect of ionic strength (IS) on surface complexation (i.e., chemisorption or inner-sphere complexation versus physisorption or outer-sphere complexation), and 10 $g \cdot L^{-1}$ kaolinite suspensions were added. Experiments were performed for the pH-dependent and concentration-control sets with equilibration for 24 h, which is long enough to achieve the steady-state as supported by the time-series sets. The applications of solute IS=0.001 $mol \cdot L^{-1}$and 0.1 $mol \cdot L^{-1}$are intended to represent natural freshwater and brines, respectively. In the following text, we defined pH≥7 as “high pH” and pH<7 as “low pH”, and IS=0.001 $mol \cdot L^{-1}$as “low IS” and IS=0.1 M as “high IS”.

Desorption experiments were carried out in the same clay-solution batch-systems to investigate Li complexation modes on kaolinite. We performed two kaolinite adsorption experiments as the control sets, which were equilibrated for 15 days at IS=0.001M, pH=8.5

(Kaolin (1)), and 4.3 (Kaolin (2)), and initial Li concentration of 75 μmol·L^{-1}. Then, clay slurry after supernatant removal was treated with three individual desorption steps for 15 days. In Step (1), solute IS was increased from 0.001 M to 0.1 mol·L^{-1}NaCl. In Step (2), 0.0001 M Hexamminecobalt (III) chloride ($[Co(NH_3)_6]Cl_3$) was added into the clay-solution system (Brazier et al., 2019). In Step (3), solute pH was decreased from 8.5 to 4.3 through dropwise acidification using 0.001 M HCl and compared with the control group. The same sampling procedure as that used for the adsorption experiments was applied. Both control and desorption sets were performed in triplicates to ensure reproducibility and accuracy.

Over the course of experiments, we did not employ any pH buffers in order to minimize undesired complexation and particle aggregation. We maintained the solute pH at ±0.2 by regular monitoring using a Thermo Scientific^{TM} Orion Star A221 portable pH meter; the pH was adjusted by doping with trace amounts of HCl and NaOH as necessary. All reagents were prepared from distilled acids and Milli-Q water to avoid contamination. Supernatants were filtered through 0.22 μm cellulose acetate syringe filters (Thermo Scientific^{TM}) and transferred into acid-cleaned centrifuge tubes. The suspensions were centrifuged at the end of the experiments, and processed kaolinite was rinsed with water, air-dried, crushed, and transferred into borosilicate vials. Samples were stored at 4 ºC for chemical analysis. Solute Li concentrations are reported as [Li] in the text. The Li isotopic compositions of the dissolved and solid phases (adsorbed Li) were analyzed and are reported relative to the international standard (see Analytical Methods) in a δ notation (δ^7Li_{aq}, dissolved Li; δ^7Li_{ad}, adsorbed Li). And, $\Delta Li_{aq\text{-}ad}$ represents the isotope fractionation between dissolved Li and adsorbed Li.

3. Analytical Methods and Models

3.1. Zeta potential analysis

To analyze the interfacial electrical fields of kaolinite, aliquots of clay dispersions from each experimental set were transferred into centrifuge tubes and re-suspended with a 10-min ultrasonic treatment. The electrophoretic mobility of the clays was measured based on their direction and velocity along with applied electric fields in a Malver^{TM} Zetasizer Nano ZS90 equipped with a red (633 nm) laser and converted to zeta potentials based on the Smoluchowski equations. At least three replicate analyses were performed for each sample in ambient conditions to estimate the reproducibility and uncertainties.

3.2. Infrared spectroscopy

To determine the changes of Li complexation on kaolinite surfaces at different pH, we measured the attenuated total reflectance Fourier transform infrared (ATR-FTIR) spectra of reacted solids. All ATR-FTIR spectra were collected in the 400–4,000 cm^{-1} range under ambient temperature, using a BRUKER^{TM} Alpha spectrometer equipped with an ATR attachment. Air-dried samples were directly coated on a diamond crystal surface and pressed tightly by a pressure head. Twenty-four scans were collected at a resolution of 2 cm^{-1}, and background spectra were acquired in clay-free areas of the diamond sample mount. The ATR-FTIR spectra data were collected and processed using the OPUS software.

3.3. Element analysis

Elemental analyses were performed on an Agilent^{TM} 7900 quadrupole inductively coupled plasma mass spectrometer (Q-ICP-MS) at the Plasma Mass Spectrometry Lab of the University of North Carolina, Chapel Hill. Concentration calibration curves were acquired by using external standards with a series of multi-element reference solutions of known concentrations (prepared by the ICP standard solutions, Inorganic Ventures^{TM}). Internal standards, including Be, Ge, Rh, In, Ir, and Bi, were added for instrumental drift correction. Data

quality was controlled based on repeated analyses of international reference materials BHVO-2 (Hawaiian basalt) and SLRS-5 (Ottawa Britannia water) (element compositions certified by the United States Geological Survey and the National Research Council of Canada, respectively) (Appendix 1). Relative standard derivation (RSD) < 3% can be achieved, and digestion yields were 100±5%. The percentage of Li adsorption onto clays was calculated based on staring and final solute Li concentrations and was reported in wt.% (weight percent).

3.4. Column purification

Prior to Li isotopic analyses, solid and liquid samples were processed in different ways. For liquid samples, filtrates were evaporated and re-dissolved in 0.2 M HCl solutions. The solid residues were completely digested by successive acid baths in Teflon beakers (Savillex^{TM}) using a concentrated HF-HNO_3-HCl mixture. The Li fraction was purified by two-step cation-exchange chromatography (Bio-Rad^{TM} AG50W X-8 resin) using HCl as the eluent. In brief, samples were evaporated to dryness and converted to HCl form in 0.2 M HCl. Samples were first passed through a cycle of the first column, which is filled with 2.4 mL AG50-X8 200-400 mesh cation-exchange resin (Bio-Rad^{TM}). After sample loading, 60 mL of 0.2 M HCl was added slowly to the column at an average elution rate of ca. 2 min·mL^{-1}. The Li fraction between 19 and 44 mL was collected. Collected 1st Li fraction was dried down, and re-dissolved in 1 mL 0.5 M HCl, and passed through another cycle of the second column, filled with 2 mL AG50-X8 200-400 mesh resin (Bio-Rad^{TM}). The Li fraction between 4 and 16 mL was collected, with Li/Na>1. We achieved satisfactory Li yields (~100%), and the total procedural blanks (0.004 ng Li) far less than the experimental Li loads had negligible impacts on the isotopic analyses. Because the matrix elements-to-Li ratios were less than 1, matrix interferences during isotope measurements can be avoided.

3.5. Lithium isotope analysis

Liquid samples were analyzed on the Thermo Scientific^{TM} Neptune Plus multi-collector inductively coupled plasma mass spectrometer (MC-ICP-MS) at Rutgers University. A concentration matched unprocessed NIST L-SVEC standard was measured before and after each sample to monitor instrument drift. The standard-sample normalization approach was adopted to correct for instrumental mass discrimination. Before isotopic analyses, the Li collected after chromatographic separation was evaporated to dryness, converted into nitric form, and diluted to 20 ppb Li in 2% HNO_3. Prepared Li solutions of 20 ppb were analyzed that, utilizing a Teledyne Cetac Aridus II and X-type Ni skimmer cone, yielded a signal exceeding 18 V on δ^7Li signals with an acid blank of < 150 mV. The high sensitivity of the instrument allows small samples to be processed through ion chromatography, which enables column calibrations to be stable. A standard–sample–standard bracketing method was used, and signals matched to within 5%. Measured isotopic ratios are reported in δ notation, as the deviation in parts per thousand of the measured ^{7}Li/^{6}Li from the to the NIST RM 8545 (L-SVEC) standard (Tomascak et al., 1999). The long-term external uncertainties (two standard deviations, 2 S.D.) of Li isotopic analyses by our MC-ICP-MS instrument are 0.6‰ (W. Li et al., 2019). The granite (GSP-2, -0.64±0.6‰) and basalt (BHVO-2, 4.7±0.6‰) USGS standards were measured, and the values fall within the uncertainties of previously reported data (Lin et al., 2016; Liu and Li, 2019) (Appendix 2). The δ^7Li_{ad} values of adsorbed Li were corrected by the deduction from the original structural Li composition in kaolinite lattice (0.2±0.6‰) following Eq. 1:

$$\delta^7\mathrm{Li}_{\mathrm{ad}} = \frac{[\mathrm{Li}]_{\mathrm{total}} \times \delta^7\mathrm{Li}_{\mathrm{total}} - [\mathrm{Li}]_{\mathrm{kao}} \times \delta^7\mathrm{Li}_{\mathrm{kao}}}{[\mathrm{Li}]_{\mathrm{ad}}} \quad (1)$$

where $[Li]_{total}$ and δ^7Li_{total} are the Li concentration and isotopic composition of reacted kaolinite, and $[Li]_{kao}$ and δ^7Li_{kao} are those of cleaned kaolinite. The isotope fractionation between adsorbed Li and aqueous Li, Δ^7Li was defined as (Eq. 2):

$$\Delta^7\mathrm{Li} = \delta^7\mathrm{Li}_{\mathrm{ad}} - \delta^7\mathrm{Li}_{\mathrm{aq}} \quad (2)$$

For calculations, analytical errors were propagated using the following equation (Eq. 3):

$$\Delta\mathrm{E} = \sqrt{(c_1\Delta\mathrm{W}_1)^2 + (c_2\Delta\mathrm{W}_2)^2 + \cdots + (c_n\Delta\mathrm{W}_n)^2} \quad (3)$$

where ΔE notates the absolute error of additive functions, c is the multiplicative factor, and W represents the additive function input. In the text, we employed the long-term analytical uncertainties for reported data, and the error of 0.6‰ keeps constant.

3.6. Kinetic models

The overall sorption rates and migration processes of the adsorbate at solid-water interfaces are controlled by surface characteristics and the resistance of the solid particles to diffusion. Therefore, the utilization of proper kinetic models can provide instructive information on the mechanism of adsorption processes such as mass transfer and chemical reaction during the entire adsorption process. Here, we use the pseudo-second-order model, the pseudo-first-order model, the intra-particle diffusion model, and the Elovich model to explore Li adsorption kinetics. Linear correlation coefficients (R^2) near or equal to 1, indicating consistency between predicted values and the experimental data, suggest that a particular model effectively describes the observed Li adsorption kinetics. One to three adsorption could be generally distinguished: the first represents the initial rapid to instantaneous adsorption of external adsorbate, the second is the rate-limited adsorption stage, and the third is the equilibrium stage, in which adsorption slows significantly due to the low adsorbate concentrations remaining in the dissolved phase.

The pseudo-first-order model (Lagergren, 1898) is based on solid capacity, which primarily involves ion-exchange physisorption in a homogeneous liquid-solid system, and is generally expressed in a linearized form as follows (Eq. 4).

$$1/q_t = k/tq_t + 1/q_e \quad (4)$$

where q_e is the equilibrium concentration of Li adsorbed on clays or adsorption capacity, q_t is the dissolved Li concentration at time t, and k_1 is the first-order model constant. Pseudo-first-order reactions are those that should occur at some higher order (>1), but occur as a first-order since the concentration of one reactant is high relative to the other(s).

The pseudo-second-order model (Ho and McKay, 1999) is based on a limited adsorbate concentration, which mainly involves chemisorption in a liquid-solid system, and is generally expressed in a linearized form as follows (Eq. 5).

$$t/q_t = 1/k_2(q_e)^2 + t/q_e \quad (5)$$

where q_e is the adsorbed amount of Li at equilibrium, q_t is the adsorbed amount of Li at time t, and k_2 notates the second-order model constant. Pseudo-second-order reactions assume solid-phase adsorption, and that the rate-limiting step is chemisorption involving valence forces through the sharing or exchange of electrons between sorbent and sorbate.

The Elovich model (Low, 1960) is another rate-based equation derived from adsorption capacity, which mainly involves chemisorption in heterogeneous systems and is generally expressed in a linearized form as follows (Eq. 6).

$$q_t = \beta Ln(\alpha\beta) + \beta \mathrm{In}t \quad (6)$$

where q_t is the amount of Li adsorbed on clays at the time t, α denotes the initial Li adsorption rate, and β represents the desorption constant related to the surface coverage and the activation energy for chemisorption. The integration of the rate equation with the same boundary conditions

as the pseudo-first- and second-order equations (as mentioned above) becomes the Elovich equation.

Alternatively, the intra-particle diffusion model (Srihari and Das, 2008) describes adsorption from a mechanistic point of view, which mainly involves diffusion mechanisms, and is expressed in a linearized form as follows (Eq. 7).

$$q_t = k_3 t^{0.5} \quad (7)$$

where q_t is the amount of Li adsorbed on clays at the time t, and k_3 is the intra-particle rate constant. The overall adsorption process may indeed be controlled by one or more steps, e.g., film or external diffusion, pore diffusion, surface diffusion and adsorption on the pore surface, or a multi-linear combination of steps. Our results show that the pseudo-second-order model achieves R^2 values closest to 1 and thus best describes the adsorption kinetics, assuming that the main rate-limiting step is chemisorption involving covalent forces through the sharing or exchange of electrons between Li^+ and clay surface hydroxyl groups.

3.7. Isotherm adsorption models

Adsorption isotherms describe chemical equilibrium and the interaction between adsorbate and adsorbent. The equilibrium state is reached when the adsorbate concentration in the dissolved phase is in the dynamic balance with adsorbent concentration. Here, we employed the widely used Langmuir (Eq. 7) and Freundlich (Eq. 8) isotherm adsorption models to fit the experimental data in concentration-control sets. Importantly, we note that the Langmuir and Freundlich models describe macroscopic data only and do not definitively prove sorption mechanisms. Therefore, the mentioned modeling approaches may imply a single adsorption process or an interplay of multiple adsorption processes.

The Langmuir model (Langmuir, 1918) implies that adsorption takes place with a mono-molecular layer arrangement on adsorbent surfaces, and there is no interaction between the adsorbed molecules. A linearized form of the Langmuir isotherm model can be expressed as follows (Eq. 8)

$$1/Q_e=1/Q_0+1/Q_0K_LC_e \quad (8)$$

Where q_e is the amount of solute adsorbed per unit weight of adsorbent, Q_0 is the theoretical maximum adsorption capacity, C_e notates the equilibrium Li concentration ($mg\cdot L^{-1}$), and K_L represents the Langmuir constant.

The Freundlich isotherm model (Freundlich, 1928) suggests that molecules are adsorbed as a mono-molecular layer or multilayer on heterogeneous adsorbent surfaces, and there is an interaction between adsorbed molecules. A Linearized form of the Freundlich isotherm model can be expressed as follows (Eq. 9)

$$\mathrm{Log}Q_e=\mathrm{Log}K_f+1/n\mathrm{Log}C_e \quad (9)$$

where Q_e is the amount of solute adsorbed per unit weight of adsorbent, C_e is the equilibrium concentration of solute in the bulk solution; n and K_f are Freundlich constants (information about bond energies between the adsorbent and the metal ions.). Generally, the energy distribution of the real solid surface is not uniform. In this case, the Freundlich adsorption model presumes that adsorption occurs on the non-uniform surface, which may be closer to the real surface of clays in nature.

Table 6. Kaolinite Li adsorption and isotope fractionation in time-series sets.

pH	Initial [Li] (uM)	Final [Li] (uM)	2 S.D.	Sorption ratio (%)	Solution δ^7Li (‰)	IS (mol·L^{-1})	Time
7	10	1.9	0.2	81.4	20.1	0.001	5 min
		1.7	0.5	82.9	n.d.	0.001	10 min
		1.7	0.4	82.9	20.6	0.001	20 min
		1.4	0.3	85.7	n.d.	0.001	30 min
		1.3	0.3	87.1	24.5	0.001	1 h
		1.1	0.3	88.6	24.1	0.001	3 h
		1.1	0.3	88.6	n.d.	0.001	5 h
		1	0.1	90	n.d.	0.001	10h
		0.9	0	91.4	25.2	0.001	1 d
		0.9	0.2	91.4	n.d.	0.001	3 d
		0.9	0.2	91.4	25.1	0.001	7 d
		0.9	0.3	91.4	26	0.001	15 d
7	10	2.7	0.6	72.7	11.2	0.1	5 min
		2.4	0.3	75.7	n.d.	0.1	10 min
		2.3	1.2	76.8	19.6	0.1	20 min
		2.1	0.9	78.6	n.d.	0.1	30 min
		2	0.5	80	20.2	0.1	1 h
		1.9	0.7	81.2	20.5	0.1	3 h
		1.9	0.3	81.1	19.9	0.1	5 h
		1.9	0.1	81.4	n.d.	0.1	10h
		1.9	0.5	81.5	20	0.1	1 d
		1.7	0.3	82.7	20.7	0.1	3 d
		1.7	0.4	82.8	22.2	0.1	7 d
		1.9	0.3	81.5	20	0.1	15 d
7	75	47	5.6	37.3	n.d.	0.001	5 min
		42.5	7.2	43.3	10.1	0.001	10 min
		38.3	2.3	48.9	n.d.	0.001	20 min
		35.7	1.1	52.4	n.d.	0.001	30 min
		31.4	2.2	58.1	14.5	0.001	1 h
		32.3	1.7	57	n.d.	0.001	3 h
		32.2	3	57.1	n.d.	0.001	5 h
		30.9	1.6	58.7	n.d.	0.001	10h
		30.9	4.3	58.9	12.4	0.001	1 d
		31.6	5.4	57.9	n.d.	0.001	3 d
		31.2	4.9	58.5	12.3	0.001	7 d
		30.9	3.4	58.9	12.3	0.001	15 d
7	75	42.5	5.1	43.3	n.d.	0.1	5 min
		38	6.5	49.3	9.3	0.1	10 min
		34.6	1.1	53.9	n.d.	0.1	20 min
		33.5	5.4	55.4	n.d.	0.1	30 min
		29.9	4.8	60.1	12	0.1	1 h
		28.5	3.4	62	n.d.	0.1	3 h
		28.4	4.1	62.1	n.d.	0.1	5 h
		28.3	1.4	62.2	n.d.	0.1	10h
		28.1	3.9	62.6	11.8	0.1	1 d
		27.9	4.7	62.9	n.d.	0.1	3 d
		27.9	2.9	62.9	11.6	0.1	7 d
		27.9	2.7	62.9	11.6	0.1	15 d

"n.d." represents not determined.

Table 7. Kaolinite Li adsorption and isotope fractionation in pH-dependent sets.

pH	Initial [Li] (uM)	Final [Li] (uM)	2 S.D.	Sorption ratio (%)	Solution δ^7Li (‰)	IS (M)	Time
3.7	75	66.6	7.3	11.2	6	0.001	24 h
4.4		65.9	1.3	12.2	6.1	0.001	
5.6		55.3	0.6	26.3	9	0.001	
6.6		39	2.7	48	10.8	0.001	
7		27.9	1.4	62.9	12.4	0.001	
7.5		14.1	1.9	81.2	18.2	0.001	
8.5		3.5	0.6	95.4	28.7	0.001	
9.1		6.5	1.4	91.3	25	0.001	
3.7	75	66.6	16.7	11.2	5.9	0.1	24 h
4.4		66.5	20.6	11.3	5.9	0.1	
5.6		59.7	7.2	20.4	8.3	0.1	
6.6		41.7	6.3	44.4	11	0.1	
7		30.7	0.3	59.1	11.8	0.1	
7.4		13.4	0.7	82.1	20.6	0.1	
8.5		2.9	0.2	96.2	29	0.1	
9.1		5.8	0.6	92.2	25.2	0.1	

Table 8. Kaolinite Li adsorption and isotope fractionation in concentration-control sets.

pH	Initial [Li] (uM)	Final [Li] (uM)	2 S.D.	Sorption ratio (%)	Solution δ^7Li (‰)	Adsorbed δ^7Li (‰)	IS (M)	Time (h)
4.3	2	0.6	2.2	72	11.6	0.8	0.001	24 h
4.3	5	2.7	0.9	45.8	9.5	-0.3		
4.3	10	6.7	1.1	32.7	8.6	-0.6		
4.3	25	17.9	4.3	28.4	6.4	-1.5		
4.3	50	42.8	6.8	14.4	6.4	-2.5		
4.3	75	65.9	5.3	12.2	6.1	-3.1		
5.5	5	0.8	0.1	84.3	16.9	1.1	0.001	24 h
5.5	10	2.2	0.4	78	14.4	0.5		
5.5	25	11.7	1.5	53.3	11.2	0.2		
5.5	50	33	5.9	34.1	8.1	-0.4		
5.5	75	55.3	9.4	26.3	n.d.	n.d.		
5.5	100	81.1	15.4	18.9	6.2	-1.1		
5.5	125	104.8	12.6	16.1	n.d.	n.d.		
5.5	5	1	0.3	79.9	19.1	0.4	0.1	24 h
5.5	10	3.1	0.7	69.3	14.9	0.6		
5.5	25	10.5	2.7	58	n.d.	n.d.		
5.5	50	30.5	7	39.1	9.4	-1.2		
5.5	75	59.7	10.2	20.4	n.d.	n.d.		
5.5	100	85.2	6.8	14.8	8.5	-2.7		
5.5	125	110.9	23.3	11.2	n.d.	n.d.		
6.5	10	0.8	0.2	92.1	16.1	1.4	0.001	24 h
6.5	25	7	1.3	72.1	11.9	-0.2		
6.5	50	22.5	4.7	55	n.d.	n.d.		
6.5	75	41.3	4.1	45	9.4	-0.8		
6.5	100	61.5	8	38.5	n.d.	n.d.		
6.5	125	79	12.6	36.8	8.5	-1.9		
6.5	5	0.5	0.1	90.1	23.2	2.1	0.1	24 h
6.5	10	1.8	0.6	82.4	18.4	1		
6.5	25	9.4	3.7	62.2	14.8	0.7		
6.5	50	23.7	3.8	52.5	13.9	0.1		
6.5	75	41.7	4.6	44.4	11	-0.5		
6.5	100	61.1	7.9	38.9	9.5	-1.4		
6.5	125	85.2	13.6	31.8	9.4	-1.4		
7.5	25	2.1	0.2	91.6	26.1	3.7	0.001	24 h
7.5	50	6.3	1.4	87.5	20.4	1		
7.5	75	14.1	2.4	81.2	18.2	0.7		
7.5	100	24.1	1.7	75.9	15.9	0.1		
7.5	125	48.6	11.2	61.1	14.3	-0.2		
7.5	250	178.4	5.4	28.6	n.d.	n.d.		
7.5	500	419.6	67.1	16.1	n.d.	n.d.		
7.5	1000	875	105	12.5	n.d.	n.d.		
8.5	25	0.2	0	99.2	39.7	3.9	0.001	24 h
8.5	50	1.6	0.3	96.7	28.4	3.2		
8.5	75	6.5	0.1	91.3	25	2.3		
8.5	100	20.6	4.1	79.4	22.6	0.5		
8.5	125	34.2	2.4	72.6	n.d.	n.d.		
8.5	250	95.4	24.8	61.8	10.8	-2.3		
8.5	500	291.3	110.7	41.7	n.d.	n.d.		
8.5	1000	771	131.1	22.9	7.7	-4.3		

Table 9. Li desorption from kaolinite and associated isotope behavior.

No.*	Rep.**	pH	Initial [Li] (uM)	Final [Li] (uM)	Sorption ratio (%)	Adsorbed δ^7Li (‰)	Note
Kaolin (1)	1	8.5	75	6.4	91.5	2.3	0.001M NaCl
	2	8.5	75	6.5	91.3	2.2	
	3	8.5	75	7.4	90.2	2.5	
Kaolin (2)	1	4.3	75	66.6	11.2	-3.1	0.001M NaCl
	2	4.3	75	68.9	8.2	-3.7	
	3	4.3	75	65.1	13.2	-3.3	
Step (1)	1	8.5	75	6.7	91.1	2.1	Ionic strength adjustment from 0.001M to 0.1M
	2	8.5	75	6.5	91.3	1.9	
	3	8.5	75	6.2	91.7	2.3	
Step (2)	1	8.5	75	5.9	92.1	2.3	Addition of 0.0001M $[Co(NH_3)_6]Cl_3$.
	2	8.5	75	7.1	90.5	2	
	3	8.5	75	6.2	91.7	2.6	
Step (3)	1	4.3	75	28.2	62.4	-0.9	pH adjustment from 8.5 to 4.3
	2	4.3	75	24.5	67.3	-0.1	
	3	4.3	75	22.4	70.2	0.2	

Note 1: The percentage of adsorbed Li (%) is calculated from (initial [Li]-final [Li])/initial [Li] (in uM) in average. Two standard deviation (2 S.D.) is calculated from the data of the experiment in triplicates. The analytical uncertainty of Li isotope analysis is 0.6‰ (2 S.D.) (W. Li et al., 2019). The Li isotope composition of LiCl is 5.8±0.6‰.
Note 2: *represents the control sets (Kaolin (1-2)) and the desorption sets (Step (1-3)).
Note 3: **represents the number of triplicates for each experiment set.

4. Results

4.1. Characterization of Li adsorption and desorption

A total of 127 batch experiments were performed in three individual experimental series. Clay adsorption results are summarized in Tables 6-8 and shown in Fig. 7. Clay desorption results are provided in Table 9. In the time-series experiments, the percentage of Li adsorbed onto kaolinite ranges from 37.3% to 91.4% (10/75 μM Li) at solute IS of 0.001M, and from 43.3% to 82.8% (10/75 μM Li) at solute IS of 0.1M. A rapid increase in the magnitude of Li adsorption was observed at the early stage of reaction (stage I, within 1000 min) and reached the equilibrium status until the end of experiments (15 days) (stage II, Fig. 7). Kaolinite surface coverages range from 0.04 to 0.24 μM Li·m^{-2}. In the pH-dependent experiments, the percentage of Li adsorbed onto kaolinite increases with pH from 3 to 10, ranging from 11.2% to 91.3% at solute IS of 0.001 M, and from 11.2% to 96.2% at solute IS of 0.1 M. Kaolinite surface coverages range from 0.04 to 0.36 μM Li·m^{-2}. In the concentration-control experiments, the percentage of adsorption on kaolinite decreases with incremental [Li] of 2 to 1000 μM and ranges from 11.2% to 99.2%. The K adsorption decreases with increases in solute IS from 0.001 M to 0.1 M at pH<7 and remains near-consistent at high/low IS at pH>7. Kaolinite surface coverages range from 0.01 to 1.14 μM Li·m^{-2}. In the desorption experiments, the percentage of Li adsorption at pH=8.5 and IS=0.001 M is 90.2% to 92.5% (Kaolin (1)), and the percentage of Li adsorption at pH=4.3 and IS=0.001 M is 65.1% to 68.9% (Kaolin (2)). With IS increasing to 0.1 M (Step (1)) or addition of 0.0001M $[Co(NH_3)_6]Cl_3$ (Step (2)) at pH=8.5, there is no apparent change (<1%) in adsorption ratios. With pH decreasing from 8.5 to 4.3 in the same batch (Step (3)), Li adsorption ratio changes from ~90% to 62.4% to 70.2%, higher than these of Kaolin (2).

4.2. Characterization of Li isotope fractionation

The isotopic compositions of aqueous and adsorbed Li are provided in Tables 6-8 and displayed in Figs. 8–9. The Li isotope data of clay desorption are provided in Table 9. The isotopic compositions of initial LiCl and pristine kaolinite are 5.8±0.6‰ and 0.2±0.6‰, respectively. In all sets, lighter isotopes were preferentially adsorbed. In the time-series experiments, aqueous isotopic compositions of Li (10/75 μM Li) ranges from 10.1‰ to 26.0‰ at solute IS of 0.001 M, and from -9.3‰ to 22.2‰ (10/75 μM Li) at solute IS of 0.1M. A transit positive isotope shift in aqueous Li from the LiCl signal was observed at the early stage of reaction (stage I, 1000 min), and approached the steady status until the end of experiments (15 days) (stage II, Fig. 8) at IS of 0.001M. Such a feature did not occur at IS of 0.1 M. In the pH-dependent experiments, Li isotope compositions of liquids remained in the fluids (δ^7Li_{aq}) range from 6.0 ‰ to 28.7 ‰ at IS of 0.001 M, and from 5.9‰ to 29.0‰ at IS of 0.1 M. It can be seen that δ^7Li_{aq} exhibit positive correlations with the adsorption ratio, in line with increases in pH in the studied pH range of 3 to 10. In the concentration-control experiments, δ^7Li_{aq} values range from 6.1‰ to 39.7‰ and adsorbed Li isotopic composition δ^7Li_{aq} ranges from -4.3‰ to 3.7‰. The Li isotope fractionation between adsorbed and aqueous Li exhibits a wide variety of -35.8‰ to -1.6‰, in negative relationships with the percentage of Li adsorption. In the desorption experiments of kaolinite, δ^7Li_{ad} values at pH=8.5 and IS=0.001 M are 2.2‰ to 2.5‰ (Kaolin (1)), and $^7Li_{ad}$ values at pH=4.3 and IS=0.001 M are -3.7‰ to 3.1‰ (Kaolin (2)). With IS increasing to 0.1 M (Step (1)) or addition of 0.0001M $[Co(NH_3)_6]Cl_3$ (Step (2)) at solute pH=8.5, there is no apparent change (uncertainty of 0.6‰, W. Li et al., 2019) in Li adsorption ratios. With solute pH decreasing from 8.5 to 4.3 in the same batch (Step (3)), δ^7Li_{ad} changes to a range of 0.9‰ to 0.2‰, while is greater than these of Kaolin (2) by ~3‰ at the same pH.

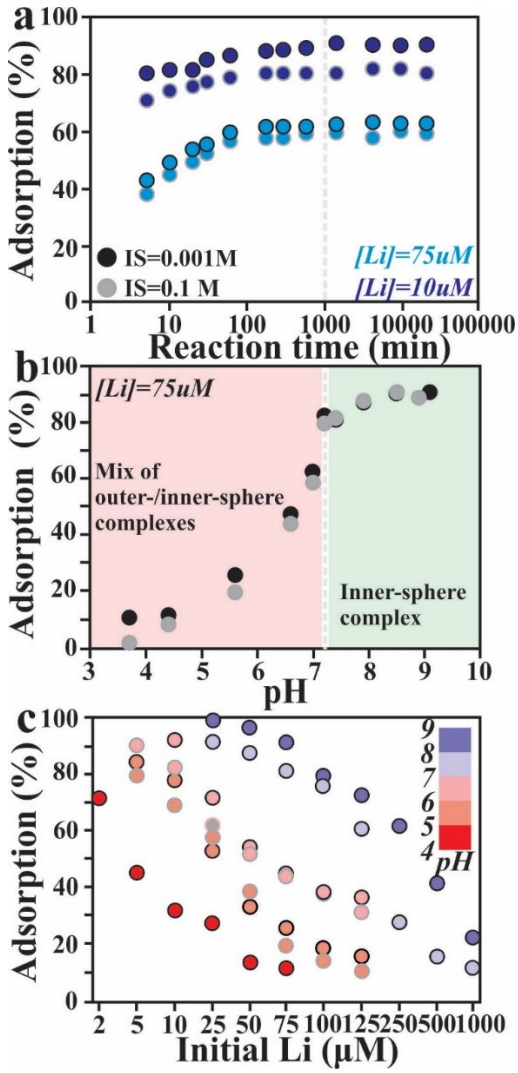

Figure 7. Kaolinite Li adsorption in the time-, pH-, and concentration-series experiments. (a) Kaolinite Li adsorption with the initial [Li]=10 and 75 μM in the time-series sets for kaolinite. (b) Kaolinite Li adsorption with initial [Li]=75 μM in the pH-dependent sets (pH ~ 4–10). (c) Kaolinite Li adsorption at a pH range of ~4–10 in the concentration-control sets ([Li]=2–1000 μmol·L^{-1}). The colors of light blue and dark blue denote time-series sets with [Li] of 75 μM and 10 μmol·L^{-1}, respectively. The colors of black and grey represent solute IS of 0.001 M and 0.1 mol·L^{-1}, respectively. The colors from red to purple show increasing solute pH from 3 to 10 in concentration-control sets. The analytical uncertainties on Li adsorption ratios using Q-ICP-MS ([Li], RSD<2‰) are smaller than the symbol sizes.

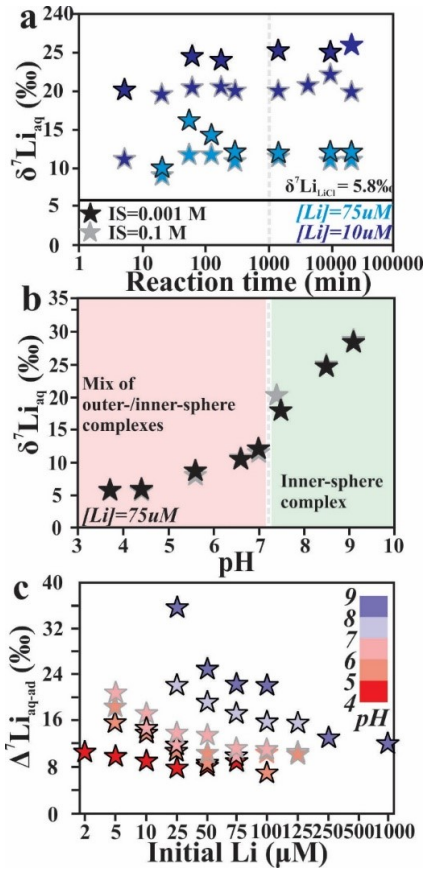

Figure 8. Solute Li isotopic compositions in the time-, pH-, and concentration-series experiments during kaolinite adsorption.

(a) Li isotopic signals of aqueous phases at initial [Li]=10 μM and 75 μM in the time-series experiments at pH 7. The aqueous Li isotopic composition at IS of 0.001 M and [Li]=75 μM reached the maximum value before decreasing to the equilibrium state. (b) Li isotopic signals of aqueous phases at [Li] = 75 μM in the pH-dependent experiments (~4–10). (c) Net Li isotope fractionation between aqueous phases and adsorbed phases at a pH range of ~4–10 in the concentration-control sets ([Li]=2–1000 μmol·L^{-1}). The isotopic composition of LiCl (δ^7Li_{LiCl}) was 5.8‰. Light and dark blue denote time-series sets with [Li] of 75 μM and 10 μmol·L^{-1}, respectively. Black and grey represent IS of 0.001 M and 0.1 μmol·L^{-1}, respectively. The colors from red to purple show increasing pH from 3 to 10 in concentration-control sets.

5. Discussion

The isotopic compositions of aqueous Li and adsorbed Li in the adsorption experiments exhibit wide variations from -4.3 to 39.7‰ under various conditions. Absolute Li isotope fractionations between aqueous and adsorbed Li in the same condition are heterogeneous (-35.8‰ to -1.6‰), positively correlated with the percentage of Li adsorption. We provide a conceptual model describing possible complexation mechanisms for Li adsorption onto kaolinite (Fig. 10). Generally, there are two adsorption sites available of different proportions on clay surfaces: (i) edge surfaces (the surface charge from hydroxyls) and (ii) basal surfaces (permanent structural charge). The pH-dependence of the edge surfaces can be verified by our zeta potential analysis, which shows increasing surface negative charge density with increasing pH. Commonly, Li^+ could be adsorbed as inner-sphere complexes (chemisorption) on clay edge surfaces and as outer-sphere complexes (physisorption) on clay basal surfaces. Our infrared spectra further confirm the site-specific Li adsorption onto clay edge surfaces, which is supported by attenuated hydroxylic Al-O (aluminols), Si-O (silanols), and Al-O-Si vibrations from alkaline to acidic conditions. Using ^{7}Li NMR, Wimpenny et al. (2015) suggested that adsorbed Li may be incorporated into gibbsite structure. Since the kaolinite sample used here is poorly-ordered and a large number of defects exist on its edge surfaces, we infer that adsorbed Li might be incorporated into the defects on edge surfaces of kaolinite samples. Two possible mechanisms (path 1, kinetic, and path 2, equilibrium) might influence the isotopic compositions of dissolved Li (Fig. 10). In the following sections, we propose and evaluate the mechanisms of Li adsorption on clays and its isotope fractionation during clay adsorption, then address potential interfacial paths controlling Li isotopic behavior. Further implications for tracing chemical weathering using Li isotopes are provided at the end.

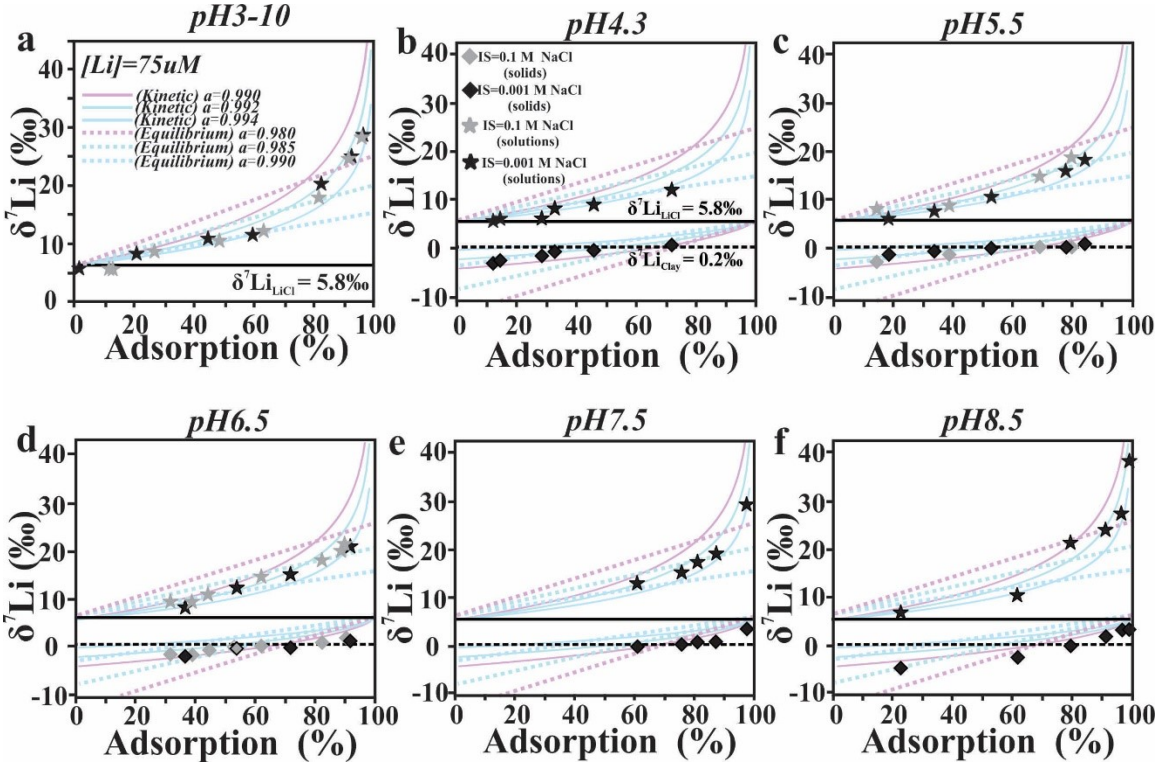

Figure 9. Modeling of the observed Li isotope fractionations during kaolinite adsorption.

Rayleigh distillation (kinetic, solid curves, α=0.990 to 0.994) and equilibrium models (dashed curves α=0.980 to 0.990) of closed-system isotope fractionation in (a) the pH-dependent experiments and (b–f) the concentration-control experiments over a range of pH values. The initial δ^7Li values of LiCl (solid black line) and pristine kaolinite (dashed black line) are 5.8±0.6‰ and 0.2±0.6‰, respectively. The isotopic compositions of dissolved and adsorbed Li phases are marked by stars and diamonds, respectively. The colors of black and grey represent solute IS of 0.001 M and 0.1 M NaCl, respectively. Long-term analytical uncertainty on δ^7Li (2 S.D.=0.6‰) is smaller than the symbol size. Modeled fractionation patterns are shown in the plot by lines in light blue (the lowest one), cyan (the optimal one), and purple (the highest one).

5.1. Li adsorption mechanism

Dissolved Li concentrations decrease parabolically as the reaction proceeds and depend on solute pH, initial [Li], and IS (Fig. 8). Time-series experiments show linear correlations between t/[Li] and t (t being time; $R^2 > 0.999$) and are best fitted by pseudo-second-order kinetics; rate constants can thus be calculated from the slopes of the t/[Li] versus t relationships. Such kinetic patterns suggest a rate-limiting step and single characteristic adsorption that is probably dominated by chemisorption rather than physisorption. The Langmuir model simulates the sorption isotherms better at high pH/IS, and the Freundlich model fits the data better at low pH and IS. This indicates that the binding energy is homogenous on the kaolinite surface at high pH and IS, but heterogeneous at low pH and IS. These results are consistent with the gradual deprotonation and activation of surface hydroxyl groups from acidic to alkaline conditions (Tombácz and Szekeres, 2006), as confirmed by zeta-potential analyses. This interpretation is also supported by Li-Na exchanges on the kaolinite surface at high IS (as supported by the deduction from adsorption; Tables 6-8). Moreover, as prepared, the kaolinite samples have finite specific surfaces and cation sorption capacities. Thus, adsorption at high pH is better described by the Langmuir rather than the Freundlich model because the Freundlich model assumes exponentially increasing adsorption amount. Combining the results from the kinetic and isotherm models, we suggest that the inner-sphere rather than outer-sphere complexation dominates the adsorbed Li pool with increasing pH and IS. Hence, monolayer adsorption and chemisorption dominate in such aqueous conditions.

Increased Li adsorption with increasing pH at both low and high IS suggests that inner-sphere complexation becomes important at pH > 5. Furthermore, identical Li adsorption ratio at high (high Na^+) and low IS (low Na^+) at pH > 7 supports that the replacement of

physically adsorbed Li^+ (outer-sphere complex) by Na^+ becomes negligible at pH > 7 (Fig. 8). Such a feature implies that inner-sphere complexation dominates in circumneutral to alkaline conditions, which cannot be easily replaced by excess Na^+ of high ionic potential (Strawn and Sparks, 1999). This conclusion is further supported by the negative charge accumulation on clay surface in response to increasing solute pH, which provides deprotonated hydroxyls located on clay edge surfaces for direct bonding (Guinoiseau et al., 2016). According to the changes in adsorption ratios at high and low IS, the concentration-controlled experiments show that both physisorption and chemisorption occur at low pH < 7, and chemisorption dominates at high pH. This interpretation is supported by the isothermal models and consistent with the increased occurrence of inner-sphere complexation with increasing solute pH from 3 to 10.

Our infrared data reveal that Li adsorption occurs exclusively on basal and edge surfaces, particularly the edge surfaces in high-pH/IS conditions, as supported by the pH dependence of edge site availability. After adsorption as outer- or inner-sphere complexes, Li is closely surrounded by oxygen atoms of water molecules (outer-sphere complex) or oxygen atoms of hydroxyls on clay surfaces that are bound to the central metal atom, displacing water molecules (inner-sphere complex). The extended X-ray absorption fine structure (EXAFS) of the local atomic coordination of Cd, Zn, and Cu complexed on clay surfaces indicates monodentate-mononuclear, monodentate-binuclear, or bidentate-mononuclear binding at high pH (e.g., Peacock and Sherman, 2004; Lee et al., 2004; Vasconcelos et al., 2008). However, the adsorption feature of Li^+ may be different from the above divalent metal ions due to its strong hydration (Rudolph et al., 1995). The interlayer spaces in kaolinite seem to be inaccessible to aqueous Li^+ due to strong interlayer hydrogen bonds. However, solid-state ^7Li NMR and scanning electron microscopy analyses suggest Li incorporation into gibbsite octahedral

vacancies (i.e., intercalation in interlayers) and Li adsorption with excess Li (Wimpenny et al., 2015). Therefore, our isotopic data aid in the understanding of dominant controls on Li isotope fractionation during soil formation, and the magnitude of isotope fractionation for structural substitution and surface adsorption needs further differentiation.

5.2. Li isotope fractionation mechanism

The Li isotopic trends observed in the time-series experiments with [Li] = 75 μM (i.e., rise-fall-plateau at low IS, and rise-plateau at high IS; Fig. 8) correspond to different Li isotopic behaviors, reflecting the influences of chemisorption and physisorption. The former trend was not observed in experiments with [Li] = 10 μM at low or high IS (Fig. 8), which may suggest the preferential occupation of strong hydroxyl sites via inner-sphere complexation. We infer that the isotopic composition of weakly fixed Li (i.e., outer-sphere complexes) is easily erased by cationic competition with Na and that only inner-sphere complexes are preserved at high IS, as reported for the successive involvement of different binding sites for Cu and Zn adsorption on kaolinite (Guinoiseau et al., 2016; Heidmann et al., 2005). Indeed, surface complexation models estimate the isotope fractionation factors of Zn in outer-sphere complexes on kaolinite basal surfaces to be about 0.18‰, regardless of aqueous chemistry (Guinoiseau et al., 2016). In comparison, the degree of equilibrium isotope fractionation of Ca^{2+} as outer-sphere complexes on soil phyllosilicates (kaolinite, montmorillonite, and muscovite) is related to the permanent negative charge of Ca on clay basal surfaces and/or in interlayers (Brazier et al., 2019). It is difficult to estimate the isotope fractionation factor of outer-sphere Li complexes using surface models due to a lack of thermodynamic parameters. Here, we infer that reversible Li adsorption (i.e., physisorption without direct bonding) follows an equilibrium isotopic mechanism, as

proposed to describe a similar Zn isotope pattern during adsorption onto Mn oxyhydroxides (Bryan et al., 2015).

To decipher between equilibrium and kinetic isotope fractionation mechanisms, we predict the Li isotopic compositions of absorbed (δ^7Li_{ad}) and dissolved Li (δ^7Li_{aq}) using the Rayleigh distillation (kinetic) and batch steady-state (equilibrium) models in closed systems, which can be expressed as (Eqs. 10-11):

$$\delta^7\mathrm{Li}_{\mathrm{ad}} = \left(\frac{\alpha \times \delta^7\mathrm{Li}_{\mathrm{LiCl}} + 1000 f_{\mathrm{Li}} \times (\alpha - 1)}{\alpha\,(1 - f_{\mathrm{Li}}) + f_{\mathrm{Li}}}\right);\ \delta^7\mathrm{Li}_{\mathrm{aq}} = (\delta^7\mathrm{Li}_{\mathrm{LiCl}} - f_{\mathrm{Li}})/(1 - f_{\mathrm{Li}})$$

(Batch steady-state) (10)

$$\delta^7\mathrm{Li}_{\mathrm{ad}} = \left(\frac{(\delta^7\mathrm{Li}_{\mathrm{LiCl}} + 1000) \times (1 - (1 - f_{\mathrm{Li}}) \times \alpha)}{f_{\mathrm{Li}} - 1000}\right);$$

$$\delta^7\mathrm{Li}_{\mathrm{aq}} = e^{[(\alpha-1)\ln f_{\mathrm{Li}} + \ln(\delta^7\mathrm{Li}_{\mathrm{LiCl}} + 1000)]} - 1000 \ \text{(Rayleigh-type)} \quad (11)$$

where $\alpha_{ad\text{-}aq}$ is the fractionation factor which defines the magnitude of isotope fractionation of adsorbed Li to dissolved Li, δ^7Li_{LiCl} is the isotope composition of the initial LiCl solution (5.8±0.6‰), and f_{Li} is the proportion of Li lest in solution after releasing from rocks and ($1 - f_{Li}$) denotes the proportion of Li removal by secondary mineral uptake.

The magnitudes of Li isotope fractionation in pH-dependent experiments increase with increasing Li adsorption ratios, and fit the Rayleigh models as opposed to the equilibrium batch models (Fig. 9). Based on the correlation between the fractionation factor α and the adsorption ratio, we estimate the kinetic fractionation factor $\alpha_{ad\text{-}aq}$ to be ~0.992. To exclude potential influence of pH variations in our model fitting, we compared closed-system models using the Li isotopic data from the concentration-control experiments at each pH conditions. At pH=4.3, Li isotope fractionations fit closed-system batch models, indicating a potential equilibrium isotopic pathway with $\alpha_{ad\text{-}aq}$ ~0.990. This finding supports our expectation of reversible Li isotopic exchange for outer-sphere complexes under acidic conditions. It is

consistent with recent clay synthesis experiments (Hindshaw et al., 2019) showing that Li in outer-sphere complexes is not significantly fractionated relative to the starting solution. Notably, all our Li isotopic data from concentration-controlled experiments under weakly acidic to alkaline conditions confirm closed-system kinetic fractionations when sorption ratios are high (>80%). A recent examination of closed-system basalt sand-natural river interactions of up to 9 months estimated a Rayleigh-type logarithmic relationship between dissolved δ^7Li (i.e., δ^7Li_{aq}) and Li/Na with $\alpha = 0.991$ (Pogge von Strandmann et al., 2019), which supports our findings.

In most cases, Li adsorption onto clays is primarily associated with kinetic isotope fractionations, contrasting the conventional assumption of equilibrium isotope fractionation (Vigier and Goddéris, 2015; Williams and Hervig, 2005) that corresponds to the changes in local atomic environments (Schauble, 2004). In previous studies focusing on clay adsorbed and/or incorporated Li, ^6Li could be preferentially trapped in octahedral sites, following the equilibrium fractionation path, which predicted that ^7Li would be preferentially retained in solutions as tetrahedral aquo-complexes. The proposed equilibrium isotope fractionation mechanism via isomorphic substitutions within octahedral sites of soils depended on both internal (atomic bond strength) and external (e.g., temperature and hydrochemistry) conditions (Hindshaw et al., 2019; Vigier et al., 2008; Wimpenny et al., 2015). For example, the negative correlation between pH and Li isotopic composition in foraminifera has been attributed to changes in Li speciation (Roberts et al., 2018). However, a possible pH control on Li isotope fractionation has not been observed during our clay adsorption experiments nor clay precipitation experiments (Hindshaw et al., 2019); thus solute pH is unlikely to affect Li isotope fractionations. It is noteworthy that the equilibrium fractionation of Li isotopes was verified during clay synthesis based on changes in local Li coordination (Hindshaw et al., 2019; Vigier et al., 2008). The directions and

magnitudes of Li isotope fractionations through clay adsorption observed in this study are comparable to those in clay synthetic experiments. Notably, a kinetic Li isotope fractionation was also suggested during stevensite precipitation at high pH (Hindshaw et al., 2019). Therefore, we suggest that both kinetic and equilibrium Li isotope fractionation mechanisms play roles during chemical weathering by Li adsorption onto and Li incorporation into secondary minerals during soil formation.

5.3. Interfacial path for Li isotope fractionation

From this study, there are two types of surface complexation during closed-system Li adsorption onto clays – chemisorption and physisorption, representing the kinetic and equilibrium fractionation processes, respectively (Fig. 10). Hence, clay adsorption occurs predominantly on kaolinite edge surfaces during Rayleigh-type kinetic fractionations ($\alpha \sim 0.992$) and on basal surfaces during equilibrium fractionations ($\alpha \sim 0.990$). And the observed $\Delta^7Li_{aq\text{-}ad}$ values probably reflect the net effect of both fractionations. The dominance of the kinetic mechanism at high pH/IS can be attributed to the inner-sphere Li complexation under those conditions. However, a critical question remains: why are covalently adsorbed Li isotopes not rapidly exchanged with the surrounding solution? Rayleigh fractionation implies that adsorbed Li can be rapidly isolated from the solution. Indeed, Li is incorporated into crystallographic defects, and interlayers of gibbsite after adsorption (Wimpenny et al., 2015) and monovalent cations intercalate into kaolinite (Smith et al., 1966). Based on these pieces of evidence, we suggest that adsorbed and kinetically fractionated Li rapidly occupy the structural defects at kaolinite edge surfaces, perhaps even diffusing into the interlayers or deep vacancies after ion dehydration (Fig. 10), where it is then inaccessible to the surrounding aqueous media. Possible Li incorporation may be supported by incomplete desorption after pre-adsorbing on kaolinite.

Likewise, Hindshaw et al. (2019) proposed that the kinetic-rate processes likely play a role in Li isotope fractionation during phyllosilicate synthesis in high-pH range, similar to Si and Ca isotopes in disequilibrium crystal-growth phenomena (e.g., Nielsen et al., 2012; Geilert et al., 2014). Studies on isotope fractionations within Ca adsorption/desorption processes on soils (Brazier et al., 2019; Ockert et al., 2013) demonstrated that the amplitude of associated isotope fractionation depended on the nature of clay minerals and adsorption site, with both kinetic and equilibrium isotope fractionation being observed. We thus interpret the Li isotopic compositions measured during our experiments to result from three stages of Li adsorption (Fig. 10): (i) two simultaneous kinetic isotope fractionations occur due to the preferential attachment of ^{6}Li onto kaolinite by inner-sphere and outer-sphere complexation; (ii) chemically adsorbed Li is structurally bound after dehydration, while an equilibrium fractionation continues by physical adsorption of Li from the solute; and (iii) the stationary Li isotopic state is reached and is linked to adsorption ratio. The equilibrium Li isotope fractionation can be reduced by increasing IS or by decreasing pH or [Li]. Nonetheless, the clay-Li coordination environment cannot be directly detected by common synchrotron-based techniques (e.g., XANES and EXAFS) and still remains an open question.

The $\delta^{7}Li_{aq}$ values observed in our experiments were as high as 39.7‰, spanning the wide range of natural observations, and could be quantified using a Rayleigh distillation model with $\alpha_{ad\text{-}aq}$ constant at ~0.992 (Figs. 11a-11b). The presence of a similar "distillation" process along the groundwater path has been postulated and simulated by Bohlin and Bickle (2019) for modeling kinetically limited weathering environments. Three distinct mechanisms might explain the observed kinetic Li isotopic behaviors. (I) Hydrated Li ions in the form of $[Li(H_2O)_4]^{+}$ pass through the clay-fluid boundary layer by diffusion, resulting in significant mass-dependent

isotope fractionation due to different diffusion coefficients. (II) The kinetic isotope fractionation of Li predominately depends on surface complexation kinetics in which isotopic exchange is limited by the large activation energy barriers that must be surpassed to break atomic bonds (Schauble, 2004). (III) The kinetic Li isotope fractionation occurs in a reaction-limited regime of surface interaction (DePaolo, 2011). The kinetic fractionation factor α depends on the ratio of net to backward reaction rates. Thus, mechanisms II and III describe a similar mechanism in which the backward reaction becomes negligible compared to the forward reaction once the maximum kinetic isotope fractionation is attained. To distinguish between mechanisms I and III, we compare our data to a molecular dynamic simulation using theoretical diffusion (Bourg et al., 2010) and ion desolvation (Hofmann et al., 2012) parameters for Li isotopes (Fig. 11c). Our data agree with the theoretical ion desolvation model with α of 0.9925±0.0014, corresponding to a quantum-mechanical mechanism of complexation and subsequent incorporation (Hofmann et al., 2012). The result of desorption experiments implies that Li clay adsorption is not fully reversible. We infer that a loose water solvation shell surrounds hydrated Li; rate-limited dehydration thus causes kinetic effects during interfacial interactions.

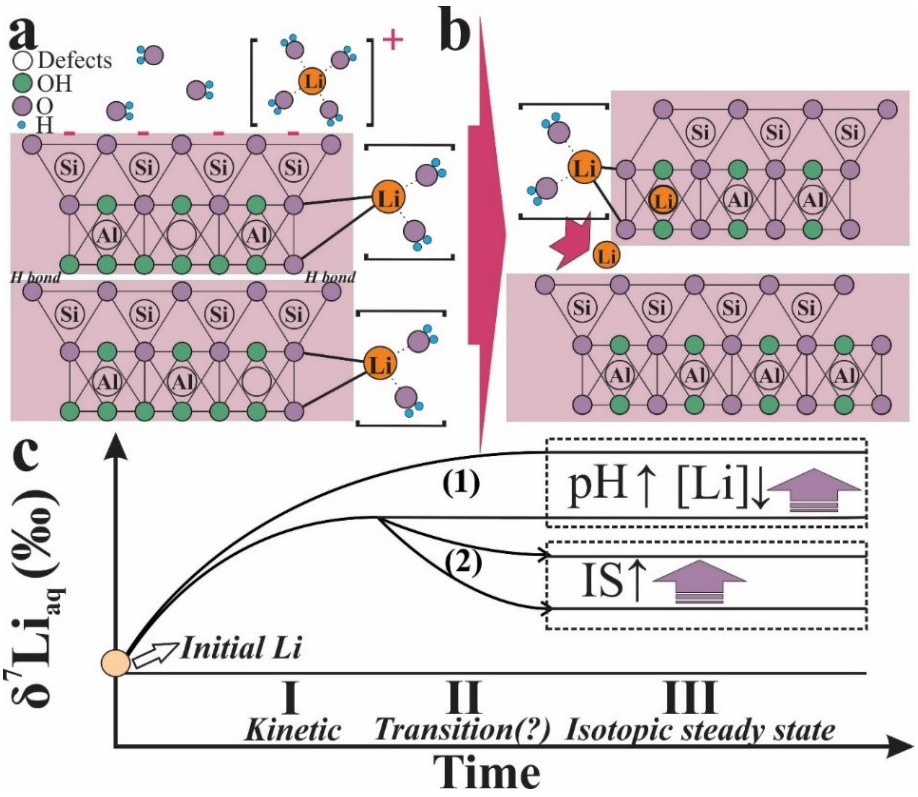

Figure 10. Conceptual plot of clay surface Li complexation and isotope fractionation.

A schematic illustration of possible processes occurring during Li^+ uptake by kaolinite and subsequent effects on δ^7Li_{aq}. (a) The adsorption of Li^+ onto kaolinite could result in the inner-sphere (chemisorption) and outer-sphere complexations (physisorption). (b) After adsorption, Li may migrate into interlayer spaces and/or occupies structural defects in clay structures. In this case, equilibrium Li isotopic exchange (i.e., the backward reaction) may be inhibited. (c) Conceptual sketch of the sorption of light Li isotopes, resulting in the enrichment of heavy Li isotopes in surrounding solutions. Observed trends imply three successive stages related to solute pH, [Li], and IS. In the plot (c), the path (1) represents the progressive establishment of the stationary isotopic state following a kinetic law. The path (2) reflects successive isotopic behavior, including (I) an initial kinetic fractionation due to preferential diffusion of ^6Li to clay surfaces/interlayers, (II) a gradual transition to isotopic equilibration with surrounding solutions, and (III) a final equilibrium with preferential ^6Li adsorption on clays.

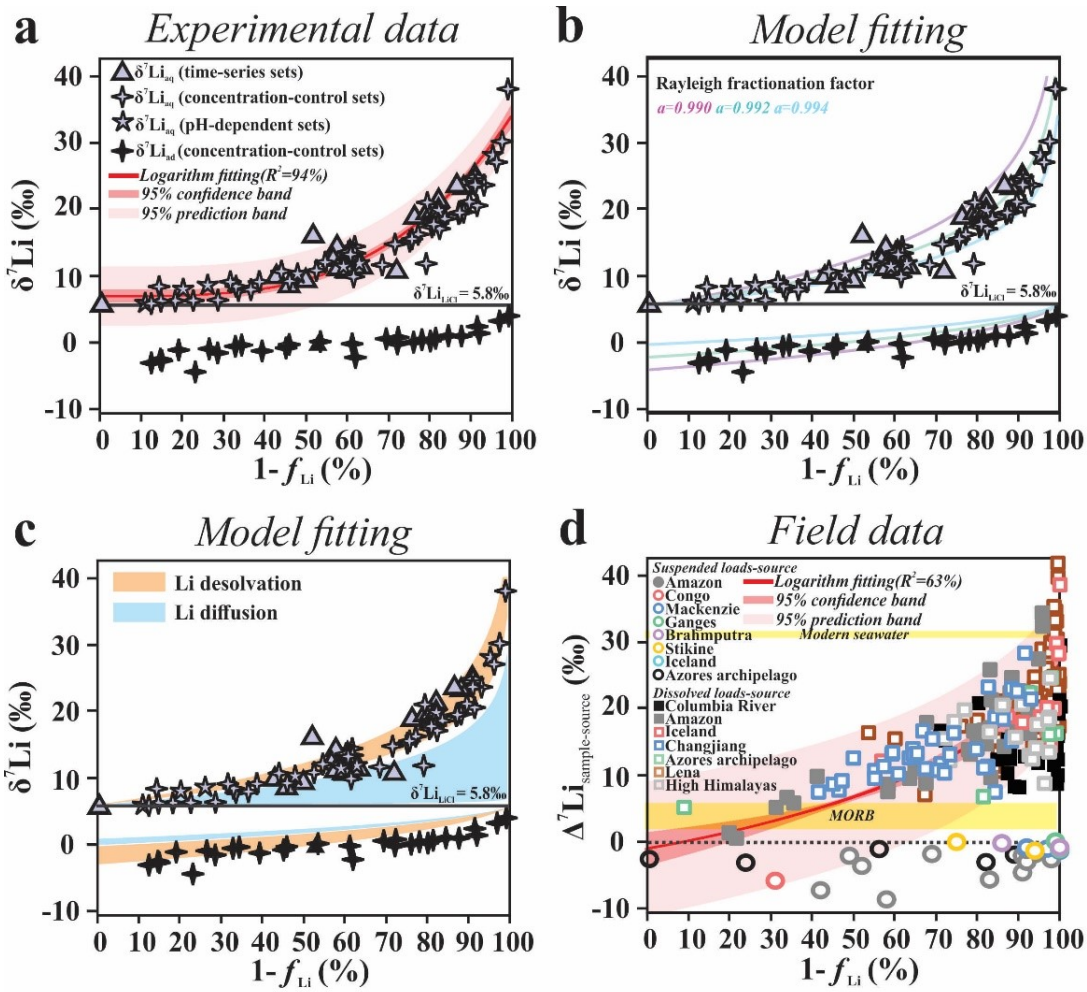

Figure. 11. Experiment and field Li isotope data compilation and integrated modeling results.

(a) Exponential fitting and (b) Rayleigh distillation model based on linear fitting to our data using fractionation factor $\alpha_{ad\text{-}aq}$ from 0.990 to 0.994. A closed-system Rayleigh distillation model produces the best fit with the $\alpha_{ad\text{-}aq}$ ~ 0.992, and agree with the range of δ^7Li values observed in continental to marine environments (data refer to Tomascak et al., 2016 and references therein). The initial Li isotopic compositions of the LiCl and pristine kaolinite are 5.8‰ and 0.2‰, respectively. (c) Molecular dynamic simulations of Li isotope fractionation via Li desolvation in aqueous systems (fractionation factor α=0.9925±0.0014; Hofmann et al., 2012) and Li diffusion in liquid water (diffusivity empirical constant, β=0.0171±0.0159, Bourg et al., 2010). (d)

Rayleigh distillation modeling of data from a literature compilation of river suspended and dissolved loads of global riverine systems. MORB: the mid-ocean-ridge basalts. Long-term analytical uncertainty on δ^7Li (2 S.D.=0.6‰) is smaller than the symbol size. f_{Li} represents the fraction of Li remaining in the liquid after lithology correction, normalized to the Li composition of source rock. If $(1\text{-}f_{Li})=1$, chemical weathering is congruent. The percentage of Li adsorption from solution $(1\text{-}f_{Li})$ is calculated using $(Li/Na)_{source}/(Li/Na)_{dissolved}$ and $(Li/Al)_{suspended}/(Li/Al)_{source}$, corresponding to Li re-incorporated into soils after initial release from silicate rocks by weathering. Plotted field data refer to the data of Amazon rivers (Dellinger et al., 2015, 2017), Congo rivers (Dellinger et al., 2017), Mackenzie rivers (Millot et al., 2010), Ganges rivers (Pogge von Strandmann et al., 2017b), Brahmputra rivers (Dellinger et al., 2014), Stikine rivers (Dellinger et al., 2017), Iceland rivers (Vigier et al., 2009; Pogge von Strandmann et al., 2016), Azores archipelago (Pogge von Strandmann et al., 2010), Changjiang rivers (Gou et al., 2019; Ma et al., 2020), Columbia rivers (Liu et al., 2014), Lena rivers (Murphy et al., 2019) and high Himalaya rivers (Kısakűrek et al., 2005). Analytical uncertainties of Li isotope analysis in mentioned publications are within the symbol size in the Y-axis.

5.4. Implications

A critical finding of this study is that the equilibrium fractionation of Li isotopes occurs through outer-sphere complexation, predominately under low pH/IS conditions. Because physically fixed outer-sphere Li should maintain four-fold coordination (similar to the four-fold coordinated hydrated Li-ions), Li isotopes are unlikely to be fractionated during outer-sphere complexation. Nevertheless, observable metal stable isotope fractionations have been reported for outer-sphere complexes. For example, Brazier et al. (2019) highlighted the importance of interlayer charges in determining the magnitude of weakly-bonded Ca (outer-sphere) isotope fractionations (Brazier et al., 2019). Hence, we postulate that electrostatic interaction affects the solvation number, though this requires further laboratory and theoretical examination. Increasingly significant kinetic control on isotopic fraction with increasing inner-sphere Li complexation (i.e., at higher pH) may be important in natural systems (e.g., rivers and oceans) under neutral to alkaline conditions. As clay sorption usually occurs prior to lattice incorporation (Pogge von Strandmann et al., 2017b), kinetic Li isotopic fractions may be preserved during soil formation. Furthermore, our interpretations are consistent with global riverine observations (Fig. 11d). The good agreement between observed and experimental δ^7Li values suggests that kinetically driven adsorption and incorporation may be a primary mechanism driving natural isotope fractionations.

The consistency between our results and natural observations demonstrates the critical role of kinetic controls on Li isotope fractionations during chemical weathering, although it invokes another question: can river systems be treated as closed systems? At first glance, riverine systems are open systems because they receive influxes from bedrock weathering and erosion, deposit sediments during transport, and, subsequently, provide outfluxes to reservoirs as oceans.

However, it takes time to follow the entire source-to-sink pathway, from bedrock via weathering profiles, to groundwaters and rivers (with potential floodplain storage), and to the marine realm. The dissolved and suspended loads travel together within rivers, especially in transport-limited weathering regions (e.g., floodplains) characterized by long water residence times (days to weeks, or longer) and low sedimentation rates. For example, the alluvial plains and vast riparian zones of rivers that carry even a low amount of suspended clays can certainly be considered as closed systems. In such cases, it is appropriate to treat the dissolved and suspended loads as being in a semi-closed system. Assuming that kinetic Li isotope fractionations are ubiquitous on Earth's surfaces, rivers potentially exert a more prominent impact on oceanic isotope mass balance compared with early expectations. It is consistent with the interpretation that enhanced weathering during the Cenozoic promoted heavy δ^7Li inputs into the oceans, contributing to a ~9‰ increase of oceanic δ^7Li (Misra and Froelich, 2012; Wanner et al., 2014). Our findings demonstrate kinetically controlled Li isotope fractionation during uptake by kaolinite, refining Li isotopic systematic as tracers of weathering and climate. This work also establishes δ^7Li as a sensitive index for clay formation during chemical weathering and also demonstrates that natural observations on Li isotope records cannot be simply treated as representing constant isotope fractionation level (e.g., Bouchez et al., 2013; Bohlin and Bickle, 2019). Previous quantitative interpretations of natural Li isotopic records thus may require refinements to account for low-temperature kinetic Li isotope fractionations during chemical weathering.

6. Conclusions

We performed systematic laboratory batch experiments to explore the mechanism and quantify the magnitude of Li isotope fractionation during the adsorption of kaolinite - a common weathering product. According to our systematic experiments, including time series-, pH- and

concentration-control sets, the liquid-solid isotopic variations range from ~0‰ to 36‰, with 10~99% starting solute Li being adsorbed. Li was removed by inner-sphere/outer-sphere surface complexation, likely followed by lattice occupation. We demonstrated that Li isotope fractionation during kaolinite uptake could be best described using a closed-system Rayleigh distillation model (α~0.992). These results are also consistent with the theoretical calculation of Li^+ desolvation (α~0.9925), and field observation of worldwide rivers. We conclude that the same kinetic isotope fractionation mechanism may be responsible for the wide ranges of Li isotopic signatures on Earth's surfaces. The importance of this finding includes that soil formation associated with kinetic controls may be the main driver for pronounced Li isotope fractionation, particularly in transport-limited weathering regions and, by extension, the continental-marine Li isotopic fluctuations during weathering over geological timescales.

CHAPTER 4: POTASSIUM ISOTOPE FRACTIONATION DURING CLAY ADSORPTION

This chapter is published as: Li, W., Liu, X. M., Hu, Y., Teng, F. Z. and Hu, Y. (2021). Potassium isotopic fractionation during clay adsorption. Geochimica et Cosmochimica Acta. 304, 160-177

1. Introduction

Continental weathering of silicate rocks is one of the key driving forces for various geological processes, including (i) shaping planetary topography, (ii) promoting pedogenesis, (iii) linking the element cycle between the lithosphere and the biosphere, and (iv) regulating atmospheric CO_2 and carbon cycle (e.g., Kump et al., 2000; Amiotte Suchet et al., 2003; Berner and Berner, 2012). From global perspectives, potassium (K) is a major element (~1.8%) in the crust, and can be significantly mobilized during chemical weathering by the dissolution of silicate rocks and subsequent transport into river runoffs (Li and Yang, 2010; Rudnick and Gao, 2013; Wang et al., 2021). Furthermore, K is known as one of the essential macronutrients for ecosystem development and sustainment (e.g., Tripler et al., 2006; Sardans and Peñuelas, 2015). Chemical weathering and biological cycling are two of the dominant drivers for the fractionation of stable isotopes at Earth's surface and further control their global elemental and isotopic budgets (Anbar and Rouxel, 2007; Liu et al., 2013; Teng et al., 2017). There are two stable K isotopes: ^{39}K (abundance of 93.26%) and ^{41}K (abundance of 6.73%), and their isotope ratios are expressed as $\delta^{41}K$. Recent advances in the analysis of K isotopes using multi-collector inductively-coupled plasma mass spectrometry (MC-ICP-MS) could produce high-precision K isotope data with analytical precisions up to 0.06‰ (2 S.D.) (Chen et al., 2019; Hu et al., 2018;

W. Li et al., 2016; Morgan et al., 2018; Wang and Jacobsen, 2016). Therefore, the isotope compositions in K reservoirs on Earth's surface can be better characterized.

The global oceanic K budget is regulated by the mass balance of dissolved K input from continental runoffs, K scavenging by marine authigenic minerals, and hydrothermal contributions (S. Li et al., 2019). The quantification of K isotope fractionation helps to characterize its isotope mass fluxes, sources, and sinks on a global scale, which is critical for understanding K cycling at Earth's surface (e.g., S. Li et al., 2019; Chen et al., 2020; Santiago Ramo et al., 2020; Sun et al., 2020; Teng et al., 2020). Currently, it is known that solid phases (rich in secondary minerals) often have lighter K isotope compositions (e.g., the upper continental crust, averaged $\delta^{41}K$: -0.44±0.05‰, Huang et al., 2020) than that of the modern seawater ($\delta^{41}K$ of ~0.14‰, Hille et al., 2019; Wang et al., 2020). Hence, stable K isotopes have the potential to decipher fluid-rock interaction processes (e.g., S. Li et al., 2019; Hille et al., 2019; Chen et al., 2020; Huang et al., 2020; Teng et al., 2020; Wang et al., 2021). Despite substantial efforts in clarifying K isotopic behaviors in Earth surface systems such as hydrothermally altered oceanic crust (Parendo et al., 2017; Santiago Ramos et al., 2020), marine sediments/pore water (Santiago Ramos et al., 2018; 2020), weathering profiles (Chen et al., 2020; Teng et al., 2020), rivers (Li et al., 2019; Wang et al., 2021), and plants (Christensen et al., 2018), a full appreciation of physicochemical processes controlling K isotope fractionation is elusive yet.

Potassium isotopes have the potential to trace biogeochemical K cycles, but first, the processes producing isotope fractionation between different K reservoirs on Earth's surface should be clarified. Previous studies on natural K biogeochemical cycles reveal that the fate of K is largely modulated by the cation exchange process (adsorption) in terrestrial environments (Pal

et al., 1999). Despite rapid clay formation promoting structural incorporation (Michalopoulos and Aller,1995; Rahman, 2019), a few recent studies have examined K cycling in aquifers and soils and emphasized the importance of clay exchangeable K (Griffioen, 2001; Chaudhuri et al., 2007; Liao et al., 2013; Simonsson et al., 2016). Among several processes that fractionate stable metal isotopes (e.g., Ni, Zn, Li, Mo; Ca and W) at the interface between river water/seawater and clays/oxides, adsorption is regarded as one of the principal causes (e.g., Pokrovsky et al., 2005; Balistrieri et al., 2008; Wasylenki et al., 2008, 2014; Goldberg et al., 2009; Bryan et al., 2015; D. Li et al., 2015; Spivak-Birndorf et al., 2018; Brazier et al., 2019; Li and Liu, 2020b). Generally, cations can be bound to various surfaces of clays: (i) external basal surfaces (permanently charged), (ii) external edge sites (pH-dependent hydroxyls such as aluminol and silanol sites), and (iii) accessible interlayer spaces (Uddin et al., 2017). Outer- sphere complex (physisorption, electrostatic interaction) and inner-sphere complex (chemisorption, covalent/ionic bonding) often form, causing isotope fractionation of different levels. Experimental studies help to understand isotope behaviors in well-constrained conditions. Compared with other isotope systems (Teng et al., 2017), little is known about the features of K isotope fractionation linked to clay sorption during chemical weathering. The adsorption of K on absorbents may result in distinguishable differences in isotope signals between sorbed and aqueous phases. Hence, clay sorption experiments provide a starting point to assess the potential of using K isotope information preserved in geologic records to decipher Earth Surface processes and biogeochemical K cycles.

This study aims to understand the K isotope fractionation mechanism during K uptake by clays. This study focuses on the pathway of K removal from water by adsorption on authigenic sediment particles and compares the difference in K isotope behaviors of clay adsorption and incorporation. Specifically, we determined K isotope composition based on experimental

constraints in the closed system where K^+ adsorption occurred on two common clay minerals (kaolinite and smectite). The objectives of this study were to investigate: (i) the amount and mode during K adsorbed onto clays under various environmental conditions; (ii) the direction, magnitude, and mechanism of K isotope fractionation between dissolved K and adsorbed K; and (iii) environment factors (adsorbents, pH, ionic strength and adsorption ratio) controlling K isotope fractionation during adsorption; (iv) K isotope behaviors during surface adsorption and structural incorporation in clays. We quantified the isotope fractionation between dissolved and adsorbed phases and examined their coordination environments. The outcome of this study allows us to elaborate on K isotopic records in a variety of sediments rich in secondary phases, which further benefits the understanding of K isotopes and the development of potential weathering and biogeochemical proxies for sediment-based research.

2. Experimental Setup

2.1. Starting materials

This study focused on K adsorption onto common naturally-occurring clay minerals, including kaolinite and smectite, which allow for the first-order analogy with natural environments. Two well-characterized clay reference materials (kaolinite KGa-2 and smectite SWy-2) were purchased from the Clay Mineral Society (CMS), which have been widely reported in literatures (e.g., Kosmulski, 2011; D. Li et al., 2015; Guinoiseau et al., 2016; Brazier et al., 2019). Critically, these clay samples were processed to recover clay-sized fractions (0.1-1 μm) and to eliminate surface impurities and labile components to avoid possible errors during chemical analyses. Hence, we used a modified washing protocol reported in Guinoiseau et al. (2016) and Brazier et al. (2019). In brief, clays were decanted in the sodium hexametaphosphate (NaHMP, dispersant)-water (deionized, 18.2 MΩ·cm) mixture for 24 h. Clay-size fractions (0.1-1

μm) were recovered based on Stokes' law (Reinholdt et al., 2013). Then NaHMP-extracted clay slurries were introduced to acid-cleaned centrifuge tubes using a pipette and treated with centrifugation at 10,000 rpm for 0.5 h, and the supernatants were discarded. A 0.5 M NaCl solution was then added into clay slurries, centrifuged at 10,000 rpm for 0.5 h, and the supernatants were discarded. After that, deionized water was added, centrifuged at 10,000 rpm for 0.5 h. This cleaning step using deionized water was repeated to eliminate surface salts until dissolved concentrations of Na and P below the detection limit of Q-ICP-MS (Agilent^{TM} 7900) at sub-ppb levels to ensure that no labile impurities affect K adsorption and solute chemistry.

Prior to adsorption experiments, we examined the possible interference of K released from clay structures based on the control group (a solid-to-liquid ratio of 10 $g \cdot L^{-1}$) in which no considerable exogenous K was introduced. To ensure experimental accuracy, the final release from clays in the control group was found to be less than 0.5 $ng \cdot g^{-1}$ K, far less than K loadings (over two orders of magnitude differences). Therefore, even if the partial release of clay K occurs in the initial stage of reaction due to the dissolution of aluminosilicates, we can reasonably infer that this contribution should be negligible, considering slight dissolution detected at the end of experiments. It was thus assumed that K loss from initial fluids during the experiments was due to its adsorption onto clays. Clay minerals obtained in wet conditions were heated at 60 ºC until dryness. The BET-N_2 specific surface areas of kaolinite (KGa-2, 20.14 $m^2 \cdot g^{-1}$) and smectite (SWy-2, 28.60 $m^2 \cdot g^{-1}$) were reported in Brazier et al. (2019), and were used in this study to calculate surface K coverages. We produced deionized water (18.2 MΩ·cm) using a Milli-Q system (Direct-Q^{TM} 3UV) for experiment groups and applied ultrapure-grade (>99.99% purity) KCl and NaHMP salts for all experiment groups to avoid potential contamination. As for clay K adsorption experiments, a 100 mM KCl stock solution has been

prepared using dissolving KCl hydrate (Acros Organic™, purity>99.99%) with deionized water (18.2 MΩ·cm). Using this stock solution, other solutions of lower K concentrations (0.005-20 mM) at circumneutral pH were made. The ionic strength (IS) of fluids was adjusted by optima-grade NaCl (i.e., background electrolyte). Commercially purchased hydrochloric acid (HCl, ACS-grade) was further purified in-house by double-distillation using the Teflon® sub-boiling still and then diluted to required molarities with deionized water. All solutions were freshly prepared prior to experiments and uniformly added into clay suspensions. Labwares have been carefully cleaned in a clean hood following an established method. This method uses diluted optima-grade HCl and HNO_3, cleaned using deionized water, and stored in the laminar flow hood (Airclean™, 600 PCR).

2.2. Experiment designs

In brief, we designed several sets of experiments, similar to those described previously (Li and Liu, 2020b). To examine the impacts of common environment factors on the K isotope fractionation between fluids and solids, three individual experiment sets were conducted in ambient conditions: (1) Time-series experiments, in which we tracked aqueous chemistry as a function of reaction time for up to 15 days, with a constant starting [K] of 0.2 mM, solute pH of 8, and solute IS of 0.001 M (sorption experiments were performed using 10 $g \cdot L^{-1}$ kaolinite and 2 $g \cdot L^{-1}$ smectite, respectively). The time-series experiments were designed to provide temporal changes in K adsorption and the time long enough to achieve the equilibria. (2) pH-dependent experiments, in which we modulated solute pH from about 4 to 10 (±0.2), with initial [K] of 0.2 mM and solute IS of 0.001 and 0.1 M for 15 days (10 $g \cdot L^{-1}$ kaolinite and 2 $g \cdot L^{-1}$ smectite). The pH-dependent experiments were designed to estimate pH influence on K adsorption during the protonation and deprotonation of clay surface binding sites. (3) Concentration-control

experiments in which we varied initial [K] ranging from 0.005 mM to 1 mM for kaolinite and 0.2 mM to 20 mM for smectite), with IS from 0.001 M to 0.5 M and solute pH of 8 for 15 days. The concentration-control experiments were designed to have different amounts of K with a constant solid-to-fluid ratio to provide a wide range of percentages of K adsorption. The tests using highly concentrated KCl solutions for smectite aim to probe into both external surface and interlayer space. For the three experiment sets, the choices for ranges in [K], IS, and pH were made based on natural environments. For example, the addition of 0.5 M IS (prepared by NaCl salt) in experiment set (3) aimed to investigate the pattern of K adsorption and associated isotope behavior in high salinity aqueous environments (e.g., seawater, brines, and some types of groundwater, Miller et al., 1986).

Each experimental group consists of a series of individual batch experiments, so that the solids and fluids could be collected and measured in all experimental conditions. All batch experiments were performed in 50 mL centrifuge tubes (acid pre-cleaned, kept sealed) filled with clay slurries under ambient conditions and continuously stirred at 150 rpm in a thermostatic water bath shaker (Thermo Scientific^{TM}). The starting solutions applied in the experiment have been pre-equilibrated with clay suspensions in the experiments. In addition, we varied the background electrolyte (NaCl) to investigate the effect of IS on surface complexation (chemisorption vs. physisorption) due to ion competition (K^+ vs. Na^+) for limited available surface sites without direct bonding (i.e., outer-sphere complexes, Guinoiseau et al., 2016). Experiment duration was set up to 15 days, which should be long enough to reach the adsorption/isotope equilibrium and short enough to avoid clay dissolution (Guinoiseau et al., 2016); this is further supported by the results of our time-series experiments. Clay adsorption normally generates slight pH variations at the start (Brazier et al., 2019) because of the amount

of H^+ exchanges with cations at clay surface sites. Thus, solute pH was monitored and adjusted every six hours using diluted NaOH and HCl solutions (small volumes, negligible compared with initial IS) for the individual reaction in each tube over the course of the experiment (15d). Solute pH analytical uncertainty is ±0.1 and fluctuations in solute pH were confirmed to be within ±0.25 of intended values. In an effort to achieve a sufficient separation of dissolved and adsorbed fractions, clay suspensions were centrifuged, and the supernatants were recovered by syringe filtration at < 0.2 μm at the end of experiments (cellulose acetate). Filtrates were acidified by HCl and stored at 4ºC. A small aliquot of the experimental solutions was used to determine the distribution of K between solutions and adsorbed phase. We note that the filtration process did not modify dissolved K concentration more than 3% (within the analytical error), and K isotope value of the filtered standard solution was identical to the $\delta^{41}K$ of KCl salt (0.20±0.06‰). Decanted clays were rinsed by pH adjusted, deionized water to exclude surface droplets until [K] in leachates below the detection limit of the Q-ICP-MS (>1 ppb K).

3. Analytical Methods

3.1. General analyses

For all the experiments, pH buffers were avoided to minimize undesired complexation and particle aggregation. Solute pH was measured using a portable pH meter (Thermo Scientific™, Orion Star A221) with an analytical precision of ±0.002 units (0.1 mV). Both solids and reference materials (BHVO-2) were digested in a mixture of concentrated HCl-HNO_3-HF acids over 150 °C, following the approach documented in Li et al. (2019). Then, filtrates were dried at 100 °C and re-dissolved in 5 mL 2wt.% HNO_3 for elemental concentration analysis. The concentrations of Li, Na, K, Mg, Al, Fe, Ca, Sr, and Ti were measured using a quadrupole inductively coupled plasma mass spectrometry (Q-ICP-MS, Agilent™ 7900) at the Plasma Mass

Spectrometry Lab, the University of North Carolina at Chapel Hill (UNC-CH). The instrument was calibrated with a range of ICP standard solutions of known concentrations. Internal standards, including Be, Ge, Rh, In, Ir, and Bi, were added for instrument drift correction. Three international basalt standard BHVO-2, a seawater standard NASS-7, and a river water standard SLRS-5 (element compositions certified by the United States Geological Survey and the National Research Council of Canada) were measured to confirm the accuracy and reproducibility of elemental analysis (Appendix 1). During our Q-ICP-MS analysis, precision less than 3% (relative standard derivation, RSD) was achieved. The RSD values were calculated based on an average of three analytical cycles of the same sample. The measurement was validated with the results obtained on reference materials, yielding an accuracy derivation less than 10% for reported elements relative to certified values of references.

Electrophoretic mobility (EM) was measured using a Zetasizer Nano (Malvern^{TM} ZS90) under ambient conditions and was converted to the zeta (ζ) potential automatically using the Helmholtz-Smoluchowski equation by the Zetasizer software. Zeta (ζ) potential values were reported in this study to quantitatively describe the electrochemical property of clay particles. The ζ potentials of clay suspensions with solute IS of 0.001 M to 0.5 M at a pH range of 4 to 10 were measured. Clay suspensions were dispersed in an ultrasonic bath for 5 min and transferred into capillary cells to measure surface charges in different settings. Averaged values (with derivations) were provided from the performance of triplicates prepared, and each was subjected to 20 light scattering measurements to generate enough dataset for statistical analyses. To determine clay mineralogy and newly-formed phases, X-ray diffractograms (XRD) were collected on a Rigaku^{TM} MiniflexII XRD diffractometer with a Cu K_{α} source over a 2θ range of 20° to 80°. The X-ray beam was operated at 40 kV (voltage) and 40 mA (current), with a step

size of 0.3° and a step rate of $3°\cdot min^{-1}$. The X-ray diffractograms of kaolinite and smectite (both reacted and pristine) and KCl salt (solid) were also measured.

3.2. K *K*-edge XANES analysis

The X-ray absorption near edge structure (XANES) is a synchrotron-based technique that can provide information of the speciation of specific elements such as K. The XANES analysis consists of measuring the photon energy spectrum resulting from focusing an X-ray beam to excite 1s electron to higher energy unoccupied p-state (Berry and O'Neill 2004). When the primary beam exceeds the binding energy of the 1s shell electron of the atom, its absorption spectrum is stepwise increased, which is called the "*K*-edge". Here, two kinds of K structure information at an atomic/molecular scale were obtained from the K XANES (i.e., K speciation and K-O coordination number). The *K*-edge XANES spectra for reacted clay samples and the model references (i.e., pristine clays and KCl salt) were collected from the Soft X-ray Micro-Characterization beamline (SXRMB, 06B1-1) at Canadian Light Source (CLS, Saskatoon, Canada) at ambient conditions. Spectra collection of pristine clays and reacted clays were designed to decipher the variations in atomic coordination among lattice K, sorbed K, and ionic K in dissolved phases, and to understand isotope behaviors related to atomic changes. This beamline was equipped by Si drift fluorescence detector and monochromated with diffraction from the InSb (111) and Si (111) double-crystals, covering a wide energy range from 1.7 to 10.0 keV. After grinding through a 100-mesh (0.15 mm) sieve, powdered samples were spread as a thin film on double-sided K-free carbon tape adhered onto a copper stick, and then placed in a vacuum chamber to reduce beam attenuation. The radiation damage effect was negligible because of satisfactory reproducibility. K *K*-edge XANES spectra were obtained in a partial fluorescence yield mode by the 7-element fluorescence detector with a dwell time of 4.0 s, and

the KCl spectrum was collected in a total electron yield mode to avoid self-absorption effects. Over a photon energy range of K *K*-edge (3550–3700 eV), the photon flux is 2×10^{10} photon s^{-1} at 100 mA, and the beam size at the target is 7 mm×1 mm ((Hu et al., 2010).

Two-step scans were set up for analysis: region I (3568.0 to 3708.0 eV, a step-size of 0.2 eV) and region II (3648.0 to 3708.0 eV, a step-size of 1.5 eV). Radiation damage should be negligible, according to the good reproducibility at the same spot and repetitive scans at different spots in the same sample. To improve the signal-to-noise ratio, five to six spectra were averaged and processed in Athena software (Ver. 0.9.20; Ravel and Newville, 2005). The linear combination fitting (LCF) was attempted for binary combinations, and an R-factor was adopted to estimate the goodness-of-fit, and significance between the fits was evaluated using the Hamilton test ($p<0.05$) (Calvin, 2013). The number of independent data calculated was normalized to a sum of 100% and determined as the data range divided by the core-hole lifetime broadening. Fits were only accepted when the sum of the contribution of references was 100±10% (Fig. 12a). The uncertainty of the XANES-LCF is difficult to quantify; as a rule of thumb, the absolute error is ~5-10% (Gu et al., 2019). The extended X-ray absorption fine structure (EXAFS) approaches could offer detailed information on the coordination environment of K. However, this approach was not applicable here due to poor signal-to-noise ratios likely caused by the limitation of tender X-ray and very low K concentrations in our samples. Please note that both unreacted and reacted clays have been measured for the K *K*-edge XANES, and the spectra of unreacted clays only reflect the feature of K in clay lattice (0.065% K_2O in KGa-2 and 0.53% K_2O in SWy-2, Source Clay Physical/Chemical Data, CMS) and the spectra of reacted clays offer a sum of spectra containing both lattice K and sorbed K that were then treated with the XANES-LCF analysis.

3.3. K isotope analysis

All chemical pretreatments were performed in the class-100 vented laminar flow workstation (Airclean^{TM}, 600 PCR) in the Plasma Mass Spectrometry Lab at the University of North Carolina at Chapel Hill (UNC-CH). An aliquot of digested sample was evaporated to dryness and re-fluxed with 2 mL 0.7 M HNO_3 before loading onto the columns. Potassium isotopic ratio was measured after column purification, following a two-step purification approach reported in Chen et al. (2019). A first column was filled with 17 mL AG50-X8 cation-exchange resin (200-400 mesh, Bio-Rad^{TM}), and conditioned using 0.7 M HNO_3. Eluted K fractions were then collected after most of matrix elements being eluted. Then collected elution was evaporated until dryness on a hotplate > 120 °C, and re-dissolved in 1 mL 0.5 M HNO_3 solution for the second column. The second column was filled with 2.4 mL AG50-X8 cation-exchange resin (200-400 mesh, Bio-Rad^{TM}), and conditioned in 0.5 M HNO_3. The K fraction was collected after rest matrix elements being eluted, and the 2nd column separation may be repeated if necessary. After chromatographic processes, pre-cuts, and post-cuts of column work were measured for K, Na, Al, Fe, Rb, and Ti concentrations on the Agilent^{TM} 7900 Q-ICP-MS. The total collecting volume of K has to be ~100% yields to exclude isotope fractionations in ion-exchange chromatography. Moreover, the weight percentage of the sum of other matrix elements to K was checked to ensure all matrix elements are below 2% of total K to minimize matrix influences on isotope analysis (Chen et al., 2019). Column blanks were > 3 orders of magnitude lower than K usage in the experiments.

Procedural K blanks were monitored for experiment runs (≤10 ng K), which were negligible in comparison to collected K fractions of natural and laboratory samples at μg-/mg-levels. Purified K solutions were introduced into the Nu Plasma II high-resolution MC-ICP-MS

at the Isotope Laboratory at the University of Washington, Seattle. The analyses of K isotopes were performed using the "cold plasma" mode (using low RF power values ranging from 750 W to 850W) with a DSN-100 desolvation system, and equipped with a Savillex™ PFA spray chamber and a C-Flow PFA microconcentric nebulizer. To correct instrumentals bias, the K isotopic ratios were measured using a sample-standard bracketing technique using a NIST SRM 3141a K solution (6-8 analytical cycles for each sample). Instrumentation and analytical details were summarized in Y. Hu et al. (2018). The isotopic composition was expressed in ‰, relative to a K reference NIST SRM 3141a (Eq. 12):

$$\delta^{41}K_{sample}\ (‰) = \left\{\frac{(^{41}K/^{39}K)_{sample}}{(^{41}K/^{39}K)_{NIST\ SRM\ 3141a}} - 1\right\} \times 1000 \quad (12)$$

The long-term reproducibility from replicate analyses of a suite of international references is better than 0.06‰ (95% confidential interval) (Hu et al., 2018; Xu et al., 2019). The granite (GSP-2) and basalt (BHVO-2) USGS standards measured along with samples, and measured values fall within the uncertainties of previously reported data (Appendix 2). Additionally, clay mineral lattices contain non-negligible amounts of K compared with total amounts of K sorbed, as mentioned in certificates (https://www.agry.purdue.edu/cjohnston/sourceclays/chem.htm). Hence, measured $\delta^{41}K_{solid}$ data were corrected by the deduction from the primary structural K composition of unreacted clays (i.e., pristine clay minerals, $\delta^{41}K_{kaolinite,\ KGa\text{-}2}$=-0.44±0.05‰ and $\delta^{41}K_{smectite,\ SWy\text{-}2}$=-0.63±0.05‰) following Eq. 13, and then to calculate the isotopic compositions of adsorbed K on reacted clays:

$$\delta^{41}K_{ad} = \frac{[K]_{solid} \times \delta^{41}K_{solid} - [K]_{clay} \times \delta^{41}K_{clay}}{[K]_{ad}} \quad (13)$$

where $[K]_{solid}$ and $\delta^{41}K_{solid}$ represent the K concentrations and its isotope compositions of reacted clays, and $[K]_{clay}$ and $\delta^{41}K_{clay}$ notate the K concentrations and its isotope compositions of pristine clays. Assuming that the removal of K from the starting solution was solely caused by K

adsorption on clay surfaces and that unreacted clay surfaces were K-free after a thorough cleaning. In addition, the isotopic compositions of adsorbed K could be calculated based on mass balance (Eq. 14), based on $\delta^{41}K_{aq}$ (aqueous K), and the percentage of K adsorption (F, %). The same method was adopted in early studies (Ge: Yuan et al., 2018; Cu and Zn: Balistrieri et al., 2008; W: Wasylenki et al., 2020).

$$\delta^{41}K_{ad} = [100 \times \delta^{41}K_{KCl} - (100 - F) \times \delta^{41}K_{aq}]/F \quad (14)$$

Since K loss during sampling cannot be prevented, we have compared the total amount of K addition in each experiment to a sum of the amount recovered in fluid/solid phases (Wasylenki et al., 2020) to confirm K recovery and the validity of the experimental results. Measured $\delta^{41}K_{ad}$ values are comparable to calculated $\delta^{41}K_{ad}$ based on the mass balance approach (Table 10), and the isotopic offset between two values is less than the analytical uncertainty by the following equation (Eq. 15):

$$[\delta^{41}K_{KCl} - (\delta^{41}K_{aq} \times (100 - \%ad) + (\text{measured } \delta^{41}K_{ad} \times \%ad)]/2 \leq 0.06‰ \text{ (95\% c.i.)} \quad (15)$$

Isotope mass balance calculation confirms that an abundance-weighted sum of isotopic values for aqueous K and adsorbed K was within the uncertainty of KCl (i.e., a sum of parts equals the whole).

Absolute isotope fractionation between adsorbed K and aqueous K, $\Delta^{41}K$ was defined as Eq. 16:

$$\Delta^{41}K_{ad-aq} = \delta^{41}K_{ad} - \delta^{41}K_{aq} \quad (16)$$

Two standard deviations (2 S.D.) and 95% confidential interval (95% c.i.) were calculated using 4 to 8 repeated runs within the same analytical sections. We note that 95% c.i. were calculated using the following equation (Eq. 17):

$$95\%\ \text{c.i.}\ (‰) = t_{n-1} \times \frac{SD}{\sqrt{n}} \quad (17)$$

where S.D. notates the standard deviation over the analytical cycle (times=n) of the sample, and t_{n-1} is the student's law factor with n-1 degrees of freedom at a 95% confidence level. The

estimated uncertainties on net fractionation $\Delta^{41}K_{ad\text{-}aq}$ were propagated using the following equation (Eq. 18):

$$\Delta E = \sqrt{(c_1 \Delta W_1)^2 + (c_2 \Delta W_2)^2 + \cdots + (c_n \Delta W_n)^2} \quad (18)$$

where ΔE is an absolute error, c is a multiplicative factor, and W denotes additive function inputs.

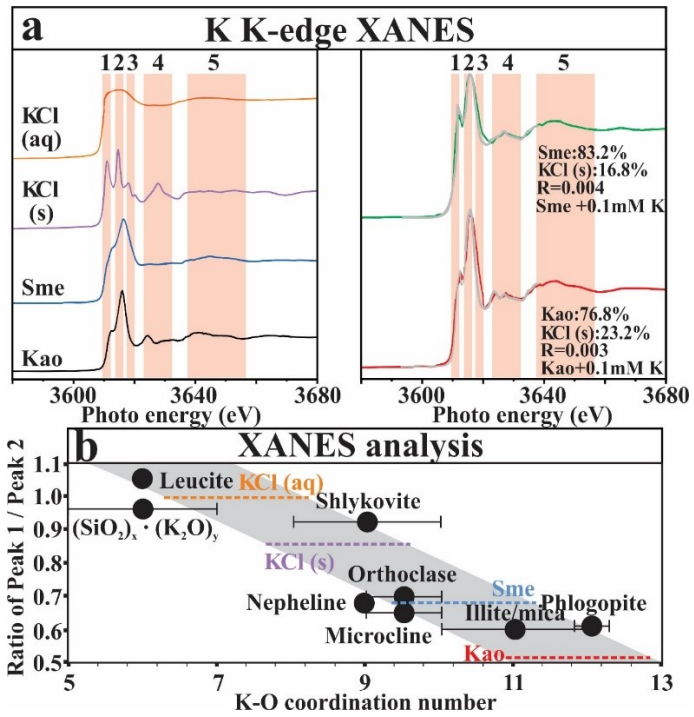

Figure 12. K *K*-edge XANES spectra of clays before and after reaction.

(a) XANES data and liner combination fitting analysis (grey lines as LCF fittings); (b) Intensity ratios between XANES Peak 1 and Peak 2 as a function of atomic K-O coordination number. Peaks 1-5 in the plot (b) reflect a result of the dipole transition of a *1s* electron to unoccupied *4p* orbital, with a small contribution of quadrupole transitions to *3d* orbitals, which could offer the coordination information. The result of XANES-LCF in the plot (b) is highlighted by grey lines, which indicates that outer-sphere K^+ became KCl (s) during the drying of clays (reacted clays have been rinsed using deionized water until K below detection limits). Relative contributions of each K speciation are provided based on the best least square fit ranked after an R-factor as the goodness of fitting. In the plot (b), data of leucite, orthoclase, K-bearing silicates, microcline, phlogopite, nepheline, shlykovite and illite/mica are from literatures (Cibin et al., 2005; Geng et al., 2020; Glezakou et al., 2006; Greaves et al., 1991; Huffman et al., 1986; Kamijo et al., 1996; Roberts et al., 2018; Spiro et al., 1986; Xu et al., 2011). The grey area demonstrates an eye-guiding trend and dashed lines show visual estimation of clays (Kao: kaolinite; Sme: semctite).

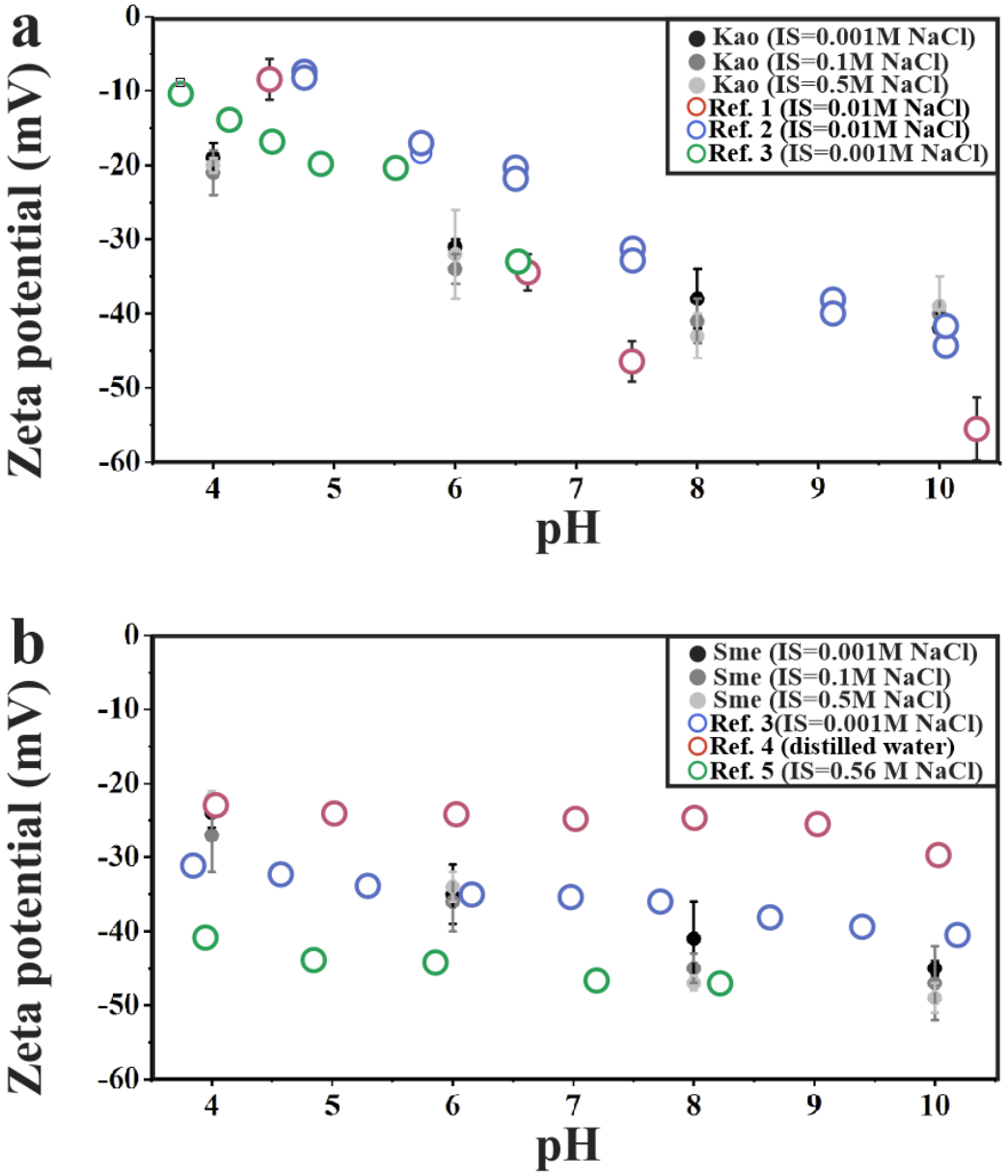

Figure 13. Zeta (ξ) potentials of kaolinite (KGa-2) and smectite (SWy-2) suspension.

Date were plotted as a function of solute pH (from 4 to 10), at solute IS from 0.001M to 0.5 M NaCl (colors from black to grey). Increases in surface negative charges are caused by progressive deprotonation of surface hydroxyls (Si-O)(Al-O)-OH) with increasing solute pH (Tombácz and Szekeres, 2006). Error bars on the Y-axis are Zeta deviation. Abbreviations: Kao: kaolinite; Sme: smectite; IS: ionic strength. Ref. 1: Coutelot et al. (2018); Ref. 2: Chemeda et al. (2015); Ref. 3: Au and Leong (2016); Ref. 4: Navrátilová and Maršálek (2012); Ref. 5: Y. Liu et al. (2018).

4. Results

4.1. Characterization of reacted clays

The data of ζ potential measurement are summarized in Fig. 13. As pH increases from 4 to 10, the ζ potentials of kaolinite and smectite suspensions decrease, ranging from -42±2 eV to -19±2 eV and from -22±1 eV to -49±2 eV, respectively. Under the same condition, smectite shows slightly higher densities of negative charge than kaolinite. There are no apparent impacts of IS on the ζ potential of clays. The results of K *K*-edge XANES are depicted in Figs. 12a and S3. There is no modification in clay mineralogy after dryness before and after the experiments. However, the characteristic peaks (I and II, Fig. 12a) of KCl in solid phases appear in the X-ray diffractogram of reacted kaolinite and smectite, which are further examined by the K X-ray absorption spectra. Based on a direct comparison between the K *K*-edge XANES spectra (peak positions and shapes) of unreacted clays and references, major absorption resonances (Peaks 2 and 3) have been observed within the energy range of 3605–3620 eV, along with the shoulder on the pre-edge peaks (Peak 1) at the rising part of spectra. Minor Peaks 4 and 5 can be observed in the after-edge regions, reflecting the crystallinity. Changes in the features of energy peaks (1-5, Fig. 12a) suggest the appearance of KCl(s) in reacted clays (i.e., 23.2±2.4% KCl for kaolinite and 16.8±2.1% for smectite after reacting with 0.1 mM [K]). The results from the XANES-LCF K atomic proportions indicate that the proportions of adsorbed K measured in the total K pool (the sum of adsorbed K and structural K) are 21.3% and 17.4%, in reacted kaolinite and smectite, respectively. Given negligible K in leachates during pre-cleaning, the KCl presence in reacted clays is likely from solid dryness after the experiments, rather than surface excess salts.

4.2. Characterization of K adsorption patterns

A total of 70 individual batch experiments were carried out in three experimental groups. Clay adsorption results were summarized in Table 10 and shown in Figs. 14–16. In time-series experiments, the percentage of K adsorbed onto clays at solute IS of 0.001M ranges from 63.4% to 74.7% (10 $g \cdot L^{-1}$ kaolinite), and from 42.3% to 54.5% (2 $g \cdot L^{-1}$ smectite). A rapid increase of the adsorbed K amount onto clays was found during the early stage of reaction (stage I, <10 h), and rapidly reached the equilibrium until the end of experiments (stage II, Fig. 14). Hence, final K adsorption coverages (adsorbed K content to clay BET surface area) are ~0.7 μmol $K \cdot m^{-2}$ (kaolinite) and ~2.8 μmol $K \cdot m^{-2}$ (smectite), respectively.

In pH-dependent experiments (Fig. 15), the final proportion of K adsorbed on clays increases that ranges from 13.2% to 80.0% (10 g·L-1 kaolinite) and from 31.1% to 57.4% (2 $g \cdot L^{-1}$ smectite), respectively, with pH increasing from 4 to 10 at solute IS of 0.001 M. At high IS of 0.1 M, the percent of K adsorption decreases to ranges from 8.1 to 17.1% (10 $g \cdot L^{-1}$ kaolinite) and 8.4 to 11.9% (2 $g \cdot L^{-1}$ smectite). Clay surface coverages are 0.1–0.8 μmol $K \cdot m^{-2}$ (kaolinite) and 1.5–2.8 μmol $K \cdot m^{-2}$ (smectite) at low IS of 0.001M, and 0.1–0.2 μmol $K \cdot m^{-2}$ (kaolinite) and 0.4–0.6 μmol $K \cdot m^{-2}$ (smectite) at high IS, respectively.

In concentration-control experiments (Fig. 16), the proportion of K adsorbed onto clays decreases with incremental [K] from 0.005 to 1 mM at IS of 0.001 M, ranging from 34.9% to 92.7% (10 $g \cdot L^{-1}$ kaolinite) at pH=8. The K adsorption decreases to 2.0–22.0% at IS of 0.1 M, and 1.7–3.4% at solute IS of 0.5 M (kaolinite) at solute pH of 8. Adsorption coverages increase from near zero to a plateau at ~1.0 μmol $K \cdot m^{-2}$, when initial [K] increases from 0.005 to 1 mM, and K coverages reach to ~zero with IS increasing. The percent of K adsorbed decreases with incremental [K] from 0.2 to 20 mM at IS of 0.001 M, ranging from 1.8% to 55.7% (2 $g \cdot L^{-1}$ smectite) at pH=8. The adsorption ratio decreases to 0.2–11.9% at IS of 0.1 M, and 0.1–1.9% at

IS of 0.5 M (smectite) at pH of 8. Clay adsorption coverages increase from ~2.0 μmol $K \cdot m^{-2}$ to ~6.0 μmol $K \cdot m^{-2}$, when starting [K] increases from 0.2 to 20 mM, and clay K coverages reach to near zero at high IS.

4.3. Characterization of K isotope fractionation

The isotopic compositions of dissolved and adsorbed K are provided in Table 10. Although the K isotope compositions of the filtrates were directly determined from measurements, those of the adsorbed K were determined from measured fluid compositions and mass balance calculations (see Eq. 14, except for four data points in the pH-dependent set). The K isotope composition of starting KCl solutions is 0.20±0.06‰. The first-order observation for all experiment groups is that heavy K isotopes sorbed onto clay minerals compared with K remained in surrounding solutions. The mass-balance calculation showed that the $\delta^{41}K_{ad}$ ranges from 0.16‰ to 0.89‰. Net isotope fractionation $\Delta^{41}K_{ad\text{-}aq}$ are negative at the incipient stage (<10 h), and become positive. Net isotope fractionation $\Delta^{41}K_{ad\text{-}aq}$ is ~0.6 to 0.8‰, despite variation in pH and initial [K] (Table10).

In time-series experiments (Fig. 14), the isotopic composition of aqueous K in solution ($\delta^{41}K_{aq}$) ranges from -0.14±0.04‰ to -0.36±0.04‰ (10 $g \cdot L^{-1}$ kaolinite), and from -0.25±0.04‰ to 0.05±0.05‰ (2 $g \cdot L^{-1}$ smectite), with solute IS of 0.001 M. The K isotope equilibria was probably achieved within the first 10-hour reaction because subsequent analyses of the same runs at the end of experiments resulted in near-identical adsorption and $\delta^{41}K_{aq}$ within analytical uncertainties.

In pH-dependent experiments (Fig. 15), K isotopic composition of the aqueous phases ($\delta^{41}K_{aq}$) ranges from -0.43±0.04‰ to 0.10±0.04‰ (10$g \cdot L^{-1}$ kaolinite) and from -0.24±0.05‰ to -0.03±0.04‰ (2$g \cdot L^{-1}$ smectite) at IS of 0.001 M. The $^{41}K_{aq}$ values negatively correlate to the

adsorption ratios, consistent to the increase in solute pH in the studied pH range (from 4 to 10±0.2). Measured isotope composition of K sorbed on clay minerals ($\delta^{41}K_{ad}$) ranges from 0.38±0.04‰ to 0.90±0.04‰ (10g·L^{-1} kaolinite) and from 0.50±0.04‰ to 0.68±0.04‰ (2 g·L^{-1} smectite) in accordance with mass-balance estimation.

In concentration-control experiments (Fig. 16), K isotopic composition of aqueous phases is in a range of -0.53±0.04‰ to 0.03±0.04‰ (10 g·L^{-1} kaolinite) at IS of 0.001 M. No isotope data of smectite in this set was measured due to limited sorption and thus minor isotope fractionations. The isotopic compositions of K left in the solutions (10 g·L^{-1} kaolinite) change to a range of 0.03–0.19‰ at IS of 0.1 M along with the reduction in K adsorption ratios. High IS inhibits K adsorption, but it does not affect fractionation between liquid and sorbed phases.

To distinguish the equilibrium from kinetic isotope fractionation mechanism, we described the K isotopic fractionations between absorbed ($\delta^{41}K_{ad}$) and aqueous K ($\delta^{41}K_{aq}$) using both equilibrium (batch steady-state, see Eq. 19) and kinetic (modeled as "Rayleigh fractionation", see Eq. 20) models:

$$\delta^{41}K_{ad} = \left(\frac{\alpha \times \delta^{41}K_{KCl} + 1000 f_K \times (\alpha - 1)}{\alpha\,(1 - f_K) + f_K}\right);\ \delta^{41}K_{aq} = (\delta^{41}K_{KCl} - f_K)/(1 - f_K) \quad (19)$$

$$\delta^{41}K_{ad} = \left(\frac{(\delta^{41}K_{KCl} + 1000) \times (1 - (1 - f_K) \times \alpha)}{f_K - 1000}\right);\ \delta^{41}K_{aq} = e^{[(\alpha-1)\ln f_K + \ln(\delta^{41}K_{KCl} + 1000)]} - 1000 \quad (20)$$

where $\alpha_{ad\text{-}aq}$ is the fractionation factor, $\delta^{41}K_{KCl}$ is the $\delta^{41}K$ value of initial KCl (0.20±0.04‰), and f_K denotes the proportion of K left in solutions (i.e., (1-f_K) is the proportion of K adsorbed on clay). The equilibrium model assumes continuous, reversible isotope exchange as the reaction continues in closed systems (Fig. 17a). In comparison, the kinetic model considers that one phase can be continuously removed from the system, which is not fully reversible (Fig. 17b). The equilibrium (batch steady-state) models provide the best fit for isotope results ($\alpha_{ad\text{-}aq}$ of ~1.00075).

Table 10. Experiment setup and data of K adsorption on clay minerals and its isotope fractionation in time-series, pH-dependent and concentration control sets.

Syst.	No.	Time	pH	$[K]_{Initial}$	Adsorption	$[K]_{ad}$	$\delta^{41}K_{aq}$	95%c.i.	$^{1}\delta^{41}K_{ad}$	$^{2}\delta^{41}K_{ad}$	$^{3}\delta^{41}K_{ad}$
		h		mM	%	μmol·m^{-2}	‰	‰	‰	‰	‰
Time-series set	10 g/L Kaolinite IS=0.001M	0.25	8	0.2	63.4	0.63	-0.14	0.04	0.40	n.d.	n.d.
		1			72.3	0.72	-0.24	0.04	0.37		
		3			71.1	0.71	n.d.	n.d.	n.d.		
		12			72.0	0.71	-0.36	0.04	0.42		
		24			74.7	0.74	n.d.	n.d.	n.d.		
		72			74.2	0.74	-0.35	0.04	0.39		
		168			77.1	0.77	n.d.	n.d.	n.d.		
		360			72.3	0.72	-0.32	0.04	0.40		
	2 g/L Smectite IS=0.001M	0.25	8	0.2	30.0	1.40	0.05	0.05	0.55	n.d.	n.d.
		1			42.3	1.48	-0.04	0.04	0.53		
		3			52.5	1.84	n.d.	n.d.	n.d.		
		12			54.6	1.91	-0.25	0.04	0.57		
		24			60.6	2.12	n.d.	n.d.	n.d.		
		72			56.3	1.97	-0.22	0.05	0.53		
		168			58.3	2.04	n.d.	n.d.	n.d.		
		360			54.5	1.91	-0.22	0.05	0.55		
pH-dependent set	10 g/L Kaolinite IS=0.001M	360	4	0.2	13.2	0.13	0.10	0.04	0.86	0.90	-0.24
			6		51.1	0.51	-0.18	0.04	0.56	n.d.	n.d.
			8		73.7	0.73	-0.35	0.04	0.40	n.d.	n.d.
			10		80.0	0.79	-0.43	0.04	0.36	0.38	-0.03
	10 g/L Kaolinite IS=0.1 M	360	4	0.2	8.1	0.08	n.d.	n.d.	n.d.	n.d.	n.d.
			6		15.1	0.15					
			8		18.2	0.18					
			10		17.1	0.17					
	2 g/L Smectite IS=0.001M	360	4	0.2	31.1	1.09	-0.03	0.04	0.71	0.68	-0.37
			6		41.6	1.45	-0.12	0.05	0.65	n.d.	n.d.
			8		55.7	1.95	-0.23	0.05	0.54	n.d.	n.d.
			10		57.4	2.01	-0.24	0.05	0.53	0.50	-0.28
	2 g/L Smectite IS=0.1 M	360	4	0.2	9.3	0.33	n.d.	n.d.	n.d.	n.d.	n.d.
			6		8.4	0.29					
			8		11.9	0.42					
			10		10.8	0.38					
Concentration-control set	10 g/L Kaolinite IS=0.001M	360	8	1	24.9	1.24	0.03	0.04	0.71	n.d.	n.d.
				0.5	47.4	1.18	-0.13	0.05	0.57		
				0.2	74.6	0.74	-0.35	0.04	0.39		
				0.1	71.4	0.35	-0.31	0.05	0.40		
				0.05	76.3	0.19	-0.41	0.04	0.39		
				0.03	81.7	0.12	-0.43	0.04	0.34		
				0.015	84.3	0.06	-0.47	0.04	0.32		
				0.005	92.7	0.02	-0.53	0.04	0.26		
	10 g/L Kaolinite IS=0.1 M	360	8	1	22.0	0.60	n.d.	n.d.	0.80	n.d.	n.d.
				0.5	18.8	0.47	0.07	0.05	0.76		
				0.2	18.0	0.18	0.06	0.05	0.84		
				0.1	14.4	0.07	0.10	0.05	0.79		
				0.05	9.4	0.02	0.13	0.04	0.87		
				0.03	2.0	0.00	0.19	0.04	0.84		
				0.015	2.0	0.00	n.d.	n.d.	0.89		
	10 g/L Kaolinite IS=0.5 M	360	8	1	3.4	0.17	n.d.	n.d.	n.d.	n.d.	n.d.
				0.5	1.7	0.04					
				0.2	1.8	0.02					
				0.1	3.1	0.02					
				0.05	2.7	0.01					
	2 g/L Smectite IS=0.001 M	360	8	20	1.8	6.29	n.d.	n.d.	n.d.	n.d.	n.d.
				10	1.9	4.98					
				5	3.1	4.11					
				2	9.3	3.25					
				1	15.7	2.74					
				0.5	35.2	3.05					
				0.2	55.7	1.95					
	2 g/L Smectite IS=0.1 M	360	8	20	0.2	2.85	n.d.	n.d.	n.d.	n.d.	n.d.
				10	0.8	2.33					
				5	1.5	1.84					
				2	3.9	1.36					
				1	4.4	0.77					
				0.5	4.8	0.42					
				0.2	11.9	0.42					
	2 g/L Smectite IS=0.5 M	360	8	20	0.1	1.08	n.d.	n.d.	n.d.	n.d.	n.d.
				10	0.3	0.69					
				5	0.5	0.65					
				2	0.9	0.34					
				1	0.9	0.16					
				0.5	1.1	0.10					
				0.2	1.9	0.07					

Note 1: IS: ionic strength (NaCl); n.d. means not determined. 95% c.i. =95% confidence interval, notates the two standard error corrected by the Student's t factor; 2 S.D.=two standard deviation;

Table 11. Experiment setup and data of K adsorption on clay minerals and its isotope fractionation in time-series, pH-dependent and concentration control sets.

Sample	Shell	CN	R (Å)	Analysis methods
KCl (aq)	K-O[1]	6	n.d.	Computational calculation
	K-O[2]	6	2.70 – 2.80	Computational calculation
	K-O[3]	6.2 – 6.5	2.82 – 2.86	Computational calculation
	K-O[4]	6.1	2.73	K *K*-edge EXAFS
$(SiO_2)_x \cdot (K_2O)_y$	K-O[5]	6	2.68 – 3.17	X-ray diffraction
	K-O[6]	7	2.75 – 3.34	X-ray diffraction
	K-O[7]	7	2.67	Computational calculation
	K-O[10]	4 – 5	2.72 – 3.10	K *K*-edge EXAFS
	K-O[8]	5 – 6	2.80	K *K*-edge EXAFS
$NaAlSi_3O_8$-$KAlSi_3O_8$	K-O[9]	8.9 – 10.4	3.00 – 3.06	K *K*-edge EXAFS
	K-O[10]	9	3.08	K *K*-edge EXAFS
	K-O[11]	6	3.01	X-ray diffraction
	K-O[12]	9	3.02	X-ray diffraction
Illite	K-O[13]	12	2.77 – 2.86	K *K*-edge XANES
Mica	K-O[14]	12	n.d.	K *K*-edge XANES
	K-O[15]	12	2.99 – 3.26	K *K*-edge XANES

Note 1: References: [1]Varma and Rempe (2006); [2]Sen and Ganguly (2010); [3]Y. Liu et al. (2010); [4]Glezakou et al. (2006); [5]Schweinsberg and Liebau (1974); [6]Yasui et al. (1983); [7]Jabraoui et al. (2016); [8]Greaves et al. (1991); [9]Jackson et al. (1987); [10]Kamijo et al. (1996); [11]Mazzi et al. (1976); [12]Simmons and Peacor (1972); [13]Spiro et al. (1986); [14]Cibin et al. (2005); [15]Xu et al. (2011).
Note 2: Shell: a simplified description of the innermost structure surrounding K atoms; CN denotes the coordination number, R (Å) represents the distance from the center atom.

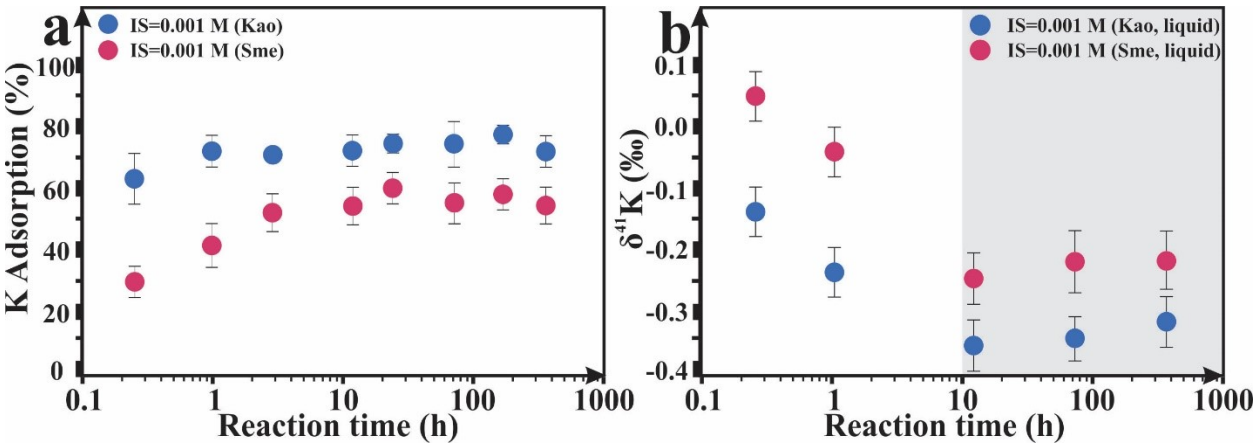

Figure 14. Illustration of K elemental and isotopic patterns in time-series experiments with 0.2mM [K] at pH=8 and IS=0.001 M.

(a) The K adsorption ratios during clay surface exchange at reaction time ranging from 0.25 to 360 h; (b) Temporal change in the isotopic compositions in liquid phases during clay surface exchange at the reaction time ranging from 0.25 to 360 h. Dissolved phases (filtered) were analyzed for K isotope composition. In the plot (b), the isotope stages I (white area) and II (grey area) reveal that initial kinetic fractionation (preferential ^{39}K diffusion) and close-to-equilibration status. Error bars on the Y-axis show (a) the 2 S.D. of triplicates, and (b) analytical uncertainties of isotopic measurements using a MC-ICP-MS at the UW - Seattle, respectively. Abbreviations: Kao: kaolinite; Sme: smectite; IS: ionic strength (background electrolyte by NaCl).

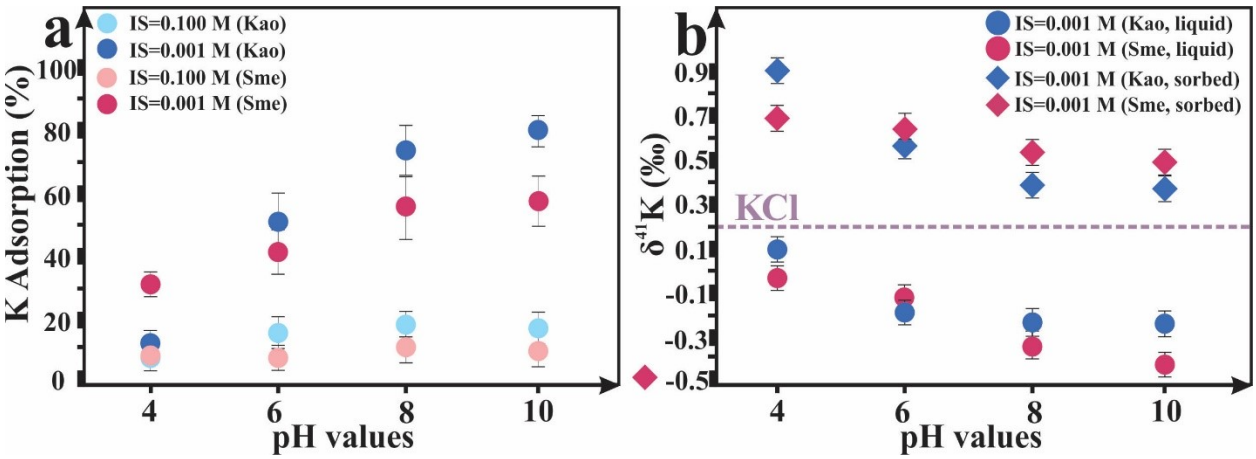

Figure 15. Illustration of K elemental and isotopic patterns in pH-dependent sets.

The clays were reacted with 0.2 mM [K] at IS of 0.001 M and 0.1 M and over a wide pH range from 4 to 10 after 15-d reaction. (a) The adsorption ratio of K during clay surface exchange; (b) The K isotope composition of liquid and sorbed phases during clay surface exchange. Please note that only $\delta^{41}K_{ad}$ data based on mass-balance calculation are plotted, and measured $\delta^{41}K_{ad}$ values are summarized in Table 10. Both dissolved (filtered) and adsorbed phases were measured for K isotope ratios. Error bars on the Y-axis are the same as those in Fig. 14. The K isotopic composition of starting KCl solution (dashed purple line) is 0.20±0.04‰. Abbreviations: Kao: kaolinite; Sme: smectite; IS: ionic strength (background electrolyte by NaCl).

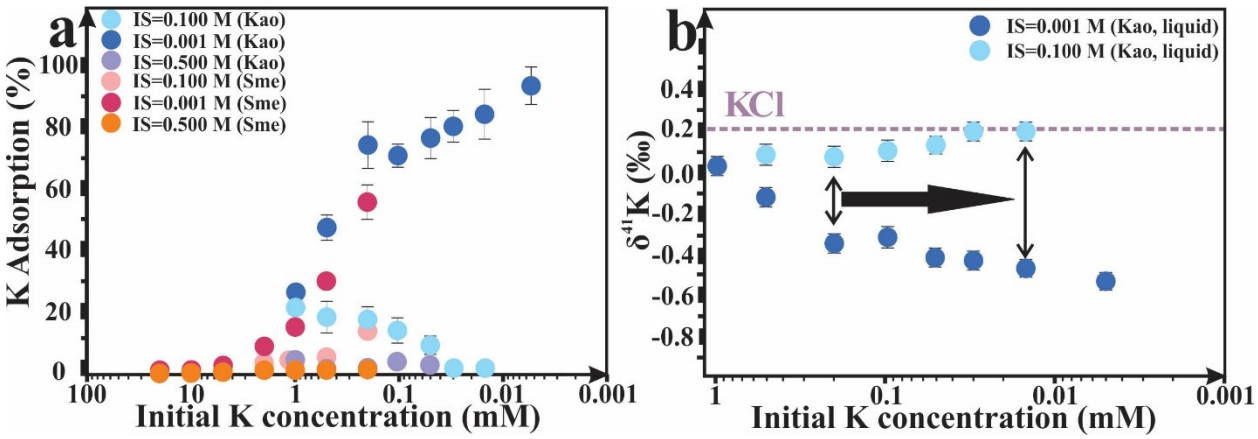

Figure 16. Illustration of K elemental and isotopic patterns in concentration-dependent sets.

The clays were reacted with 0.005-1 mM [K] for kaolinite and 0.2-20 mM [K] for smectite at pH=8 and IS of 0.001 - 0.2 M after 15-d reaction. (a) The absorption ratio during clay surface exchange; (b) The isotopic composition of aqueous K. Only dissolved phases were analyzed for K isotopic composition. Error bars on the Y-axis are the same as those in Figs. 14 and 15. The black arrows in the plot (b) displays the degrees of K isotopic variation between aqueous K (filtered) in kaolinite and smectite sets with changing [K] (or sorption ratio). K isotope compositions of dissolved phases in smectite tests were not measured due to low sorption ratios, and thus limited isotope fractionation. The isotopic value of KCl (dashed purple line) is 0.20±0.04‰. Abbreviations: Kao: kaolinite; Sme: smectite; IS: ionic strength (background electrolyte by NaCl).

5. Discussion

Our experimental results indicate that K isotopes substantially fractionate during K adsorption onto clay minerals, resulting from the equilibrium isotopic exchange process; heavier K isotopes are preferentially adsorbed onto kaolinite and smectite. Consequently, the K isotope fractionation factors between aqueous and adsorbed phases remain almost identical ($\Delta^{41}K_{ad\text{-}aq}$ about 0.6–0.8‰), although the isotopic compositions of dissolved and adsorbed K in experiments vary widely from -0.53‰ to 0.90‰ in various experimental conditions. This feature may be explained by variations in adsorption percent following the same isotope fractionation mechanism. Below, we determined K isotope fractionation mechanisms during clay adsorption. we evaluated the difference in K isotope behavior between clay adsorption and incorporation. Implications for tracing chemical weathering using geologic K records were presented in the end.

5.1. K isotope fractionation during clay adsorption

The near-constant net isotope fractionations ($\Delta^{41}K_{ad\text{-}aq}$) of ~0.6–0.8‰ shown in Fig. 18, and the parallel linear pattern depicted in Fig. 17 suggest that the K isotope behavior could be best described using the equilibrium isotope fractionation law with $\alpha_{ad\text{-}aq}$ of ~1.00075. The parallel trends defined by the K isotope compositions over various K fractions sorbed are indicative of an equilibrium isotope fractionation law with a rapid and continuous exchange between dissolved and sorbed K. Therefore, the fractionation should be thermodynamically driven, and the forward and backward reactions (i.e., adsorption and desorption) are fully reversible. Clay K desorption at high IS is near-complete in all the experiments, implying reversible sorption (Table 10). It is possible that high IS may induce a small amount of particle clumping, thus inhibiting binding access. Nonetheless, K^+ probably has lower affinities for the exchange pool relative to Na^+ and multivalent cations (Appelo et al., 1996), and surface K^+

complexes are hydrated and readily exchangeable due to low hydration energy (Lee et al., 2017). Moreover, Brazier et al. (2019) reported fully exchangeable Ca^{2+} sorbed on clays. Since K has a lower Gibbs free energy of hydration and a faster exchange rate with water ($10^9 \cdot s^{-1}$) relative to Ca ($10^8 \cdot s^{-1}$) (e.g., Lincoln and Merbach, 1995; Markham et al., 1996; Schott et al., 2009), fully exchangeable K on clay surfaces is theoretically expected.

Over the course of experiments, isotopically heavy K was adsorbed onto clays (Fig. 19). In most cases, a short-lived kinetic isotope pattern (transient scatters with heavier K isotopes enriched in solutions) occurs at the initial adsorption stage (Tl, Nielsen et al., 2013; Zn, Dong and Wasylenki, 2016; Ca; Brazier et al., 2019; Se, W. Xu et al., 2020), and rapidly diminishes as the equilibrium is reached. The kinetic trend is not apparent for K that may be ascribed to overprints of subsequent isotope equilibrium. A conceptual scheme depicted for K adsorption and its isotopic fractionation on clays is provided here (Fig. 20a): (i) a kinetic K isotope fractionation step promoted by diffusion, (ii) an isotopic transition from kinetic to equilibria with the gradual contribution of backward reactions, and (iii) eventually an equilibrium status of surface ion complexation with cations in surrounding media. Initial diffusion of isotopically lighter K towards external surfaces (and the interlayer space of smectite) with restrained backward reactions (Bourg et al., 2010) could generate an enrichment of heavier K isotopes in solutions. Such a transient feature could be masked by rapidly established K isotope equilibria. In brief, there is a gradual accumulation of isotopically heavier K on clays, and the lightest isotopic composition in solutions is attained until an isotopic plateau corresponding to the maximum adsorption of K at thermodynamic equilibrium. Observed reduction in net isotopic composition of solvated K could be facilitated by increases in IS and initial [K], or decreases in pH, because of the desorption of ^{41}K ascribed to limited surface loading capacities of both clays.

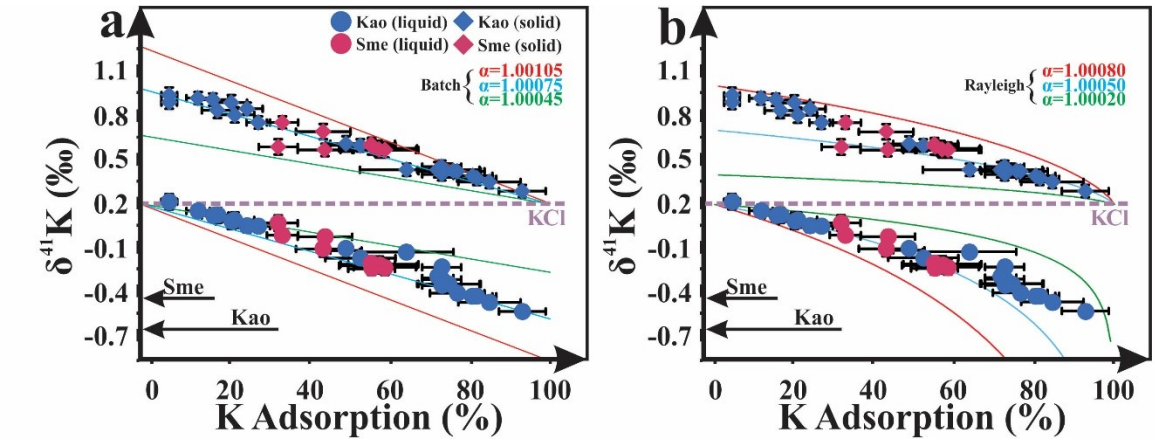

Figure 17. The K isotope fractionation plotted against the adsorption percent.

(a) Batch model fits of isotope composition in dissolved and adsorbed K (only using calculated $\delta^{41}K_{ad}$) during adsorption onto clay minerals vs. the percentage of K adsorption; (b) The Rayleigh model fits of K isotopic fractionation in dissolved and adsorbed K (calculated $\delta^{41}K_{ad}$) during adsorption on clay minerals vs. the percentage of K adsorption. Isotope data are described by a best-fit equilibrium path using fractionation factors $\alpha_{ad\text{-}aq}$ of ~1.00075. Analytical uncertainties could be smaller than the symbol sizes. The arrows in the plots (a-b) denote the K isotopic composition of kaolinite (-0.44±0.05‰) and smectite (-0.63±0.05‰). The K isotopic composition of starting KCl solution (dashed purple line) is 0.20±0.04‰. Kao: kaolinite; Sme: smectite; IS: ionic strength; [K]: initial K concentration. Please note that the isotope composition of adsorbed K was estimated by mass balance calculation.

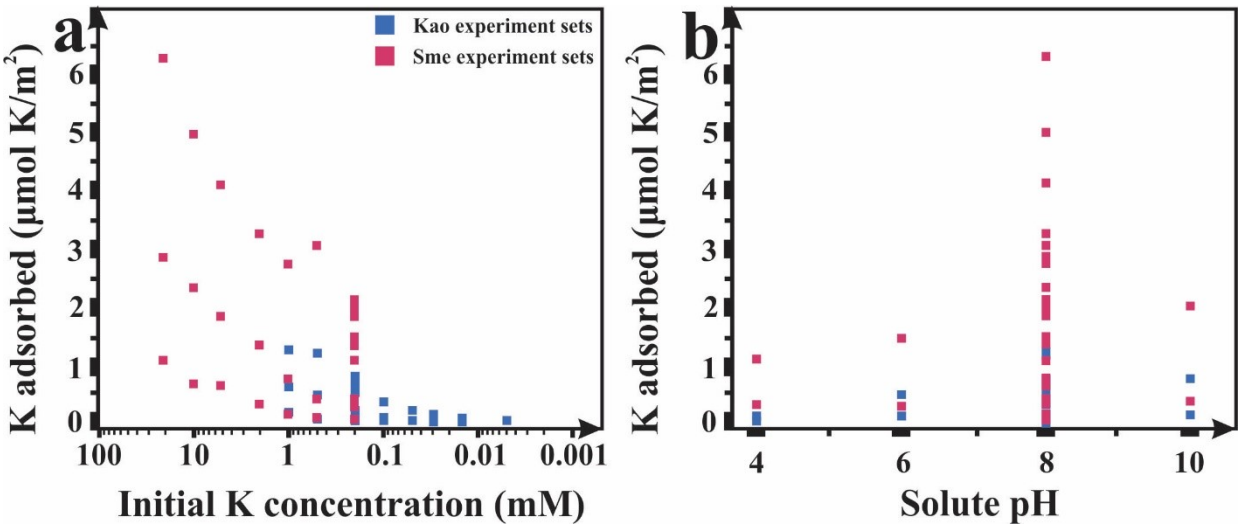

Figure 18. Illustration of clay surface K coverage.

The data are shown as a function of (a) Initial [K] and (b) solute pH. Kao: kaolinite; Sme: smectite. Data points are marked by kaolinite (blue) and smectite (red). Clay K coverages were calculated by adsorbed K divided by BET-N_2 specific surface areas of kaolinite (KGa-2, 20.14 $m^2 \cdot g^{-1}$) and smectite (SWy-2, 28.69 $m^2 \cdot g^{-1}$) (Brazier et al., 2019).

In general, two cation complexation modes often exist on clay surfaces: inner-sphere complexes (chemisorption, with direct bonding to surface sites) and outer-sphere complexes (physisorption, with electrostatic attraction). The two modes may generate different isotope behaviors and can be easily differentiated based on the consequence of ionic strength variation because weakly adsorbed cations can be easily replaced with excess Na^+ at high IS (Lützenkirchen, 1997; Wasylenki et al., 2014; Dong and Wasylenki, 2016; Guinoiseau et al., 2016). Based on our results, adsorbed K^+ are dominated by outer-sphere complexes since almost all K can be desorbed at high IS at 0.1 M and 0.5 M NaCl, regardless of substantial variations in pH and initial [K] (Figs. 14-16). Based on our experiments processed with large IS ranging from 0.001 to 0.5 M, labile K adsorption on kaolinite and smectite can be better characterized by the electrostatic attraction between ionic K^+ in solution and negatively charged clay surfaces within the pH range. The occurrence of outer-sphere complexed K is further supported by K *K*-edge XANES spectra (Fig.12). In addition to pristine clay K features, only the features of KCl (s) can be identified in XANES spectra. This might be caused by the transformation of physically adsorbed $K\cdot(H_2O)_6^+$ into solid-state KCl salt after dehydration (drying clays during sample processing) after experiments. We consider it is very likely since Cl^- could be strongly complexed to surface Al^{3+} vacancy of clays and might be bounded to K^+ as anion-bridged ternary complexes (≡Si/Al-Cl-K, Vasconcelos et al., 2007). similar physical complexation has been documented for Cs^+, which is physicochemically similar to K^+ (Durrant et al., 2018). In sum, outer-sphere K complexation controls the equilibrium isotope fractionation during adsorption.

Major factors modulating equilibrium isotope fractionation include temperature, relative mass differences between isotopes, and bond stiffness related to bond length and coordination number (Schauble, 2004). In the absence of temperature change, the isotope

fractionation between ^{39}K and ^{41}K is likely modulated by atomic coordination. The same mechanism has been reported for outer-sphere Zn^{2+} on kaolinite, Ca^{2+} hosted within mica interlayer spaces, and Ni^{2+} adsorption on calcite (Guinoiseau et al., 2016; Brazier et al., 2019; Alvarez et al., 2020), producing discernable isotope fractionations during adsorption. So far, the molecular mechanics responsible for the fractionation of stable metal isotopes with respect to outer-sphere complexation on clay surfaces remain elusive. Although coordination number of K may not vary when forming outer-sphere complexation, slight distortions of bond length and angle probably occur. It is reasonable because water molecules bind to metal ions mainly through ion-dipole bonds of apparent electrostatic characters. The general rule for equilibrium isotope fractionation states that heavier isotopes of an element prefer to concentrate in the species where they form the stiffest bond (Schauble, 2004). Therefore, ionic K^+ in surrounding waters enriched in heavier isotopes should form stiffer (or shorter) K-O bond compared to surface K complexes, consistent with what we observed in all the experiments.

In addition to outer-sphere K complexation, another possible adsorption reaction scenario may be responsible for isotope fractionation is surface polymerization. Complexation geometry may be modified during polymerization that depends on both pH and excess ion loading, and equilibrium isotope fractionation arising from the variations in atomic coordination. This dependence has been reported in previous adsorption experiments (Ge: Pokrovsky et al., 2014; Zn: Gou et al., 2018; Ga: Yuan et al., 2018; Li: Li and Liu et al., 2020b; W: Wasylenki et al., 2020). It is unlikely the case of K, because the observed K isotope fractionation does not correlate with clay surface K coverage (Fig. 19). In-solution isotope exchange among various dissolved species is also unlikely to be the main reason since K^+ conserves its hydration sphere

with coordination numbers of 6 or 7 based on hybrid quantum mechanical/molecular mechanics (Varma and Rempe, 2006; Rowley and Roux, 2012).

Next, we want to understand whether the isotope fractionation factor for kaolinite differs from that of smectite. Despite similarities in K complexation mode (i.e., outer-sphere complex), it was inferred that the equilibrium isotope fractionation during clay adsorption might be site-dependent (basal surface, edge surface vs. interlayer space, Fig. 820). Specifically, adsorption-driven isotope fractionation may be closely linked to clay charge density in different sites, as reported in a case of Ca adsorption on kaolinite, montmorillonite, and muscovite (Brazier et al., 2019). Only limited isomorphic substitution of tetrahedral Si and/or octahedral Al exists in kaolinite, with pH-dependent charges developing on hydroxyls at edge surface and little pH-independent negative basal charges (Au and Leong, 2013; Schoonheydt and Johnston, 2006). By contrast, considerable permanent negative layer charges present at the interlayer sites of smectite. Above features is consistent with decreases in ζ potentials of clay suspensions promoted by hydroxyl deprotonation with increments in pH, and its decrease with pH in smectite (SWy-2) is dramatically less significant than kaolinite (KGa-2). Such a near-flat ζ-pH pattern of smectite is less obvious in collected ζ data in this study relative to reported ζ data, but it is acceptable considering uncertainties (zeta derivation). However, their isotope patterns are similar, and our data cannot tell the difference in the isotope fractionation factors between the two clays (Fig. 18). It is due to high starting [K] to ensure enough K entered into the interlayer space cannot produce high adsorption ratios of K on smectite to allow for sufficient model fitting (Fig. 18) in the experiments. Specifically, to reach the interlayer space of smectite in addition to external surfaces, high initial [K] is needed, resulting in small adsorption ratios (Table 10). This makes it difficult to distinguish which isotope fractionation model fit better (Fig. 18), since deviations

from linearity would be most apparent in samples with high proportions of sorbed K. Therefore, we are unable to fully distinguish the mineralogy-dependence of K isotope fractionation factor based on the isotope trends in kaolinite and smectite with the present data set.

5.2. Discrepancy in experiment and field data: sorption vs. incorporation

We note that the direction of K isotope fractionation in the adsorption experiments (heavier K preferentially sorbed on clays) is opposite to previous field observations (lighter K scavenged in secondary minerals, S. Li et al., 2019; Chen et al., 2020; Santiago Ramos et al., 2020; Teng et al., 2020; Wang et al., 2020). To solve the discrepancy, we stressed the importance and clarified the mechanism of structural incorporation in comparison with adsorption in responsible for K isotope fractionation during clay formation based on K XANES data of unreacted clays (without sorbed K after extensive cleaning) (Fig. 12b). From our experimental data, isotopically heavy K prefers to be fixed on clay surface by electrostatic attraction without direct bonding (Fig. 18). By contrast, K incorporation within clay lattice prefers light K and has a substantial contribution to the observed K isotope fractionation in weathering environments. Two potential explanations have been proposed for the lighter K isotopic composition in secondary minerals formed at Earth surface environments than the Bulk Silicate Earth (BSE, $\delta^{41}K$ of -0.48±0.03‰, Wang and Jacobsen, 2016). First, rate-limiting processes are pervasive for mineral formation at low-temperature geochemical systems (DePaolo, 2011; Watkins et al., 2017). Therefore, it is plausible that kinetic K isotopic signatures may be partially preserved in the lattice of secondary minerals that isotopically light K potentially co-precipitate with clays through ion diffusion and/or dehydration (Bourg et al., 2010; Hofmann et al., 2012). Alternatively, isotopically lighter K in clay lattice may be explained by equilibrium isotope processes which can be ascribed to changes in atomic coordination.

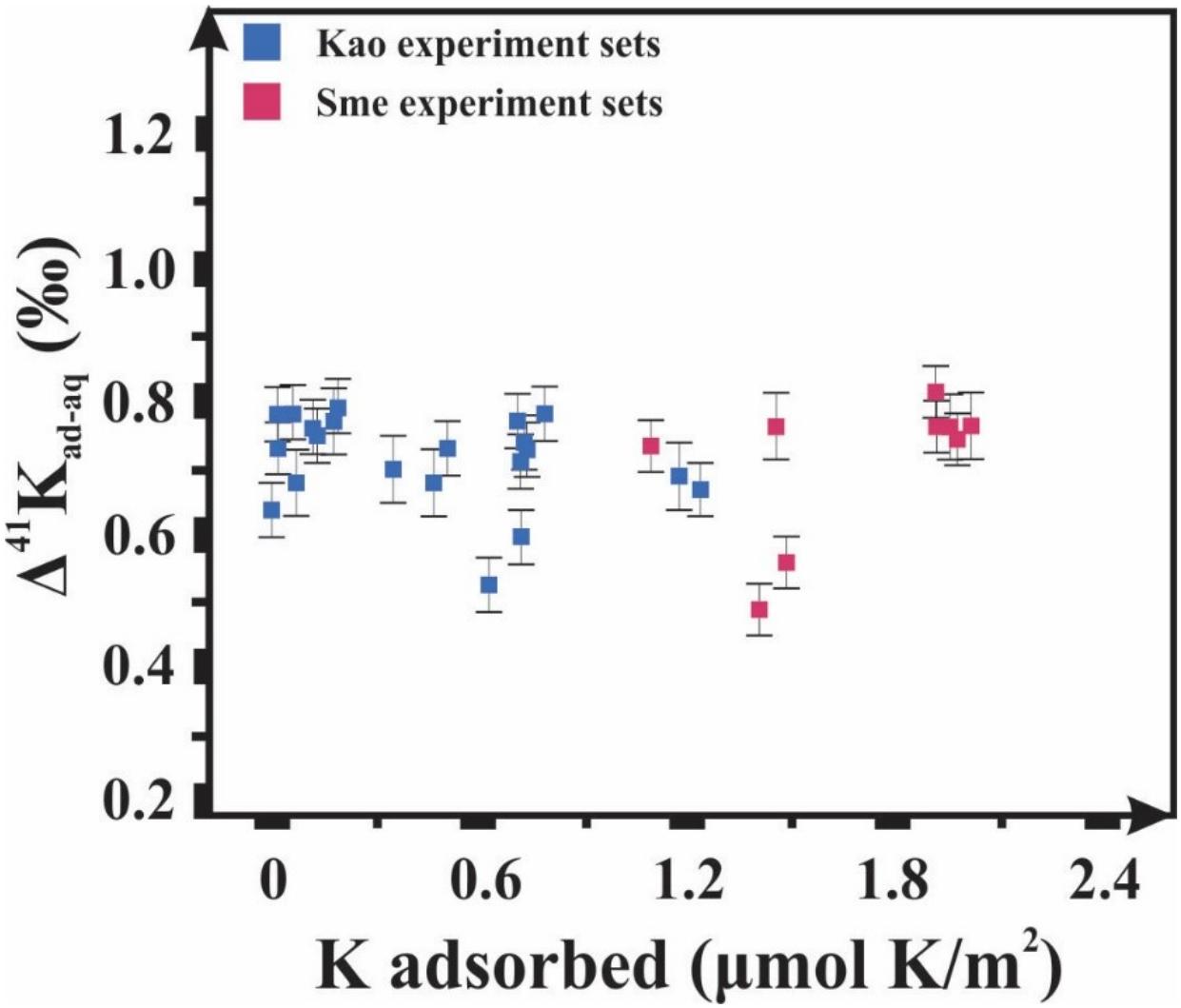

Figure 19. Illustration of K isotope fractionation as a function of clay surface K coverage (μmol K·m^{-2}).

Kao: kaolinite; Sme: smectite; Data points are marked by kaolinite (blue) and smectite (red). Clay K coverages were calculated using adsorbed K divided by BET-N_2 specific surface areas clays. The isotopic composition of sorbed K was calculated by mass-balance, and used to estimate $\Delta^{41}K_{ad-aq}$.

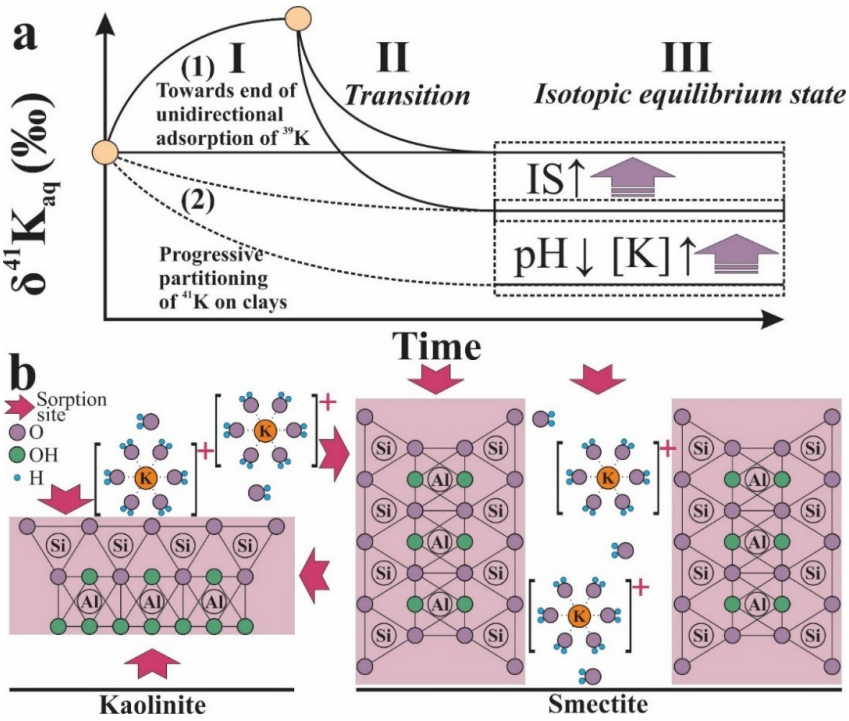

Figure 20. Conceptual illustration of K adsorption and isotope fractionation.

The scheme shows (a) temporal isotope variations in dissolved K, dependent on time, pH, initial concentration ([K]), and ionic strength (IS) and (b) K adsorption modes on kaolinite and smectite at the external surface and the interlayer space, and. In plot, the path (1) reflects successive K isotope behaviors during sorption, including (I) an initial kinetic isotope fractionation due to preferential diffusion of ^{39}K to clay surfaces/interlayers, (II) transition to isotopic equilibria with surrounding aqueous medium, and (III) an eventual equilibrium isotope fractionation with preferential ^{41}K sorption on clays. The path (2) implies gradual establishment of isotopic equilibria without kinetic processes. In the dashed box, isotope fractionations between dissolved K and initial KCl become smaller with lower degrees of adsorption, as IS and initial [K] are higher, and/or solute pH is lower. Isotopically lighter K is prone to be incorporated into clay structures based on field observations (S. Li et al., 2019; Chen et al., 2020; Santiago Ramos et al., 2020; Teng et al., 2020; Wang et al., 2020) and heavier K tends to be sorbed on clay surfaces.

Coordination environment identification can further be obtained from XANES spectra (Fig. 112). Extracting qualitative structural information, as coordination numbers, from the K *K*-edge XANES is a critical step in extending XAFS studies of low concentration systems. Based on the Random Forest Models, Zheng et al. (2020) suggested that the feature of the pre-edge (1) and dominant peak (2) are the most suitable for such interpretation. The trend line between the K-O coordination number and the intensity ratio of Peak1/Peak2 is shown in Fig. 12b (reported for Fe and Ga XANES, Nishi et al., 1998; Wilke et al., 2001). It predicts that K in clay minerals (e.g., illite, kaolinite, and smectite) lattices likely situates in higher-coordinated environments compared with those of $KCl_{(aq)}$ and $KCl_{(s)}$. The empirical pattern is consistent with spectral analyses and theoretical calculations (Table 11). The data demonstrate that K is potentially fixed into clay lattice of higher coordination numbers (K in illite, kaolinite, and smectite) compared with that of K^+ in water (hexacoordination). Hence, our results reflect a slightly stronger, stiffer bonding environment in lattice K compared with ionic K in water. If K isotope fractionation follows an thermodynamic equilibrium path during incorporation, preferential uptake of isotopically lighter K is expected following the stable isotope theory (Schauble, 2004). The K isotope fractionation is stemmed from coordination differences in aqueous K (weaker K-O bonds) and clay structural K (stiffer bonds). This trend is consistent with previous reports based on theoretical calculations, which imply equilibrium isotope fractionation between K^+ in water and K fixed within illite $\Delta^{41}K_{aq\text{-}illite}$ of 0.24‰ at 25 ºC (Zeng et al., 2019). Thus, the importance of clay K incorporation over adsorption in weathering environments could explain the positive K isotopic offset of ~0.6 ‰ in seawater from the upper crusts (Hille et al., 2019; Huang et al., 2020; Wang et al., 2021). In sum, two points need to be clarified. First, the atomic environments of lattice K, sorbed K, and aqueous K are different, and their bond stiffness of K-O likely follow

the order of clay lattice K < aqueous K < sorbed K. Second, structural incorporation rather than sorption is more critical for K cycling and isotope fractionation in natural environments.

5.3. Geochemical implications

This study improves the understanding of the behaviors of K isotope fractionation on Earth surface (e.g., soils, rivers, and oceans), where K-containing solutions react with clay minerals such as kaolinite and smectite. Experimental results indicated the isotope fractionation between aqueous K and adsorbed K is about 0.6–0.8‰ under ambient conditions following the equilibrium isotope fractionation law ($\alpha_{ad\text{-}aq}$ of 1.00075). Based on the XANES spectra, we suggest that K is bounded onto clays as outer-sphere complexes, susceptible to variations in ionic strength (the presence of competitive cations), and the net isotope fractionation between two K pools is probably constant. Although K isotope behavior during co-precipitation with clay minerals has not been experimentally examined, our K *K*-edge XANES data indicate the higher coordination numbers of structural K compared with K^+ in waters. It is suggested that the mass of K removed by co-precipitation with clays is far more important in natural systems, from observations of rivers draining silicate rocks (S. Li et al., 2019; Teng et al., 2020). However, K adsorption may be critical for soils (and regolith) because there are relatively high proportions of water-soluble and exchangeable K (up to ~100%) in global soils (Howard et al., 2012; Pal et al., 1999), positively correlates with the clay content in depth. Since clay uptake of lighter K was observed in natural environments (S. Li et al., 2019; Chen et al., 2020; Huang et al., 2020; Teng et al., 2020; Wang et al., 2020), we consider that most K associated with clays is in the structure of minerals. Despite simplified experiment setup and a less important role of clay adsorption in nature, our result could be applicable to specific terrestrial environments such as calcareous soils (Griffioen, 2001), given high surface affinity to cations of clays at high pH. Moreover, a survey

of K isotopic composition in river water globally collected show a wide range of $\delta^{41}K$ higher, lighter, or comparable to the composition of the continent crust (Wang et al., 2020). Hence, the contribution of clay K adsorption may need further consideration. Despite a lack of evidence, we tentatively expect adsorption-driven K isotope fractionation to be considerable in arid alkaline environments, and the densities of surface negative charge on clays are high. In contrast, K adsorption and its impact on K isotope behaviors are minor in humid acidic settings. It is promising to reconstruct paleoclimate using K isotope information in soils (paleosoils, the soil profiles of long residence times over 10^5 years). Moreover, for extremely weathered rocks whereas structural K is mostly depleted, adsorption-mediated K fractionation should be considered.

The outcomes contribute to understanding the mass balance in the global oceanic K budget. The results of experiment sets and synchrotron-based analyses together confirm the opposite K isotope fractionation patterns driven by surface adsorption and structural incorporation into lattice during chemical weathering and pedogenesis (e.g., S. Li et al., 2019; Chen et al., 2020; Huang et al., 2020; Teng et al., 2020). Adsorption of K on clays potentially modify the K isotopic composition in fluid phases, including rivers, groundwaters, and pore waters, since it is a ubiquitous process in Earth's surface environments. It should be noted that in rivers with circumneutral pH and low salinities, K can be transported as both adsorbed phases on colloids or suspended species and truly dissolved phases. Critically, a large K pool may be transferred to the dissolved pools in the estuarine mixing zone between freshwater and seawater as a result of clay desorption. Tipper et al. (2021) further reported a great flux of mobile elements (such as exchangeable Na and K) with sediments into the ocean could be replaced by

Ca^{2+}. If so, desorption from suspended sediments in estuaries could introduce a considerable flux of K enriched in ^{41}K to the ocean, which needs additional attention.

6. Conclusions

In this study, we experimentally examined the direction, degrees, and mechanisms of K isotope fractionation during K adsorption on two naturally occurring clay minerals (kaolinite and smectite) in the closed system at room temperature over a range of solute parameters (ionic strength and pH). All experiment results reveal that heavy K isotopes are preferentially adsorbed on clays. The enrichment of the solution in lighter K isotopes relative to adsorbed K on clays yielded an average fractionation factor between adsorbed and aqueous phases ($\Delta^{41}K_{ad\text{-}aq}$) of ~0.75‰, which could be best described by an equilibrium fractionation mechanism with constant $\alpha_{ad\text{-}aq}$ of 1.00075 in closed systems. Isotopic equilibria were rapidly achieved after 10 hours, and the net isotope fractionation ($\Delta^{41}K_{ad\text{-}aq}$) does not depend on solute pH, ionic strength, nor starting KCl solution molarity. Ionic K in water was probably bound to clay surfaces as outer-sphere complexes (physically adsorption), which could be easily exchanged with cations with high ionic strength (Na^+ in this study). Although net isotope fractionation ($\Delta^{41}K_{ad\text{-}aq}$) keeps near-constant, increases in the heaviness of the isotopic composition of reacted solutions $\delta^{41}K_{aq}$ have been observed along with dramatic decreases in the percentage of K adsorption at high ionic strength. Therefore, we conclude that differences in atomic coordination on clay surfaces (outer-sphere complex) and within structures (increases in coordination number relative to ionic phase) may be responsible for the opposite directions of K isotope fractionation in sorption experiments and field observations. We highlight the dominance of clay incorporation controlling K isotope behaviors in weathering environments and possible K desorption from river suspended loads in coastal environments affecting marine K isotopic budget.

CHAPTER 5: LITHIUM AND POTASSIUM ISOTOPE FRACTIONATION DURING SILICATE ROCK DISSOLUTION: AN EXPERIMENTAL APPROACH

This chapter is published as: Li, W., Liu, X. M., Wang, K. and Koefoed, P. (2021). Lithium and potassium isotope fractionation during silicate rock dissolution: An experimental approach. Chemical Geology, 568, 120142.

1. Introduction

Chemical weathering is one of the key drivers of crustal evolution on Earth (Goldich, 1938). Chemical weathering shapes Earth's surface, modulates nutrient supplies from land to ocean, and regulates the long-term carbon cycle and habitability over geologic timescale (Gaillardet et al., 1999; Amiotte Suchet et al., 2003; Hartmann et al., 2013; Eiriksdottir et al., 2015). Continental-marine elemental inventories and associated isotope fractionation help with the reconstruction of chemical weathering processes (Edmond, 1992; De La Rocha and DePaolo, 2000; Bayon et al., 2009; Misra and Froelich, 2012; Li et al., 2020a), advancing the understanding of climate change. Hence, assessing the mechanics and contribution of chemical weathering to carbon cycles and oxygenation shifts in the atmosphere, hydrosphere, lithosphere, and biosphere have received extensive attention (Stallard, 1995; Henderson, 2002; Holland, 2005; Misra and Froelich, 2012; Bataille et al., 2017; Li and Liu, 2020a). Thus, constraining the intensity (the degree of alteration in weathered materials) and rate (i.e., the mass of change in weathered materials per unit time) of chemical weathering using geochemical proxies, such as stable isotope ratios of $^{7}Li/^{6}Li$ and $^{39}K/^{41}K$, have been investigated extensively (Dellinger et al., 2015; Tomascak et al., 2016; S. Li et al., 2019; Chen et al., 2020; Li and Liu, 2020b; Teng et al., 2020; Wang et al., 2021). In the case of highly mobile Li and K during continental weathering,

the primary influx of Li and K to the marine systems is produced from silicate dissolution (e.g., Huh et al., 1998; Liu and Rudnick, 2011; S. Li et al., 2019; Wang et al., 2021). Therefore, understanding the controlling factors of isotope fractionation of Li and K (i.e., direction, magnitude and mechanism) during silicate dissolution is significant when applying them as tracers of continental weathering.

Commonly, chemical weathering can be conceptually divided into two possible processes generating isotope fractionation: (i) rock dissolution and (ii) soil (and secondary mineral) formation. So far, experimental silicate rock leaching has been shown to exhibit negligible Li isotope fractionation (e.g., Pistiner and Henderson, 2003; Millot et al., 2010; Wimpenny et al., 2010). Therefore, the utilization of Li isotopic signals to trace weathering is mostly linked to the preferential scavenging of isotopically lighter Li in secondary minerals during adsorption and incorporation, based on both field observations (e.g., Huh et al., 2001; Kisakurek et al., 2005; Pogge von Strandmann and Henderson, 2015; Henchiri et al., 2016; Murphy et al., 2019; Li and Liu, 2020b; Li et al., 2020a; Ma et al., 2020), and laboratory experiments (e.g., Williams and Hervig, 2005; Vigier et al., 2008; Wimpenny et al., 2015; Hindshaw et al., 2019; Pogge von Strandmann et al., 2019; Li and Liu, 2020b). By contrast, there is a lack of knowledge of K isotope fractionation during weathering induced by rock dissolution and pedogenesis. This is because high-precision K isotope measurements (2 S.D.~0.1 ‰) have only become possible due to recent improvements in the analytical method (e.g., W. Li et al., 2016; Wang and Jacobsen, 2016; Morgan et al., 2018; Y. Hu et al., 2018; Chen et al., 2019). So, the impact of silicate dissolution on K isotope behavior remains elusive, requiring further constraints.

Dissolution impacts on Li and K isotope fractionation might be more complicated than previous expectations. For example, the kinetic isotope effect likely exerts additional impacts on

Li isotope fractionation during silicate dissolution before reaching equilibrium, as ^{6}Li diffuses faster than ^{7}Li in liquids (Bourg et al., 2010; Hofmann et al., 2012). A similar effect was observed in experimental studies that recorded the preferential release of ^{6}Li from minerals into solution at the starting period of forsterite/basalt alteration in through-flow reactors (Wimpenny et al., 2010) and batched systems (Verney-Carron et al., 2011). The signal of kinetic effects might be overprinted by successive isotopic equilibrium after reaching the steady-state. Likewise, such a kinetic-to-equilibrium transition trend has been found in multiple metal isotope systems during proton-driven and ligand-driven dissolution (Fe: Brantley et al., 2004; Wiederhold et al., 2006; Kiczka et al., 2010a; Zn: Weiss et al., 2014; Cu: Wall et al., 2011; Mg: Ryu et al., 2011). Exceptions could be attributed to the dependence on the primary mineralogy of silicates (Mo: Voegelin et al., 2012), dissolution congruency (Mg: Balland-Bolou-Bi et al., 2019), oxidative dissolution (Cu: Kimball et al., 2010; Fernandez and Borrok, 2009), ligand-ion complexation (Fe, Chapman et al., 2009; Kiczka et al., 2010b),backward reaction (Li, Wimpenny et al., 2010), and the persistent isotopic equilibrium through reactions (Sr: Mavromatis et al., 2017; Ba: Mavromatis et al., 2016). Hence, a systematic investigation is required to achieve an in-depth understanding of Li and K isotope fractionation during rock dissolution, with leaching experiments under constrained settings being suitable. Since Li and K are chemically comparable (e.g., redox-insensitive and free ionic phases in water), we hypothesize that Li and K isotopes should behave similarly during dissolution and be undiscernible to organic ligands.

The objective of this study is to investigate the direction and magnitude of Li and K isotope fractionation via the dissolution of igneous rocks in time-series. Basalt and granite are the most common exposed silicate rocks, meaning they can provide critical information on chemical weathering in Earth's surficial environments. The combination of dissolution

stoichiometry and Li and K isotope data potentially provides novel insights into the significance and mechanisms of unidirectional dissolution (ultra-acidic settings prepared by 0.8 M HNO_3) and the impact of organic acids (natural analogy) on Li and K isotopic behavior during rock dissolution. By sampling supernatants at different time intervals, we determined the isotopic variations of Li and K from source rock signals at far-from-equilibrium (chemical) conditions, close-to-equilibrium (chemical) conditions, and possible back-reaction in isotope disequilibrium. In this paper, the term "chemical equilibrium" represents the equilibrium of the elements between the solid and fluid phases irrespective of their isotopic signals. A far-from-equilibrium state to a close-to-equilibrium state refers to the approach to equal forward and reverse reactions, i.e., negligible overall reaction. The term "isotope equilibrium" stands for the equilibrium distribution of isotopes between the solid and the fluid phases based on the stable isotope theory (Schauble, 2004). The change of kinetic fractionation to equilibrium fractionation refers to a change from unidirectional isotope fractionation to a partial separation of isotopes between two or more phases in equilibrium. The above definitions are widely used in dissolution systems (Pearce et al., 2012). This study offers direct evidence of dissolution-promoted Li and K isotope fractionation, which is of great interest for future research on chemical weathering.

2. Experimental Setup

2.1. Samples and regents

Deionized water (Milli-Q, 18.2 MΩ·cm) produced by the Milli-Q Direct-Q 3UV (Millipore^{TM}) system was used in all experiments, unless otherwise marked. Double-distilled nitric acid from a Teflon® sub-boiling still system (Savillex^{TM}) was diluted using deionized water to the required molarity. Ultrapure-grade oxalic acid and citric acid (hereafter referred to OA and CA as their abbreviations, respectively) were sourced from Fisher Scientific Inc. All

polyethylene wares and Teflon® beakers were cleaned with 2 wt.% HNO_3 and then rinsed thoroughly using deionized water. Research-grade Hawaiian basalt (BHVO-2) and Colorado granodiorite (GSP-2) standards were obtained from the United States Geological Survey to preclude grain-size effects. In consideration of contamination and initial non-linear reaction kinetics due to fine particles adhered to rocks, labile components were removed through ultrasonic treatment in deionized water, followed by methanol rinses (Kiczka et al., 2010a; Weiss et al., 2014). After cleaning, the concentrations of Li, K, Al, and Si in eluents are lower than the detection limits of the quadrupole inductively-coupled-plasma mass spectrometer (Q-ICP-MS). Rock powders were then dried in ambient conditions and stored for future analyses.

2.2. Experiments

To determine the behaviors of Li and K during liberation from silicate frameworks through chemical weathering and their associated isotope fractionation, powdered igneous rocks were subjected to acidic treatment under constrained conditions (e.g., solute pH, reaction time, and temperature). Two individual experimental sets were designed and conducted in batch closed-systems, including (1) proton-driven dissolution of basalt and granite using 0.8 M HNO_3 at 25 or 80 °C; (2) ligand-driven dissolution of basalt and granite using 5 mM CA/OA at 25 °C. We note that prepared 0.8 M HNO_3 was adopted to simulate corrosive environments where backward reactions would be significantly precluded, thus resulting in approximate unidirectional dissolution (Pistiner and Henderson, 2003). Such an ultra-acidic condition (pH~0.2) favors forward dissolution reactions and exerts strong controls against back-reactions, ensuring liberated cations are isolated in the surrounding solution. In addition to the ambient condition of proton-driven dissolution, a water temperature of 80°C was applied to simulate basalt-hosted geothermal systems (Olasolo et al., 2016). It is known that the presence of organic

acids (or ligands) largely affects mineral dissolution kinetics and stoichiometry (Li and Liu, 2020a). To approximate Earth's surface conditions with biological interferences (e.g., soils) and maintain consistency with previous studies of ligand-controlled silicate dissolution (Wiederhold et al., 2006; Chapman et al., 2009; Weiss et al., 2014), 5 mM of the organic acids were chosen for the reacted solution. Low- molecular-weight organic acids such as OA and CA are ubiquitous on Earth's surface, normally playing a substantial role in biogeochemical weathering processes (Hausrath et al., 2011). In addition, possible backward processes can also be evaluated in the experiments with organic acids (e.g., Chapman et al., 2009; Weiss et al., 2014) at relatively high pH. Solute pH was not buffered but was routinely monitored using the pH meter at each sampling step. A pH electrode with 3 M NaCl internal electrolyte solutions rather than 3 M KCl was used to avoid any K contamination during pH adjustment and lateral pH measurement. The pH meter (Thermofisher^{TM}) was calibrated using the standard pH references (Fisher Scientific^{TM}, pH=4/7/10). As for experiment design, basalt was subjected to more acid treatments than granite to test Li and K isotope behaviors. The main reason for this is basalt weathering is responsible for more than 30% of global CO_2 consumption (Gaillardet et al., 1999), so it needs comprehensive environmental constraints in a dissolution study such as this.

Prior to reaction, approximately 500±0.1 mg rock samples were suspended in borosilicate Erlenmeyer flasks (Corning^{TM}) on a thermostatic plate, filled with 250 mL 0.8 M HNO_3 or 5 mM organic acids. Continuous agitation is important during dissolution, affecting solute distribution in solutions and boundary film formations on solids. The size of the reactor was 250 mL, and the solid-to-solution ratio was kept constant at 2.0 $g \cdot L^{-1}$. The initial ionic strength of solutions was adjusted to 10 mM using NaCl (K- and Li-free, extra pure). Reactors were kept in atmospheric conditions, and continuously mixed at 550 rpm using magnetic stir bars to ensure efficient

solution-rock contact and surface-reaction controlled dissolution (Wimpenny et al., 2010). Through the entire experiment, the dissolution systems changed from far-from-equilibrium to near-equilibrium over a period of 15 days. A periodical sampling of filtered supernatant while manually shaking the reactor was allowed to homogenize the solid-fluid phases. Liquid extracts (~0.5 mL) using syringe samplers were centrifuged and separated from solid residues by 0.22 um cellulose acetate syringe filters (Thermo Fisher Scientific^{TM}), then transferred into acid-clean polypropylene tubes. The silicate residues were separated from the liquids at the end of the experiment, rinsed with deionized water, dried, and stored at 4°C. Each silicate-regent combination was carried out in replicates to ensure data reproducibility and accuracy. Experiment conditions are listed in Tables 12-13.

Table 12. Kinetic parameters of silicate rock dissolution during proton-driven dissolution.

Sample	T	Solute chemistry ($EXP_{(1)}$)								Solute chemistry ($EXP_{(2)}$)		
		δ^7Li (‰)	2S.D. (‰)	δ^{41}K (‰)	95%c.i. (‰)	N	Released Li (%)	Released K (%)	Released Si (%)	Released Li (%)	Released K (%)	Released Si (%)
Granite (GSP-2) 0.8 M HNO_3	10 min	n.d.	1.1	n.d.	n.d.	n.d.	7.6	4.3	2.6	8.1	4.6	2.7
	30 min	-4.7	1.1	-0.99	0.04	11	14.3	8.0	6.3	11.2	8.1	5.8
	1h	-4.6	1.1	n.d.	n.d.	n.d.	18.8	7.0	8.5	16.7	6.6	6.7
	3h	-2.6	1.1	-0.90	0.06	7	29.7	13.8	12.9	27.6	14.1	13.2
	5h	-2.2	1.1	n.d.	n.d.	n.d.	42.5	21.5	20.7	42.1	21.2	21.6
	9h	-1.8	1.1	n.d.	n.d.	n.d.	56.7	25.2	26.2	52.0	24.7	27.1
	1d	-1.8	1.1	-0.58	0.04	8	73.6	32.3	35.2	71.4	33.8	35.5
	3d	-1.7	1.1	n.d.	n.d.	n.d.	78.1	33.2	36.8	79.2	31.6	37.2
	7d	-1.5	1.1	-0.44	0.06	11	78.3	33.3	37.2	82.7	33.5	38.2
	15d	-1.5	1.1	-0.40	0.04	n.d.	79.2	34.7	39.1	87.5	35.0	40.1
Basalt (BHVO-2) 0.8 M HNO_3	10 min	n.d.	1.1	n.d.	n.d.	n.d.	1.2	2.1	0.5	1.6	1.9	0.6
	30 min	-4.2	1.1	-0.93	0.04	9	3.7	3.1	1.2	3.3	3.0	1.1
	1h	-3.6	1.1	n.d.	n.d.	n.d.	4.2	3.6	2.3	4.6	3.9	2.5
	3h	-1.3	1.1	-0.52	0.04	7	8.7	7.7	4.6	9.5	7.7	5.2
	5h	-0.2	1.1	n.d.	n.d.	n.d.	9.4	9.0	4.9	10.4	9.8	5.7
	9h	0.3	1.1	n.d.	n.d.	n.d.	11.5	11.0	5.7	11.8	11.6	6.3
	1d	1.5	1.1	-0.48	0.04	9	11.6	11.1	6.7	13.9	12.1	6.9
	3d	2.3	1.1	-0.47	0.04	9	18.6	12.8	8.8	20.4	14.9	9.1
	7d	2.2	1.1	-0.45	0.04	10	26.9	19.7	16.3	26.6	20.6	16.1
	15d	1.9	1.1	-0.46	0.05	10	29.6	22.5	17.6	28.1	23.1	18.1
Basalt (BHVO-2) 0.8 M HNO_3	10 min	n.d.	1.1	n.d.	n.d.	n.d.	2.8	2.2	1.7	2.6	1.6	1.6
	30 min	-4.0	1.1	-1.20	0.06	9	4.4	2.7	2.0	5.1	3.2	1.8
	1h	n.d.	1.1	n.d.	n.d.	n.d.	7.7	3.8	3.8	8.7	4.1	3.2
	3h	1.5	1.1	-0.93	0.06	9	10.0	4.3	3.3	10.4	5.1	3.3
	5h	n.d.	1.1	n.d.	n.d.	n.d.	19.9	9.8	7.8	21.1	11.1	7.8
	9h	4.3	1.1	-0.76	0.04	9	26.3	16.6	12.1	27.8	18.9	12.6
	1d	n.d.	1.1	n.d.	n.d.	n.d.	39.5	22.4	22.7	41.1	25.6	21.7
	3d	4.5	1.1	-0.56	0.05	10	48.9	32.0	23.7	50.9	37.6	23.7
	7d	n.d.	1.1	n.d.	n.d.	n.d.	55.1	48.7	27.1	58.0	50.1	27.1
	15d	4.6	1.1	-0.59	0.04	11	65.7	56.3	34.5	67.6	62.7	34.9

Note 1: Li isotopes were measured using a Q-ICP-MS method (Liu and Li, 2019); K isotopes ere measured using a MC-ICP-MS method (Chen et al., 2019). Experiments were conducted in duplicate and isotope data of $EXP_{(1)}$ were reported.Note 2: N: the number of isotope analytical cycles. We note that N=7 for Li isotope analysis. 95% c.i.: 95% confidence interval; 2 S.D.: two standard deviation corrected by the Student's *t* factor. Net isotope fractionation $\Delta^7Li_{l\text{-}s}$ and $\Delta^{41}K_{l\text{-}s}$ during dissolution reported in this paper could be calculated by the difference between dissolved isotopic composition (shown in this table) and initial rock isotopic composition. n.d.: not determined. Temp.: temperature.

Table 13. Kinetic parameters of silicate rock dissolution during ligand-driven dissolution.

Sample	Time	Solute chemistry ($EXP_{(1)}$)								Solute chemistry ($EXP_{(2)}$)		
		δ^7Li (‰)	2S.D. (‰)	δ^{41}K (‰)	95%c.i. (‰)	N	Released Li (%)	Released K (%)	Released Si (%)	Released Li (%)	Released K (%)	Released Si (%)
Granite (GSP-2) 5 M CA	10 min	n.d.	1.1	n.d.	n.d.	n.d.	7.2	2.0	3.1	5.9	1.6	3.3
	30 min	-4.5	1.1	-0.98	0.03	9	8.9	2.5	5.5	8.0	2.4	5.0
	1h	n.d.	1.1	n.d.	n.d.	n.d.	10.3	3.1	6.2	9.4	3.0	5.7
	3h	-4.2	1.1	-0.80	0.06	8	11.5	3.3	7.3	11.0	3.2	7.4
	5h	n.d.	1.1	n.d.	n.d.	n.d.	12.7	3.4	7.9	12.2	3.5	7.3
	9h	-1.6	1.1	-0.66	0.07	8	15.7	3.7	8.9	15.0	3.7	8.4
	1d	-0.4	1.1	n.d.	n.d.	n.d.	31.5	3.8	15.3	30.8	3.9	14.3
	3d	0.4	1.1	-0.58	0.05	8	25.4	3.9	16.2	27.8	4.0	15.7
	7d	1.4	1.1	-0.53	0.03	8	21.6	4.2	16.8	21.1	4.4	16.2
	15d	2.3	1.1	-0.39	0.04	11	17.8	4.2	17.4	16.6	4.5	16.8
Basalt (BHVO-2) 5 mM CA	10 min	n.d.	1.1	n.d.	n.d.	n.d.	3.2	0.6	1.1	3.6	2.0	0.9
	30 min	-0.4	1.1	-0.90	0.04	11	4.3	1.9	1.7	4.5	2.9	2.7
	1h	n.d.	1.1	n.d.	n.d.	n.d.	6.3	5.1	3.5	6.4	5.4	3.5
	3h	0.2	1.1	-0.75	0.04	9	11.4	6.4	6.7	12.2	6.2	6.2
	5h	n.d.	1.1	n.d.	n.d.	n.d.	13.0	6.7	7.3	13.9	6.6	7.6
	9h	1.8	1.1	n.d.	n.d.	n.d.	18.9	7.8	9.0	17.7	7.3	8.4
	1d	3.2	1.1	-0.57	0.04	11	13.8	9.0	11.9	15.7	9.3	11.4
	3d	4.7	1.1	-0.50	0.05	10	5.6	9.8	12.7	12.8	9.7	12.2
	7d	4.9	1.1	n.d.	n.d.	n.d.	3.0	10.1	13.2	4.1	10.7	12.9
	15d	5.0	1.1	-0.47	0.05	10	1.9	10.6	13.9	2.4	11.2	13.4
Basalt (BHVO-2) 5 mM OA	10 min	n.d.	1.1	n.d.	n.d.	n.d.	8.9	4.4	3.0	8.4	4.1	3.1
	30 min	-5.7	1.1	-1.41	0.04	6	21.1	9.3	9.1	18.9	9.1	8.6
	1h	n.d.	1.1	n.d.	n.d.	n.d.	26.8	9.9	11.4	25.9	9.5	12.4
	3h	-2.3	1.1	-0.84	0.05	10	34.2	10.1	12.1	31.8	10.6	13.6
	5h	n.d.	1.1	n.d.	n.d.	n.d.	39.1	11.5	14.1	40.5	11.7	14.6
	9h	0.2	1.1	-0.70	0.03	10	51.1	12.2	18.1	49.0	12.0	18.6
	1d	n.d.	1.1	-0.53	0.06	8	57.8	12.6	18.9	64.5	12.4	19.9
	3d	1.3	1.1	-0.51	0.03	9	77.7	12.8	20.9	79.3	12.3	21.9
	7d	1.9	1.1	-0.56	0.05	11	42.5	14.0	21.3	46.5	13.9	22.3
	15d	2.4	1.1	-0.45	0.05	10	20.1	14.5	22.1	24.1	15.6	22.5

Note 1: Li isotopes were measured using a Q-ICP-MS method (Liu and Li, 2019); K isotopes ere measured using a MC-ICP-MS method (Chen et al., 2019). Experiments were conducted in duplicate and isotope data of $EXP_{(1)}$ were reported.

Note 2: N: the number of isotope analytical cycles. We note that N=7 for Li isotope analysis. 95% c.i.: 95% confidence interval; 2 S.D.: two standard deviation corrected by the Student's *t* factor. Net isotope fractionation $\Delta^7Li_{l\text{-}s}$ and $\Delta^{41}K_{l\text{-}s}$ during dissolution reported in this paper could be calculated by the difference between dissolved isotopic composition (shown in this table) and initial rock isotopic composition. n.d.: not determined. Temp.: temperature.

3. Analytical Methods

3.1. Elemental analysis

All chemical pretreatments were performed in a class-100 vented laminar flow workstation (Airclean™, 600 PCR) in the Plasma Mass Spectrometry Lab at the University of North Carolina at Chapel Hill (UNC-CH). To complete a compositional description of major elements, solid pellets were measured using X-ray fluorescence (XRF) at ALS Chemex Labs following a $Li_2B_4O_7$ fusion approach. After weighing, both international geostandards and samples were digested using a mixture of concentrated HCl-HNO_3-HF acids at > 150 °C, following an approach reported in W. Li et al. (2019). Solid and dissolved concentrations of Li, Na, K, Mg, Al, Fe, Ca, Sr, Nb, Si, and Ti were determined using a Q-ICP-MS (Agilent™ 7900) at UNC-CH. The instrument was calibrated by a series of ICP standard solutions of known concentrations. Internal standards, including Be, Ge, Rh, In, Ir, and Bi were employed for signal drift correction. International references BHVO-2 (basalt), GSP-2 (granodiorite), and JG-2 (granite) were measured in the same batch to ensure analytical accuracy and reproducibility (Appendix 1). The elemental compositions of international references were certified by the United States Geologic Survey (USGS) and the Geological Survey of Japan (GSJ). During analysis, a precision of <3% (relative standard derivation, RSD) was achieved. The RSD value was calculated based on an average of six analytical cycles of the same sample. The measurement was validated with the results obtained on different reference materials, yielding an accuracy <10% for reported elements (relative to reference certified values), and data are justified from a compilation of inter-laboratory comparisons (Appendix 1).

3.2. Solid characterization

Mineralogical identification on powdered soils was conducted using X-ray diffraction (XRD) at UNC-CH. Solid samples were ground into powders with an agate mortar and pestle and smeared on glass slides. X-ray spectra were obtained on an XRD diffractometer (Rigaku™) with Ni-filtered Cu Kα radiation (40 kV, 40 mA) and the scan range from 3° to 65° 2θ with a 0.01° step-size and 10 s acquisition time (Fig. 21). Infrared spectroscopy has advantages in surface sensitivity to acquire information on the alteration level of reacted silicates. Attenuated total reflectance Fourier transform infrared spectroscopy (ATR-FTIR) spectra were measured using the Bruker™ Hyperion 1000 with Tensor 27 spectrometer (Fig. 22). This instrument was equipped with an MCT-A detector and a platinum diamond ATR crystal accessory in order to reach high interface sensitivity. Vacuum-dried solids from different experimental groups were loaded on a plate, and the spectra were collected (256 scans) with a 2 cm^{-1} resolution and background subtraction.

Surface silica phases were characterized by X-ray photoelectron spectroscopy (XPS). The high-resolution scans of Si_{2p} XPS with fittings are shown in Fig. 23. The survey scans were collected over a range of binding energy (BE) from 0 to 1100 eV with a step size of 700 meV and dwell time of 75 ms. A narrower binding energy range and step size were applied to acquire higher resolution scans of Si atoms, with a range of 96–112 eV, with 0.25 eV step size and 100 ms dwell time, and processed with CASAXPS.

3.3. Chromatography

All isotope pretreatments were performed in a class-100 vented laminar flow workstation (Airclean™, 600 PCR) in the Plasma Mass Spectrometry Lab at UNC-CH. An aliquot of the digested samples was evaporated to dryness and re-fluxed by 2 mL 0.7 M HNO_3 prior to loading onto columns. Lithium and potassium fractions were obtained after column purification,

following the two-step approach modified by Liu and Li (2019) and Chen et al. (2019). The first column was packed with 17 mL AG50-X8 cation-exchange resin (200-400 mesh, Bio-Rad™), and conditioned in 0.7 M HNO_3. The first Li fraction was collected with Na before most of the matrix elements being eluted, and the first K fraction was collected with Rb after Li was eluted. Collected elution cuts were evaporated to dryness on a hotplate and re-dissolved in 1 mL 0.2 M HCl for the second Li column and 1 mL 0.5 M HNO_3 for the second K column, respectively. The setup of the second Li and K columns were identical to the first except for volume and inner diameter. The second Li fraction was collected after other matrix elements (namely Na) were eluted, with a third (identical) column purification done if necessary (if Li/Na<0.1). The second K fraction was collected after the rest of the matrix elements (namely Rb) were eluted, and a third (identical) column separation was performed if needed. After the chromatographic process, the pre-cuts and post-cuts of column chemistry (fractions recovered before and after K-collecting volumes) were checked for Li, K, Na, Al, Fe, Rb, and Ti on the Agilent™ 7900 Q-ICP-MS, to guarantee satisfactory Li and K yields (~100%) and low matrix contents, ensuring the reliability of isotope analyses by Q (MC)-ICP-MS (Chen et al., 2019; Liu and Li, 2019).

3.4. Isotope analysis

Procedural blanks (10 mM NaCl) were monitored for experiment runs (≤0.01 ng Li), which were negligible in comparison to collected Li fractions of natural and laboratory samples at μg-levels. The Li isotope analysis was performed using the same Q-ICP-MS instrument as the elemental analysis and the detail was previously reported in Liu and Li (2019). Prior to measurement, samples and standards were matrix matched to a concentration of 0.5 ppb Li in 2% HNO_3. We adopted a microflow self-aspirating (Agilent™, 200 $\mu L \cdot min^{-1}$) PFA nebulizer, quartz spray chamber, quartz torch, and 2.5 mm internal diameter injector. To reach high signal stability and

low background, we optimized the carrier gas flow (0.95 $L \cdot min^{-1}$) and the make-up gas flow (0.35 $L \cdot min^{-1}$). The instrumental sensitivity was about 250,000 cps on ^{7}Li for 0.5 $\mu g \cdot L^{-1}$ solution. Because of the low sample concentration (0.5 ppb Li), a long washing time (180 s) was used during sample transition to maintain low background signals and control memory effects. The sample-standard bracketing method (7 cycles) was used, and concentration matching between standards and samples was limited to >95%. Since the NIST L-SVEC is no longer available and the IRMM-016 standard has an identical Li isotopic composition, and the IRMM-016 standard was used here. The Li isotopic composition is expressed as $\delta^{7}Li$, the per mil deviation from the IRMM-016 standard ratio:

$$\delta^{7}\mathrm{Li}_{\mathrm{sample}}\ (‰) = \left\{\frac{(^{7}\mathrm{Li}/^{6}\mathrm{Li})_{\mathrm{sample}}}{(^{7}\mathrm{Li}/^{6}\mathrm{Li})_{\mathrm{IRMM-016}}} - 1\right\} \times 1000 \qquad (21)$$

The USGS granite (GSP-2) and basalt (BHVO-2) standards were analyzed along with samples for quality control, and the Li isotope values fall within the uncertainties of previously reported data (Appendix 2). Net Li isotope fractionation between dissolved Li and Li hosted in the rocks, $\Delta^{7}Li$ was calculated using the following equation (Eq. 22):

$$\Delta^{7}\mathrm{Li}_{\mathrm{l-s}} = \delta^{7}\mathrm{Li}_{\mathrm{liquid}} - \delta^{7}\mathrm{Li}_{\mathrm{pristine\ solid}} \qquad (22)$$

The long-term external precision is 1.1‰, derived from the 2 S.D. of 1-year repeat analyses of IRMM-016 and standard igneous rock references JG-2 and BCR-2 (Liu and Li, 2019).

Procedural K blanks were monitored for experiment runs (≤10 ng K), which were negligible in comparison to collected K fractions of natural and laboratory samples at µg-/mg-levels. Purified K solutions were introduced into a Neptune Plus MC-ICP-MS (Thermo Scientific™) at the Isotope Cosmochemistry Laboratory, Washington University in St. Louis. Here, we employed the cold plasma technique to residual and isobaric ($^{40}Ar^{1}H^{+}$ on $^{41}K^{+}$ and $^{38}Ar^{1}H^{+}$ on $^{39}K^{+}$) argides (Chen et al., 2019). In addition to monitoring of ^{41}K and ^{39}K, we measured $^{40}Ar(^{40}Ca)$ and ^{44}Ca to account for interferences and/or contamination. Samples were

introduced into the instrument through an Elemental Scientific™ APEX omega, equipped with a desolvation membrane to improve sensitivity and reduce the generation of hydride and oxide. A sample-standard bracketing technique (>6 cycles) was used with the K NIST SRM 3141a standard to correct instrumental mass bias. Instrumentation and analytical details are documented in Chen et al. (2019). Sample isotopic composition is reported in a δ-notation, as the per mil (‰) deviation from the K NIST SRM 3141a isotope standard (see Eq. 23):

$$\delta^{41}\mathrm{K}_{\mathrm{sample}}\ (‰) = \left\{\frac{(^{41}\mathrm{K}/^{39}\mathrm{K})_{\mathrm{sample}}}{(^{41}\mathrm{K}/^{39}\mathrm{K})_{\mathrm{NIST\ SRM\ 3141a}}} - 1\right\} \times 1000 \quad (23)$$

A long-term reproducibility from replicate analyses of a suite of international references is better than 0.11‰ (2 S.D.) (Chen et al., 2019). The granite (GSP-2) and basalt (BHVO-2) USGS standards were analyzed for quality control, and the isotope values fall within the uncertainty of previously reported data (Appendix 2). Net K isotope fractionation between dissolved K and K hosted in pristine rocks, Δ^{41}K was defined by the following equation (Eq. 24):

$$\Delta^{41}\mathrm{K}_{\mathrm{l-s}} = \delta^{41}\mathrm{K}_{\mathrm{liquid}} - \delta^{41}\mathrm{K}_{\mathrm{pristine\ solid}} \quad (24)$$

The two standard deviations (2 S.D.) and 95% confidential interval (95%c.i.) provided in Tables and in figures were calculated from 7 to 11 replicates of δ^{41}K measurement of each sample. Estimated uncertainty on isotopes was propagated based on the following equation (Eq. 25):

$$\Delta E = \sqrt{(c_1\Delta \mathrm{W}_1)^2 + (c_2\Delta \mathrm{W}_2)^2 + \cdots + (c_n\Delta \mathrm{W}_n)^2} \quad (25)$$

where ΔE is an absolute error, c is a multiplicative factor, and W is additive function inputs.

4. Results

4.1. Solid characterization

X-ray diffractogram displays variations in the intensity of mineral-specific peaks in reacted and pristine rocks (Fig. 21). The order of the decrease in the intensities of mineral-specific peaks is proton-driven dissolution (HNO_3, 80 ºC) > proton-driven dissolution (HNO_3,

25ºC) > ligand-driven dissolution (OA and CA, 25ºC). The apparent decreases in ~8º and~ 27º (2θ) in the spectra imply the preferential dissolution of mica and feldspar minerals. Based on XRD spectra, there is no evidence in support of secondary phase precipitation. ATR-FTIR spectra reveal vibrations in the bonds between O, Si, and Al atoms, in particular for proton-driven dissolution (Fig. 22). Spectra bands at 925/990 cm^{-1} and 1056 cm^{-1} represent the stretching vibrations of the SiO_3 groups and the bending (Si–O_b–Si) (Yin et al., 2010). There is no detectable infrared signal of secondary minerals on solids from both systems. The high-resolution scans of Si_{2p} XPS with the least R square (best fits to the data) are illustrated in Fig. 23, which mainly consist of two sets of peaks (spin-orbit split doublets with a spacing of 0.62 eV, $Si_{2p1/2}$ and $Si_{2p3/2}$, Sutherland et al., 1992), offering more information of surface Si alteration during silicate dissolution. The ratios of SiO_2/SiO_x of pristine basalt and granite are 1.93 and 2.00, respectively. After the reaction, SiO_2/SiO_x ratios increase to 2.26 (proton-driven) and 2.09 (ligand-driven) for granite at 25 ºC. The SiO_2/SiO_x ratios increase to 2.28 (proton-driven) and 2.04–2.24 (ligand-driven) for basalt at 25 ºC, while keeping consistent with the original value of 1.93 during proton-driven dissolution at 80 ºC.

4.2. Silicate dissolution

Dissolution kinetics and solute pH of leachates are shown in Fig. 24 and summarized in Tables 12-13. During proton-driven dissolution in 0.8 M HNO_3 at 25/80 °C, solute pH raised by ~0.05, and remained near-constant at ~0.2, with a deviation of <0.1 over the course of basalt and granite experiments. As for ligand-driven dissolution in 5 mM OA/CA at 25° C, solute pH increased from 2 to 4 within the first 24 h of the reaction, and reached a plateau of ~4.5 during the late stage of experiments (>24 h) (Figs. 24a-24b). The release of Li and K mostly followed a parabolic pattern as solute pH evolved in both dissolution systems. At the early dissolution stage

< 24 h, rapid accumulation of Li and K in leachates occurred, followed by retarded dissolution > 24 h in both proton-driven and ligand-driven dissolution systems dependent on the distance from equilibrium. During the late stage of ligand-driven dissolution, dissolved Li concentrations decreased after ~100 h of reaction (Figs. 24c-24f). By the end of the experiment (15 days), 29.6-79.2 wt.% rock-hosted Li was liberated during proton-driven dissolution, and 1.9–20.1 wt.% Li was liberated by ligand-driven dissolution. In comparison, 22.5-56.3 wt.% primary K was released during proton-driven dissolution, whereas only 4.2–14.5 wt.% K was liberated during ligand-driven dissolution. The kinetics of dissolution can be visually divided into two to three successive stages: (I) steep, incipient leaching far from equilibrium (<24 h), followed by (II) a mild, prolonged steady-state stage approaching chemical equilibrium after 24 h, or (III) with an intermediate, backward state. Dissolution stoichiometry is shown in Fig. 25 and provided in Tables 12-13. The stoichiometry of ion liberation exhibits differences between proton-driven and ligand-driven dissolution systems. Linear correlations can be found in proton-driven dissolution, and element ratios (based on ion release fractions of fresh rocks) derived from the 1:1 line (except for a case at 80ºC). In contrast, ligand-driven dissolution produces non-linear stoichiometric patterns.

4.3. Li isotope fractionation

The experiment setup of this study is different from earlier studies (Table 14), which leads to unique isotope patterns. The evolution of Li isotopic compositions in the liquid and the liquid relative to the solid (i.e., expressed as $\Delta^7Li_{l\text{-}s} = \delta^7Li_{liquid} - \delta^7Li_{solid}$) are plotted in Fig. 26, and tabulated in Tables 2-3. Pristine granite has a δ^7Li value of 0.6±1.1‰ and pristine basalt shows a δ^7Li value of 4.6±1.1‰. Both proton-driven and ligand-driven dissolution systems exhibit preferential liberation of light isotopes at the early stage of dissolution of basalt and

granite (<24 h). The lowest isotopic values appear at the onset of dissolution (~30 min), with the isotope shifts from the initial rock signal being reduced or revered as the reaction proceeded. In proton-driven dissolution, silicates in strongly acidic settings (0.8 M HNO_3) produced dissolved phases depleted in ^7Li with δ^7Li of -4.7‰ (for granite) after 14 wt.% Li leached and δ^7Li of -4.2‰ (for basalt) after ~4 wt.% Li removed at 25 °C; and δ^7Li of -4.0‰ (basalt) after nearly 4 wt.% Li leached out at 80 °C at the start of reaction (~30 min). While allowing for some deviations, dissolved phases progressively reached values almost equal to the pristine δ^7Li signals through early to late dissolution stages. Dissolved $\Delta^7Li_{l\text{-}s}$ ranges from -1.0‰ to -2.7‰ at 25 °C after ~79 wt.% Li in granite and ~30 wt.% Li in basalt leached from silicate skeletons and reaches ~0‰ at 80 °C after removing 66 wt.% Li from basalt. In ligand-driven dissolution, weak organic acid treatments yielded both isotopically light and heavy Li signatures in dissolved phases. Solute δ^7Li is -4.5‰ for granite after 9 wt.% Li removed and -0.4‰ for basalt after 4 wt.% Li removed in CA, and -5.7‰ for basalt after 21 wt.% Li leached in OA at the starting point of dissolution (~30 min). Initial enrichment of lighter Li isotopes in solutions is followed by a transition towards heavier Li isotopic composition compared to the starting δ^7Li. Aqueous $\Delta^7Li_{l\text{-}s}$ values range of 2.8‰ to 0.4‰ after 18 wt.% Li for granite and 2 wt.% Li for basalt leached from silicates with CA, and -2.2‰ after 20 wt.% Li for basalt leached in 5mM OA.

4.4. K isotope fractionation

The evolution of K isotopic signals in the liquid and the liquid relative to the solid (i.e., expressed as $\Delta^{41}K_{l\text{-}s} = \delta^7K_{liquid} - \delta^7K_{solid}$) are plotted in Fig. 27, and listed in Tables 2-3. Pristine granite has a $\delta^{41}K$ value of -0.46±0.05‰, and pristine basalt shows a $\delta^{41}K$ value of -0.40±0.05‰. Both proton-driven and ligand-driven dissolution systems exhibit preferential liberation of lighter isotopes at the early stage of dissolution of basalt and granite (<24 h). The

lowest isotopic values occur at the very start of dissolution (~30 min), with the isotope shifts from the initial rock signal being reduced or revered as the reaction proceeded. During proton-driven dissolution, the strong acidic reaction (HNO_3) of silicates yielded dissolved phases depleted in ^{41}K with $\delta^{41}K$ of -0.99‰ (for granite) after 8 wt.% K removed and $\delta^{41}K$ of -0.93‰ (for basalt) after 3 wt.% K removed at 25 °C; and $\delta^{41}K$ of -1.20‰ (basalt) after 3 wt.% K leached out at 80 °C at the very beginning of reaction (about 30 min), compared with pristine silicates (basalt, -0.40±0.05‰; granite, -0.46±0.05‰). Allowing for some deviations, dissolved phases progressively approached values almost identical to the pristine $\delta^{41}K$ signals through early to late dissolution stages. Aqueous $\Delta^{41}K_{l\text{-}s}$ ranges from 0.06‰ to -0.06‰ at 25 °C after 35 wt.% K in granite and 23 wt.% K in basalt leached from the silicate frameworks and reached -0.19‰ at 80 °C after removing around 56 wt.% K in basalt. During ligand-driven dissolution, weak acidic treatment yielded an isotopically light signal in dissolved phases. Solute $\delta^{41}K$ is -0.98‰ for granite after 3 wt.% K leached and -0.90‰ for basalt after ~2% K removed at 25 °C, and -1.41‰ for basalt after ~9 wt.% K leached at 25 °C at the starting point of dissolution (~30 min). Following a similar pattern as K in proton-driven dissolution, the $\delta^{41}K$ in dissolved phases reached the rock signal while allowing for some scatter by the end of the experiment (15 days) at 25 °C. Aqueous $\Delta^{41}K_{l\text{-}s}$ range from 0.07‰ to -0.07‰ after ~4 wt.% K for granite and ~11 wt.% K for basalt leached from the silicate skeleton with 5 mM CA, and reached -0.06‰ after ~14 wt.% K for basalt leached using 5 mM OA at 25 °C. The evolution patterns of liquid $\delta^{41}K$ in the two acid systems are indistinguishable.

Table 14. Comparison of dissolution experiments between this and previous work for Li isotopes.

Reference	This study	Pistiner and Henderson (2003)	Millot et al. (2010)	Wimpenny et al. (2010)	Verney-Carron et al. (2011)
Solid reactant	Granite/ basalt	Granite/ basalt	Basalt	Basaltic glass/ forsterite	Basaltic glass
Liquid reactant	0.8 M HNO_3/ 5 mM OA/ 5 mM CA	0.8 M HNO_3	Seawater	HCl (NH_4Cl buffered)	Pure water/ 0.001 M HCl/ 0.0001 M NaOH
Solid-to-liquid ratio ($g \cdot L^{-1}$)	2	20/30	10	10 to 50	1
Temperature (°C)	25/80	Ambient/45	25/75/ 200/250	25 to 55	50/90
Stirring speed (rpm)	550	n.d.	n.d.	>350	n.d.
Length of experiment (day)	Up to 15	Up to 7	Up to 245	Up to ~3	Up to 63
Solute pH	0.2 to 4.4	n.d.	n.d.	2 to 4	3 to 10
Techniques applied	XRD, Raman, XPS	n.d.	TEM/FTIR	N_2-BET	N_2-BET
Percentage of dissolution	(2%) to (87%)	n.d.	n.d.	n.d.	n.d.
Observed $\Delta^7Li_{l\text{-}s}$	(-10.8‰) to (2.8‰)	(-8.2‰) to (0.9‰)	(6.7‰) to (19.4‰)	(-1.1‰) to (-0.5‰)	(-5.4‰) to (0.2‰)

Note 1: n.d.: not determined. $\Delta^7Li_{l\text{-}s}$: Li isotope fractionation between liquid and solid phases.
Note 2: Abbreviations: OA: oxalic acid; CA: citric acid; XRD: X-ray diffraction; XPS: X-ray photoelectron spectroscopy; TEM: transmission electron microscopy; FTIR: Fourier transform infrared spectroscopy; N_2-BET: nitrogen gas adsorption/ desorption analysis based on the Brunauer-Emmett-Teller (BET) theory.

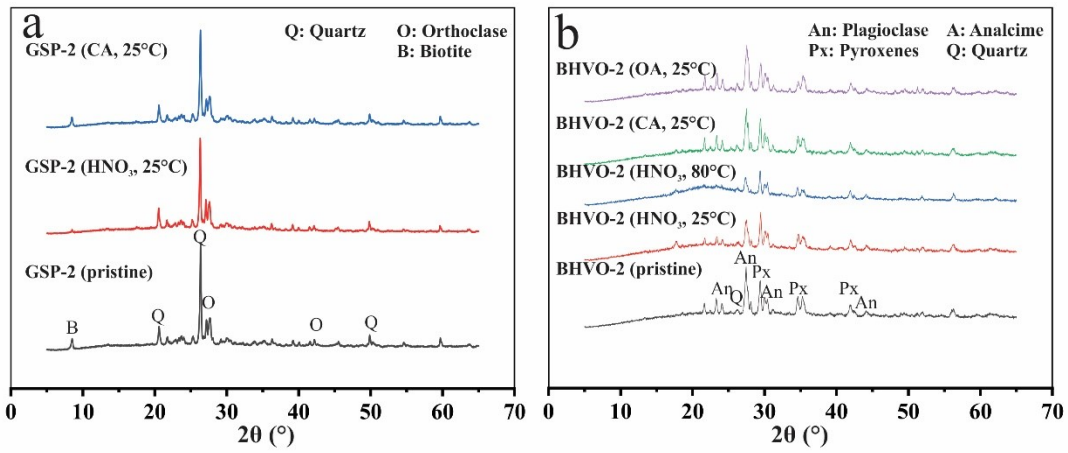

Figure 21. Normalized XRD spectra of reacted (a) granite and (b) basalt during proton-driven and ligand-driven dissolution.

Abbreviations: OA: oxalic acid; CA: citric acid; Q: quartz; O: orthoclase; B: biotite; An: plagioclase; Px: pyroxenes; A: analcime. There are measurable changes in mineral-specific peaks before and after reactions, revealing heterogeneous dissolution (or selective dissolution of some mineral phases).

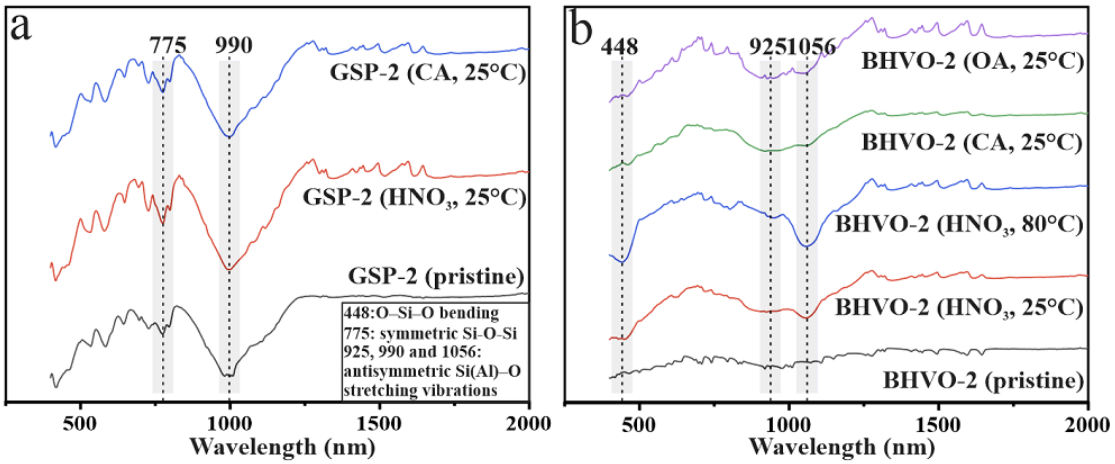

Figure 22. Measured ATR-FTIR spectra for reacted silicate rocks after dissolution reactions of (a) granite and (b) basalt.

Variations in the band at 925/990 cm^{-1} and 1056 cm^{-1} suggest the breakdown of SiO_3 groups and Si-O-Si framework by proton-driven and ligand-driven dissolution (Yin et al., 2010). The changes in the band vibration conform to the dissolution stoichiometry determined in our study (Tables. 12-13), which imply more intensive alteration of the silicate rock skeleton at lower pH (0.8 M HNO_3) and/or higher temperature (80 ºC).

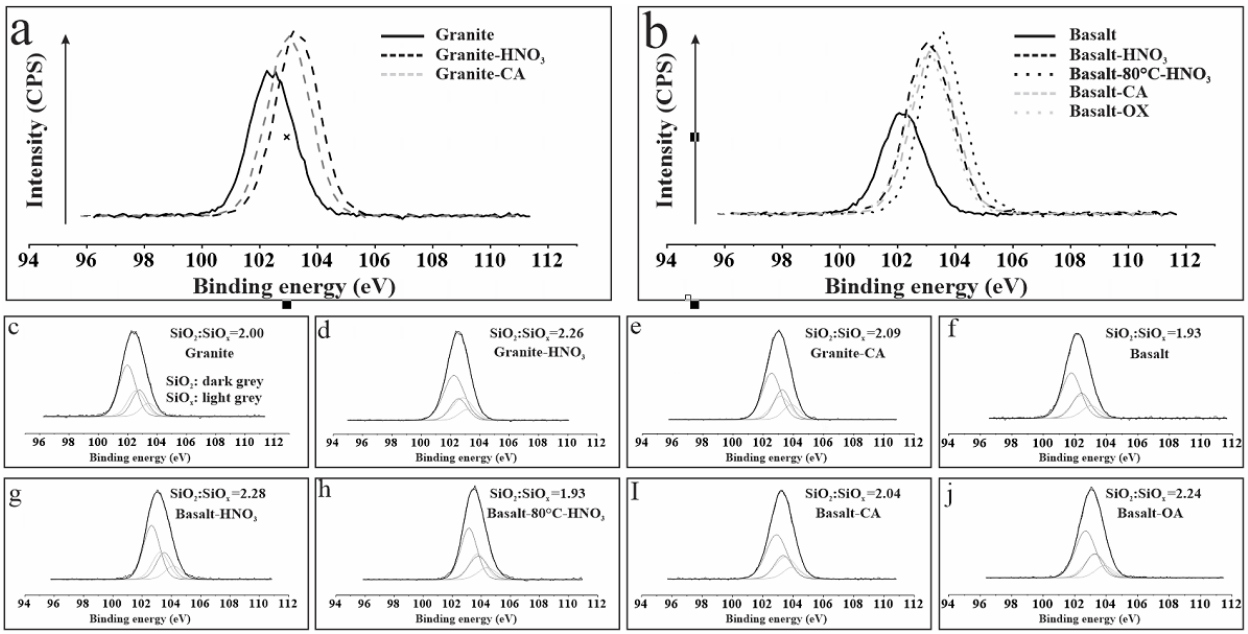

Figure 23. Fitted high-resolution Si 2p XPS peaks of pristine silicate rocks (basalt and granite) and reacted solids.

Only SiO_x (x>2) in the high bonding energy region of ~103-104 eV and SiO_2 in the low high bonding region of ~102-103 eV can be identified without polymeric Si. In the plots (a-b), Si XPS spectra of pristine (solid lines) and reacted rocks (dashed lines) in proton-driven (black lines) and ligand-driven experiments (grey lines) are displayed. In the plots (c-j), the original spectra of rocks (envelops) are marked using black solid lines, and the doublets of two Si species (SiO_2 and SiO_X (x>2)) are marked by grey solid lines. The ratio of SiO_2/SiO_x over 2.00 (unreacted granite) or 1.93 (unreacted basalt) implies the development of amorphous silica layer on the surface of reacted rocks (i.e., leached layer).

5. Discussion

5.1. Dissolution and fractionation patterns

Both proton-driven and ligand-driven dissolution of basalt and granite display substantial variations in solute isotopic compositions of Li and K in time-series (Figs. 26-27). The Li and K isotope fractionation between fluids and initial silicates display an undulating trend with an initial increase, followed by a decrease to about zero. There is no apparent difference in the isotope fractionation degree at the initial dissolution stage during proton-driven and ligand-driven dissolution. This reveals the negligible role of the ligand-cation complexation of Li^+ and K^+ and associated isotope behavior in comparison to multivalent ions of high ionic potential (as Fe^{3+}). In contrast, Fe isotope fractionation in the presence of organic ligands, is different from that of mineral acids (Wiederhold et al., 2006; Chapman et al., 2009; Kiczka et al., 2010a). The main reason for this is the high affinity of Fe to organic ligands and the excess of dissolved Fe related to Li^+ and K^+. A similar argument has been made for Zn (Weiss et al., 2014). We distinguish three phases of ion release in the dissolution profiles of Li and K (Figs. 24-27): (i) an incipient period of rapid release with significantly low initial pH and the liberation of light isotopes into fluids (only over days), followed by (ii) slower, long term dissolution with decreasing isotope fractionation, and/or end up with resorption of isotopically light isotopes to solids. This isotopic variation reflects an interplay of several fractionation processes. In principle, three compatible mechanisms potentially affect the degree of Li and K isotope fractionation during silicate dissolution: (i) incongruent dissolution of various silicate phases, in which overall isotopic effects rely on the isotopic compositions and dissociation kinetics of each silicate phases (ii) backward reaction involving the uptake of pre-released cations, which probably balance or retard the dissolution and (iii) the competition between kinetic and

equilibrium fractionation including multi-steps with different isotopic effects. Herein, each of above possibilities is discussed.

5.2. Differential dissolution of minerals

Silicate dissolution involves simultaneous dissociation of a mixed assemblage of minerals of varying solubility and isotopic composition. One way to circumvent the experimental problems related to studied polyminerallic systems is the ideal of free isotope mixing of two or more pools with distinct isotopic signals in silicate rocks. One piece of evidence in support of this hypothesis is recent theoretical calculations performed (Li et al., 2017; Y. Li et al., 2019; Zeng et al., 2019) that show isotope fractionations between surrounding water medium and precipitated minerals ($\Delta^{41}K_{solu\text{-}miner}$) are largely variable (from negative to positive) and dependent on mineralogy. Additional evidence can be derived from experimental and field observation of magmatic diffusion, which can cause large Li isotope fractionation between rock-forming minerals (e.g., Richter et al., 2006; 2014; Wunder et al., 2007; Li et al., 2018).

Nevertheless, differential rock dissolution is unlikely a primary factor of observed isotope fractionation. A major reason is that time-series Li and K isotope patterns are nearly identical, independent of lithology (basalt vs. granite) and the preferential dissolution of micaceous or feldspar minerals based on XRD. In addition, a lack of the correlation between $\delta^{41}K_{bulk}$ and K_2O in lavas at Northeast China opposes the argument of fractionation of K-bearing minerals in controlling isotopic difference in lavas (Sun et al., 2020). As lines of supportive evidence, K-Li isotope fractionation during magmatic differentiation is minor (Tomascak et al., 1999; Tuller-Ross et al., 2019). Both experiment and field studies have implied rock dissolution without Li isotope fractionations (Pistiner and Henderson, 2003; Lemarchand et al., 2010). We infer that differential dissolution is not a primary control in the experiments.

5.3. Evaluation of backward reactions

Through fluid-rock interaction, backward reactions such as resorption and reprecipitation, potentially results in interferences with dissolution stoichiometry and the degree of isotope fractionation as the reaction continues. In closed batch sets, the gradual accumulation of ions in the solute and reduction in dissolution kinetics drive solutions to saturation, and isotope behavior may be scaled by the relative intensity between forward and backward reactions.

As for Li isotopes, positive shifts in solute isotopic composition from initial silicate sources imply the resorption of lighter Li isotopes during the late stage of ligand-driven dissolution. This feature is explained by two possible mechanisms. First, pre-released Li is isotopically lighter during the early dissolution stage, and subsequent resorption could cause the Li left in solutions isotopically heavier. The resorption of Li is supported by decreases in solute Li concentration after 100 h (Fig. 23), and a sudden transition in Li/Si stoichiometry is a result of Li^+ resorption at the late dissolution stage (Fig. 24). Second, the resorption of lighter Li is facilitated by enhanced surface electrostatic attraction and subsequent complexation onto silicates (Pistiner and Henderson, 2003; Millot and Girard, 2007; Wimpenny et al., 2015; Li et al., 2020a). Alternatively, surface reprecipitation potentially incorporates light Li isotopes in newly-formed phases (Vigier et al., 2008; Hindshaw et al., 2019; Pogge von Strandmann et al., 2019). For example, as the solute pH increases in excess of ~ 5, the spontaneous precipitation of isotopically heavy Fe becomes vital during the dissolution of phyllosilicates and goethite (Chapman et al., 2009; Wiederhold et al., 2006). However, Li sinks in secondary phases are less plausible according to XRD data. We note that such a reverse pattern in the Li isotopic behavior was not found during proton-driven dissolution due to the protonation of solid surface sites at low pH. In contrast, there is no observation of K resorption and associated isotope shifts in both

acidic systems. We infer that surface complexation of K^+ is limited by the weaker hydration of K^+ (-320 kJ·mol^{-1}) relative to Li^+ (-520 kJ·mol^{-1}). Cation replacement by Fe^{3+} and Al^{3+} inhibits the direct bonding of K^+ to solids.

Reasons for the backward reaction of Li during ligand-driven dissolution can be envisaged. First, silicate residuals have a higher density of negative surface charges because of the deprotonation of silanol (≡Si–OH) sites at a higher pH~4.5 of ligand-driven dissolution compared to a lower pH~0.2 during proton-driven dissolution (e.g., Wetzel et al., 2014; Thanh and Sprik, 2016). Supportively, the point of zero charges (pH_{pzc}) of biotite, quartz, and feldspar, is in a range of 2–3 (Weiss et al., 2014); so these minerals may electrostatically retain or bond to released cations. A dominant dissolved Li phase is ionic $Li(H_2O)_4^+$ under acidic conditions, and cations are strongly electrostatically attracted with pH increasing. Second, forward dissolution to back-reaction rate ratio is high in proton-driven dissolution, and backward reactions may not appear and interfere with the isotopic effects of the forward reactions. Since deprotonated silanol groups on silicates favor polymerization along with the adsorption of monovalent cations, forward dissolution of Si was retarded, which is the case in ligand-driven dissolution (Dultz et al., 2016). Moreover, the presence of organic acids affects the isotope exchange between solids and waters, which is common in nature.

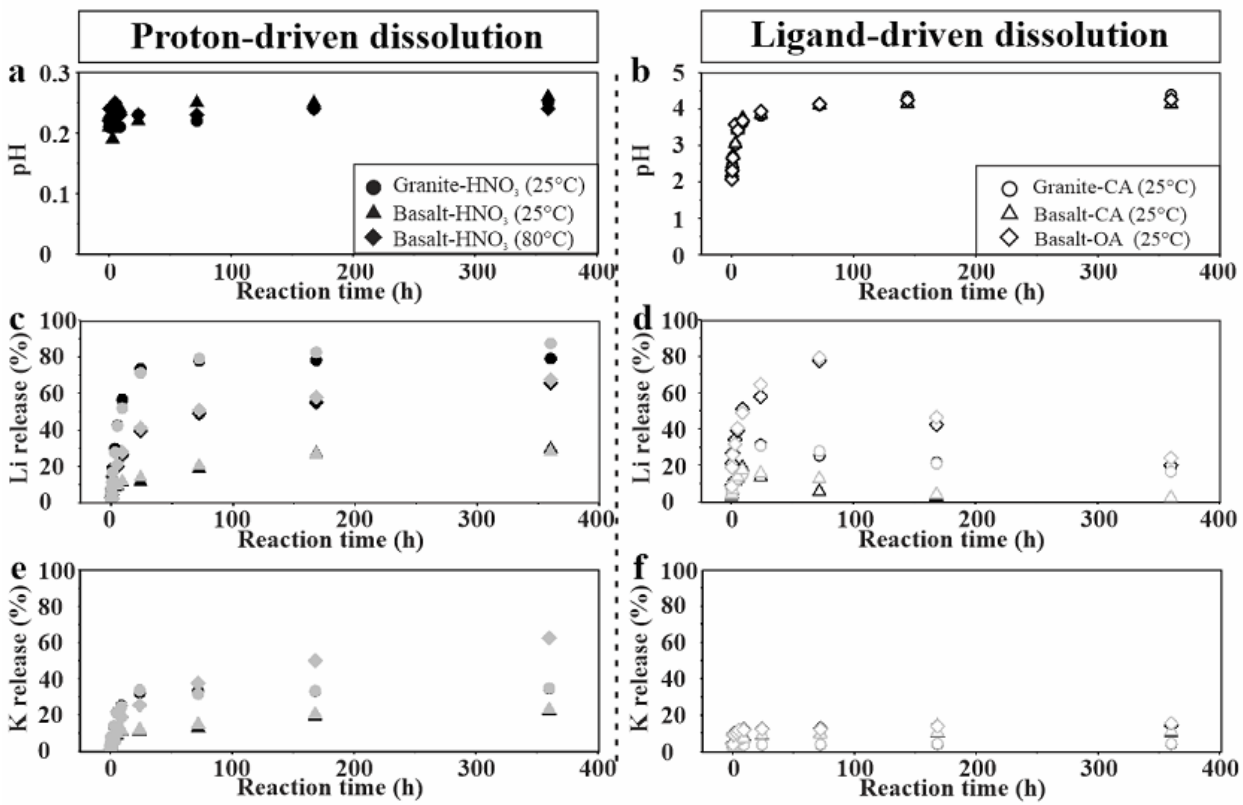

Figure 24. Characterization of aqueous chemistry as a function of reaction time during proton-driven (solid symbols) and ligand-driven (hollow symbols) dissolution.

Experiments were conducted in duplicate (black: $EXP_{(1)}$; grey: $EXP_{(2)}$). (a-b) solute pH vs. reaction time; (c-d) Li release (wt.%, the percentage of starting solid Li being liberated into solutions); (e-f) K release (wt.%, the percentage of starting solid K being liberated into solutions). Note that the most significant changes in water chemistry occurred at ~24 h in both dissolution sets.

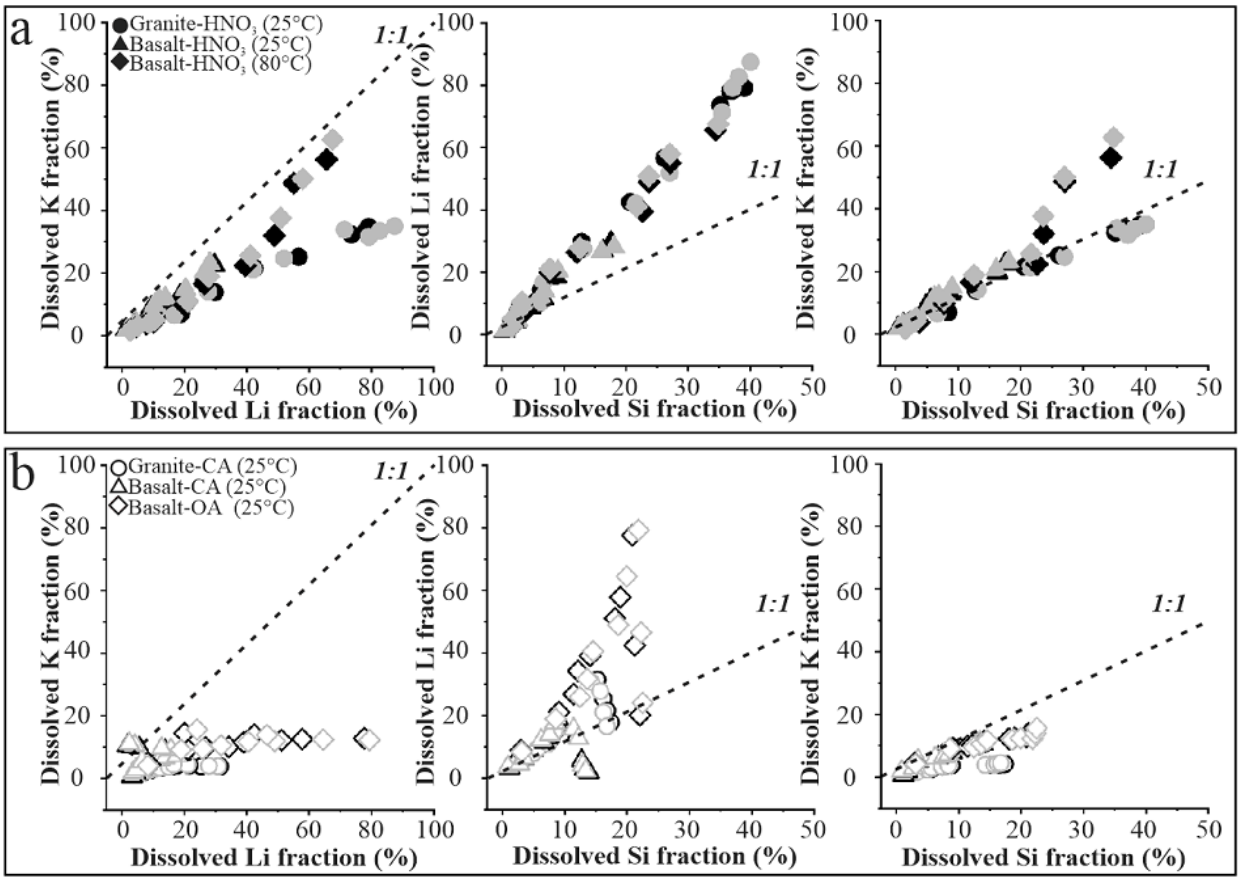

Figure 25. Stoichiometric characterization of the silicate dissolution during proton-driven (solid symbols) and ligand-driven (hollow symbols) dissolution.

In the proton-driven experiments, the features of (a) Li to K, Si to Li and Si to K are shown. In the ligand-driven experiments, the features of (b) Li to K, Si to Li and Si to K are shown. Dashed lines of idealized element fraction ratio in the total element pool in silicates (1:1) are exhibited and can be compared for stoichiometry. All experiments were conducted in duplicate (black: $EXP_{(1)}$; grey: $EXP_{(2)}$).

5.4. Kinetic and equilibrium controls

To examine another hypothesis (kinetic vs. equilibrium), Li and K isotopic mass balances are required to interpret isotopic fluctuation. A simple method for a quantitative interpretation of Li and K isotopic behavior is the application of the Rayleigh-type model (Figs. 26c-26d and Figs. 27c-27d). This model simply assumes Li and K isotopes are homogeneously distributed in rocks and then released from silicate structures in a rate-limiting step, which could be described by the follow equations. Although well mixed Li and K isotopes in the solids and homogeneous releases in the experiment are unlikely, we tentatively used the Rayleigh model to approximate isotope fractionation processes, given the limited isotope fractionation of Li and K during magmatic processes (Tomascak et al., 1999; Tuller-Ross et al., 2019).

$$\delta^7\mathrm{Li}_{\mathrm{Liquid}} = \left(\frac{\alpha \times \delta^7\mathrm{Li}_{\mathrm{rock}} + 1000 f_{\mathrm{Li}} \times (\alpha - 1)}{\alpha\,(1 - f_{\mathrm{Li}}) + f_{\mathrm{Li}}}\right);\ \delta^{41}\mathrm{K}_{\mathrm{liquid}} = \left(\frac{\alpha \times \delta^{41}\mathrm{K}_{\mathrm{rock}} + 1000 f_{\mathrm{K}} \times (\alpha - 1)}{\alpha\,(1 - f_{\mathrm{K}}) + f_{\mathrm{K}}}\right) \quad (26)$$

Where *f* denotes the percentage of Li or K released from rocks and the fractionation factor $\alpha=[(^7\mathrm{Li}/^6\mathrm{Li})_{\mathrm{fluid}}/(^7\mathrm{Li}/^6\mathrm{Li})_{\mathrm{soli}}$ or $[(^{41}\mathrm{K}/^{39}\mathrm{K})_{\mathrm{fluid}}/(^{41}\mathrm{K}/^{39}\mathrm{K})_{\mathrm{solid}}$. As for isotope interpretation, Li^+ and K^+ diffusion in liquid water ($\beta_{Li}=0.0171\pm0.0159$; $\beta_K=0.049\pm0.017$; Bourg et al., 2010) was modeled, which partially explained the initial kinetic isotope signal (i.e., light isotopes in fluids). However, one perplexing issue is that the initial Li isotope ratios in the solutions are even lower than the diffusion fits. The kinetic ion-desolvation theory reported in Hofmann et al. (2012) has been applied to explain isotope effects during interfacial precipitation. Because both ion-solvation and desolvation reactions in the non-equilibrium states follow the reaction-rate theory (Hänggi et al., 1990), we tentatively used reported parameters for curve fitting. Ion-solvation fractionation was modeled ($\alpha_{Li}=0.9925\pm0.0014$; $\alpha_K=0.9976\pm0.0004$), which explains the significant enrichment of light Li isotopes near the onset of the experiment.

The presence of the leached layer has been verified by XPS analysis and is a prerequisite for kinetic isotope effects during dissolution (Brantley et al., 2004). Since Si has a higher electronegativity value (1.9) than multivalent cations in silicates (Fe, 1.8; Mg, 1.3; Al, 1.6), electrons in mineral structures preferentially move towards Si atoms, rendering their lower binding energies (BE) and higher energy intensities. Hence, Si bonding energy measured by XPS shifts to higher energy ranges after the cation is released from the lattice. This reveals reduced valence electron density on the Si nuclei, along with the release of metal cations from basalt and granite during dissolution (Fig. 23a-23b). Silicate dissolution often involves a gel-like film, commonly known as "the leached layer of silicate structure". The chemically and structurally distinct zone is expected to be formed and restructured, releasing silica units via different degrees of polymerization (Casey et al., 1993; Weissbart and Rimstidt, 2000), resulting in changes in BE. We thereby determined two major silicon species, i.e., SiO_x (x>2) in the high BE range (~103-104 eV) and SiO_2 in the low BE range (~102-103 eV). Because of surface hydrolysis and condensation, silica-enriched leached layers were subsequently developed through gradual transformation of crystalline SiO_X to amorphous silica phases. Since SiO_X sites have been recognized to be chemically more reactive than SiO_2 sites (Iler, 1979), the formation of the leached layer made silicate surfaces less prone to elemental exchange with coexisting dissolved phases. Therefore, we adopted the ratio of SiO_2/SiO_x in reacted solids relative to pristine rocks as the criteria for determining leached layer formation (low SiO_x/SiO_2 ratios imply more developed leached layer). The development of the leached layer in both dissolution systems (25 ºC) could be identified.

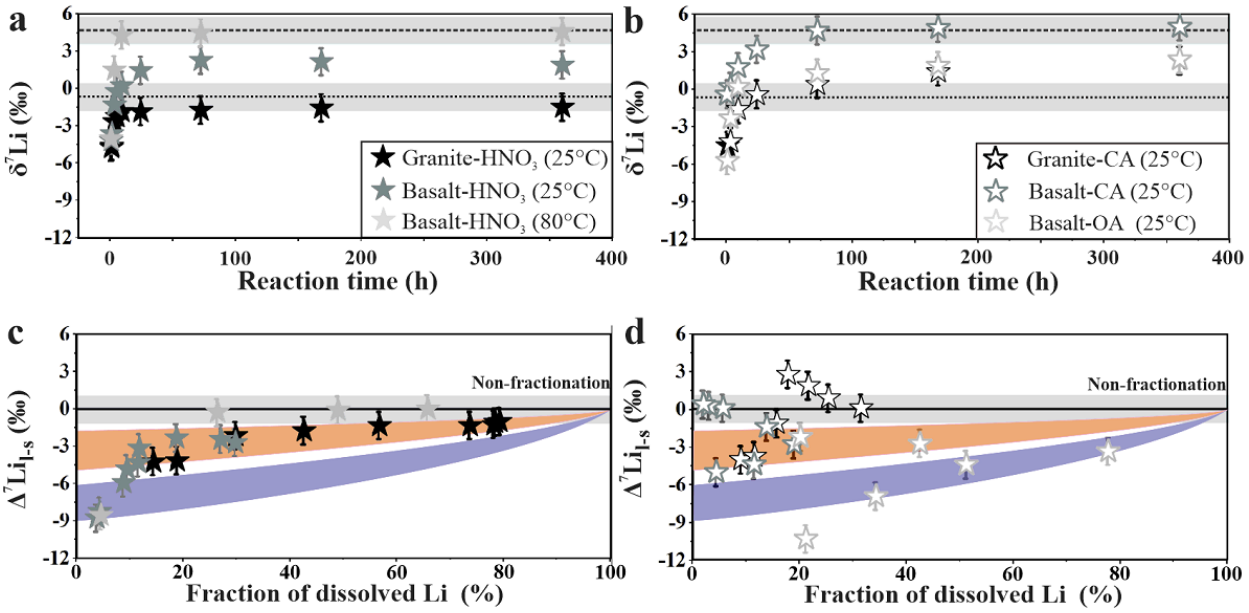

Figure 26. The isotope fractionation of Li during silicate dissolution. Aqueous δ^7Li as a function of reaction time during (a) proton-driven and (b) ligand-driven dissolution.

The dashed and dotted lines represent the Li isotopic compositions of BHVO-2 (4.6‰) and GSP-2 (0.6‰), respectively. The error bar (grey area) is the long-term analytical uncertainty (2 S.D.=1.1‰). Net isotope fractionations between liquids (l) and solids (s) $\Delta^7Li_{l\text{-}s}$ as a function of dissolved Li during (c) proton-driven and (d) ligand-driven dissolution. The orange and purple regions show curve-fit data of the mass-dependent Li^+ diffusion in liquid water (Bourg et al., 2010, β=0.0171±0.0159) and surface ion desolvation (Hofmann et al., 2012, α=0.9925±0.0014).

We note that solute K isotope patterns cannot be reasoned by the two kinetic paths, which are likely affected by sluggish K liberation supported by the dissolution stoichiometry (Fig. 25). During proton-driven dissolution, silicate-hosted Li was preferentially released relative to structural K in the lattice or interlayer space, and releasing tetrahedral Si was retarded. This feature is derived from data overlapping the line of 1:1 unit slope passing through an origin (Fig. 25a), implying higher proportions of Li than the release of K-Si. Only at 80 ºC, K release was near stoichiometric to the liberation of Li. During ligand-driven dissolution, Li liberation was not stoichiometric to K-Si release, and K release was retarded at a higher level compared to the pattern of proton-driven dissolution (Fig. 25b). Retarded K release kinetics was reported by Kiczka et al. (2010a), with respect to Fe isotope fractionation in a similar dissolution system. This feature is reasoned by the incongruent dissolution of octahedral and tetrahedral units in K-bearing silicate minerals. As supportive evidence, congruent silicate dissolution could be endorsed by the dissolution stoichiometry (Fig. 25).

During the late-stage dissolution, the disappearance of Li and K isotope fractionation can be reasoned by (i) masking effects from intensive dissolution without isotope fractionation, (ii) subsequent destruction of $^{7}Li/^{41}K$-enriched leached layers, and/or (iii) the equilibrium fractionation depending on structural coordination change between solids and liquids. The first mechanism has been reported in Wiederhold et al. (2006), who stated that If the cation release is accompanied by its coordinating oxygen atoms within the silicate structures, i.e., Li/K-O bonding is complete, no isotopic fractionation should appear. The second mechanism is induced by enrichment of heavy isotopes in the leached layer by incipient kinetic effects, and lateral dissociation of the leached layer. Theoretical and spectroscopic data confirm that ionic K^{+} has a lower coordination number (~6) and shorter K-O bonding length ($(2.7–2.8) \cdot 10^{2}$ pm) than those

of K^+ in silicate structures (N~6–9, (2.7–-3.2) · 10^2 pm) (Kamijo et al., 1996; Cibin et al., 2005; Glezakou et al., 2006; Liu et al., 2010). The third mechanism enables partitioning of isotopically heavier K into solutions due to the coordination change, compensating for initial kinetic effects. Likewise, dissolved Li^+ has a lower coordination number (~4) and a shorter Li-O bond length (~1.9 Å) than Li in silicate lattices (N~6, ~1.9–2.3 Å) (Hannon et al., 1992; Yamaguchi et al., 2010; Liu et al., 2018). Therefore, kinetic and equilibrium reactions during successive dissolution steps control fluid isotope signals.

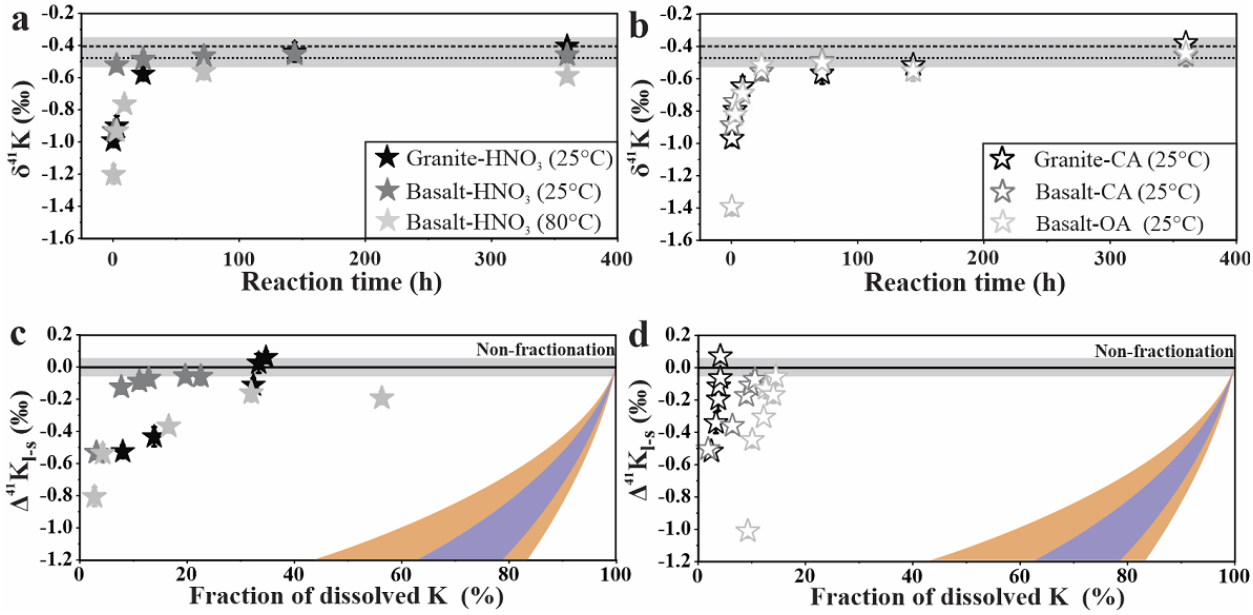

Figure 27. The isotope fractionation of K during silicate dissolution. Aqueous $\delta^{41}K$ as a function of reaction time during (a) proton-driven and (b) ligand-driven dissolution. The dashed and dotted lines denote the K isotopic compositions of BHVO-2 (-0.40‰) and GSP-2 (-0.46‰), respectively. The error bar (grey area) displays the 95% confidence interval calculated from standard error of the mean corrected using the Student *t*-factor (95%c.i., see details in Y. Hu et al., 2018). We note that the error bar is almost identical to the symbol size used in the plots. Net K isotope fractionations between liquids (l) and solids (s) $\Delta^{41}K_{l\text{-}s}$ as a function of dissolved K during (c) proton-driven and (d) ligand-driven dissolution. Orange and purple regions show the curve-fit result of mass-dependent diffusion of K^+ in water (Bourg et al., 2010, β=0.049±0.017) and surface desolvation (Hofmann et al., 2012, α=0.9976±0.0004).

6. Summary and Implications

We experimentally investigated Li and K isotope fractionation during closed, batch silicate dissolution. A combination of stoichiometry, spectroscopic analysis, and isotope analysis in proton-driven and ligand-driven dissolution experiments offer insights into Li and K isotopic behavior. The results do not fully conform to our hypothesis (i.e., Li and K isotopes behave similarly in both systems). The two experiment systems show distinct solute chemical features (i.e., ligand type and pH) over the course of this study (15 days), yet the fundamental isotopic responses of Li and K released into fluids are initially the same (kinetic isotope fractionation caused by ionic diffusion and/or solvation). Nevertheless, the isotope fractionation of Li is reversed during the late stage of dissolution, whereas the fractionation of K reached both chemical and isotope equilibrium subsequently. The behaviors of Li and K during ligand-driven and proton-driven dissolution are not the same, and the difference is reasoned by ligand-cation interactions and backward-reactions. Previous investigations under similar experimental conditions have shown that this is also the case for other metal isotopes (e.g., Fe and Zn) (Wiederhold et al., 2006; Chapman et al., 2009; Kiczka et al., 2011; Weiss et al., 2014). In summary, the exchange of metals and isotopes during dissolution likely occurs in multiple steps: (i) kinetic loss of ions from silicate minerals in rocks into fluids, (ii) the break-down of primary silicates and (iii) back-reactions (adsorption and/or precipitation). The first step promotes the liberation of light isotopes, which then can be balanced by the second step (or affected by ligand-cation interaction). The third step may occur, producing different isotope behaviors.

The results of this study have significant implications for the interpretation of isotopic signatures in natural weathering systems. First, the preservation of kinetic isotope imprints should be the case in natural environments, despite its transit feature in this study. The kinetic

isotope signals may be recorded in incomplete or unidirectional reactions with substantial undersaturation. Based on the observation of our work, the kinetic Li and K isotope signals could be overprinted within one day. We note that these experiments were performed in batch systems rather than reactors in flow-through mode. The dissolution of silicate minerals in both basalt and granite is controlled by pH, concentrations of organic ligand, and activities of some major cations such as Fe^{3+} and Al^{3+}. The concentration of multivalent cations gradually increases as dissolution progresses, and affects the overall reaction rate since the saturation state of minerals changes during reactions. Therefore, the time period that fluids are at far-from-chemical equilibrium conditions may be extended. Given that, natural kinetic isotope imprints during dissolution might be preserved in some cases, such as persistent strong disequilibria in soil porewater. Or, reacted solutions can be instantaneously isolated from reacted solids in weathering and hydrothermal settings where the reaction process is rapid under continuous fluxes. As for the former, the diffusion of Li has been documented in the saprolites formed on a diabase dike at South Carolina (Teng et al., 2010). As for the latter, the high δ^7Li values in altered ocean crust (on-axis) are most readily ascribed to diffusive fractionation of isotopes during leaching from plagioclase (Brant et al., 2012). In addition, the outcome suggests that the isotope behaviors of Li and K are independent of kinetics, stoichiometry, or lithology during dissolution, which can be affected by temperature (25-80 ºC) and organic ligands. Long-term back-reaction and the corresponding isotope effect cannot be ignored in the presence of organic ligands and/or increases in solute pH for Li^+, as well as Mg^{2+}, Fe^{3+} and Al^{3+} during silicate dissolution (e.g., Brantley et al., 2004; Wiederhold et al., 2006; Ryu et al., 2011). Critically, the resorption of Li^+ could result in significant isotope effects. It is reasonable to infer that surface K may be structurally replaced by coexisting cations. If so, clay incorporation rather than

adsorption is a major control on K isotope fractionation in weathering. Systematic clay adsorption experiments are needed to test this hypothesis. In comparison, Li isotope fractionation could be induced by adsorption and incorporation with different fractionation magnitudes (e.g., Vigier et al., 2008; Wimpenny et al., 2015; Hindshaw et al., 2019; Li and Liu et al., 2020b). The contributions of the two competing mechanisms in controlling Li isotopic behavior are difficult to determine, complicating the interpretation of geological Li records. Hence, we consider K isotopes to be more promising as an isotope tool for weathering reconstruction as K isotopes have been fractionated by weathering with less interference compared to Li isotopes in nature.

CHAPTER 6: LITHIUM ISOTOPE BEHAVIOR IN HAWAAIN REGOLITHS: SOIL-ATMOSPHERE-BIOSPHERE EXCHANGES

This chapter is published as: Li, W., Liu, X. M. and Chadwick, O. A. (2020). Lithium isotope behavior in Hawaiian regoliths: Soil-atmosphere-biosphere exchanges. Geochimica et Cosmochimica Acta, 285, 175-

1. Introduction

Chemical weathering is one of the primary sinks of atmospheric carbon dioxide over geological timescales, modulating Earth climate and habitability (e.g., Gaillardet et al., 1999; Kump et al., 2000; Kasting and Catling, 2003; Beaulieu et al., 2012; Li and West, 2014). Its significance in controlling the evolution of continent-ocean-atmosphere systems has stimulated the development of multiple geochemical proxies to understand weathering history (e.g., Kamber et al., 2005; Pogge von Strandmann et al., 2013; Vigier and Goddéris, 2015; Bataille et al., 2017;). In particular, the isotope fractionations of light elements (Li, Mg, Ca, and Si, etc.) during chemical weathering provides valuable information on Earth's climate evolution and nutrient supplies from continents to oceans (e.g., Georg et al., 2007; Blättler et al., 2011; Li and West, 2014; Liu et al., 2013, 2014; Pogge von Strandmann and Henderson, 2015).

The lithium (Li) isotope system appears to be an ideal proxy for tracing silicate weathering (Tomascak, 2004) because the two stable isotopes (^{6}Li and ^{7}Li) have large relative mass difference (~17%), producing considerable isotope fractionation on Earth's surface (up to 60‰, Penniston-Dorland et al., 2017). Unlike bio-essential nutrients such as Ca, Si and Mg, Li is not considered to be an important component in the biosphere, because of (i) its non-micronutrient nature (Pogge von Strandmann et al., 2012), (ii) low concentrations of Li in biomass, and (iii) unsystematic isotope fractionation between plant tissues and in plant-soil

systems (e.g., Lemarchand et al., 2010; Clergue et al., 2015). Furthermore, Li has only one redox state (+1), so it is insensitive to redox changes. In addition, the riverine Li isotope budget is dominated by weathering of silicate rocks, even in carbonate-dominated catchments due to its high abundance in silicate rocks compared to their carbonate counterparts (Tomascak, 2004). During chemical weathering, ^{6}Li is preferentially sequestered into secondary minerals; therefore, Li isotopic signatures preserved in weathering products could be quantitatively related to weathering intensities, rates or regimes (e.g., Vigier et al., 2008, 2009; Millot et al., 2010a; Pogge von Strandmann and Henderson, 2015; Hindshaw et al., 2019; Murphy et al., 2019). Commonly, the Li isotopic signals preserved in marine carbonates offer key information on silicate weathering over Earth's history (Liu and Rudnick, 2011; Misra and Froelich, 2012).

Recently, weathering-driven Li isotope fractionation in Earth's surface environments has received great attention (see review in Penniston-Dorland et al., 2017). Geological δ^{7}Li records have been examined to interpret: (i) Li budget balances between riverine inputs and submarine reverse weathering outputs (Misra and Froelich, 2012), (ii) oceanic Li isotope mass balance influenced by global weathering regimes (Li and West, 2014), (iii) Li isotope fractionation between soils and waters produced by modern chemical weathering (Kisakürek et al., 2004; Pistiner and Henderson, 2003; Wanner et al., 2014), and (iv) eolian imprints on soil Li isotopic signatures (Lemarchand et al., 2010; Liu et al., 2013; Ryu et al., 2014). Broadly, weathering of terrestrial rocks leaves an isotopically light regolith, balancing the heavy Li isotope reservoirs in rivers and oceans. Previous studies have demonstrated a wide δ^{7}Li range of weathering products retained in the regolith, which may be complicated by soil formation, pore-fluid advection/diffusion, and atmospheric inputs (marine aerosol and dust) (Huh et al., 2004; Liu et al., 2013; Teng et al., 2010). However, Li accumulation or depletion and the isotopic signals in

the regolith are complex, and the interpretation of regolith Li records is not well constrained. In addition, the key controls under different climate conditions may vary largely.

In this study, we compared the processes of soil-atmosphere-biosphere exchanges for Li isotope fractionation in regolith profiles developed on same-age lavas in humid and arid climatic conditions in the Kohala Mountain, Hawai‘i. Previous work on Hawaiian soils along a humid chronosequence with ~2500 $mm \cdot a^{-1}$ annual rainfall (Ryu et al., 2014) and a 150-ka climosequence (Huh et al., 2004) documented Li isotopic responses to weathering mass budgets and atmospheric inputs. However, these studies mainly focused on solid-phase regolith and less on potential biological or aqueous influences. Hence, we conducted a systematic biogeochemical investigation on regolith profiles, plants, and groundwater and river waters to understand potential influences on Li isotope geochemistry. We sampled two ~350 ka regolith profiles previously studied by Goodfellow et al. (2014). They developed under contrasting climatic conditions with mean annual rainfall (MAP) of 385±53 $mm \cdot a^{-1}$ (arid, PO) and 1730±57 $mm \cdot a^{-1}$ (humid, BE) (Giambelluca et al., 2013). In addition to Li and radiogenic Sr isotope analysis of bulk soils, we used operationally defined sequential extraction methods to determine the Li isotopic compositions in different soil compartments. We also measured the Li isotopic compositions of bulk plants and plant tissues to understand the controls of biological activities on Li geochemistry. Lastly, we estimated Li input and output fluxes of the regolith using a mass balance box model, and addressed broader implications.

2. Geological Overview

The Kohala Mountain is the northwestern-most and oldest volcano making up Hawai‘i Island. It has a strong windward - leeward contrast in rainfall, which is useful for evaluating the climatic impacts on chemical weathering over long time scales (Chadwick et al., 2003). There

are two chemically distinct surface lavas exposed on the Kohala Mountain: the Pololū volcanics that are composed mainly of tholeiitic basalts ~350 ka in age, and the Hāwī lavas that form an alkalic cap over the central part of the mountain ~150 ka in age (Chadwick et al., 2003; Spengler and Garcia, 1988). We sampled the profiles on minimally eroded locations on the Pololū flows and assume that the radiometric age of the lava flows is equivalent to the duration of weathering (~350 ka). We evaluated the behavior of Li isotopes in the arid (PO) and humid (BE) regoliths, which have been characterized in detail by Goodfellow et al. (2014) (Fig. 28).

The humid profile (BE) is located in the roadcut along the Highway 270 in the vicinity of the Bond Estate site (20.228843, -155.78962; MAP: 1,730±57 $mm \cdot a^{-1}$) covered with pasture grasses and macadamia nut trees, and the arid profile (PO) is located in another roadcut along the same highway between Mahukona and Kaiwaihae (20.135715, -155.8859; MAP: 385±53 $mm \cdot a^{-1}$) covered with sparse pasture grass (e.g., Porder et al., 2007; Giambelluca et al., 2013). The exposed portion of the humid regolith is approximately 15 m vertically, which has been sub-divided into 13 vertically distributed units according to texture, color, hardness, and fracture spacing, etc. (Goodfellow et al., 2014). We sampled the upper five regolith units from a backhoe pit reaching from the surface to 350 cm depth. The arid road-cut exposure has a thickness of ~3.5 m, which can be divided into 5 units in a vertical order. The top 1 m is strongly weathered, whereas the rock is minimally weathered in the 1 to 2 m depth range, and below, there is little evidence of weathering except along fractures in the rock. Detailed physicochemical characterizations, including field observation, X-ray fluorescence analysis, digital terrain analysis, and division, are provided by Goodfellow et al. (2014).

In response to rainfall differences and its associated long-term water balance, the two studied regolith profiles exhibit differences in mineral weathering, elemental losses, and

weathering depth. On an annual basis, local water balance (precipitation vs. evapotranspiration) is slightly positive in the humid regolith but highly negative in the arid regolith. The humid regolith is strongly weathering because of strong water infiltration, while the arid regolith experienced moderate weathering in the near surface (< 1m) and little weathering below 1 m. To assess Li geochemical behaviors and regolith processes, we used the term "shallow regolith" to refer to horizons <1 m deep, and "deep regolith" >1 m deep to the deepest horizon available. We note that the shallow regolith is almost completely depleted in primary minerals, and enriched in secondary minerals including gibbsite, kaolin (kaolinite and halloysite), Fe (hydr)oxides, and amorphous intermediates such as allophane and ferrihydrite. The deep regolith is less-weathered with some primary minerals remaining, and is marked by the "discontinuities" (i.e., humid, the corestone zone; arid, the carbonate-enriched layer). Particularly, Li abundance (represented by $\tau_{Li,Nb}$, an index of the loss or gain of Li in the regolith) increased upwards in the shallow regolith and downwards in the deep regolith. We further defined "rhizospheric soils" as part of A horizons (~20 cm depth) with a high density of plant roots. A total of 27 solid samples from the regoliths were collected along vertical profiles, with non-equidistant sampling intervals (i.e., few centimeters to meters). Three Pololū basalts and two Hāwī ash samples (~150 ka) (20.043328, -155.734678) were sampled. Plants (humid: fountain grass; arid: buffel grass) and associated water was recovered, such as rainwater, local seawater, groundwater, and river water. All water samples were filtered using 0.22 μm cellulose acetate filters (Whatman™) immediately after sample collection. Then these water samples were acidified using HNO_3 and stored at 4 °C.

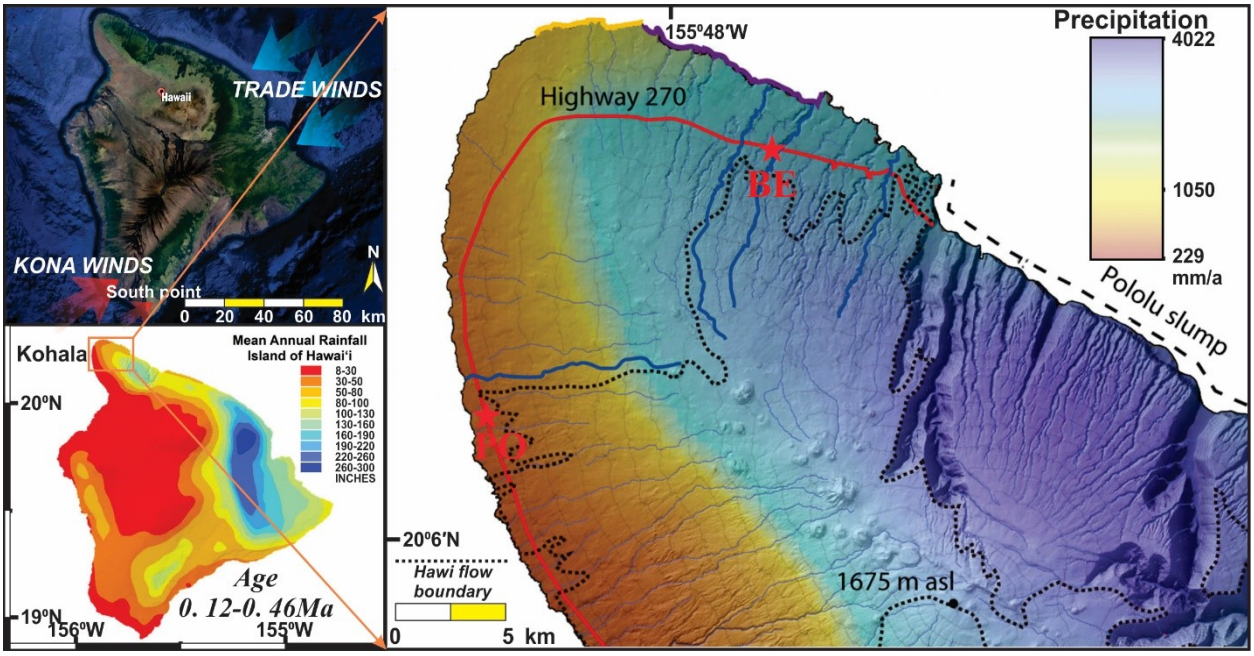

Figure 28. Maps showing the location, geomorphology, and climate of the humid (BE) and arid (PO) regolith profiles on the Pololū flow (~350 ka).

Due to critical orographic effects, moisture-bearing Trade Wind and Kona Wind deliver heavy precipitation to the NE flank and the south point of the island. The substrate ages are provided by Chadwick et al. (1999), and the mean annual precipitation (MAP) refers to Giambelluca et al. (2013) and 2011 Rainfall Atlas of Hawai‘i by the Department of Geography of University of Hawai‘i at Mānoa.

3. Methods

3.1. Sample characterization

Regoliths were sampled by horizons from surface soils to pristine substrates, air-dried and crushed. Soil fractions (<2 mm size) were separated by air-dried sieving of the bulk soils. The physicochemical characterizations, including bulk density, soil organic carbon content (C_{org}), and pH were performed at the University of California, Santa Barbara. Soil C_{org} values was measured through dry combustion at 1,423 K with an Elementar^{TM} Vario EL III CNS analyzer. Soil pH was measured potentiometrically by a soil-water mix ratio of 1:1 v/v. To obtain refined compositional description of major elements, solids were analyzed by XRF techniques at the ALS Chemex Labs following the $Li_2B_4O_7$ fusion method. Mineralogical analysis was performed on a Rigaku^{TM} XRD diffractometer (Cu/Kα radiation), operating at 40 mA/40 kV. XRD spectra were obtained in the 2θ range from 20° to 80° at a step interval of 0.01° and a scan rate of 0.5°·min^{-1}. Short-range-order (SRO) minerals as ferrihydrite and allophane were quantified by weight loss after NH_4Ac extraction (Chadwick et al., 2003).

3.2. Organic matter – Li experiments

To evaluate possible interactions between Li^+ and organic matter, we performed batch experiments by mixing 50 mL humic acid (HA, Aldrich^{TM}) slurry (4 g·L^{-1}) with prepared LiCl solutions (25/250 uM Li) at pH=4 and 7 in 50 mL polypropylene centrifuge tubes, and equilibrated for 3 days. To avoid artificial isotopic effects from organic matter, HA powders were rinsed with acidic Milli-Q water until Li concentrations were below the detection limit of the instrument. After experiments, an aliquot of filtrate was separately passed by <0.2 μm and <0.02 μm filtration (Waterman^{TM}), and <10 kDa and <1 kDa (Millipore^{TM}) ultrafiltration. All size-fractions were determined for both elemental and isotopic compositions of Li.

3.3. Sequential extraction

To understand Li elemental and isotopic behaviors in the shallow regolith, a standardized sequential extraction procedure (Community Bureau of Reference, BCR, see Table 15) was used. Li distribution among soil compartments was evaluated based on operationally defined extractions of topsoils. It was applied to extract Li hosted in soil fractions including (1) exchangeable fractions (exchangeable and carbonate phases), (2) reducible fractions (Fe/Mn (hydr)-oxides), (3) oxidizable fractions (sulfides and organic matter), and (4) residual fractions (silicate phases). Soil-free blanks were performed, and percent recoveries were calculated from the sum of individual fractions and then compared to the bulk digestion. We noted that Li mass loss occurred during sequential extraction, and only repeats with Li recoveries >90% were reported (Table 16). To evaluate the mass balance of the BCR protocol, we compared measured δ^7Li values of bulk soils and calculated total soil stocks using the following equation (Eq. 26):

$$\delta^7\mathrm{Li}_{\mathrm{Calc}} = \sum_{f=1}^{n}(\delta^7\mathrm{Li}_i \times \mathrm{C}_i^{\mathrm{Li}}) / \sum_i \mathrm{C}_i^{\mathrm{Li}} \quad (26)$$

where C_i^{Li} and δ^7Li_i respectively denote the relative Li fraction (a sum of 100%) and the isotope signature of individual fraction obtained from sequential extraction step i (i=1-4).

3.4. Sample dissolution for elemental analysis

A total of 27 regolith samples (~100 mg) were placed in Teflon beakers and digested via the HF-HNO_3-HCl protocol (W. Li et al., 2019). In addition, powdered grass samples (freeze-dried) were dissolved in concentrated HNO_3-H_2O_2-HCl mixtures, and heated to >150 °C for 14 days. Residues were refluxed by concentrated HCl solutions, dried, and then dissolved in 2% HNO_3. Elemental concentrations of sampled material were measured on a Quadrupole-inductively coupled plasma-mass spectrometry (Agilent™ 7900 Q-ICP-MS) at the plasma mass spectroscopy laboratory, University of North Carolina at Chapel Hill (UNC-CH). Elemental

concentrations were determined using a series of calibration standards of known concentrations. Internal standards, including Be, Ge, Rh, In, Ir, and Bi in 2 % HNO_3, were used to correct instrumental drifts. The analytical errors of concentration analysis are < 2% (RSD).

3.5. Sr isotope analysis

After digestion, Sr fraction was separated following a standard ion exchange protocol (2.5 M HCl, Bio-Rad™ AG50W-X12), and isotopic compositions were measured using a Neptune™ Plus Multi-collector ICP-MS (MC-ICP-MS) at the State Key Laboratory of Marine Geology in Tongji University. During the period of data acquisition, the mass fractionation and the instrument bias were normalized by $^{86}Sr/^{88}Sr = 0.1194$ following the exponential law. $^{88}Sr/^{86}Sr = 0.1194$ was used to calibrate mass bias during isotope analysis, and the NBS SRM 987 standard was measured with samples to confirm the quality of analysis, yielding an average $^{87}Sr/^{86}Sr$ of $0.710271 \pm 18 \times 10^{-6}$ (2 S.D., N=10). Two United States Geological Survey (USGS) basalt standards were adopted for accuracy evaluation, BCR-2 (Columbia River basalt, $0.704995 \pm 18 \times 10^{-6}$) and BHVO-2 (Hawaiian basalt, $0.703454 \pm 13 \times 10^{-6}$). Analyses of the two references are consistent with published data (the mean values, 0.704958, BCR-2; 0.703435, BHVO-2) (Raczek et al., 2001; H. Liu et al., 2012).

3.6. Li chromatographic purification

Lithium fractions in samples were isolated following a dual-column chromatographic method (W. Li et al., 2019). Before column chemistry, solid samples were digested in a 3:1 mixture of double-distilled HF and HNO_3 at 180 °C on a hot plate until samples were totally dissolved. Samples in aqueous phases were dried, refluxed in *aqua regia*, and then in concentrated HCl solutions, and subsequently dissolved in 0.2 M HCl for further purification. The chromatography was composed of two steps to ensure high sample loading and a fixed

elution range. The isolation of Li from most matrices was achieved by cation-exchange chromatography with pre-cleaned Bio-Rad™ AG50W-X8 resin (200-400 mesh), and 0.2 M HCl solution as the eluent. The further isolation of Li was achieved using the same resin and 0.5 M HCl solution as the eluent. All final solutions after column separation were checked on an Agilent™ 7900 Q-ICP-MS to guarantee high yields (~100%) and low matrix influence (Na/Li <1) in collections, ensuring the reliability of isotope analysis.

3.7. Li isotope analysis by Q-ICP-MS

The Li isotope analysis was performed using the same Q-ICP-MS instrument as the elemental analyses, and the detail was previously reported in Liu and Li (2019). A brief description of the analytical method is given here. Prior to isotope analysis, samples and geostandards were matrix matched to a concentration of 0.5 ppb Li in 2% HNO_3. We used an Agilent™ microflow self-aspirating (200 $\mu L \cdot min^{-1}$) PFA nebulizer, quartz spray chamber, quartz torch, and 2.5 mm internal diameter injector. To achieve high signal stability and low background, we optimized the carrier gas flow (0.95 $L \cdot min^{-1}$) and the make-up gas flow (0.35 $L \cdot min^{-1}$). The instrumental sensitivity was ~250,000 cps on ^{7}Li for 0.5 $\mu g \cdot L^{-1}$ solution. Because of the low sample size (0.5 ppb), long washing time (180 s) was adopted to maintain low background, so that memory effects can be controlled. For each sample, the ratio of the concentration of all matrix elements to Li is limited to be < 2 to eliminate potential matrix effects. The sample-standard bracketing method was employed, and the concentration match between samples and standards was limited to be >95%. We reported Li isotopic composition expressed as $\delta^{7}Li=\{[(^{7}Li/^{6}Li)_{sample}/(^{7}Li/^{6}Li)_{standard}]-1\}\times 1000$, relative to the IRMM-016 Li standard. The long-term external precision is 1.1‰, from the 2 S.D. of nearly one-year repeat analyses of IRMM-016 and USGS igneous rock standards JG-2 and BCR-2 (Liu and Li, 2019). During the course of this study, we used two USGS basalt standards

BCR-2 and BHVO-2, to ensure accuracy for Li isotopic analysis. The BCR-2 yields δ^7Li of 2.92‰ (N=10), and the BHVO-2 yields δ^7Li of 4.74‰ (N=10) with a long-term 2 S.D. of ±1.1‰ (Appendix 2), falling within the isotope range reported in previous studies.

4. Results

4.1. Li mobilization and distribution

Chemical depletion profiles of specific elements are shown in Fig. 29, and listed in Table 17. Element mass transfer function (τ) calculation is given here (Chadwick et al., 1999, Eq. 27):

$$\tau_{x,w} = \rho_w C_{x,w} \rho_p C_{x,p} (\varepsilon_{x,w} + 1) - 1) \quad (27)$$

where $\varepsilon_{x,w}$ is the strain factor (an index of soil volume change), $C_{x,p}$ is the concentration of element *x* in the protolith (e.g., unweathered parent material, bedrock), $C_{x,w}$ denotes the concentration of element *x* in the weathered product, and ρ_p and ρ_w are the bulk density of the protolith and weathered soils, respectively.

Here, we divided the regolith profile into two parts (see explanation in the section 2.2) regarding the extent of Li depletion: (i) less-depleted or enriched shallow regolith; (ii) partially depleted deep regolith. The Li concentrations increased upward to an order of magnitude higher, from 7,170 ng·g^{-1} to 65,410 ng·g^{-1} (humid) and 32,440 ng·g^{-1} (arid), respectively. Similar patterns have also been found in an arid site E (MAP=570 mm·a^{-1}) and a humid site J (MAP=1,380 mm·a^{-1}) along the Hāwī lava climosequence (Huh et al., 2004). The Li stocks in the plant samples (70–350 ng·g^{-1}) were much lower than bulk soils, consistent with reports of low Li bioavailability (e.g., Lemarchand et al., 2010; Pogge von Strandmann et al., 2012; Clergue et al., 2015). Elemental ratios for Li/Nb and Li/Na Indicate Li enrichment in both strongly and weakly weathered regoliths. The elemental ratios increased upward to the maximum in the shallow regolith (< 1m) and gradually approached the Li/Nb and Li/Na ratios of the vegetation grown on the top.

The shallow regolith exhibits local-scale enrichment of Li and some rock-derived elements (e.g., K, Mn, Fe, and Al) in the surface soils (Fig. 29), reaching the maximum $\tau_{Li,Nb}$ of 10.9 in the humid site and $\tau_{Li,Nb}$ of 2.8 in the arid site. Different from observations made by Huh et al. (2004), the organic-rich soil layers (O horizons and upper A horizons) display high Li contents (up to 60 ug·g^{-1}). Calculated Li mass flux in a vertical order ranges from -0.01 to 0.55 mg·cm^{-2} (humid) and -0.02 to 1.78 mg·cm^{-2} (arid), exhibiting similar patterns as $\tau_{Li,Nb}$, reaching the maximum in rhizospheric soils (Figs. 29-30). As a result of absolute accumulation, integrated net Li mass gains in the shallow regolith are 30.6 mg·cm^{-2} (humid) and 40.6 mg·cm^{-2} (arid), respectively. The average rates of Li mass gain were calculated to be 0.09 μg·yr^{-1}·cm^{-2} (humid) and 0.12 μg·yr^{-1}·cm^{-2} (arid), respectively, based on an assigned age of 350 ka for the Pololū lava. Although Li^+ is more prone to be leached from regoliths than high field strength elements (e.g., Zr, Nb, Ta, Ti and Th, Liu et al., 2013), preferential retention of Li with respect to Nb is found in both humid and arid shallow regoliths.

4.2. Bulk isotopic compositions

The basalt substrates display an average δ^7Li of 2.2‰, within analytical error (± 1.1‰) of that reported for Hawaiian basalts (Mauna Loa flows, δ^7Li of 2.8-3.1‰, Pistiner and Henderson, 2003) (Table 17, Fig. 30). The shallow regolith (< 1m) displays a wide range of heavier Li isotopic compositions than that of the parent basalt. The δ^7Li values of weathering residues range from -2.7‰ to 9.9‰ in the humid site, and from 2.2‰ to 13.9‰ in the arid site. Samples with lighter isotopic composition than basalt in the upper section of the deep humid regolith can be explained by the preferential scavenges of the light Li by clays (Pistiner and Henderson, 2003). In the humid regolith, δ^7Li gradually reaches a heavy composition of 9.1‰ near the discontinuity divided by the corestone zone (Region II, Fig. 3), and decreases upwards to -2.7‰ at ~2 m depth

in the deep regolith. In the shallow regolith, δ^7Li increases towards soils that reach an isotopic plateau of ~4.0‰, then sharply raises up to 9.9‰ near the top of the regolith. In the arid regolith, δ^7Li increases from 3.3‰ to 11.8‰ at the carbonate-enriched layer (Region II, Fig. 3), and decreases upwards to ~2.2‰ at 1 m. The δ^7Li values of the shallow regolith are heavy, showing a positive excursion in soils with a peak value of 13.9‰, and ultimately decrease to 10.1‰ in the topsoil. Bulk plants (Table 17) from humid/arid sites share nearly identical Li isotope compositions around 9-10‰, while the Li isotopic compositions in plant tissues vary. The δ^7Li values of roots/rhizomes (12.2–13.6‰) are higher than the δ^7Li of rhizospheric soils (<20 cm, 9.9-11.3‰). Grass roots/rhizomes are isotopically heavier than stems by up to 3.4‰. Stems are isotopically heavier than the grass-foliage ($\Delta^7Li_{stem\text{-}foliage}$ up to 2.9‰). The δ^7Li value of river water at the humid side is 15.4‰, very close to that of sampled groundwater (11.1–18.3‰), and that of exchangeable soil fractions by the BCR extraction (10.3–16.4‰). The rainfall sample has a δ^7Li of 25.1‰, lower than that of the marine aerosol (30.5‰). The $^{87}Sr/^{86}Sr$ signals in the arid regolith are mostly homogeneous (0.703309–0.706129), approaching to a basalt-like feature (0.703774), and the humid shallow regolith has much more radiogenic $^{87}Sr/^{86}Sr$ (0.718142–0.722325) compared with that of the deep regolith (0.703958–0.715493).

4.3. Li distribution and isotopic ratios in soil fractions

The Li concentration and δ^7Li in the sequential-extracted fraction of soils from the shallow regolith are tabulated in Table 16, and displayed in Fig. 31. As expressed relative to the bulk soil mass, Li yields range from 98% to 102%. Notably, soil Li was heterogeneously distributed in fractions, showing Li mobilization and redistribution in compartmentalized soil fractions. The residual fractions preferentially scavenged light ^{6}Li, showing a range of 86–93% total Li in the humid regolith and a range of 59-84% total Li in the arid regolith. Because only a

trace amount of Li resides in quartz, its influence on residual (silicate) fractions should be negligible. The exchangeable soil fractions demonstrate the lowest Li content, accounting for <2% Li. The reducible fraction is the second-largest reservoir, particularly in the arid regolith (3-28%). Soil oxidizable fractions have a small Li fraction of 1–5%, and no statistically significant correlation between soil Li content and soil organic carbon (C_{org}) can be found.

Following the BCR sequential extraction, Li fractions in four extractions spanned a wide range of isotopic compositions compared with bulk soil compositions (Fig. 31). The match between measured and calculated soil δ^7Li verifies the applicability of the sequential extraction within analytical uncertainties, which is expected because of the complete recoveries of extracted Li fractions. Previous studies have shown that soil residual fractions presumably made up of clay minerals are isotopically lighter than their parent basalt (e.g., Vigier et al., 2008; Hindshaw et al., 2019; Pogge von Strandmann et al., 2019). However, we found that Li trapped in residual soil fractions is isotopically heavy (humid, 4.2–10.1‰; arid, 2.8–15.8‰), compared to their parent rock (2.2‰). The residual fractions of topsoils are heavier than that of subsoils by up to ~7‰ in the humid site. Soil exchangeable (10.3–16.4‰) and reducible (11.1–17.2‰) fractions are isotopically similar. Mean δ^7Li differences between soil exchangeable/reducible fractions and soil residual fractions are 8.4‰ (humid, BE) and 4.1‰ (arid, PO), respectively. Substantial enrichment of light Li was found in soil oxidizable fractions, ranging from -8.2‰ to -5.7‰ (humid, BE), and from -7.7‰ to -1.5‰ (arid, PO), respectively.

4.4. Li distribution and isotopic ratios in humic fractions

Since plants and soil organic fractions are rich in light Li isotopes, long-term biological influences on terrestrial Li isotope fractionation require investigations. To examine the influence of soil organic matter on Li isotope behavior, we experimentally tested the fractionation of Li

isotopes by organic molecules of different sizes. Lithium partitioning and isotope fractionation in experimental HA-Li interactions using filtration. In a low Li loading setting (25 μM), about 13% total Li remained in the 1 kDa-0.2 μm fractions at pH=4, while ~ 21% total Li was recovered in the 1 kDa-0.2 μm fractions at pH=7. Compared with the initial LiCl source (δ^7Li=5.8‰), dissolved δ^7Li in filtrates ranges from 4.4‰ in the <0.02 μm fractions to 5.3‰ in the <1 kDa fractions at pH=4, and from 3.3‰ in the <0.02 μm fractions to 5.0‰ in the <1 kDa fractions at pH=7, respectively. The δ^7Li values in different size-fractions at pH=4 are identical, within the analytical uncertainty (2 S.D.=1.1‰), to that of the initial Li solution (δ^7Li of 5.8‰). The outcome confirms apparent Li isotope fractionations between Li pools at pH=7. The retention of isotopically light Li in the 10 kDa-0.02 μm fraction reveals that medium-weighted organic molecules rich in functional groups (e.g., aromatic moieties) preferentially complex with the light Li. In the high Li loading setting (250 μM), almost all Li resides in the <1 kDa fractions, regardless of pH change. The δ^7Li values in all size-fractions are similar to the initial Li source (LiCl, 5.8‰). There is no distinguishable isotope fractionation among size-fractions with high Li/TOC ratios.

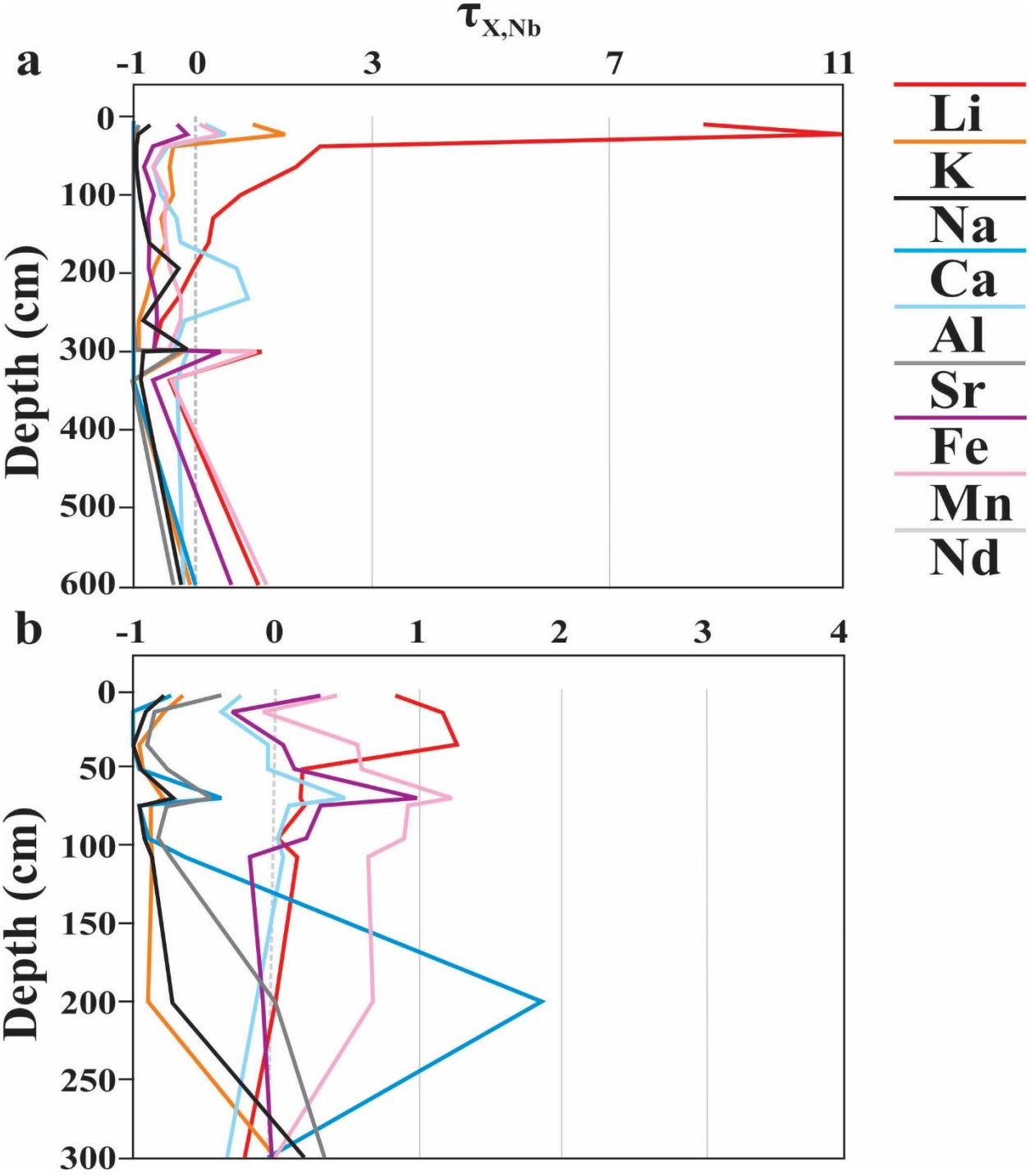

Figure 29. In-depth cation mass transport functions of (a) the humid (BE) regolith, and (b) the arid (PO) regolith.

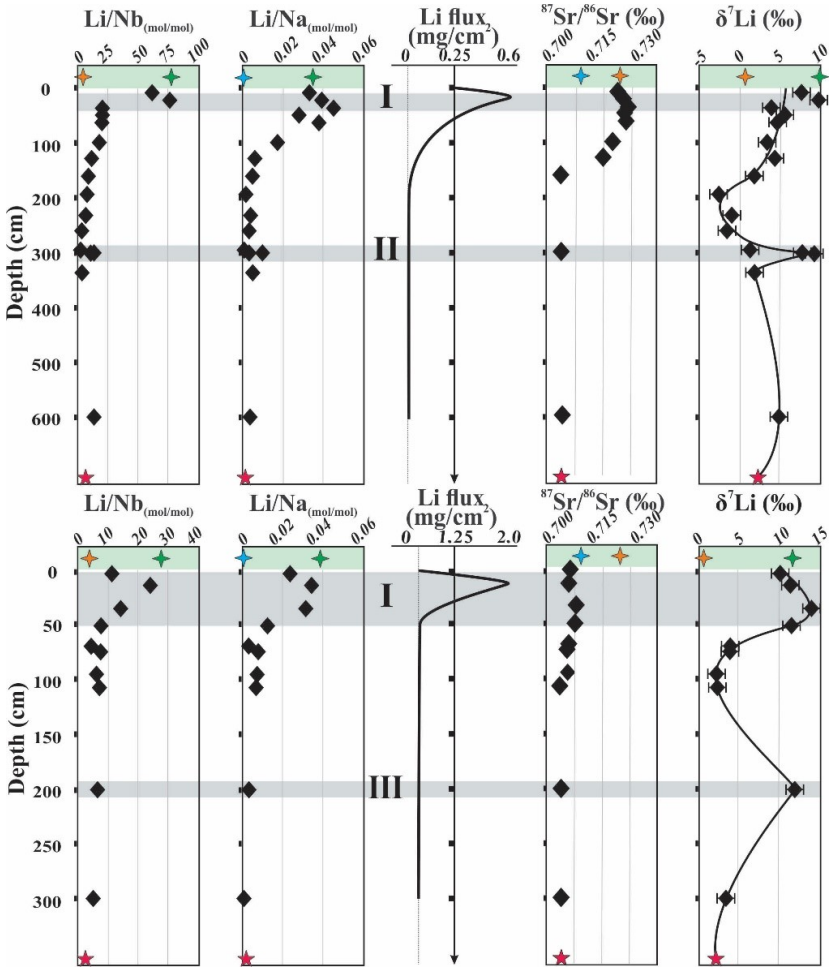

Figure 30. In-depth characterization of the humid (BE, upper panel) and the arid (PO, lower panel) regolith profiles.

The date include Li/Nb and Li/Na molar ratios, Li mass flux, $^{87}Sr/^{86}Sr$ and $\delta^{7}Li$ signals. The grey region I indicates the surface horizon with remarkable Li gains; the grey regions II and III denote the "regolith discontinuities": the corestone zone in the humid regolith and the carbonated-enriched layer in the arid regolith, respectively. The blue stars represent marine aerosol (seawater, $^{87}Sr/^{86}Sr$=0.7092, Hess et al., 1986). The green stars indicate collected bulk grass. The yellow stars represent dust deposition (continental dust, $^{87}Sr/^{86}Sr$~0.722, Lam et al., 2013; the upper continental crust, $\delta^{7}Li$=0.6‰, Sauzéat et al., 2015). The red stars at the bottom represent the composition of parent Pololū basalt.

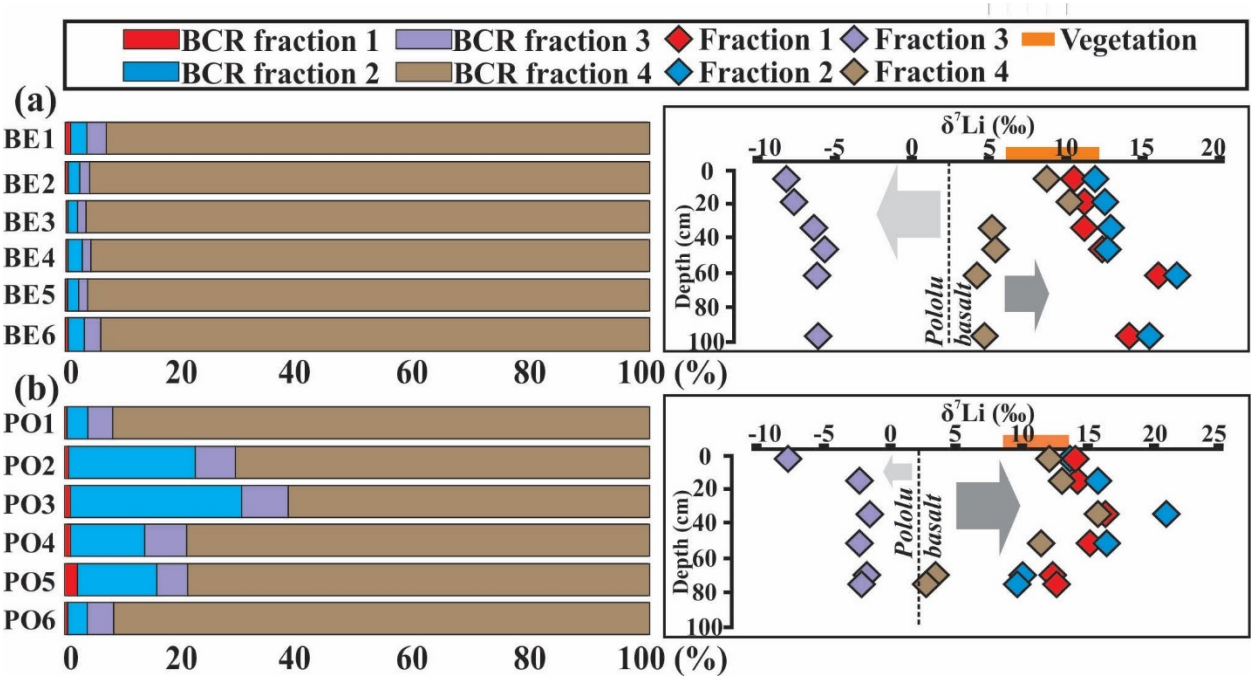

Figure 31. In-depth variations of the relative proportions of Li in soil extractions (left panel) and the δ^7Li of soil fraction (right panel) in (a) the humid and (b) the arid regolith. Fraction 1 represents exchangeable components and carbonates; fraction 2 represents the Fe and Mn (hydr)-oxides; fraction 3 represents organic phases; and fraction 4 represents residual silicates. Error bars on the x-axis refer to the long-time reproducibility (2 S.D.=1.1‰) of Q-ICP-MS analysis, which is smaller than the symbol sizes.

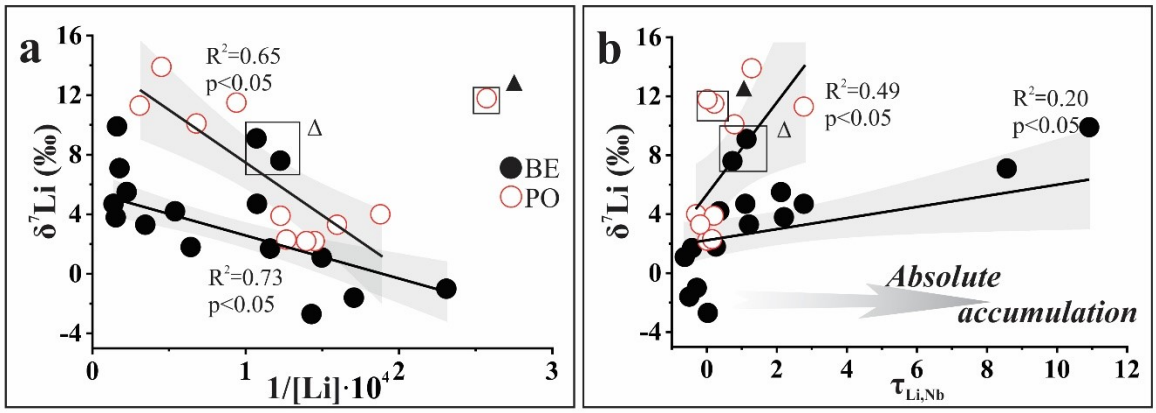

Figure 32. Li isotope fractionation as a function of (a) 1/[Li] and (b) $\tau_{Li,Nb}$.

Linear smoothers are shown with black lines, and the shaded areas represent the 95% confidence intervals. Data points located in boxes were excluded for linear fitting due to anomalous δ^7Li. In the plot, Δ denotes the corestone zone in the humid regolith, and ▲ denotes the carbonate-enriched layer in the arid regolith.

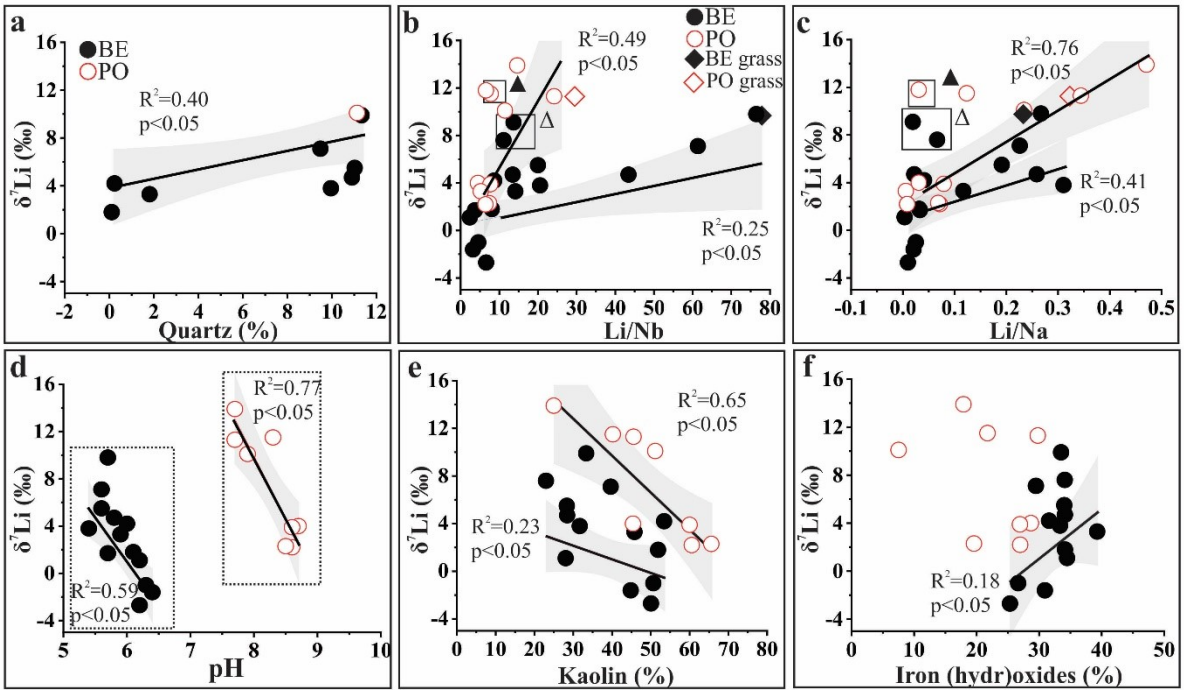

Figure 33. Regolith Li isotope fractionation as a function of (a) quartz contents, (b) Li/Nb ratios, (c) Li/Na ratios, (d) regolith pH, (e) kaolin group abundance, and (f) Fe (hydr)-oxide contents.

Linear fittings are shown by black lines, and the shaded areas reveal the 95% confidence intervals. Data points in the boxes were excluded for linear fitting. Δ: The corestone zone in the humid site; ▲: The carbonate-enriched layer in the arid site.

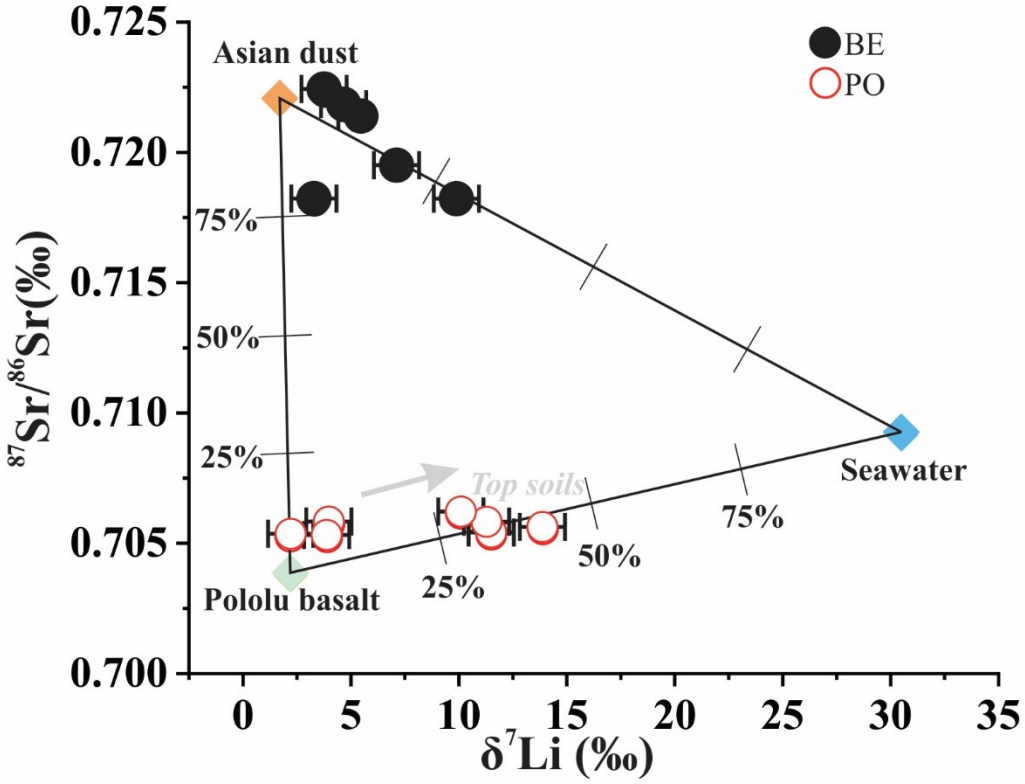

Figure 34. Bulk δ^7Li versus ^{87}Sr/^{86}Sr of the shallow regolith in the humid and arid sites.

Solid lines denote a theoretical isotope mixture in molar fractions between end-member values.

Table 15. BCR sequential extraction procedures.

Step	Fraction	Targeted phase	Reagent	Procedure
I	Exchangeable	Surface ions and carbonates fractions	CH_3COOH (0.11 M)	0.5 g powders reacted with 20 ml extracant for 16 h at ambient conditions (~22.5 °C).
II	Reducible	Fe/Mn (oxy)hydroxides	$NH_2OH{\cdot}HCl$ (0.5 M, pH1.5)	Residues from step 1 reacted with 20 ml extractant for 16h at ambient conditions (~22.5 °C).
III	Oxidisable	Organic matter	H_2O_2 (30%) CH_3COONH_4 (1 M, pH2)	Residues from step 2 reacted with 5 ml 30% H_2O_2 for 1 hr at ambient conditions (~22.5 °C). The mixtures was evaporated (repeated twice). Dried residues reacted with 25 ml CH_3COONH_4 for 16 h under ambient conditions (~22.5 °C).
IV	Residual	Silicates	HF, HNO_3 and HCl	Residues from step 3 digested using the HF-HNO_3-HCl mixture.

Table 16. Elemental and isotopic compositions of chemical extraction.

Sample	Depth (cm)	Li (%)	δ^7Li (‰)	Sample	Depth (cm)	Li (%)	δ^7Li (‰)
BE-1		100.0	7.1	DRC-15		100.0	10.1
F1		0.7	10.3	F1		0.2	13.7
F2	5	2.7	11.4	F2	2.5	3.0	14.1
F3		3.2	-8.2	F3		4.0	-7.7
F4		87.7	7.8	F4		83.9	12.1
BE-2		100.0	9.8	DRC-16		100.0	11.3
F1		0.4	11.1	F1		1.7	14.3
F2	18.5	1.8	12.4	F2	15.5	13.1	15.8
F3		1.5	-7.7	F3		4.8	-2.3
F4		87.1	10.1	F4		74.7	13.1
BE-3		100.0	3.8	DRC-17		100.0	13.9
F1		0.3	11.2	F1		0.5	16.4
F2	33.5	1.6	12.9	F2	34.5	12.0	21.0
F3		1.3	-6.4	F3		6.7	-1.5
F4		89.4	5.2	F4		74.7	15.8
BE-4		100.0	5.5	DRC-18		100.0	11.5
F1		0.5	13.5	F1		0.6	15.2
F2	46	2.3	13.7	F2	51.5	28.1	16.5
F3		1.5	-5.7	F3		7.6	-2.3
F4		92.7	5.4	F4		59.1	11.5
BE-5		100.0	4.7	DRC19*		100.0	4.0
F1	61	0.3	16.0	F1	70	0.4	12.4
F2		1.7	17.2	F2		20.1	10.1
F3		1.3	-6.2	F3		6.5	-1.7
F4		89.8	4.2	F4		66.2	3.5
BE-6		100.0	3.3	DRC-19		100.0	3.9
F1		0.4	14.1	F1		0.4	12.6
F2	96.5	2.4	15.4	F2	75	20.7	9.7
F3		2.6	-6.1	F3		3.7	-2.1
F4		85.7	4.7	F4		69.8	2.8

Table 17. Elemental and isotopic compositions of regolith profiles, vegetation and waters.

Region	Sample	Li (ug·g^{-1})	$\tau_{Li, Nb}$	δ^7Li (‰)	$^{87}Sr/^{86}Sr$	$\tau_{Al, Nb}$	$\tau_{K, Nb}$	$\tau_{Ca, Nb}$	$\tau_{Mn, Nb}$	$\tau_{Fe, Nb}$	$\tau_{Sr, Nb}$	$\tau_{Nd, Nb}$
Humid	Grass-blades	n.d.	n.d.	6.2	n.d.	n.d.	n.d.	n.d.	n.d.	n.d.	n.d.	n.d.
	Stems	n.d.	n.d.	9.1	n.d.	n.d.	n.d.	n.d.	n.d.	n.d.	n.d.	n.d.
	Rhizomes	n.d.	n.d.	12.2	n.d.	n.d.	n.d.	n.d.	n.d.	n.d.	n.d.	n.d.
	Mifed grass	8.32E+01	n.d.	8.5	n.d.	0.00	n.d.	n.d.	n.d.	n.d.	n.d.	n.d.
	BE1	5.65E+01	8.57	7.1	0.719414	0.23	1.04	-0.97	-0.28	0.13	-8.64E-01	-0.34
	BE2	6.22E+01	10.93	9.9	0.718107	0.54	1.56	-0.97	-0.07	0.50	-8.45E-01	-0.14
	BE3	6.54E+01	2.21	3.8	0.722325	-0.62	-0.34	-1.00	-0.77	-0.65	-9.62E-01	-0.79
	BE4	4.48E+01	2.12	5.5	0.721289	-0.38	-0.32	-0.99	-0.68	-0.45	-9.62E-01	-0.80
	BE5	7.25E+01	1.76	4.7	0.721769	-0.65	-0.40	-1.00	-0.76	-0.63	-9.63E-01	-0.80
	BE6	2.90E+01	0.78	3.3	0.718142	-0.53	-0.33	-0.99	-0.69	-0.46	-9.44E-01	-0.78
	BE7	1.85E+01	0.36	4.2	0.715493	-0.24	-0.50	-0.99	-0.74	-0.48	-9.47E-01	-0.85
	BE8	1.56E+01	0.26	1.8	0.703751	-0.22	-0.44	-0.99	-0.72	-0.43	-9.58E-01	-0.86
	BE9	7.00E+00	0.03	-2.7	n.d.	0.75	-0.64	-0.99	-0.72	-0.37	-9.66E-01	-0.90
	BE10	4.33E+00	-0.29	-1.0	n.d.	0.97	-0.80	-0.99	-0.60	-0.20	-9.76E-01	-0.91
	BE11	5.86E+00	-0.50	-1.6	n.d.	-0.09	-0.91	-1.00	-0.60	-0.17	-9.91E-01	-0.96
	BE12	6.69E+00	-0.63	1.1	n.d.	-0.36	-0.96	-1.00	-0.68	-0.38	-9.96E-01	-0.98
	BE13	8.16E+00	0.73	7.6	0.703847	0.53	-0.84	-0.98	1.74	1.86	-9.77E-01	0.44
	BE14	9.34E+00	1.14	9.1	n.d.	-0.12	-0.16	0.00	0.46	1.05	-2.11E-01	0.28
	BE15	8.63E+00	-0.42	1.7	n.d.	-0.26	-0.97	-1.00	-0.65	-0.32	-9.97E-01	-0.98
	BE16	9.31E+00	1.10	4.7	0.703958	-0.15	-0.04	-0.05	0.68	1.27	-2.86E-01	0.19
Dry	Grass-blades	n.d.	n.d.	8.7	n.d.	n.d.	n.d.	n.d.	n.d.	n.d.	n.d.	n.d.
	Stems	n.d.	n.d.	10.2	n.d.	n.d.	n.d.	n.d.	n.d.	n.d.	n.d.	n.d.
	Roots	n.d.	n.d.	13.6	n.d.	n.d.	n.d.	n.d.	n.d.	n.d.	n.d.	n.d.
	Buffcl grass	2.60E-01	n.d.	9.8	n.d.	n.d.	n.d.	n.d.	n.d.	n.d.	n.d.	n.d.
	PO1	1.47E+01	0.79	10.1	0.706129	-0.22	-0.61	-0.64	0.43	0.48	-3.76E-01	0.00
	PO2	3.24E+01	2.77	11.3	0.705754	0.13	-0.60	-0.96	0.22	0.56	-7.40E-01	0.70
	PO3	2.22E+01	1.28	13.9	0.705535	-0.05	-0.93	-0.98	0.05	0.56	-8.74E-01	0.03
	PO4	1.06E+01	0.22	11.5	0.705327	-0.04	-0.91	-0.95	0.13	0.61	-7.33E-01	-0.33
	PO5	5.32E+00	-0.30	4.0	0.705730	-0.10	-0.87	-0.62	0.18	0.31	-6.76E-01	-0.39
	PO6	8.15E+00	0.20	3.9	0.705232	0.13	-0.87	-0.93	0.32	0.93	-7.62E-01	-0.31
	PO7	6.90E+00	0.01	2.2	0.705340	0.05	-0.87	-0.87	0.21	0.91	-8.36E-01	-0.23
	PO8	7.90E+00	0.15	2.3	0.703309	0.07	-0.87	-0.63	-0.21	0.65	-7.27E-01	-0.33
	PO9	3.89E+00	0.02	11.8	n.d.	0.02	-0.90	1.93	-0.09	0.69	1.17E-02	-0.05
	PO10	6.27E+00	-0.19	3.3	0.703671	-0.32	0.00	-0.03	-0.05	0.00	3.69E-01	0.19
Bedrock	Pololū	7.17E+00	0.00	2.2	0.703774	0.00	0.00	0.00	0.00	0.00	-1.67E-15	0.00

Note 1. $\tau_{x,Nb}$ is the mass transfer function of x, indexed to an immobile element (i.e. Nd, this study, Kurtz et al., 2001). Note 2. The 2 S.D. error of δ^7Li is 1.1‰ (long-term analytical uncertainties for Q-ICP-MS analysis, Liu and Li, 2019). Note 3. n.d.: not determined.

5. Discussion

5.1. Atmospheric addition

Observed Li enrichment in soils suggests the atmospheric deposition derived from two main sources (Fig. 29). The addition of tephra from more recent Hāwī eruptions (~150 ka) could have contributed Li to the surface of the soils, because Li concentration in Hāwī volcanic ejecta is ~9.5 $ug \cdot g^{-1}$ slightly higher than that of the Pololū basalt (~6.5 $ug \cdot g^{-1}$). Furthermore, the high Li concentration in long-distance transported continent dust (i.e., the Li chemistry of dust is taken as equal to that of the upper continental crust, 30.5±3.6 $ug \cdot g^{-1}$ Li, Sauzéat et al., 2015) probably results in the near-surface Li enrichment (Table 17). Accreted volcanic ash could affect Li abundance in soils, but may not alter δ^7Li relative to that of underlying basalt, due to their similar chemical and isotopic compositions. To simplify the calculation, ash fractions are not distinguished from primary basalt fractions. Since studied Hawaiian soils develop over time, atmospheric addition exerts cumulative impacts on the geochemical budget of the shallow regolith, providing additional Li and crustal Li isotopic signatures. Likewise, the Li accumulation and heavy δ^7Li in Hawaiian soils were explained by eolian and marine aerosol additions along with climatic and chronologic changes (Huh et al., 2004; Ryu et al., 2014).

The “bowed” shape of Li isotopic compositions in the shallow regolith is probably produced by the addition of dissolved or particulate Li from dust or seawater (Fig. 30). Soil Li abundance positively correlates with soil δ^7Li values (Fig. 32). The δ^7Li of upper soils converges to ~10.0‰, revealing external Li components of heavy isotopic signatures. Based on the slope of the linear fitting, the arid regolith preserves more marine-derived Li signals than the humid regolith. Here, we consider that seawater imprints on soils introduced by sea salt-enriched liquid droplets or evaporated particulates could be preserved during strong evapotranspiration in the

arid site (Hsieh et al., 1998). The preservation of seawater signals is also true for Sr and its radiogenic isotopes at the South point of the Island of Hawai‘i, under a semi-arid climate (Whipkey et al., 2000). The lighter δ^7Li signal of rainwater than seawater δ^7Li can be attributed to dissolved dust components (δ^7Li=0.6±0.6‰, the upper continental crust, Sauzéat et al., 2015) that dilutes the marine signals. Not surprisingly, global rainfall compilations display large Li isotopic variations in both oceanic settings (e.g., 33.3‰, snow, Iceland, Pogge von Strandmann et al., 2006; 33‰, Azores Archipelago, Pogge von Strandmann et al., 2010; 11.2-26.4‰, throughfall, Guadeloupe, Clergue et al., 2015) and continental settings (3.2-95.6‰, monitoring stations in Brest, Dax, Orléans, Thonon and Avignon, France, Millot et al., 2010a; 26‰, the Mackenzie Basin, Canada, Millot et al., 2010b; 9.3‰, Yellow River, Gou et al., 2019), implying strong local and seasonal dependence.

The data of quartz-enriched surface horizons in the humid regolith provide quantitative evidence of dust addition. The correlation between quartz contents and δ^7Li signals in the shallow regolith of the humid profile indicates that dust addition exerts a vital control on Li isotopic variations in the humid regolith (Fig. 33). The most radiogenic Sr isotope signal occurs in the humid shallow regolith, highlighting the influence of slow but continuous eolian dust addition (^{87}Sr/^{86}Sr~0.722, Lam et al., 2013). Therefore, the eolian addition gradually replaces the original basalt Sr that has been depleted by chemical leaching. The arid shallow regolith exhibits mixed ^{87}Sr/^{86}Sr values derived from both basalt (0.7038) and marine aerosol (0.7092). The deep regolith is barely influenced by atmospheric deposition, evidenced by its homogeneous ^{87}Sr/^{86}Sr (0.703-0.704, equal to the basalt signals). We assume that leaching only has limited influence on soil Li in the shallow regolith, since the Li isotopic values of the shallow regolith are heavier or

equal to basalt isotopic compositions. Herein, we infer that the soil Li-Sr isotope signals reflect a mixing of three dominant end-members, following Eqs. 28-30:

$$f_P + f_D + f_S = 1 \quad (28)$$

$$f_P C_P \delta^7 Li_P + f_P C_P Li_D + f_S C_S \delta^7 Li_S = (f_P C_P + f_P C_P + f_S C_S) \times \delta^7 Li_{Soil} \quad (29)$$

$$f_P c_P \delta^{87} Sr/\delta^{86} Sr_P + f_D c_D \delta^{87} Sr/\delta^{86} Sr_D + c_S f_S \delta^{87} Sr/\delta^{86} Sr_S = (f_P c_P + f_P c_P + f_S c_S) \times \delta^{87} Sr/\delta^{86} Sr_{Soil} \quad (30)$$

where (f_P, f_D, f_S), (δ^7Li_P, δ^7Li_D, δ^7Li_S) and ($^{87}Sr/^{86}Sr_P$, $^{87}Sr/^{86}Sr_D$, $^{87}Sr/^{86}Sr_S$) represent the fractional contributions of Li isotopes and radiogenic Sr isotopes from parent basalt (P), dust (D) and seawater (S), respectively. The C and c denote the concentrations of Li and Sr in each compartment, respectively. On the δ^7Li versus $^{87}Sr/^{86}Sr$ diagram (Fig. 34), the isotope composition of each end-member and uncertainties theoretically define the multicomponent mixing envelopes. We observe that dust addition is significant in the humid regolith, while the isotope contribution of seawater can be identified in the arid regolith despite low rainfall. Porder et al. (2007) also demonstrated a strong rainfall dependence on the dust addition to Kohala soils. We note that this mixing plot only provides a lower limit of marine contribution, since light Li prefers to be scavenged into clays (Vigier et al., 2008).

Soil pore water extraction provides additional insights into the atmospheric contribution. The Li addition from wet and dry deposition (containing marine aerosols) is mostly preserved in the soil solutions extracted from the shallow regolith. In both arid and humid regoliths, heavier Li isotopic compositions in soil residual fractions (Δ^7Li up to 10.9‰) in the shallow regolith reflect the deposition from isotopically heavy Li of seawater origin. In Kohala soils, neo-formed secondary minerals preserve the oxygen isotopic signal of the soil solution (Ziegler et al., 2003). Thus, we suggest that it may be applicable for soil Li isotopes as well. Local water balance (i.e.,

rainwater infiltration vs. evapotranspiration) is closely related to the migration of pore water, and the water-balance threshold of MAP~500 $mm \cdot a^{-1}$ for Hawaiian soils was reported (Hsieh et al., 1998). Using soil oxygen isotopes, Hsieh et al. (1998) quantified evapotranspiration relative to precipitation along the Kohala climosequence. The arid regolith loses water by evapotranspiration with Li enrichment in secondary products, and a part of soil Li was derived from the marine aerosol. Nearly all rain into those areas is evaporated from arid soils (and plants on top). Therefore, marine signals could be retained in arid soils, despite limited rainfall. In the humid regolith, isotopically heavy Li dissolved in the seepage can be easily transported into the deep regolith and/or nearby runoff, because of the positive water balance (precipitation > evapotranspiration). Next, dust-derived isotopically heavy Li signals can be partially inherited in the shallow regolith through soil formation in the humid regolith. In addition, the preservation of marine signals may be ascribed to long-neglected biological cycle as well, which is discussed in details in the next section (5.2).

5.2. Vegetation cycling

Phytoextraction and subsequent deposition in necromass induce substantial elemental distribution in soils; we use the term bio-lifting to describe this process. The function of Li in plant physiology has been emphasized in the literature (e.g., Anderson, 1990; Shahzad et al., 2016, and references therein). For example, Robinson et al. (2018) suggested that soluble Li in soils can be taken up into leaves without a reduction in plant biomass in New Zealand, producing a bioaccumulation coefficient larger than 5. Kalinowska et al. (2013) used hydroponic experiments and demonstrated that lettuce accumulated Li in leaves at concentrations tenfold higher than the original nutrient solutions. Thus, we consider that biological influence on soil Li could not be excluded. Rather, several lines of evidence support the importance of

biological effects on natural Li cycling between soils and plants and within plant organs and tissues in the studied area.

The δ^7Li values in plant tissues vary from 6.2 to 13.6‰ with a mean value of 9.8‰. Plant δ^7Li values are lighter than the Li isotopic compositions of the exchangeable and reducible soil fractions that range from 11.2 to 21.0‰ with an average of 13.8‰. It is shown that the isotopic composition of temporal pore water could be reflected by soil exchangeable and reducible fractions (e.g., Wiegand et al., 2005; White et al., 2009; Bullen and Chadwick, 2016). Intra-plant transport probably allows the upward transfer of light Li isotopes, since light Li isotopic compositions have been found in leaves (Table 17). Litterfall returns isotopically light Li into soils annually, which results in isotopically light Li in soil oxidizable fractions (Table 16). From the result of the sequential extraction, estimated δ^7Li values in pore water (i.e., soil exchangeable fractions) are 13 to 14‰, lower than rainwater δ^7Li (14.3 to 25.1‰). Therefore, we interpret the Li signal of pore water as a weighted sum of: (i) marine-derived Li, (ii) basaltic Li from the parent rock and dust during dissolution, (iii) residual Li in pore water, and (iv) Li from litterfall. It is supported by isotopically light Li in soil exchangeable and reducible fractions, and increases in the isotopic heaviness of soil bioavailable fractions with depth (Fig. 31). Bio-cycled Li is released into soil at or near the surface, whereas rock Li is released by weathering throughout the soil but particularly near the regolith – rock contact and therefore rock Li is more likely to be leached. It is a continuous process which can feed differences in Li isotopic signals that is incorporated into secondary minerals at different depth locations.

Differential δ^7Li signals in higher plants have been reported so far (Δ^7Li_{max}>16‰, spruce and beech, Myška et al., 2010; 3.1‰, spruce, Lemarchand et al., 2010; 1.3‰, spruce, Clergue et al., 2015). In this study, grass foliage bears lighter δ^7Li (6.2-8.7‰) than stems (9.1-10.2‰) and

roots (12.2-13.6‰), revealing upward ^{6}Li transport in plants. Such a feature may be attributed to ion diffusion via a chromatographic-like process (Bagard et al., 2013). The isotope fractionation of Li among the stems, branches and leaves might result from chromatographic exchange, enriching ^{6}Li in carboxylate (RCOO-) sites (Putra et al., 2018). In contrast, Myška et al. (2010) reported isotopically heavier Li in stems than roots for *Picea sp.* and *Fagus sp.* Specific isotope fractionation among plant types (angiosperm or gymnosperm) prevailing in (sub)tropical regions have not been systematically studied, and can be vastly different in magnitudes as mentioned for Mg isotope studies (Chapela Lara et al., 2017; Kimmig et al., 2018; Opfergelt et al., 2014). The physiological properties of Li (i.e., availability and bio-sensitivity) have been studied (Anderson, 1990; Barker and Pilbeam, 2016; Gillaspy et al., 1995; Robinson et al., 2018). Therefore, it is reasonable to expect Li partitioning and isotope fractionation in soils relevant to plant growth. Hyperaccumulation and biolifting of soil elements have been addressed in a series of studies (e.g., Bullen and Chadwick, 2016; Gupta et al., 2019; Hausrath et al., 2011; Palumbo et al., 2000; Stille et al., 2009), providing context for interpreting net Li accumulation in soils. Such processes may exert a crucial control on the translocation of nutrients, nonessential (toxic) heavy metals like Cu, Co, Ni, Cr and rare earth elements, and even conservative elements as Zr into the rooting zones.

The peak accumulation of Li in the rhizospheric soils has been observed in the humid ($\tau_{Nb,Li}$=10.9) and arid ($\tau_{Nb,Li}$=2.8) regoliths. One possible explanation is the apparent dust accumulation in surface soils. The extent of Li enrichment is particularly significant in the humid regolith with dense vegetation coverage. Based on homogeneous ^{87}Sr/^{86}Sr signals in soil horizons, vertical distribution of dust fractions within the shallow regolith should be homogeneous. So, the peak Li enrichments found in topsoil horizons cannot be fully explained

by atmospheric inputs. Alternatively, it may be a consequence of biologically mediated accumulation. Hence, we postulate that the soil Li enrichments are related to the development of the "biogenic profiles" (Fang et al., 2019). Such a process normally exhibits distinct peak enrichments of elements at or close to regolith surfaces, which is associated with release promoted by organic medias and accumulation in rooting zones (Brantley and White, 2009). If released elements are taken up by plants, or recycled into the rhizospheric soils, and a biogenic profile develops (Jobbágy and Jackson, 2001). Previous studies revealed the importance of vegetation pump in redistributing nutrient as well as non-nutrient metals (Imseng et al., 2018; Reimann et al., 2009). Consistently, the rooting zone has heavy δ^7Li compared with that of adjacent soil layers (Table 17). The ratios of Li/Nb and Li/Na in bulk soils systematically increase upward, and Li isotopic compositions approximate plant signals in surface soils (Fig. 30). We observe overall positive correlations between Li/Nb and Li/Na ratios with δ^7Li values in the regolith (R^2=0.25-0.76). The element ratios and Li isotope compositions became systematically close to those of bulk vegetation (Fig. 32) rather than dust or ash compositions (Table 17). This feature may be explained by the plant dieback effect or the plant dilution effect (Lemarchand et al., 2010). We consider that biological controls on Li isotopic compositions in rivers and seawater should be negligible since the plant Li fraction is much lower than silicate fractions. However, Li isotopic compositions in aging forest soils could be influenced by biogeochemical processes, as explained in this study.

Sequential extraction experiments suggest that soil organic matters (humic substances) play a role in Li cycling, showing large isotope variations (Fig. 31). Organic matter is expected to promote silicate dissolution and Li desorption from secondary minerals. Thus, organo-mineral associations minimize Li retention and its isotope fractionation, as supported by the low δ^7Li of

the organic-rich “black waters” compared to the organic-poor “clear waters” in the Amazon River (Dellinger et al., 2015). Further insights into bio-interferences on isotopic behaviors were gained with the aid of size-fraction analysis of HA-Li association. Despite large errors, we suggest that medium-size humic molecules (1 kDa-0.02 uM) preferentially complex with light ^{6}Li. The complexation between HA and Li becomes more obvious at pH=7, corresponding to the dissociation of functional groups (Zhang et al., 2017). The negative δ^{7}Li associated with organic phases could be explained by the following mechanisms: (i) supply of light Li by litterfall; (ii) complexation of isotopically light Li with humic substances produced from biodegradation; (iii) associations of organic coatings and Li prior-adsorbed on clays.

5.3. Secondary mineral synthesis

In addition to weathering, the patterns of Li are determined by surface adsorption and subsequent incorporation into secondary mineral structures. The Li isotope fractionation could be promoted during the deprotonation of surface hydroxyl groups with increasing pore water pH. Increasing soil pH along depth profiles can facilitate high uptake ratios of Li, driving bulk soils to lighter δ^{7}Li (Fig. 33). Therefore, pore water with heavier Li isotopic compositions would be transported downwards, and then accumulated in the “regolith discontinuities”. This supports the development of high δ^{7}Li values by pore water infiltration and subsequent deposition. Moreover, mobilized elements could be withheld from rapid leaching by chemically reactive colloids, acting as capillary barriers impeding eluviation. Still, these potential sinks for Li are relatively minor since the Li abundance in soil exchangeable fraction is small, compared to soil residual fractions. It seems likely that Li adsorption on clay surfaces leads to subsequent clay incorporation (Huh et al., 2004) with consequent preservation of heavy Li signals. Despite strong leaching loss in the humid site, it seems that Li is scavenged by secondary silicates, when

combined with bio-lifting, leads to Li peak accumulation in the rhizospheric soils. Clays and soils/saprolites demonstrate large variations in δ^7Li, ranging from -20.2‰ to 26.8‰, relative to the Bulk Silicate Earth (BSE, ~4‰, Penniston-Dorland et al., 2017). Both laboratory experiments and natural observations reveal that Li isotope fractionation during weathering is mineral-specific (Clergue et al., 2015; Millot and Girard, 2007; Pistiner and Henderson, 2003; Pogge von Strandmann and Henderson, 2015; Wang et al., 2015; L. Zhang et al., 1998). The sequestration of Li in secondary aluminosilicates (e.g., kaolinite) have been regarded as one of the dominant isotope fractionation mechanisms for weathering residues. Soil Li isotope compositions correlate with kaolin abundance not Fe (hydr)oxides (Fig. 33), indicating adsorption on kaolinite rather than Fe (hydr)oxides probably drives ^{6}Li retention in soils.

In contrast, atmospheric and biological processes exert little influence on the deep regolith, whereas water percolation and ion accumulation control the fate of Li. The narrow range of $\tau_{Li,Nb,}$ shifts from intermediate loss to gain (Fig. 29). So, the deep regolith could be further divided into two separate parts, (i.e., "depletion-enrichment profiles", Fang et al., 2019), divided by the "regolith discontinuities" including the corestone zone in the humid profile and the carbonate-enriched layer in the arid profile. The regolith above the "discontinuities" showed light δ^7Li values and moderate Li loss upwards, in a large part promoted by the preferential retention of ^{6}Li over ^{7}Li in the regolith during clay formation. Lithium gains or losses were not apparent in the arid regolith, because of restricted Li mobilization within the stagnant fluid-pore networks. At the "discontinuities", heavy δ^7Li exist in both sites while net Li gains only present ($\tau_{Li,Nb}$=1.13) in the humid regolith. Rapid weathering of the lava provides available Li that dominates vertical migration. To account for the Li anomalies at the "discontinuities", several possibilities are proposed here: (i) preferential retention of original Li stock during weak

alteration of the corestones; (ii) extra derivations from neighboring weathered detritus by downward-percolating meteoric waters enriched in isotopically heavy Li passing through the deep regolith; (iii) seasonal infiltrative pulses with atmospheric signals led to heavy δ^7Li during carbonate precipitation; (iv) downward transfer of pore water with heavy Li signals driven by clay formation. The regolith horizon below the "discontinuities" shows up-gradient heavier δ^7Li signature, potentially derived from the down-seepage enriched in ^{7}Li, and subsequent concentration at deeper levels of the regolith. This is supported by the relative enrichment of most cations compared with the feature of the shallow regolith (Fig. 29). Therefore, we suggest that downward percolation and subsequent accumulation is the dominant driving force for the heavy Li isotopic composition in the "regolith discontinuities" of both humid and arid regolith. Heavy δ^7Li signals in the deep saprolite units derived from meteoric water and clay-water partitioning from upper parts.

5.4. Li budget in shallow regolith

Our work presents a preliminary investigation of a series of regolith processes controlling Li elemental and isotopic signatures in the terrestrial weathering settings. As discussed above, Li geochemistry in the shallow regolith of the study area is impacted by basalt weathering, allochthonous deposition (dust, ash, and rainwater), and leaching in a state of approximate dynamic equilibrium. Although we are not able to directly determine the input and output fluxes of the regolith, we could use Li concentrations and its isotopic compositions to model the importance and contribution of these fluxes in soil horizons and compare weathering in humid and arid sites. We assume that mass input and output fluxes are identical if soil thickness is constant. Here, we built a simple isotopic mass-balance model for the shallow regolith, which has captured the loss and gain budgets of Li, to characterize leaching fluxes and primary mineral

weathering contributions. Net Li mass gains (Δ_{Li}) relative to original basalt stock over 350 ka are identical to the difference between allochthonous Li inputs and the total Li outputs. Primary Li influxes include rainfall (F_{Rain}), Asian dust (F_{Dust}), rock weathering (F_{Wea}), and the principle output flux is leaching loss (F_{Leach}). We note that the possible contribution of ash is included in basalt weathering because of the similarity in isotopic compositions. Since the deep regolith is often inaccessible to fine root tips, bio-lifting could be negligible, and not considered in our model setup in Eqs. 31-32:

$$\frac{dLi_{Soil}}{dt} = \Delta Li = F_{Rain} + F_{Dust} + F_{Wea} - F_{leach} \quad (31)$$

$$(\Delta Li \cdot \Delta^7 Li) = ((F_{Rain} \cdot \delta^7 Li_{Rain}) + (F_{Dust} \cdot \delta^7 Li_{Dust}) + (F_{Wea} \cdot \delta^7 Li_{Basalt}) - (F_{Leach} \cdot \delta^7 Li_{Leach}) \quad (32)$$

Where Δ_{Li} is the net mass gain of Li in the shallow regolith; Δ^7Li is the isotopic composition of the net mass gain of Li, which is equal to the isotopic difference between the bulk soil and the parent rock. The absolute changes demonstrate the Li mass and isotopic offsets between primary and current materials as a function of input and output fluxes. In the above equations, F_X and $\delta^7 Li_X$ represent the values of accumulated Li fluxes over 350 ka and the constrained isotopic ratio of respective fluxes, respectively. The isotopic compositions of migrated dust, local rainfall, mineral weathering, and leach loss are obtained by direct measurement. Thus, the Li isotopic compositions of the shallow regolith are calculated using Eq. 33:

$$\delta^7 Li_{Shallow\ regolith} = \frac{\sum_{i=1}^{n} \delta^7 Li_i mLi_i}{\sum_{i=1}^{n} mLi_i} \quad (33)$$

where $\delta^7 Li_{Shallow\ regolith}$ is the mean isotopic composition of the total reservoir in the shallow regolith, $\delta^7 Li_i$ is the isotope composition of a measured layer (i) in the shallow regolith and mLi_i is the Li mass in layer (i). The rainfall Li inputs were calculated by Li concentration (0.15 ppb) in rainwater and geological time, and the dust Li inputs were obtained by the product of quartz-

based dust mass (Kurtz et al., 2001) and mean dust Li concentration (30.5 ug·g^{-1}, the upper continental crust, Sauzéat et al., 2015). Fixed parameters include the Li isotopic compositions of the shallow regolith ($\delta^7Li_{Shallow\ regolith}$), dust ($\delta^7Li_{Dust}$), weathering ($\delta^7Li_{Wea}$), rainfall ($\delta^7Li_{Rain}$) and leach loss ($\delta^7Li_{Leach}$), and total Li inputs from rainfall (F_{Rain}) and dust (F_{Dust}) (Table 18). The weathering and leaching Li fluxes were calculated to achieve a balanced model by rearranging and solving the above equations (Fig. 35). Jackson et al. (1971) suggested that orographic rainfall in Hawai‘i efficiently washes dust out of trade wind clouds. We consider that increases in dust inputs with rainfall is reasonable since wet deposition potentially removes dust from the atmosphere. Our conclusion agrees with the interpretation of Parrington et al. (1983) that atmosphere transport and deposition of dust act as the condensation nuclei for raindrops. Increases in mineral weathering with rainfall are plausible, given weathering leaching becoming more intense driven by interstitial flows. Although marine aerosol flux in the arid site is small, the pattern of heavy Li isotopes may be reasoned by minor outputs by leaching. Water balance and associated pore water migration patterns are critical for Li geochemical behavior within the regolith. Such an interpretation is supported by a climate-driven threshold of 1400 mm·a^{-1} in the study area which has been evidenced by soil base cation storage (Chadwick et al., 2003), labile soil $^{87}Sr/^{86}Sr$ (Stewart et al., 2001) and meteoric ^{10}Be signals (Dixon et al., 2018).

Table 18. Li isotopic mass balance in regolith profiles under contrasting climate conditions.

Site (350 ky)	$\delta^7Li_{Shallow\ regolith}$	Net gain ΔLi	$\Delta\delta^7$ Li	F_{Rain}	δ^7Li_{Rain}	F_{dust}	δ^7Li_{Dust}	F_{wea}	δ^7Li_{Wea}	F_{Leach}*	δ^7Li_{Leach}
	‰	$mg \cdot cm^{-2}$	‰	$mg \cdot m^{-2}$	‰	$mg \cdot m^{-2}$	‰	$mg \cdot m^{-2}$	‰	$mg \cdot m^{-2}$	‰
BE (humid)	5.2	30.6	2.9	90.8	19.7	1.4	0.6	66.2	2.3	127.8	14.5
PO (arid)	8.4	40.6	6.1	20.3	19.7	0.1	0.6	36.5	2.3	16.3	14.5

Note 1. ΔLi is the absolute gain of Li per unit volume of bedrock over 350 ka.
Note 2. Fx is the mass contribution of the flux x to the bulk soil pool over 350 ka.
Note 3. Δ7Li is equal to the isotopic difference between bulk soils ($\delta^7Li_{Shallow\ regolith}$) and the parent rock ($\delta^7Li$=2.3‰).
Note 4.To have positive ΔLi values, weathering Li inputs and additional Li inputs from atmospheric sources need to be greater than leaching outputs, i.e., $\Delta Li = (F_{Wea} + F_{Rain} + F_{Dust}) - F_{Leach} > 0$.

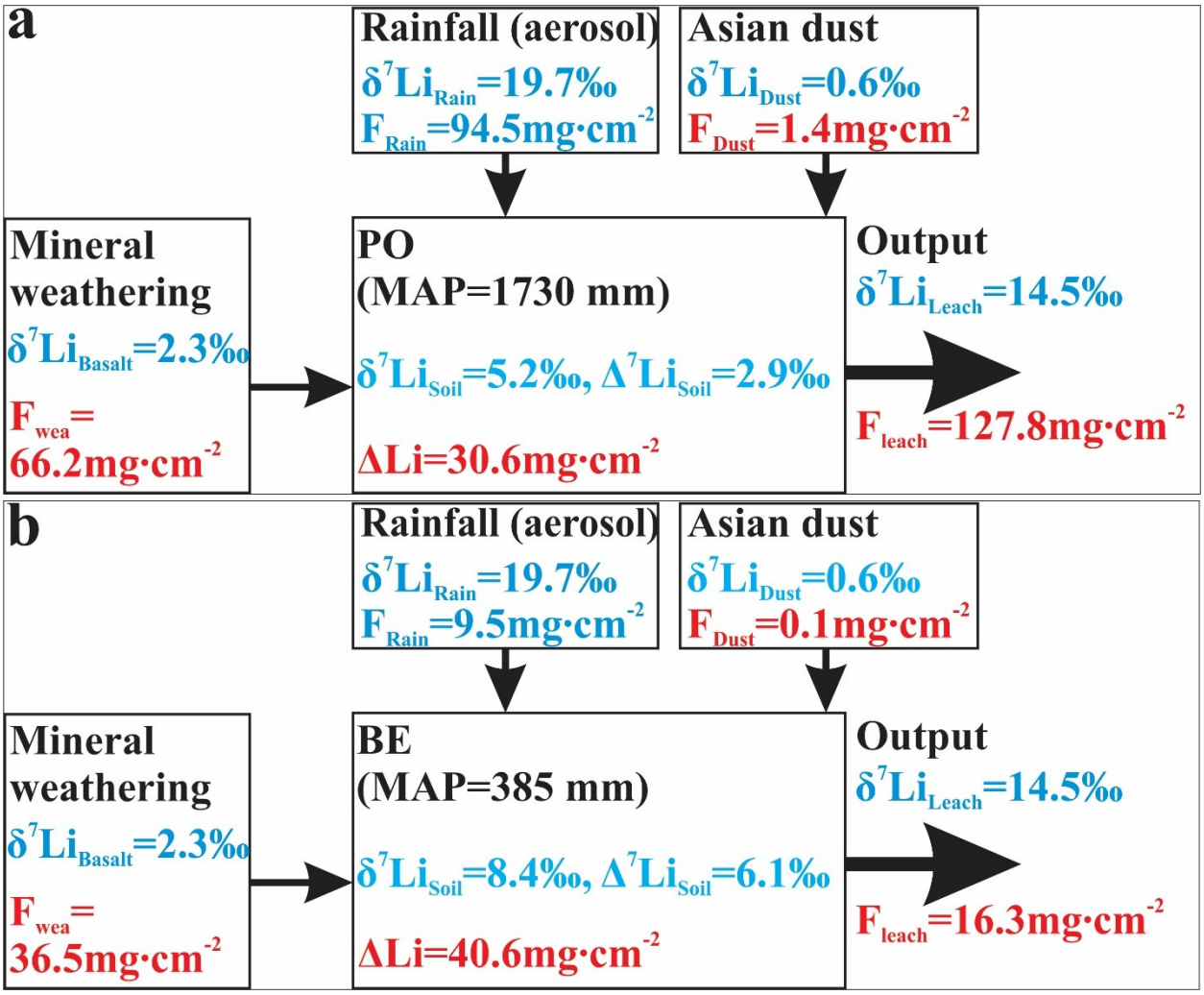

Figure 35. Illustrations of box models of the Li budget in shallow regolith of (a) the humid regolith (MAP~1730 mm·a^{-1}) and (b) the arid regolith (MAP~385 mm·a^{-1}).

Measured parameters are marked in blue and calculated parameters are marked in red. The volcanic ash input is included in mineral weathering. As the MAP increases, the contribution of atmospheric inputs increases. The leaching flux of Li increases with increasing rainfall and is generally enriched in heavy Li isotopes (δ^7Li_{Leach}=14.6‰, equal to the mean value of groundwater). ^{6}Li is residually accumulated in soils (δ^7Li_{Humid}=5.2‰, δ^7Li_{Arid}=8.4‰. Mineral weathering and leaching fluxes were calculated using Eqs. 6-7.

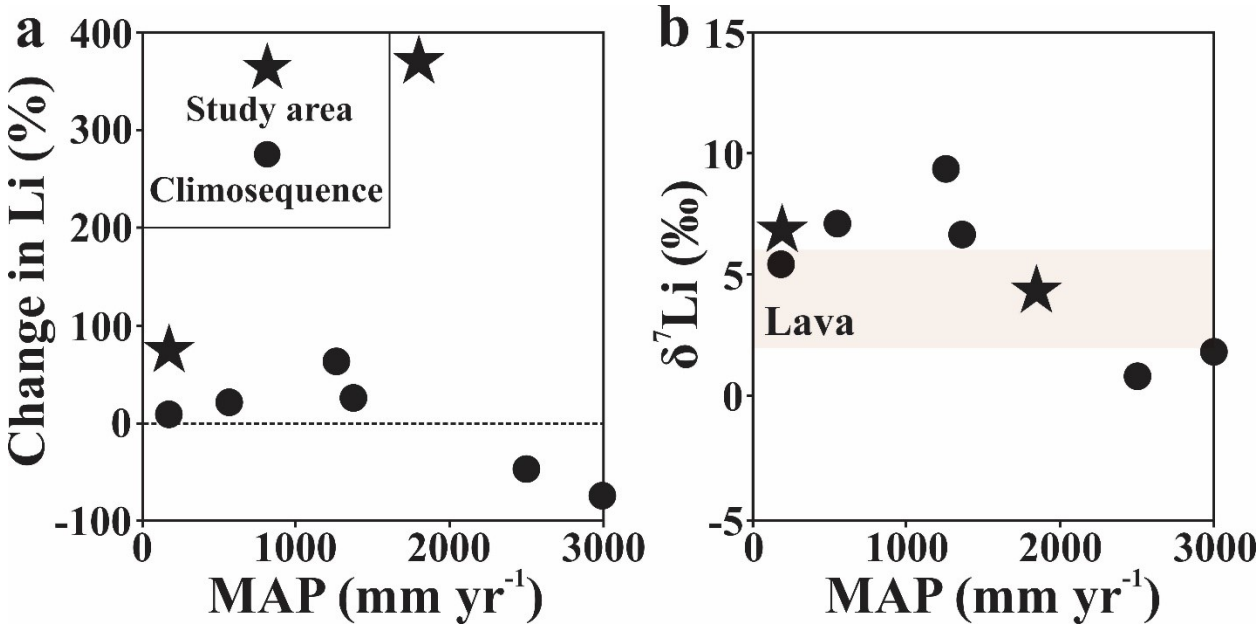

Figure 36. Depth-integrated (a) soil Li loss / gain, and (b) δ^7Li across a Hawaiian climosequence (170 ka, Ryu et al., 2014) and regoliths (humid and arid, 350 ka, this study). The black circles represent the data of the climosequence sites at the age of ~150 ka. The stars represent the data of the study area (the humid and arid regoliths).

5.5. Implications

The Li geochemical data of the humid and arid sites with those collected on the island of Hawai‘i along a climosequence of 150 ka age lava are shown in Fig. 36. Along the Hawaiian soil climosequence, depth-weighted average concentrations for Li with annual rainfalls up to 1,500 $mm \cdot a^{-1}$ are greater than these of parent lavas, and progressively became depleted after receiving greater annual rainfalls (Fig. 36a). The humid profile (BE) displays the most significant Li enrichment among all sampling sites, highlighting the importance of biological regulation (i.e., biolifting) for ~350 ka, in addition to atmospheric inputs. Another supportive evidence can be provided by higher Li enrichment levels in the arid profile (PO) compared to another site with similar annual rainfall but less development time. The conservation of Li in soils collapsed along at the sites receiving heavy rainfall over 2,000 $mm \cdot a^{-1}$. The Li isotopic composition of soils became heavy with annual rainfalls up to ~1,200 $mm \cdot a^{-1}$ and decreased with increasing rainfall (Fig. 36b). Heavy isotopic compositions could be explained by the preservation of aerosol-derived signals in less humid environments (<1,500 $mm \cdot a^{-1}$), while marine signals could be easily overprinted by rainwater in more humid conditions. In sum, our results highlight considerable climatic and biological controls on Li cycling in terrestrial settings.

Here, we compiled most reported Li elemental and isotopic data in weathered regoliths and fluvial sediments at global scales (Fig. 37). During continental weathering, the isotopically light Li is preferentially held by locally developed regolith through adsorption onto clay surfaces and incorporation into secondary clays (Pogge von Strandmann et al., 2008; Vigier et al., 2008; Millot et al., 2010a; Dellinger et al., 2015). Therefore, the Li transferred into river dissolved loads are isotopically heavy. In addition, as Li is further scavenged by secondary phases in fluvial sediments, river sediments become more Li-enriched and isotopically lighter from upper

to lower reaches (Dellinger et al., 2015; Liu et al., 2015; Wang et al., 2015). Various processes (e.g., chemical weathering, diffusion, atmospheric addition and bio-interference) potentially result in the differentiation of Li isotopes in weathering products relative to the parent rock, depending on environmental conditions. For example, compiled data show that regoliths dispaly a wide range of Li concentrations from 0.4 to133 $ug \cdot g^{-1}$ (Lemarchand et al., 2010; Liu et al., 2013) and δ^7Li from -20.2‰ to 26.7‰ (Pogge von Strandmann et al., 2012; Rudnick et al., 2004). Part of variabilities in Li geochemistry come from atmospheric addition of dusts, rainwaters, and marine aerosols (e.g., Pogge von Strandmann et al., 2012; Liu et al., 2013; Ryu et al., 2014). In addition, Li isotope fractionation driven by diffusion along the pore water-filled grain-boundary may account for the extremely negative δ^7Li values in the scapolite (Teng et al., 2010). Particularly, we conclude that the biological influences emphasized in our study can be important in tropical forests, although further studies are needed. Given that, interpretations of Li isotopic composition in complex terrestrial environments require further considerations of sources and sinks, as well as controlling processes.

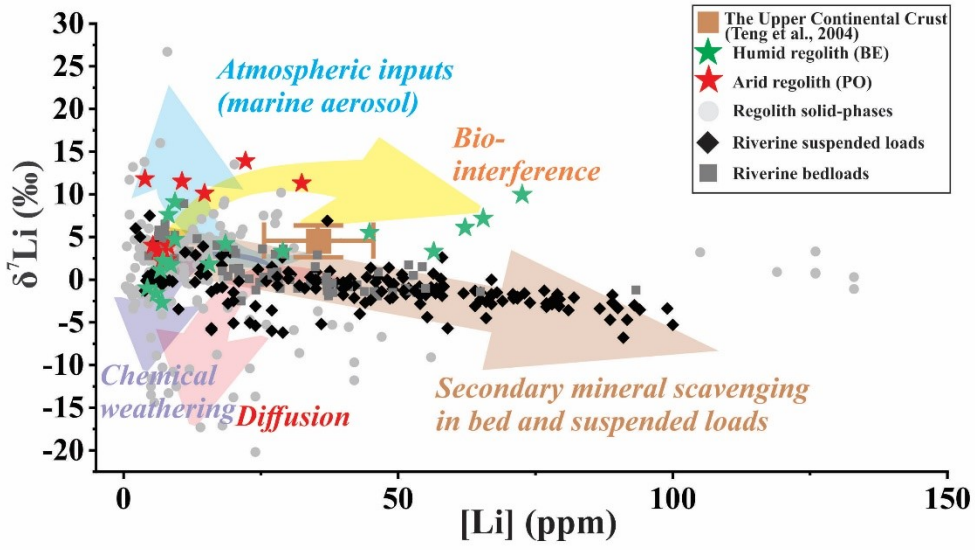

Figure 37. The compilation of Li element concentration vs. isotopic composition in regolith profiles and river sediments (suspended and bed loads) at global scales.

Data sources: (regolith: Clergue et al., 2015; Henchiri et al., 2016; Huh et al., 2004; Lemarchand et al., 2010; Liu et al., 2013; Pistiner and Henderson, 2003; Pogge von Strandmann et al., 2006; Rudnick et al., 2004; Ryu et al., 2014. River: Dellinger et al., 2015; Gou et al., 2019; Kisakürek et al., 2004; Liu et al., 2015; Romain Millot, Vigier, et al., 2010; Wang et al., 2015).

6. Conclusions

Our study provides detailed information on Li geochemistry in rocks, saprolites, soils, vegetation, and surrounding waters of the regolith profiles developed in the humid and arid sites of Hawai‘i. Compared with previous Hawaiian Li studies, our work highlights climate-regulated contribution to the Li cycle in the regolith. Therefore, δ^7Li signatures in the regolith should be treated with caution before using Li isotope system as a chemical weathering tracer. The Li geochemistry in the shallow regolith is mainly affected by atmospheric addition, vegetation cycling, and mineral synthesis, while it is controlled by pore fluid percolation and accumulation in the deep regolith. Dust input influences soil Li isotopic compositions in the humid site, and marine aerosol controls δ^7Li in soils from the arid site via secondary precipitation in equilibrium with temporal pore water. Continental dust and the ash inputs from recent Hāwī eruptions (~150 ka) supports the Li enrichment in topsoils. The fidelity of biogeochemical cycling via biolifting resulted in peak Li accumulations in the rhizospheric soils, and light Li upward translocation as plant growth, and subsequently return into pore fluids by vegetative decay. Organic matter acts as an underestimated host of ^{6}Li in soils, which is supported by experimental humus-Li complexation. Biological activities greatly influence the humid site with dense plant covers. Secondary mineral formation and associated environments (e.g., mineral assemblages and pH) are also crucial for the retention, redistribution, and isotope fractionation of Li. The Li isotopic compositions in the deep regolith are similar to parent materials (the Pololū basalt), and downward infiltrative fluids generate accumulation zones (“regolith discontinuities”) in both sites. The result of this study emphasizes the climate and long-neglected biological controls on terrestrial Li cycling.

CHAPTER 7: POTASSIUM ISOTOPICFRACTIONATION DURING CHEMICAL WEATHERING IN HUMID AND ARID HAWAIIAIN REGOLITHS

1. Introduction

Chemical weathering is one of the primary drivers for multiple geologic processes, including (1) shaping planetary topography, (2) promoting soil formation, (3) regulating terrestrial nutrient supplies to the ocean, and (4) modulating atmospheric CO_2 and carbon cycle (Royer et al., 2007; Berner and Berner, 2012). Chemical weathering promotes element cycling between atmosphere, hydrosphere, lithosphere and biosphere (Vance et al., 2009; Lerman and Meybeck et al., 2012). constraining the intensity (i.e., the degree of weathering alteration and decomposition of minerals and minerals) and rate (the amount of change in weathered materials per unit time) of weathering using robust proxies is important to trace climate change on geologic time scales (e.g., Liu et al., 2011; Berner and Berner, 2012; Vigier and Godderis, 2015). Previous studies demonstrated that non-traditional isotopes can be fractionated by weathering reactions, in particular for $^{7}Li/^{6}Li$ and $^{26}Mg/^{24}Mg$ with relatively large differences in isotope mass (e.g., Anbar and Rouxel, 2007; Teng et al., 2010; 2019; Opfergelt et al., 2014; Liu et al., 2013, 2014; Pogge von Strandmann et al., 2012;2020). The extent of isotope fractionation by chemical weathering can be linked to multiple factors, like climate and weathering regime. Geologic isotope records may provide a connection between isotope fractionation and Earth's surface processes as well as controls of such processes.

During fluid-mineral interaction across Earth's surface, potassium (K) as a major alkali metal is released from silicate rocks and partitions between waters (rivers, pore water and groundwater) and clays. By such reactions, CO_2 could be consumed by silicate breakdown and return to ocean-atmosphere continuum during secondary mineral formation, which also causes fractionation of K isotopes (S. Li et al., 2019; Ramos et al., 2020; Chen et al., 2020; Huang et al., 2020; Teng et al., 2020; Li et al., 2021B). The analytical advances enable precise measurement of K isotope ratio ($^{41}K/^{39}K$) using multi-collector inductively-coupled plasma mass spectrometry (MC-ICP-MS) to detect fractionation of K isotopes with improved analytical precision (up to 0.06‰, 2 S.D.) (e.g., Wang and Jacobsen, 2016, W. Li et al., 2016; Hu et al., 2018; Morgan et al., 2018, Chen et al., 2019; X. Li et al., 2020; Moynier et al., 2021). It is confirmed that the $\delta^{41}K$ values of bulk silicate Earth (-0.48‰) and upper continental crust (-0.44‰) is near 0.5‰ lower than that of modern seawater (0.12‰) (Wang and Jacobsen, 2016; Hille et al., 2019; Wang et al., 2020; Huang et al., 2021). It can be ascribed to chemical weathering and hydrothermal contribution (S. Li et al., 2019). Thus, K isotopes have potentials to track weathering processes and understand Earth's CO_2-thermostat.

A full view of isotope mass fluxes and sinks on Earth's surfaces is vital but poorly resolved for K isotopic mass balance in seawater. Field studies on marine sediments, weathering profiles and rivers, and laboratory experiments reveal that clays preferentially scavenge lighter isotopes in their structure, with isotopically heavy K being partitioned to water phases (S. Li et al., 2019; Chen et al., 2020; Huang et al., 2020; Teng et al., 2020; Li et al., 2021a; 2021b). However, it is poorly constrained about the control on terrestrial K isotope information including soil formation processes, regolith signatures masked by atmospheric imprints and comparative contributions of K phases to the isotopic record. Here, we evaluate the processes responsible for

changes in the K isotopic composition during weathering and regolith development in contrasting climate settings, including a humid (rainfall~1730 mm/yr) and an arid site (~350 mm/yr) on the Island of Hawai‘i. In this work, we determine regolith K phase by synchrotron-based spectroscopy, and measure the isotopic compositions of regoliths and associated water samples (river water and rainwater). We examine the effects of soil formation, atmospheric addition and biological cycling on regolith K composition and link regolith K isotopic record in Hawai‘i with corresponding climate condition.

2. Geological Background

Kohala Mountain is the northwestern-most and oldest volcano making up the Hawai‘i Island (McDougall, 1964). It has a tropical, mountainous-oceanic climate, forming a strong windward-leeward rainfall contrast, which is useful for assessing climatic impacts on weathering alteration (Chadwick et al., 2003). There are two aerially exposed lavas showing different physicochemical features in occurrence on Kohala Peninsula, the most geographically extensive and volumetric: (1) the Pololū lava majorly composed of tholeiitic basalts (~350 kyr in age) and (2) the Hāwī lava forming an alkalic cap covering the entire central region (~150 kyr in age) (Spengler and Garcia, 1988; Chadwick et al., 2003). The ages of regoliths are difficult to constrain. we considered the radiometric ages of the lava flows to be equivalent to the duration of chemical weathering since the constructional surface of the lava flow was only minimally eroded (Goodfellow et al., 2014).

There are two sites receiving distinct mean annual precipitation (MAP) on Pololū substrate that were originally characterized in Goodfellow et al. (2014). The humid (BE, MAP of 1730±57 mm/yr) and arid (PO, MAP of 385±53 mm/yr) are arrayed on a climosequence across Kohala Mountain ranges (Fig. 38). The humid regolith (BE) is located in the roadcut along

Highway 270 (the vicinity of the Bond Estate, N: 20.2288, W: -155.7896), and the arid regolith (PO) situates in another roadcut along the same highway between Mahukona and Kaiwaihae (N: 20.1357, W: -155.8859). At the foot of mountain, perennial stream flows were found at the humid site. Since regolith is an open chemical and physical system, it could be influenced by weathering of native lava and allochthonous inputs of minerals or soluble ions. In Hawai‘i, atmospheric inputs of dust and marine aerosols become important determinants of soil chemistry because basaltic phases are depleted during weathering (Kennedy et al., 1998; Vitousek et al., 1999; Chadiwck et al., 2009). In response to MAP variation, mineralogy, ecology, and geomorphology of regolith are different, and have been well characterized (e.g., Capo et al., 2000; Chadwick et al., 2003; Giambelluca et al., 2013; Goodfellow et al., 2014). Hence only a brief description of regoliths is provided below.

Based on the vertical transition in chemical composition, texture, color, hardness and fracture spacing, the outcrop of humid regolith (~15 m in thickness, intensely weathered) can be divided into 13 units (Goodfellow et al., 2014). The regolith is near-completely depleted of native phases and mainly composed of gibbsite, kaolin minerals (kaolinite and halloysite), iron hydroxides, and amorphous intermediates (short-range-ordered minerals as allophane). A sandwiched “corestone zone” between saprolites and soils appears at 3-m depth. The outcrop of arid regolith (~3.5 m in thickness) can be divided into 5 units (Goodfellow et al., 2014). Arid regolith is less weathered, and mostly composed of primary phases from basaltic materials. The shallow horizon (<1 m) is highly weathered, and the deeper layer is minimally weathered in the depth range from 1 to 2 m, with little evidence of weathering below 2-m depth. A carbonate-enriched layer occurs between 1- and 2-m depth (Capo et al., 2000). Sporadic volcanic debris has been observed in soils, which can be explained by the deposition of volcanic ash during the most

recent Hāwī eruptions (~150 kyr, Moore et al., 1992). Products from Hāwī and Pololū volcanisms are isotopically similar in radiogenic Nd-Sr (Table 19) and have comparable elemental composition. Therefore, they are difficult to differentiate. The more recent Hāwī tephra that may have been incorporated into the older Pololū soils (i.e., collectively called "basaltic substrate"). In both regoliths, the weathering intensity (represented by CIA and $\tau_{K, Nb}$, Table 20) gradually decreases downwards. Such a pattern is unexpected because K-bearing minerals in the basalts are prone to be progressively lost during weathering. Kaolin group is another useful weathering intensity index (Teng et al., 2020), which shows progressive enrichment upwards (Table 21). Since previous studies confirmed contribution of Asian dust to Hawaiian soil cation budgets (Chadwick et al., 1999; Kurtz et al., 2001; Li et al., 2020b; Vogel et al. 2021), we consider K from dust source as well. We tentatively use data from the upper continental crust (UCC, Huang et al., 2020) to characterize possible K inputs from this source. Here, we use the term "mineral aerosol" instead of "dust" for long-distance transported material. Mineral aerosol addition is positively linked to age and rainfall (Chadwick et al., 2003).

Three groups of samples were collected from the field. The first set of samples is designed to evaluate local sources includes parent basalts (Pololū lava) and Hāwī ash that have incorporated into the older Pololū soils. We sampled Pololū basalt and Hāwī ash from nearby outcrops. The second set of samples is designed to determine K isotope value in the regolith. The upper five units were sampled from a backhoe pit reaching to ~5-m depth for the humid regolith and ~3.5-m depth for the arid regolith, and. For better interpretation, we refer "the shallow regolith" to soil horizons <1m depth, and "the deep regolith" >1m depth to the deepest saprolitic unit available. A total of 26 samples were collected to characterize regoliths, and biomaterials were removed from samples. The third set of samples includes rainwater and river water close to

the humid site. Six river water samples were collected during 2018 and 2019, and there is no river water available in the arid site. Water was collected using polyethylene bottles after filtration < 0.45 μm (cellulose acetate, Thermo Scientific™) with diluted HNO_3 acidification and sent out for chemical analysis.

3. Analytical Methods

3.1. Mineralogy analysis

X-ray diffraction (XRD) was obtained on an XRD diffractometer (Rigaku™) with Ni-filtered Cu Kα radiation (40 kV, 40 mA). Prior to measurements, soil and rock samples were ground into fine powders using an agate mortar and pestle. Analysis was performed in a 2θ range from 5° to 60° (step interval: 0.01°; scan rate: 0.5°/min) (Table 20). Details of the analytical procedures were provided in Chadwick et al. (2003). In brief, we used 30% H_2O_2 (buffered to pH=5 using NaAc) to remove organic matter. Short-range-order minerals as ferrihydrite, allophane, and amorphous Fe-Al oxides were quantified by recording weight losses after NH_4-oxalate extraction. For clay analysis, samples were saturated with K^+ and oriented mounts were prepared for high resolution.

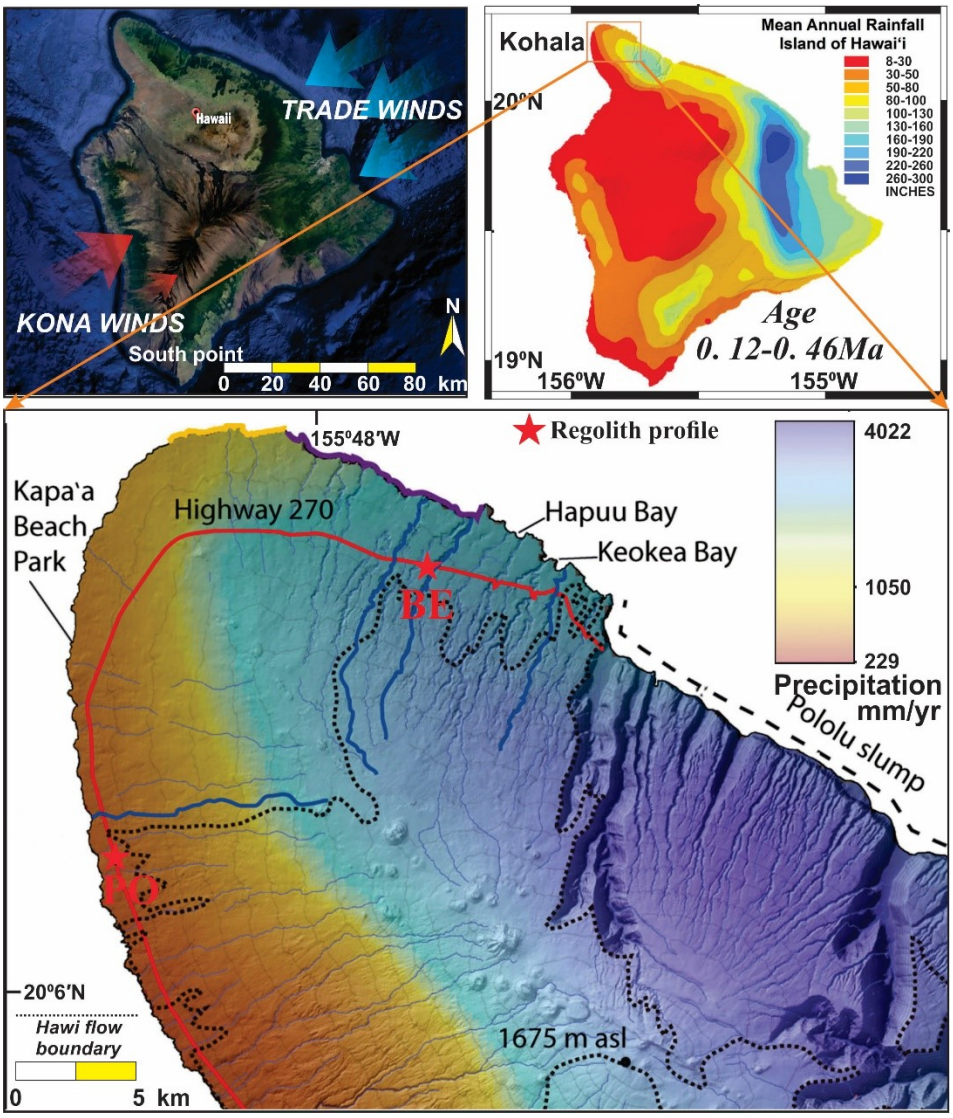

Figure 38. Geological maps showing the location of the humid (BE) and arid (PO) regoliths at the Kohala mountain in the Island of Hawai'i.

Substrate ages are reported in Chadwick et al. (1999), and mean annual precipitation (MAP) is documented in Giambelluca et al. (2013) and the 2011 Rainfall Atlas of Hawai'i by Department of Geography of University of Hawai'i at Mänoa. Due to the orographic effect, moisture-bearing Trade and Kona winds deliver heavy rainfall to the NE flank and the south point of the island, causing marked difference in MAP in two sampling sites.

3.2. Element analysis

To obtain oxide composition, samples were analyzed with X-ray fluorescence (XRF) by ALS Chemex Labs using a $Li_2B_4O_7$ fusion method. Element analysis was completed on an Agilent™ 7900 Q-ICP-MS at the Department of Geological Sciences, University of North Carolina, Chapel Hill. About 100 mg samples were transferred to 15 mL Teflon vessels and dissolved in a mixture of concentrated HCl HNO_3+HF (Li et al., 2019). Reactors were transferred onto a hotplate at 120 °C until solution clear (complete dissolution). After evaporation, the residues were refluxed with 5 mL 2% HNO_3 for analysis. Internal standards of Be, Ge, Rh, In, Ir, and Bi were added for drift correction. Elements including K, Mg, Al, Sr, and Nb were measured for samples and two USGS references (BHVO-2, basalt; GSP-2; granodiorite). Data were allowed to proceed with RSD<3% (Table A1). External accuracy <5% was enabled, and total yields (measured data to reported data) were ~100%. The relative gain ($\tau_{K,Nb}>0$) or loss ($\tau_{K,Nb}<0$) of K with depth at regplith profile was estimated as follows (Brimhall and Dietrich, 1987; Chadwick et al., 1990): $\tau_{j,w} = (C_{j,w} \times C_{i,p})/ (C_{j,p} \times C_{i,w}) -1$, where *C* denotes the concentration of an element of interest, *w* and *p* are weathered, and pristine materials (basaltic substrate), respectively, and *i* and *j* are the immobile and mobile elements in samples, respectively. Niobium (Nb) in Hawaiian soils was taken as the least mobile element (Kurtz et al., 2000), and thus elemenmt concentration is indexed to Nb for calculation.

3.3. Potassium isotope analysis

Chemical processes were conducted in a vented laminar flow hood (class-100) (Airclean™, 600 PCR). Samples were processed with double-distilled acids and ultrapure reagents. An aliquot of sample (in 2% HNO_3) was evaporated to dryness at 120 °C and laterally dissolved in 2 mL 0.7 M HNO_3 for chromatography. The purification of K was performed

following the step described in Chen et al. (2019). Samples in 0.7 M HNO_3 were firstly loaded onto the "big column" (ID of 1.5 cm), containing 17 mL AG50-X8 cation-exchange resin (200-400 mesh, Bio-Rad^{TM}). The 1st K fraction was collected after Na fractions were eluted, and evaporated to dryness and converted to a nitric form using 0.5 M HNO_3. Samples (in 20.5 M HNO_3) were passed through the second cycle of a "thin column" (ID of 0.5 cm), filled with 2.4 ml AG50-X8 resin (200~ 400 mesh, Bio-Rad^{TM}). To enhance total recovery, collected matrix cuts containing residual K were additionally passed through the same column. The pre- and post-cuts were checked particularly for K, Na, Al, Rb, and Ti to confirm quantitative K recoveries >99.5%. Total procedural blanks were monitored for each chromatography cycle (~0.1 μg K), and in all cases, negligible compared to total K mass of sample at μg-/mg-levels. The elution was evaporated to dryness and redissolved in 2% HNO_3.

Potassium isotope analyses were performed on a Nu Plasma II high-resolution MC-ICP-MS at the Isotope Laboratory, University of Washington, Seattle. K isotope analysis was conducted in a "cold plasma" mode (i.e., the RF forward power ranging from 750 to 850W) using a DSN-100 desolvation system, equipped with a PFA spray chamber and a C-Flow PFA microconcentric nebulizer. The K isotopic ratios were measured using a sample-standard bracketing protocol (6-8 cycles for each sample). Instrumentation and analytical details were provided in Hu et al. (2018). K isotopic composition was expressed in per mil (‰) relative to a NIST SRM 3141a K standard:

$$\delta^{41}\mathrm{K}\ (‰) = \left\{\frac{(^{41}\mathrm{K}/^{39}\mathrm{K})_{\mathrm{sample}}}{(^{41}\mathrm{K}/^{39}\mathrm{K})_{\mathrm{NIST\ SRM\ 3141a}}} - 1\right\} \times 1000 \qquad (1)$$

Two standard deviation (2 S.D.) and 95% confidence interval (95% c.i.) were provided in Table 20 and we reported 2 S.D. value in the text and plots. USGS references BHVO-2 yields δ^{41}K of -0.49±0.10‰ and -0.48±0.07‰, and GSP-2 yields δ^{41}K of -0.46±0.09‰ and -

0.43±0.07‰, which are in line with inter-laboratory comparison (Table A2). We used a notation $\Delta^{41}K_{x\text{-}y}$ equal to $\delta^{41}K_x$-$\delta^{41}K_y$ to express isotope fractionation between the components x and y. We note that confidential intervals (95% c.i.) were used to reflect statistical clarity of data from each sample, calculated as:

$$95\%\ \text{c. i.}\ (‰) = t_{n-1} \times \frac{S.D.}{\sqrt{n}} \quad (2)$$

where S.D. denotes the standard deviation over analytical sessions (n times) of samples, and t_{n-1} denotes student's law factor with (n-1) degrees of freedom at a 95% confidence level.

3.3. Nd-Sr isotopes

Radiogenic Sr-Nd isotopes were measured on a Neptune Plus MC-ICP-MS at the State Key Laboratory of Marine Geology (Tongji University). $^{87}Sr/^{86}Sr$ ratio was monitored using SRM987 standard (0.710248) for detector efficiency drift, yielding a $^{87}Sr/^{86}Sr$ ratio of 0.710271±18 (2 S.D.). In data acquisition, mass fractionation and instrument bias were normalized by $^{86}Sr/^{88}Sr$=0.1194, following an exponential function. The Nb isotopes mass bias was normalized to the $^{146}Nd/^{144}Nd$ ratio of 0.7219. Measured isotope values were expressed as εNd, equal to $[(^{143}Nd/^{144}Nd)_{Measured} / (^{143}Nd/^{144}Nd)_{CHUR}\text{-}1]\times10^4$, in which the CHUR (chondritic uniform reservoir) ratio is 0.512638. two USGS references BHVO-2 and BCR-2 (basalts) were comparably monitored over the course of this study. Measurements of BHVO-2 give $^{143}Nd/^{144}Nd$ of 0.512987 and $^{87}Sr/^{86}Sr$ of 0.703506, and analyses of BCR-2 yield $^{143}Nd/^{144}Nd$ of 0.512655 and $^{87}Sr/^{86}Sr$ of 0.705064. Total blanks <100 pg Sr and 30 pg Nd are negligible relative to the amounts of Nd and Sr in regolith samples processed. A Bayesian Monte-Carlo (BMC) Nd-Sr isotope mixing model was used (Arendt et al., 2015) by coding (MATLAB) aimed to quantify the comparative contribution of various sources, including uncertainties derived from variabilities in the isotopic composition and corresponding uncertainties during analysis. The

model considers purely Gaussian and uncorrelated uncertainty on Sr-Nd isotopic compositions, which follows a straightforward Monte Carlo sampling scheme:

$$\sum f_{End-memeber} = 1 \quad (3)$$

$$L \propto \exp\left[\frac{(\varepsilon Nd_p - \varepsilon Nd_o)^2}{2\sigma^2_{\varepsilon Nd}}\right] \times \exp\left[\frac{(^{87}Sr/^{86}Sr_p - ^{87}Sr/^{86}Sr_o)^2}{2\sigma^2_{^{87}Sr/^{86}Sr}}\right] \quad (4)$$

Where $f_{End\text{-}member}$ represents mass fraction of each end-member to the bulk. εNd_p, $^{87}Sr/^{86}Sr_p$, and εNd_o, $^{87}Sr/^{86}Sr_o$ represent the predicted and observed Nd-Sr isotopes, respectively. $\sigma_{\varepsilon Nd}$ and $\sigma_{87Sr/86Sr}$ denotes uncertainties in measurements. These calculations assume that there are mainly three contributing end-members (i.e., Pololū basalt, Asian dust, and seawater, Kurtz et al., 2001), which demonstrate substantial contrasts in the Nd-Sr isotopic compositions. The Hāwī volcanic ash was taken as the basaltic substrate rather than a major end-member, because of isotopic and chemical similarities to parent basalts (Table 19). For each cycle, we examined $>10^7$ model runs, and only accepted the results as posterior samples, in proportion to their relative possibility of the corresponding prediction. This model has been applied for the estimation of source mixing effect in Hawaiian chronosequence (Arendt et al., 2015), and is used in this study for the same reason.

3.4. K *K*-edge XANES analysis

Geological K phases can be determined using X-ray absorption near edge structure (XANES) (Li et al., 2020b) The XANES features arise from the contribution depending on local structural arrangements of atoms around K absorber, and electronic contribution of K from the interactions with its direct surrounding. The K *K*-edge XANES spectra of regolith samples and the references were obtained at the Soft X-ray Micro-Characterization beamline (SXRMB) at Canadian Light Source. The beamline was equipped with an ionization chamber, PIPS/Lytle detectors, a Si drift fluorescence detector and monochromated via diffraction from two sets of

crystals (InSb(111) - Si(111)), covering an wide energy range from 1.7 to 10 keV (Hu et al.,2010). After grinding with a 100-mesh (0.15mm) sieve, powdered samples were thinly spread over a double-sided K-free C tape adhered onto a Cu stick, prior to being placed in a vacuum chamber. The K *K*-edge spectra were acquired in the fluorescence yield mode using a four-element fluorescence detector, with a dwell time of 4 s. The spectra of references were acquired in a total electron yield mode to avoid self-absorption effects. Over the photon energy range of K *K*-edge (from 3550 to 3700 eV), the photon flux is around 2×10^{10} photon s^{-1} at 100 mA, and the beam size at a target is ~7mm×1mm. Two-step scans were programmed: region I (3568.0-3708.0 eV, a step-size of 0.2 eV) and region II (3648.2 to 3708.0 eV, a step-size:1.5 eV. Radiation damage is negligible because of the good reproducibility and repetitive scans at various spots of the same sample. Analysis was conducted under the ambient condition in the vacuum to minimize air-induced beam attenuation (Fig. 39).

To improve signal-to-noise ratio, spectra were averaged and processed in an Athena software (Version 0.9.20; Ravel and Newville, 2005). After background removal and normalization, data were subjected to principal component analysis and linear combination fitting for the quantitative identification of K phase. A number of K reference spectra is provided and fitting was attempted for ternary to quaternary combinations with five most likely spectra (illite-K, kaolin-K, feldspar-K, humic-K (K hosted in humic substances), and K_2SiO_3 (undefined silicate K phase as volcanic glass) (Fig. 39). Humic-K spectrum is provided since cations are often bounded to soil organic matter, and organic-K complexes are reported in Hawaiian plants, which may be added into soils (Li and Liu, 2020a; Li et al., 2021c) The spectrum of kaolinite-K is given to represent K hosted in kaolinite and halloysite (kaolin group), because of a lack of standardized halloysite-K spectrum. Through there is a large amount of Fe hydroxides occurring

in regolith, it seems that they are not major K hosts based on spectral features. It could be explained by exclusion of K impurities from Fe hydroxides by multiple dissolution-crystallization cycles over 350 kyr. An R-factor was used to evaluate the goodness-of-fit, and the significance between fits was assessed by a Hamilton test (p<0.05; Calvin, 2013). The number of independent data points calculated was re-normalized to a sum of 100%, and determined as the data range divided by core-hole lifetime broadening. Fits were only accepted when the a of the percentages of included references were 100 ± 10%. When adding more references for comparison, LCF with fewer references were preferred if an R-factor is not significantly better based on a Hamilton test, in order to avoid overfitting. If both fits with the same number of references were similar, XANES-LCF data were averaged and reported here.

Table 19. Radiogenic Nd-Sr isotopic compositions of the Hāwī and Pololū laves.

Sample	Type	Volcanic	Volcanic	K_2O (%)	$^{143}Nd/^{144}Nd$	$^{87}Sr/^{86}Sr$	Nb (ppm)
02AKA-1	Basalt	PS	Hāwī	1.54	0.512986	0.70352	66
02AKA-2				1.99	0.512987	0.70353	61
02AKA-3				1.8	0.512988	0.70351	58
02AKA-4				2.9	0.513008	0.70353	15
02AKA-5		LS	Pololū	0.8	0.512993	0.70365	25
02AKA-6				0.61	0.512996	0.70365	54
02AKA-7				0.65	0.512969	0.70363	70
This study				0.58	0.512993	0.70377	23

Note 1. The Nd-Sr isotopic data of 02AKA sample series are from Hanano et al. (2010).
Note 2. PS: Postshield; LS: Late Shield.

Table 20. Physicochemical characterization of Hawaiian humid and arid regolith profiles, basaltic substrate and water.

Region	No.	Depth (cm)	CIA	pH	K (mg/g)	$\tau_{K,Nb}$	$\delta^{41}K$ (‰)	95% c.i. (‰)	N	εNd	$^{87}Sr/^{86}Sr$
Humid (BE) MAP=1730±57 mm·a^{-1}	BE1	2.5	87	5.6	18.7	0.93	-0.54	0.04	7	-8.15	0.71941
	BE2	17.5	93	5.7	30.1	0.45	-0.49	0.04	7	-7.79	0.71811
	BE3	33.5	93	5.4	15.3	-0.34	-0.62	0.05	6	-7.92	0.72233
	BE4	46	93	5.6	11.1	-0.32	-0.51	0.04	7	-7.20	0.72129
	BE5	61	93	5.8	11.8	-0.03	-0.55	0.05	6	-6.60	0.72177
	BE6	96.5	94	5.9	4.5	-0.70	-0.49	0.04	6	-5.43	0.71814
	BE7	127	97	6.0	7.7	-0.50	-0.44	0.05	6	-4.40	0.71549
	BE8	158.5	97	6.1	7.9	-0.44	-0.42	0.04	7	-1.89	0.70375
	BE9	192	98	6.2	2.8	-0.64	-0.53	0.05	6	n.d.	n.d.
	BE10	230	99	6.3	1.4	-0.80	-0.42	0.05	6	n.d.	n.d.
	BE11	259	99	6.4	1.3	-0.91	-0.63	0.05	6	n.d.	n.d.
	BE12	297.5	99	6.2	0.7	-0.96	-0.72	0.04	6	-0.14	0.70385
	BE13	300	n.d.	n.d.	0.8	-0.84	-0.31	0.05	6	n.d.	n.d.
	BE14	300	n.d.	n.d.	4.2	-0.16	-0.52	0.04	7	n.d.	n.d.
	BE15	337.5	99	5.7	0.4	-0.97	-0.76	0.05	6	n.d.	n.d.
	BE16	600	85	n.d.	4.8	-0.04	-0.50	0.04	8	4.40	0.70396
Arid (BE) MAP=385±53 mm·a^{-1}	PO1	2.5	68	7.9	0.9	-0.85	-0.25	0.05	7	-0.29	0.70613
	PO2	17.5	96	7.7	1.9	-0.81	-0.03	0.04	6	3.80	0.70575
	PO3	34.5	98	7.7	0.8	-0.90	-0.37	0.08	6	4.78	0.70554
	PO4	51.5	96	8.3	1.2	-0.87	-0.43	0.05	7	6.66	0.70533
	PO5	70	94	8.7	2.1	-0.75	-0.23	0.05	4	6.62	0.70573
	PO6	75	93	8.6	2.0	-0.74	-0.34	0.04	6	6.45	0.70523
	PO7	96	85	8.6	3.0	-0.61	-0.37	0.04	7	6.58	0.70534
	PO8	108.5	74	8.5	1.1	-0.87	-0.37	0.04	6	6.70	0.70331
	PO9	200	55	n.d.	0.4	-0.90	-0.02	0.04	6	n.d.	n.d.
	PO10	300	45	n.d.	8.8	0.00	-0.39	0.04	6	5.12	0.70367
Rainwater	R1						-0.23	0.03	6	n.d.	n.d.
	R2						-0.16	0.04	6	n.d.	n.d.
Ash	Hāwī	n.d.	-0.48	0.08	n.d.	n.d.	-0.48	0.08	6	n.d.	0.70423
Bedrock	Pololū	n.d.	36	n.d.	8.1	0.00	-0.48	0.04	7	6.93	0.70377

Table 21. Physicochemical characterizations of Hawaiian humid and arid regolith profiles.

Region	Sample	Isotope mixing model				XANES-LCF					R
		Basalt-	2	Eolian-	2	Feldspa	Illite	Kaoli	K_2SiO	Humi	
		(%)	(%)	(%)	(%)	(%)	(%)	(%)	(%)	(%)	
Humid (BE) MAP=1730±57 mm·a^{-1}	BE1	4.6	1.2	95.2	4	0 (0)	73	22 (2)	0 (0)	5 (1)	0.00
	BE2	5.2	1.4	94.4	5.3	2 (2)	75	17 (3)	0 (0)	7 (1)	0.00
	BE3	1	0.6	98.9	2	7 (1)	70	22 (4)	0 (0)	2 (1)	0.00
	BE4	2.3	0.9	97.6	3.1	5 (1)	76	19 (2)	0 (0)	0 (0)	0.00
	BE5	4	1.3	96	4.6	10 (2)	75	16 (3)	0 (0)	0 (0)	0.00
	BE6	8.8	1.3	91	5.8	11 (1)	72	17 (4)	0 (0)	0 (0)	0.00
	BE7	12.6	1.3	87.3	9	9 (3)	70	20 (2)	0 (0)	0 (0)	0.00
	BE8	17	1.9	82.8	7.7	3 (1)	72	24 (3)	0 (0)	0 (0)	0.00
	BE9	n.d.	n.d.	n.d.	0	6 (1)	72	23 (4)	0 (0)	0 (0)	0.00
	BE10	n.d.	n.d.	n.d.	0	27 (3)	49	24 (2)	0 (0)	0 (0)	0.00
	BE11	n.d.	n.d.	n.d.	0	25 (5)	49	26 (4)	0 (0)	0 (0)	0.00
	BE12	n.d.	n.d.	n.d.	0	37 (3)	37	26 (3)	0 (0)	0 (0)	0.00
	BE13	52.5	3.2	47.3	17.	51 (4)	25	23 (2)	0 (0)	0 (0)	0.00
	BE14	n.d.	n.d.	n.d.	0	70 (7)	28	2 (1)	0 (0)	0 (0)	0.00
	BE15	n.d.	n.d.	n.d.	0	74 (3)	0 (0)	21 (4)	6 (2)	0 (0)	0.00
	BE16	99	5.5	0.7	18	78 (3)	0 (0)	15 (2)	7 (3)	0 (0)	0.00
Arid (BE) MAP=385±53 mm·a^{-1}	PO1	58	5	40.4	30	53 (4)	36	7 (2)	0 (0)	4 (1)	0.00
	PO2	72.4	4.5	27.2	17.	42 (5)	41	17 (3)	0 (0)	0 (0)	0.00
	PO3	77.6	4.4	22.1	14.	47 (4)	31	22 (3)	0 (0)	0 (0)	0.00
	PO4	85.4	3.8	14.4	11	87 (3)	0 (0)	13 (2)	0 (0)	0 (0)	0.00
	PO5	85	4.2	14.8	11.	93 (6)	0 (0)	7 (2)	0 (0)	0 (0)	0.00
	PO6	77.8	3.7	22	10.	90 (5)	0 (0)	10 (2)	0 (0)	0 (0)	0.00
	PO7	81.9	3.8	17.8	9.7	80 (4)	0 (0)	10 (1)	10 (3)	0 (0)	0.00
	PO8	79	3.7	20.6	9.9	80 (3)	0 (0)	10 (1)	10 (0)	0 (0)	0.00
	PO9	n.d.	n.d.	n.d.	0	80 (5)	0 (0)	5 (2)	15 (7)	0 (0)	0.00
	PO10	89.3	4.6	10.6	14.	55 (7)	0 (0)	0 (0)	45 (9)	0 (0)	0.00
Bedroc	Pololū	100	0	0	0	94 (8)	0 (0)	0 (0)	6 (3)	0 (0)	0.00

Note 1. The Bayesian Monte Carlo isotope mixing model and the code is provided in Arendt et al. (2015) and the XANES-LCF analysis (fitting uncertainties given in the parentheses) was completed using the Athena software (Ravel and Newville, 2005).

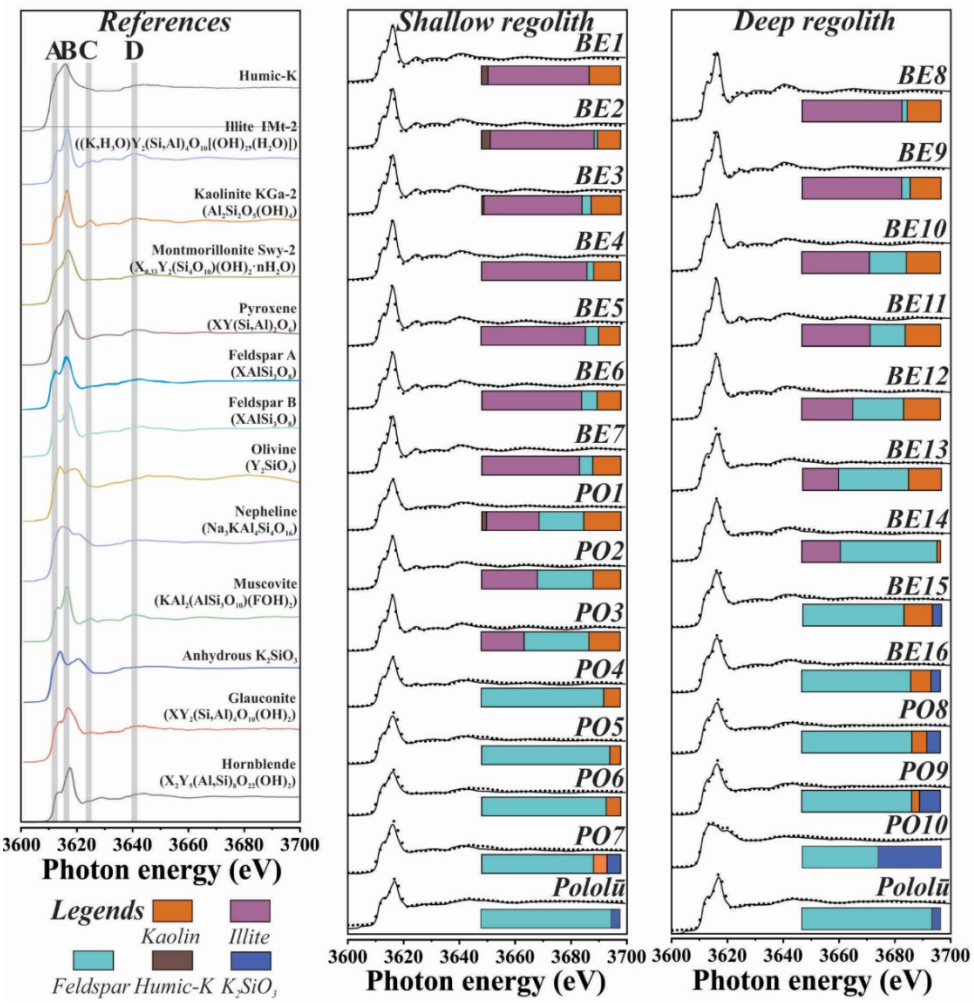

Figure 39. K *K*-edge XANES analysis of references and regolith samples.

Fractional distribution of the mean weight of K phases by XANES-LCF analysis was recalculated to total K, including humic-K, illite-K, kaolin-K, feldspar-K, and K_2SiO_3-K phases. Peaks A - D denote characteristic energy peaks of K. Peaks A and B are dependent on the local structural arrangement of the atoms around K absorber (i.e., bond length and orientation). An intense peak C potentially indicates the strong interaction between photoelectrons emitted from K atoms as well as Fe and Al (octahedral substitution), Peak D represents the long-distance ordered structures surrounding K. The result of XANES-LCF (solid line, raw spectra; dotted line, fitting curve) in the plot is provided in Table 21.

Table 22. End-member isotopic compositions for the isotope mixing model (Arendt et al., 2015).

Type	$\delta^{41}K$ (‰)	2 S.D. (‰)	εNd			$^{87}Sr/^{86}Sr$		
Upper	-0.44	0.05	-11	to	-8	0.718	to	0.72
Pacific	0.14	0.02	-10	to	-8.5	0.709	to	0.709
Oceanic	-0.41	0.16	-10	to	-5	0.702	to	0.706

Note 1. Upper continental crust values represent eolian composition; Pacific seawater values represent marine aerosols composition; Oceanic Island basalt values represent basaltic substrate.
Note 2. Data on the upper continental crust refer to Huang et al. (2019), Chauvel et al. (2014), and Gaschnig et al. (2014). Data of the Pacific Ocean seawater refer to Hille et al. (2019), Lacan et al. (2012), and Palmer and Edmond (1989). Data of the oceanic island basalt refer to Tuller-Ross et al., (2019b), and White et al. (2010).

4. Results

Mineralogy, K elemental and isotopic data in the regolith, water, and Hāwī ash are provided in Table 20 and depicted in Fig. 40.

Kaolin minerals are a major phase in the regoliths, making up for near-half of the mineralogy pool, which can be found across the profile. Quartz can be identified in the upper section of both profiles, accounting for 10% in the humid, shallow regolith and the top layer of the arid regolith.

The humid regolith is more enriched in K (0.4 to 30.1 $mg \cdot g^{-1}$) compared to the arid regolith (0.4 to 3.0 $mg \cdot g^{-1}$). Across the humid regolith, there is an overall K enrichment from the deep to the shallow regolith ($\tau_{K,Nb}$ of -0.97 to 0.93). Local-scale K enrichment is marked at the top (<20 cm, $\tau_{K,Nb}$ of 0.45 to 0.93). In the deep regolith, the corestone zone (BE14) and the bottom layer (BE16) exhibits relatively weak K depletion ($\tau_{K,Nb}$ from -0.16 to -0.04). In the arid regolith, the level of K loss in depth is consistent relative to that of the humid regolith ($\tau_{K,Nb}$ of -0.61 to 0.93), except for the bottom layer close to the substrate (PO10, $\tau_{K,Nb}$ of 0.0).

Regolith K phases can be classified into two types, including secondary K (kaolin-K, illite-K, and humic-K) and primary K (K_2SiO_3-K and feldspar-K) (Table 21). Total K in the Pololū basalts consists of 94±8% feldspar-K and 6±3% K_2SiO_3-K. The humid regolith is composed of 0 to 76 ± 7% illite-K, 0 to 78 ± 5% feldspar-K, 2±1 to 26±5% kaolin-K, 0 to 7 ± 3% K_2SiO_3-K, and 0 to 7±1% humic-K. The arid regolith is composed of 0 to 41±6% illite-K, 55±7 to 93± 6% feldspar-K, 0 to 22 ± 7% kaolin-K, 0 to 45±9% K_2SiO_3-K, and 0 to 4±1% humic-K. We found that illite-K could be critical in the profile, proportionating up to ~80% K, yet, its abundance dramatically drops below the shallow regolith. Kaolin-K fraction (K hosted in kaolinite and halloysite) shows enrichment at the shallow regolith, and feldspar-K dominates in

the deep units. There are minor amounts of humic-K, making up < 10% K and only be identified near surface soil layers (Fig. 39).

The humid regolith has $\delta^{41}K$ values ranging from -0.76 ± 0.08 to -0.31 ±0.06‰. This range is relatively narrow in the shallow regolith (-0.62 ± 0.03 to -0.49 ± 0.06‰) that approximates to the values of the Pololū basalt (-0.48±0.06‰) and Hāwī ash (-0.48±0.10‰). In humid, deep regolith, most samples exhibit negative $\delta^{41}K$ shifts from the basaltic K values. The arid regolith has $\delta^{41}K$ ranging from -0.43±0.11 to -0.02±0.06‰, mostly higher that these of the basaltic substrate and the ranges previously reported for weathering profiles (Chen et al., 2020; Teng et al., 2020). The highest $\delta^{41}K$ value (-0.02 ± 0.06‰) is identified at the carbonate-enriched zone (1-2 m depth) in the arid, deep regolith. Collected rainwaters have $\delta^{41}K$ values of -0.23±0.05‰ and -0.16±0.07‰, and river water near the humid regolith shows a $\delta^{41}K$ range from 0.03 ± 0.07‰ to 0.15 ± 0.06‰. The Sr isotopic composition in the regoliths has been reported for the same set of samples in Li et al. (2020a). The Pololū basalts have εNd and $^{87}Sr/^{86}Sr$ of 6.93 and 0.70377, respectively. Both sites show increasing radiogenic isotopic composition towards the shallow regolith (humid, εNd of -8.15 to -5.43, $^{87}Sr/^{86}Sr$ of 0.71811 to 0.72233; arid, εNd of -0.29 to 6.66, $^{87}Sr/^{86}Sr$ of 0.70523 to 0.70613), in particular for the humid profile. River water from the streams adjacent to the humid site exhibits an $^{87}Sr/^{86}Sr$ range from 0.70397 to 0.70537, which falls within a range of basaltic value (0.702-0.706) and is less radiogenic than that of nearby seawater (0.709, Table 22)

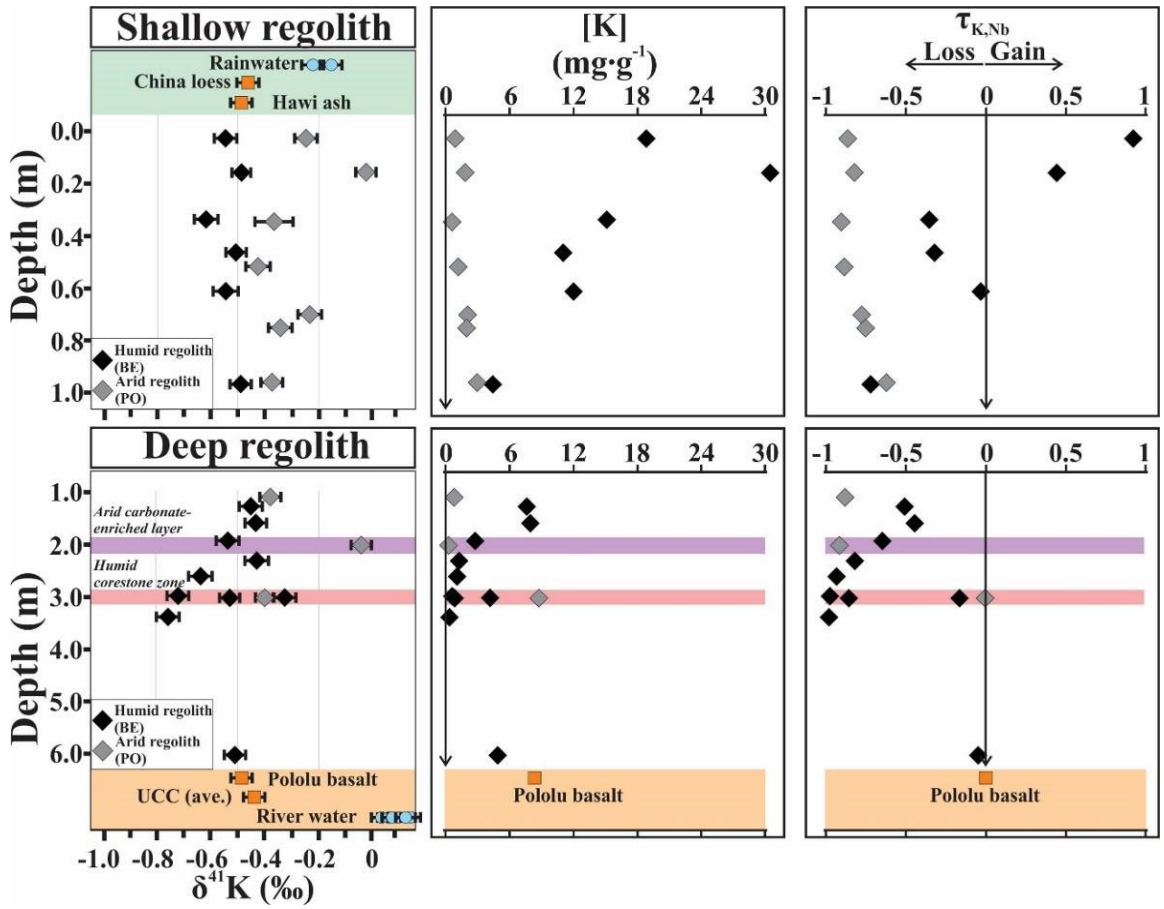

Figure 40. Vertical distribution of $\delta^{41}K$ (K isotopic composition), [K] (K concentration) and $\tau_{K,Nb}$ (K mass transfer coefficient).

Data of shallow and deep horizons of the humid and arid regoliths are provided, with corresponding data of terrestrial components (in orange boxes at the bottom) and atmospherically added materials (in green boxes at the top). Regolith "discontinuities" -- the corestone zone (pink bar, humid) and the carbonate-enriched layer (purple bar, arid) in the deep regolith are labeled.

5. Discussion

From the comparison of $\tau_{K,Nb}$ (an index of K gains/loss) versus $\delta^{41}K$ (Fig. 41a), we found three directions of element-isotope co-variations revealing various factors act to fractionate K isotopes within the profile. In the humid, shallow regolith, there are two samples exhibiting K enrichment (relative to the basaltic substrate) and basaltic $\delta^{41}K$ values. In most humid regolith samples, their $\delta^{41}K$ values decrease with progressive depletion. In contrast, $\delta^{41}K$ in most arid regolith samples increases with gradual K loss. We summarize three main factors potentially controlling K isotope fractionation in regoliths, including clay formation, atmospheric accretion and biological cycling.

5.1. Chemical weathering and soil formation

Chemical weathering promotes (i) the breakdown of rocks and primary minerals, and (ii) the formation of clays. Marked partitioning of isotopically lighter K in humid, deep regolith is likely produced by weathering-driven isotope fractionation (Fig. 40). This argument can be supported by lighter isotopic compositions with higher CIA values, corresponding to more intense weathering alteration (Fig. 41b). We consider that breakdown of primary minerals exerts negligible effects on isotope fractionation in the regolith based on two lines of evidence. First, $\delta^{41}K$ heterogeneities in basalts are minor during magma differentiation (Y. Li et al., 2019; Tuller-Ross et al., 2019a) that are nearly a magnitude lower than observed $\delta^{41}K$ variation in the regolith. Therefore, differences in susceptibilities of minerals in polymineralic basalts to weathering leaching is unlikely to cause discernable impacts on regolith K isotopic records. Second, Li et al. (2021b) performed silicate dissolution experiments of two igneous rocks (basalt and granite) in closed systems and reported non-fractionation of K isotopes in several days (far less than regolith ages). Secondary minerals as clays are important weathering products and sinks of K released

from basalts during chemical weathering, causing partitioning of light K isotopes in clays (S. Li et al., 2019; Chen et al., 2020; Huang et al., 2020; Teng et al., 2020) and heavier K isotopic composition in waters (river water near the humid site, this study; global river water, Wang et al., 2021). Quantitative XRD analysis suggests that kaolin occurrence is important in the regolith (Table 20). The proportion of K bound to kaolin is considerable and K associated to feldspar is negligible in the humid regolith based on XANES-LCF data (Table 21). With increases in kaolin-K fraction, there is a reduction in regolith $\delta^{41}K$ (Fig. 41c), and hence kaolin minerals have a critical control on K isotope fractionation in the regolith. However, this influence from kaolin scavenging is likely restricted to the humid regolith due to higher $\delta^{41}K$ in the arid regolith than these of the basaltic substrate. Although pedogenesis and weathering is expected to be kinetically limited in arid climate (Stewart et al., 2001; Qafoku, 2015), kaolinite seems to be more enriched in the arid regolith, with a maximum up to 66%. This contradiction is resolved by two mutually non-exclusive factors: clay incorporation and sorption.

Clay exchangeable complexes, including K^+ adsorbed onto phyllosilicates and oxides, prefer isotopically light K (Li et al., 2021b). Based on laboratory sorption experiments, Li et al. (2021a) reported a higher affinity of K^+ to exchangeable sites of clay minerals (kaolinite and smectite) at higher pH due to hydroxyl deprotonation, resulting in higher $\delta^{41}K$ of sorbed complexes. There is no published data of K isotope fractionation during oxide adsorption. We infer K adsorption onto oxides is less important. Ion adsorption on soils is primarily linked with the electrostatic field on clay surfaces, which can be assessed by the pH of the point of zero charges (pH_{pzc}). The pH_{pzc} of alumino-silicate clay minerals are relatively low (falling in the range of ~2 to 5), and the pH_{pzc} of Al- and Fe-hydroxides (e.g., gibbsite, ferrihydrite, and hematite) are high (falling in a range of 6 to 9) (Taubaso, 2004; Kosmulski, 2006). Adsorption-

driven K isotope fractionation is supported by higher $\delta^{41}K$ in the arid regolith (alkaline) and lower $\delta^{41}K$ in the humid regolith (circumneutral to acidic) (Fig. 41d). In addition, XANES-based kaolin-K is more enriched in the humid regolith than the arid profile, opposite to XRD-based kaolin pattern (Tables 1-2). Therefore, we conclude that secondary K^+ mostly stays on clay surface rather than entering into the lattice in the arid site. In the humid profile, kaolin incorporation is a major control, prone to take isotopically light K by kinetic processes, or equilibrium reactions by forming stiffer lattice K-O bonds (Li et al., 2021b). Supportively, halloysite was found to be a vital K host forming in soils from northern California, USA (Takahashi et al., 2018). It is likely that K^+ is intercalated into the interstitial and distorted spaces such as structural defects within kaolin minerals. This process might promote kaolin-illite transformation (Cuadros et al., 2017). Although illite is an abundant K carrier in the regolith, no monotonous correlation between regolith $\delta^{41}K$ and XANES-based K fraction locked within illite interlayer space can be found (Fig. 42a). Deeply weathered saprolites contain less illite-K fraction and more heterogeneous $\delta^{41}K$ values. This observation demonstrates that regolith illite is not primarily of a pedogenic origin, and illite provenance is evaluated in the following section.

Overall, two clay formation processes (structure incorporation vs. surface adsorption) explain our observation that the humid regolith in low-pH conditions (pH=5–6) shows lighter K isotopic composition (averaged $\delta^{41}K$: -0.53‰) than that of the arid site in alkaline conditions (averaged $\delta^{41}K$: -0.28‰). Hence, climate-dependent soil formation processes regulate K isotopic behaviors.

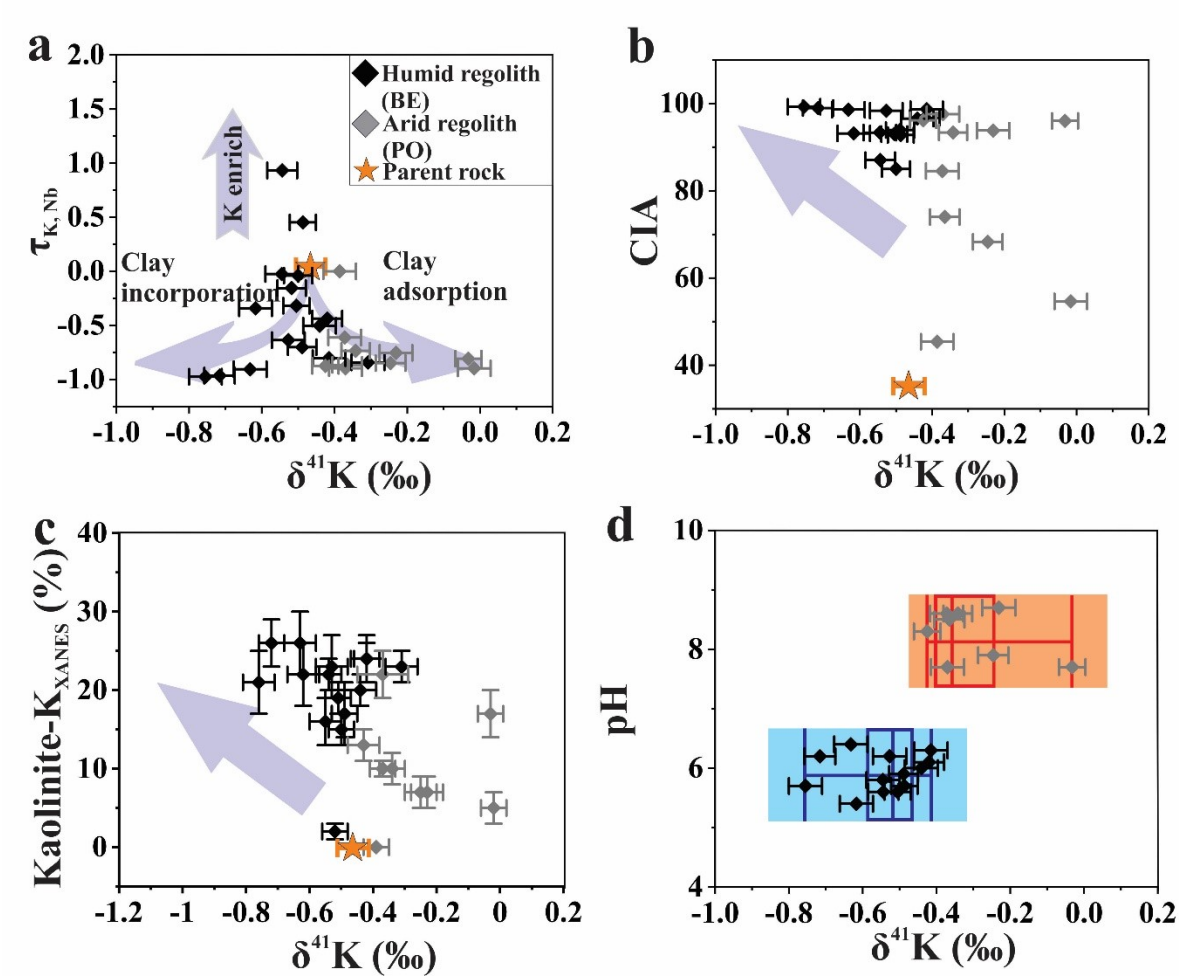

Figure 41. Interrelationships of regolith $\delta^{41}K$ with (a) normalized $\tau_{K,Nb,}$ (b) CIA, (c) fractional contribution of kaolinite-K using XANES-LCF and (d) regolith pH.

The data of the Pololū basalt is symbolized with an orange star. The data of humid (BE) and arid (PO) regoliths are marked by black and grey diamonds (95% c.i. analytical uncertainty), respectively. The trajectory of purple arrows in the plot (a) represent different soil formation processes (incorporation vs. adsorption). Data in the plot (d) are divided by boxplots (i.e., blue, acidic - humid and orange, alkaline - arid).

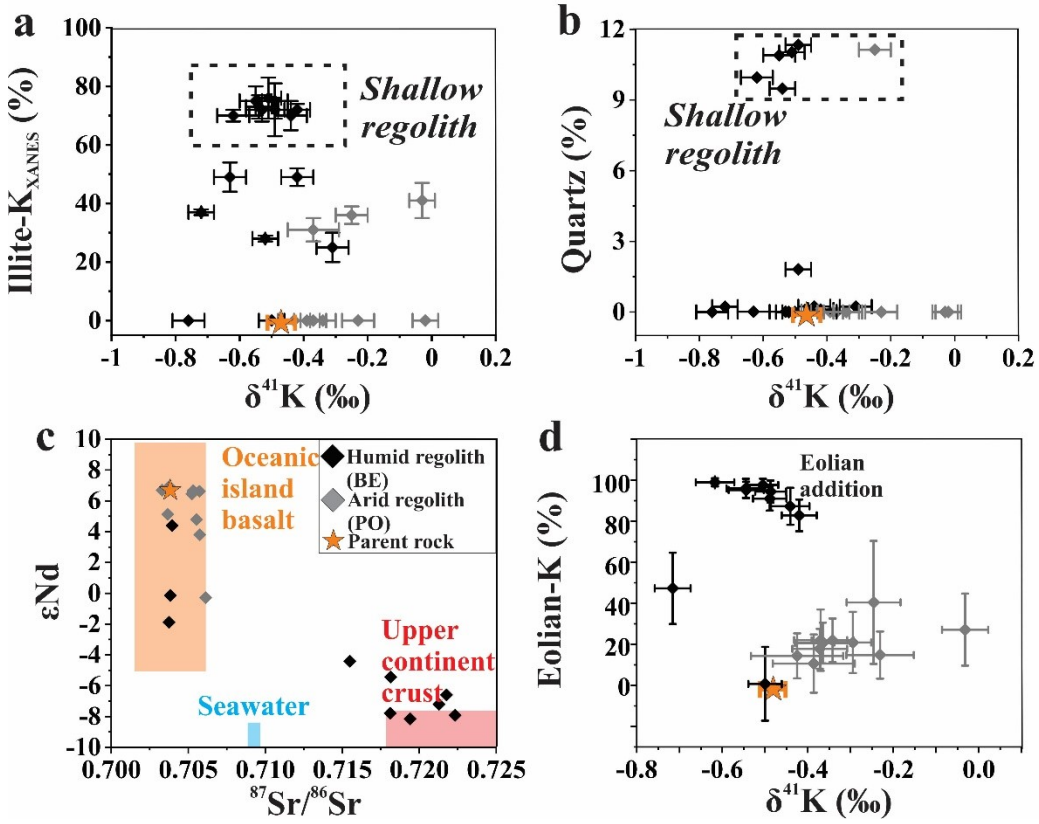

Figure 42. Interrelationships of regolith $\delta^{41}K$ with (a) fractional contribution of illite-K based on XANES-LCF (Table 21), and (b) quartz content.

Data of humid (BE) and arid (PO) regoliths are marked with black and grey diamonds (95% c.i. analytical uncertainty), respectively. Data falling in dashed boxes in the plots (a) and (b) reflect marked dust influences on shallow regolith (<1m). Interrelationships between regolith (c) $^{87}Sr/^{86}Sr$ and εNd, and (d) $\delta^{41}K$ and model-derived eolian-K fraction. The isotopic ranges of upper continental crust (UCC, red), oceanic island basalt (OIB, orange) and Pacific Ocean seawater (blue) are shown in the plot (a) (Table 22). Data of Pololū basalt is marked with an orange star, and data of humid and arid regoliths are symbolized using black and grey diamonds, respectively. Eolian fractions was estimated using the Bayesian Monte Carlo isotope mixing model, which was applied to Hawaiian chronosequence soils (Arendt et al., 2015). The error bars of $\delta^{41}K$ and eolian-K show 95% c.i. and XANES-LCF errors, respectively.

5.2. Atmospheric addition

As regolith develops, atmospheric inputs become increasingly critical in modulating regolith mineralogy and chemistry, particularly for the shallow regolith (0-1 m depth). The deposition of eolian materials to Hawaiian soils has been reported in literatures, and accreted mineral aerosols take on various extents of significance in regolith elemental and isotopic budget in Hawai‘i (e.g., Kurtz et al., 2001; Ziegler et al., 2005; Wiegand et al., 2005; Chadwick et al., 2009; Ryu et al., 2014; Li et al., 2020a). The contribution of mineral aerosols to soil budget is positively linked to local rainfall (MAP, Porder et al., 2007), and hence, the humid regolith is expected to has strong dust interference. This interpretation is supported by lines of evidence. First, there is an reduction in the degree of K depletion ($\tau_{K,Nb}$) in humid shallow regolith (Table 20) since eolian addition can balance leaching losses of soluble ions as K^+ during chemical weathering (Chadwick et al. 1999). Moreover, humid, shallow regolith samples display homogeneous $\delta^{41}K$ identical to that of upper continent crust (UCC, Huang et al., 2020), in line with marked enrichment of illite-K and quartz (Figs. 42a-42b). XRD-based mineralogy allows for quantitative assessments of eolian inputs (Table 20). Assuming a quartz content of 20% in mineral aerosols (Kurtz et al., 2001), we could calculate a minimum estimation of K in shallow regolith of eolian origins: ~30% for the humid profile and ~3% for the arid site. For this calculation, we did not consider any physical erosion and used the crustal K content of $27 mg \cdot g^{-1}$ as an approximation of mineral aerosols (Rudnick and Gao, 2003). We suggest that seepage percolation and subsequent accumulation also affect the budget of K in the deep regolith. The highest $\delta^{41}K$ value of -0.02±0.06‰ was found at the carbonate layer of the arid regolith, corresponding to the highest δ^7Li (Li et al., 2020a). It was inferred that downward- infiltrative meteoric water and sea sprays rich in isotopically heavy Li and K passing through the regolith.

Marine imprints can be well preserved in the arid regolith without rapid leaching due to high evapotranspiration relative to precipitation (Li et al., 2020a). In addition, when rainwater (~-0.2‰) and sea sprays (~0.12‰) are deposited on the arid soil, a fraction of its ^{41}K is retained via sorption by weathering products like clays. At the corestone zone of the humid regolith, a sample close to the corestone (BE13) has $\delta^{41}K$ of -0.31‰ higher than basaltic $\delta^{41}K$. This anomaly can be attributed to derivations from neighboring detritus mixed with rainwater infiltrating downwards.

Previous studies have elucidated that radiogenic Nd and Sr isotopes are powerful tracers for estimating comparative contributions of atmospheric and native materials in Hawaiian soils (e.g., Chadwick et al., 1999; Kurtz et al., 2001). The cross-plot of regolith $^{87}Sr/^{86}Sr$ and εNd values can distinguish three end-members in regoliths (i.e., basaltic substrate, continental dust and seawater, Fig. 42c). Clearly, the humid profile received substantial dust inputs with UCC composition while the arid profile preserved more basaltic information. Despite the chemical property of K differs from that of Sr and Nd, it is suggested that regolith K cycles can be traced by radiogenic isotopes given that during weathering these elements are released from primary minerals into soil solution at similar depth (Uhlig et al., 2020). We tentatively constrain the fractional contributions of each end-member in the regolith by Bayesian Monte-Carlo Nd-Sr models. To simplify the calculation, we calculated K contribution f^K for end-members based on a Monte-Carlo isotope mixing model (Arendt et al., 2015), and K concentration in each source (basalt, 8.1 $g \cdot kg^{-1}$, this study; mineral aerosol, 27.1 $g \cdot kg^{-1}$, Rudnick and Gao, 2003; seawater, 0.4 $g \cdot kg^{-1}$, GeoRem NASS-5) (Table 22).

$$f_{End-member}^{K(i)} = (C_{K(i)} \times f_{Endmember}^{M(i)}) / \sum C_{K(i)} \times f_{Endmember}^{M(i)} \quad (5)$$

Where $C_{K(i)}$ denotes the mass contribution of K from each end member, provided in Table 21. The results imply that seawater fractions in both regoliths are negligible and eolian-K

fractions make up ~11-40% K in the arid site and ~1-99% K in the humid site. It is estimated that over 90% K in humid shallow regolith is derived from eolian inputs, resulting in crust-like $\delta^{41}K$ values (Fig. 42d). We would expect $\delta^{41}K$ closer to UCC signature with more eolian contributions. However, humid regolith samples with higher model-based eolian influence have lower $\delta^{41}K$ values deviated from crust $\delta^{41}K$. To reconcile this discrepancy, we consider that i) Nd and Sr are available in relatively high quantities in lavas, and K concentration is high in atmospherically sourced mineral aerosols; (ii) K is mostly held in non-refractory minerals susceptible to weathering compared to Nd and Sr. This Nd-Sr model offers a direct measure of Sr-Nd sources, but may not precisely resolve K fate.

5.3. Biological cycling

Regolith K budget is expected to be biologically influenced because K is a macronutrient and actively cycled by plant (uptake-return cycling of inorganic nutrients from depth to surface soils, Uhlig et al., 2020; Schlesinger, 2020). This control is supported by apparent K enrichment at the surface soil of humid regolith (positive $\tau_{K,Nb}$, Fig. 40), which cannot be reconciled by eolian inputs due to relatively similar K-Nb composition (Rudnick and Gao, 2003). This trend is not observed in the arid site, which can be attributed to sparse vegetation. Because Hawaiian plants (both trees and grasses) growing at the same sites preferentially take isotopically lighter K by roots (Li et al., 2021c), we expect low $\delta^{41}K$ in the shallow regolith relative to deep regolith, especially the humid site with dense vegetation covers. Nevertheless, the shallow regoliths of both sites do not display negative isotopic excursions with distinguishable plant imprints (Fig. 40). In addition, there are no correlations between regolith $\delta^{41}K$ with soil organic matter content and K/Rb ratio (an index of vegetative cycle, Chaudhuri et al., 2007) (Figs. 43a-43b). They are several possibilities to reconcile it. Humid shallow regolith has ~90% K hosted in silicates

(Table 22), and humic-K consists less than 10%. Li et al. (2021c) inferred that plant K imprint on soils may be masked by atmospheric materials. Second, clay adsorption experiments by Li et al. (2021a) found that sorbed K^+ is easily exchanged with cations of higher ionic potential. Plant-derived K in soils could be replaced with multivalent ions as Al^{3+} or imprinted by exogenous K. Moreover, K is highly mobile and cannot be tightly held by soils (Sawhney, 1972). Plant-cycled K is easily leached down to the deep units and/or water systems (e.g., river water or groundwater), and soil K is replenished by atmospheric K. Additional studies are needed to compare biological imprints on K budgets of soils and rivers.

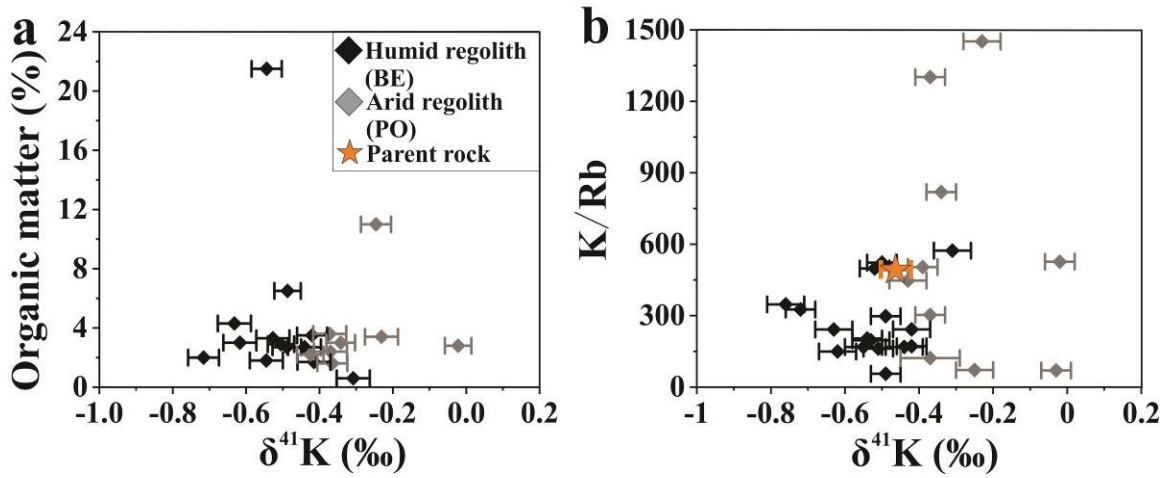

Figure 43. Interrelationships of $\delta^{41}K$ values with (a) organic matter content and (b) K/Rb ratio.

5.4. Summary and Implications

A consensus reported in previous studies is that K isotopic composition in solid weathering residuum would become lighter with more intensified weathering (S. Li et al., 2019; Chen et al., 2020; Huang et al., 2020; Teng et al., 2020). However, this study illustrates that K elemental and isotopic behaviors in the arid and humid regoliths in Hawai‘i are more complex than previously studied weathering profiles in humid, (sub)tropical environments (Chen et al., 2020; Teng et al., 2020). Two distinct weathering systems under contrasting climate conditions can be sketched: 1) the arid profile, where primary K phases dominate, and positive K isotopic fractionation from the basaltic substrate is mainly attributed to clay adsorption of ^{41}K; and (2) the humid profile, where secondary phases dominate, and negative isotopic fractionation is ascribed to clay incorporation of ^{39}K. Moreover, regolith K budget may be affected source mixing with atmospheric inputs and biological cycling dependent on climate. Given that, $\delta^{41}K$ signature in terrestrial records may be used as a proxy to interpret weathering processes and paleo-climate (humid vs. arid) based on the directionality of fractionation. Our work together with other previous studies (Santiago Ramos et al., 2018; S. Li et al., 2019, Chen et al., 2020; Teng et al., 2020; Li et al., 2021b), confirm large K isotopic fractionation occurs during water-rock interactions on Earth’s surfaces. Interpretation of portioning features of K and its isotopes via chemical weathering helps us to understand wide K isotopic variations in river waters (S. Li et al., 2019; Wang et al., 2021). In humid climate, strong downward eluviation results in more advanced weathering and higher output fluxes into adjacent river systems. Isotopically light K can be scavenged within clays, which produces large K fluxes with high $\delta^{41}K$ values. In addition, groundwater flows through deeper part of soil profiles, and apart from receiving ^{41}K-rich soil solutions from infiltration. The output of isotopically heavier K is consistent with the scenario

outlined by S. Li et al. (2019) for the negative correlation between $\delta^{41}K$ in river dissolved loads and the indices of weathering intensity by corresponding sediments. In comparison, occasional wetting events follows by rapid evapotranspiration in arid conditions, which largely limits deep water K fluxes and runoffs (Hsieh et al. 1998). Although up to ~70% of K in global rivers are expected to be cycled by plants (Chaudhuri et al., 2007), we suggest that biological contribution to Hawaiian riverine $\delta^{41}K$ is minor. The process would produce negative isotope shifts, which is not the case in our river samples (0.03-0.15‰, Table 20) and reported data (Wang et al., 2021). In addition, marine influence on river K budget is probably minor because more basaltic-like $^{87}Sr/^{86}Sr$ in river water (Table 20). River water reported and in previous studies has overall heavy isotopic signals, indicating that clay K incorporation is the main contributor to high $\delta^{41}K$ in rivers. However, studies on riverine $\delta^{41}K$ variations dependent on distance, seasons, and vegetation are needed. As for the fate of long-term stable K reservoirs, clays in sediments and regoliths are key ^{39}K pools vital for balancing ocean sinks and hydrothermal inputs (Parendo et al., 2017; S. Li et al., 2019; Teng et al., 2020; Hu et al., 2020; Santiago Ramos et al., 2020).

6. Conclusions

The element, phase and isotopic compositions of K in two regoliths developed on basalt weathering profiles in humid and arid sites are reported. Main conclusions are summarized here:

1. The humid regolith is heavily weathered and has K isotopic composition (-0.76 to -0.31‰) similar to or lighter than the parent rock (-0.48 ‰). This indicates the preferential incorporation of ^{39}K into clays, releasing ^{41}K into river waters (0.03 to 0.06‰). By contrast, the arid regolith is less weathered and has K isotopic composition (-0.39 to -0.02‰) heavier than the basalt, which is mainly caused by clay adsorption favorable for ^{41}K in alkaline conditions and marine aerosols.

2. The relatively narrow $\delta^{41}K$ range from -0.62 to -0.49‰ in humid shallow regolith (<1 m) reflects long-term eolian dust addition with crustal K composition (~ -0.44‰). In comparison, a wide $\delta^{41}K$ range (-0.43 to -0.03‰) in arid shallow regolith mainly results from clay sorption with minor eolian impacts. The imprints of rainfall and marine aerosols are recorded in the deep units.

3. Kaolin and illite are dominant secondary K hosts in the regolith. Kaolin group minerals are a long-neglected sink for K, driving the partitioning of isotopically light K into weathered solids. Although illite is an important sink of K, it is sourced from eolian origins with crust $\delta^{41}K$ signals.

4. Plant imprints on soil K pools are negligible in both sites, potentially ascribing to masking effects of atmospheric addition, poor preservation due to rapid leaching, and/or low plant covers.

5. Clays are not necessarily a universal reservoir for light K depending on climate conditions, making $\delta^{41}K$ signals in terrestrial archives a powerful tracer of weathering processes and climate.

CHAPTER 8: POTASSIUM ISOTOPIC FRACTIONATION IN A HUMID AND ANA ARID SOIL-PLANT SYSTEM IN HAWAI‘I

This chapter is published as: Li, W., Liu, X., M., Hu, Y., Teng, F. Z., Hu, Y. F., Oliver, A. Chadwick (2021) Potassium isotopic fractionation in a humid and an arid soil-plant system in Hawai‘i, Geoderma. 400(15), 115219.

1. Introduction

Vegetation influences the K biogeochemical cycle by enhancing its weathering release, biological uptake, and bio-cycling (Alexandre et al., 1997; Song et al., 2012). Potassium plays an important role in metabolic and physiological processes during plant growth and development, such as photosynthesis, enzyme activation and osmoregulation (Shabala, 2003; White and Karley, 2010). Plant roots can take up K from soil solution via mass flow during transpiration. Soil solution (bioavailable pool) K is supplied via (i) leaching from the canopy and stem by rainwater; (ii) release from decaying organic materials; (iii) mineral weathering; (iv) dry deposition of K-containing aerosols on plant outer surfaces and lateral wash-off; and (v) wet deposition of K-bearing rainwater particularly for studied Hawaiian Islands (Chadwick et al., 1999; Holmqvist et al., 2003; Weis and Weis, 2004; Kayser and Isselstein, 2005; Tripler et al., 2006; Chaudhuri et al., 2007; Kopáček et al., 2009). For acidic, highly-weathered soils, long-term weathering of K-bearing minerals and leaching probably limits the availability of K, particularly on K-poor parent substrates (e.g., Tripler et al., 2006; Sardans and Peñuelas, 2015). Loss of soil K contributes up to ~70% of dissolved K in global rivers (Chaudhuri et al.,2007).

Plants fractionate stable isotopes in macronutrients as Ca and Mg and micronutrients like Cu, Fe, and Zn (e.g., Weiss et al., 2005; Guelke and Von Blanckenburg, 2007; Bolou-Bi et al., 2010; Caldelas et al., 2011; Cobert et al., 2011; Jouvin et al., 2012; Schmitt et al., 2013; Christensen et al., 2018). The stable K isotope ratio ($^{41}K/^{39}K$) has been measured in extraterrestrial silicates (Humayun and Clayton, 1995), terrestrial rocks and lunar soils (Humayun and Koeberl, 2004), barley plants (Becker et al., 2008), and animals including bioproducts (Murphy et al., 2002). However, distinguishing K isotopic fractionation in natural soil-plant systems has relied on laborious isotope spiking treatment to reach the required analytical precision. Recent advances in analytical methods using multi-collector inductively coupled plasma mass spectrometry (MC-ICP-MS) allows for high-precision measurement (optimal 2 S.D. better than 0.06‰) of stable K isotope ratios (expressed in a δ notation, per-mille) to determine K isotopic fractionation produced by Earth's surface processes (e.g., W. Li et al., 2016; Morgan et al., 2018; Hu et al., 2018; Chen et al., 2019; X. Li et al., 2020; Moynier et al., 2021).

Stable K isotopes are fractionated during chemical weathering and biological cycling (e.g., Santiago Ramos et al., 2018; S. Li et al., 2019; Chen et al., 2020; Huang et al., 2020; Teng et al., 2020; Li et al., 2021a; Li et al., 2021b). Considerable K isotopic fractionation between plants and igneous rocks (taken as the K sources) ($\Delta^{41}K_{Plant\text{-}Rock}$) of ~0.8‰ was reported in Li et al. (2017), suggesting that terrestrial plants mostly prefer isotopically light K; however this interpretation is equivocal because the source of plant K was not reported. Recently, Morgan et al. (2018) documented isotopically heavier K in commercial banana fruits ($\Delta^{41}K_{Plant\text{-}Seawater}$~0.4‰) and lighter K in potato tuber ($\Delta^{41}K_{Plant\text{-}Seawater}$~0.1‰), in comparison with the modern seawater (homogeneous $\delta^{41}K$ ~ 0.14‰, Hille et al., 2019; Wang et al., 2020). Such a comparison with seawater is used in this instance because K fertilizers are often produced by

marine evaporates (Barker and Pilbeam, 2016; Li, 2017). By contrast, Christensen et al. (2018) reported partitioning of light K isotopes ($\Delta^{41}K_{Source\text{-}Plant}$ up to 1.67‰) into different types of crops (soybean, rice, and wheat) from cultured media in hydroponic experiments. So far, few plant species have been investigated, and we know little about the mechanisms of K isotopic fractionation in terrestrial ecosystems.

In this study, we investigate K speciation and K isotopic composition in trees (*Macadamia integrifolia* Maiden & Betche; *Prosopis chilensis* (Mol.) Stuntz) and grasses (*Pennisetum setaceum* (Forssk.) Chiov.; *Cenchrus ciliaris* L.) sampled from a humid and an arid soil-plant system in Hawai‘i. We determine the variations in soil-root and intra-plant K isotopic fractionation and evaluate the controlling mechanism. Our aim is to understand K isotopic fractionation in two natural soil-plant systems by measuring the isotopic composition of soils and plant tissues. Furthermore we evaluate the location of K in plant tissues by using synchrotron measurements to model the immediate chemical environment associated with plant K.

2. Geology and Materials

Kohala Mountain is the northwestern-most and the oldest volcano making up the Island of Hawai‘i (McDougall, 1964). It has a strong windward-leeward contrast in rainfall, which is useful for evaluating climatic influences on chemical weathering (Chadwick et al., 2003). Two chemically distinct lavas are exposed on Kohala Mountain: 1) the Pololū lava that is composed mainly of tholeiitic basalts ~350 ka in age, and 2) the Hāwī lava that forms an alkalic cap over the central region of the mountain ~150 ka in age (Spengler and Garcia, 1988; Chadwick et al., 2003). The ages of the regoliths are difficult to constrain, and we considered the radiometric age of the lava flows to be equivalent to the duration of silicate weathering because the constructional surface of lava flows was minimally eroded.

We sampled two sites receiving different mean annual precipitation (MAP) on the Pololū substrate, which were originally sampled by Goodfellow et al. (2014). Each site supports plant species introduced for commercial purposes. Specifically, the humid site (BE, forest) is located at the intersection of Highway 270 and Iole road (Iole Ahupua'a) (Location: N20.2288, W-155.7896; MAP of 1730±57 $mm \cdot a^{-1}$), densely covered with pasture grasses and macadamia trees. The arid site (PO, grassland) is located on Highway 270 between Mahukona and Kaiwaihae in the Kaiholena Ahupua'a (Location: N20.1357, W-155.8859; MAP of 385±53 $mm \cdot a^{-1}$) and supports buffel-grass and mesquite.

Mean annual rainfall data are derived from the University of Hawai'i's digital climate map (Giambelluca et al., 2013). In response to local climate, the soil properties of the two sites differ in terms of weathering depth and leaching intensity but are similar in mineralogy assemblage except that the arid site exhibits development of a calcareous layer (calcite and dolomite) at ~1-m depth (Capo et al., 2000; Goodfellow et al.,2014). We collected the following plant species: *M. integrifolia* (Macadamia nut tree) and *P. setaceum* (Fountain grass) in the humid site, and *P. chilensis* (Chilean mesquite tree) and *C. ciliaris* (Buffel-grass) in the arid site. Although we have no direct knowledge of fertilizer additions to the sampling sites, local experts told us that K fertilization was not been common on lands similar to the sparsely vegetated dry site or on the macademia nut orchard on the humid site. In addition, we found no direct evidence of anomalous K addition (e.g., elevated K concentrations) in soils based on published elemental and Sr isotopic data in soil NH_4Ac extracts (exchangeable pools) in Hawai'i (Whipkey et al., 2000; Chadwick et al. 2009; Li et al., 2020a). Therefore, anthropogenic impacts should be minor. Based on soil features as color, mineralogy, and gains (losses) of elements (Li et al., 2020a), we separated the soil into two soil depth layers (the topsoil, 0-30 cm; the subsoil, 30-100 cm)—the

shallower layer corresponds to stronger biological influences and the deeper one is more strongly influenced by the basalt substrate (see Ziegler et al., 2005; Vitousek and Chadwick, 2013). In sum, three sets of samples were collected from the field, and details are given below.

The first suite of samples—designed to investigate potential K sources—includes parent basalt substrate (Pololū basalts) and the more recent Hāwī tephra that may have been incorporated into the older Pololū soils (i.e., collectively called "basaltic substrate"). Since previous studies demonstrate contribution of Asian dust to Hawaiian soil cation budgets (e.g., Chadwick et al., 1999; Kurtz et al., 2001; Li et al., 2020a; Vogel et al. 2021), we consider K from that source as well. A likely source for Asian dust is the Chinese Loess Plateau (CLP) (An et al., 1990), so we tentatively use data from a Chinese loess sample JX-1 (Huang et al., 2020) to characterize possible K contribution from this source. We use the term "mineral aerosol" instead of "dust" for this long-distance transported material.

The second suite of samples was designed to investigate the interaction among soil-plant systems. It includes rainwater (filtered) collected during separate rainfall events, bulk soils (<2mm size, the topsoil and subsoil), and soil saturation extracts (see Methodology for details). Biologically available K in soil can be extracted using this method. Soil waters were not collected because it is hard to use lysimeters for soil water collection in the arid site, and the installation probably disturbs soil integrity and causes preferential flow pathway resulting in perturbed, unrepresentative infiltration of porewater (Uhlig et al., 2020). Rainfall samples were collected with a plastic funnel inserted into a 2-L Erlenmeyer flask (acid-washed using 1M HCl followed by rinses with deionized water). The humid soil was classified as very-fine, parasesquic, isohyperthermic Typic Humustepts, and the arid soil was classified as fine, mixed, semiactive, isohyperthermic Sodic Haplocambids (Soil Survey Staff, 2014). The

physicochemical properties of the two soils were reported in Li et al. (2020a). Coarse particulate organic matter and root residues were manually removed during soil sampling and we did not characterize organically bound K separately from the <2-mm soil fraction.

The third suite of samples was used to assess K speciation and its isotopic composition within plant tissues. Samples include roots, stems, bark, aboveground shoots (a sum of stems and leaves), reproductive tissues (seeds and flowers), and leaves (fresh and dead leaves attached to grass stems or young branches) sampled during October 2018 and July 2019 (Table 23). Individual specimens of grasses (*P. setaceum* and *C. ciliaris*) were sampled from the field and separated into reproductive tissues, leaves (live and dead), stems, and roots (without distinguishing between fine and coarse roots). The grass roots were partially collected. Tissues of trees (*M. integrifolia* and *P. chilensis*) were collected. Specifically, tree bark was sampled from small stems near the end of a branch at the height of ~1.5 m, and tree leaves were sampled from branches within accessible height (~1.5 to 2 m). We note that tissues were not collected along the entire height of the tree. The root tissue and the cellulose-rich part of the heartwood were not collected as a part of this reconnaissance effort. Dead leaves were sampled from standing plants to avoid direct contact with soils to preclude K transfer from the K-rich soil to K-poor litter materials.

Collected tissues were rinsed using deionized water (Millipore^{TM}, 18.2 MΩ·cm) and then freeze-dried using liquid N_2 treatments at the Phytotron, North Carolina State University. Tissues of the same plant type were homogeneously mixed to obtain the representative sample. Samples were powdered in a mortar with a pestle and weighted before analysis.

3. Methodology

3.1. Extraction, digestion, and element analysis

Soil K residing in different chemically defined pools was determined through sequential treatment with progressively harsher chemical extractants. Four individual K fractions were extracted, including water-soluble K, K adsorbed onto clay surfaces, K interlayered within mica/illite (and/or halloysite), and K occluded within non-swelling silicate minerals (Cox et al.,1999). Soil water-soluble and exchangeable K were extracted using deionized water and 0.1 M NH_4Ac, respectively. Interlayered K hosted into illite/mica and halloysite was quantified by sodium tetra-phenyl borate ($NaBPh_4$) solutions (a mixture of 0.25 $mol \cdot L^{-1}$ $NaBPh_4$ + 1.7 $mol \cdot L^{-1}$ NaCl + 0.01 $mol \cdot L^{-1}$ EDTA, Cox et al.,1999). Soil occluded K was calculated by subtracting above three K fractions from soil total K pool. In addition, soil saturation extraction has been applied, and we used the $\delta^{41}K$ of soil saturation extracts to approximate the $\delta^{41}K$ of bioavailable pools. The extracts were obtained by mixing dry soil samples with deionized water until forming saturated pastes in equilibration and then treated with vacuum-filtration extraction (Soil Survey Laboratory Staff, 1992). Saturated paste extraction of soil is a standard chemistry procedure that produces more comparable results than water-soluble K extraction procedures, and is in the same state of equilibrium with respect to soil phases as soil solutions residing in soil during unsaturated stages (as opposed to macropore flow) (Burt, 1995). Hence, it likely reflects the chemistry properties of porewater for biological usage. Bioavailable K was derived from relatively concentrated basaltic substrate initially, but with continued weathering and rapid K leaching may reflect increasing contributions of mineral aerosols derived from dust accretion and relatively dilute marine aerosols over time (Chadwick et al. 1999).

To extract K adsorbed on outer root surfaces (including root extracellular excretion), roots were soaked in ice-cold 1 M HCl (5°C, 40 $g \cdot L^{-1}$) for 3 min (Chaignon et al., 2002; Aucour et al., 2015). Besides extraction, fresh root tissues were digested using a mixture of 6 mL

concentrated HNO_3 (sub-boiled distilled) and 2 mL 30% H_2O_2 in Teflon beakers >150 °C. Digested residues were evaporated and subsequently re-dissolved in 5 mL 2% HNO_3 solution for chemical analyses (Tang et al., 2016). Soils were digested following a HCl-HNO_3-HF protocol in Li et al. (2019). Residues were converted to a nitric form by adding 2% HNO_3 solutions and measured using a quadrupole ICP-MS (Q-ICP-MS, Agilent™ 7900) at the University of North Carolina at Chapel Hill. Element analysis was calibrated by multi-elemental standards of known concentrations. Internal standards, including Be, Ge, Rh, In, Ir, and Bi, were used for instrument drift correction. Geostandards BHVO-2, GSP-2, SBC-1, and ERMBC382 were used to evaluate the accuracy and reproducibility (Table A1). External analytical accuracy less than 10% (2 S.D.) was achieved, and total yields (measured date relative to reported data) were satisfactory (100 ± 5%).

3.2. K column chemistry

An aliquot of digested sample was evaporated to dryness and refluxed using 2 mL 0.7 M HNO_3 before loading onto the columns. Potassium isotopic compositions were measured after column purification, following the two-step purification approach reported in Chen et al. (2019). A first column was filled with 17 mL AG50-X8 cation-exchange resin (200-400 mesh, Bio-Rad™) and conditioned in 0.7 M HNO_3. Eluted K fractions were then collected after most of the matrix elements being eluted. Then collected K elution was evaporated until dryness on the hotplate and re-dissolved in 1 mL 0.5 M HNO_3 solution for the second column. The second column was filled with 2.4 mL AG50-X8 cation-exchange resin (200-400 mesh, Bio-Rad™) and conditioned in 0.5 M HNO_3. After chromatographic processes, the fractions recovered before and after the collected volumes were checked for K, Na, Al, Fe, Rb, and Ti on the Agilent™ 7900 Q-ICP-MS. Collected fractions of K reached ~ 100% yields to exclude possible isotopic

fractionation in ion-exchange chromatography. The mass ratios of a sum of all other matrix elements to K were measured to ensure a sum of matrix elements is below 2% of total K to reduce potential matrix effects on isotope analysis (Chen et al., 2019). If necessary, chromatographic processes were repeated to achieve acceptable matrix/K ratios for instrumental analysis. Column blanks were at least three orders of magnitude lower than the K mass used in the analytes. Procedural blanks (<5 ng) are negligible relative to total K mass (10–14 μg) used for instrumental analysis.

3.3. K isotope analysis

For K isotope analysis using MC-ICP-MS, samples and bracketing standards were diluted using 3% HNO_3 to a K concentration of 5 to 8 $mg \cdot L^{-1}$, corresponding to ^{39}K signals of 5 V to 11 V. The isotopic compositions were measured using the Nu Plasma II HR- MC-ICP-MS at the Isotope Laboratory, University of Washington, Seattle. After digestion, samples were converted into a nitric form using 3% HNO_3 and diluted to match a K concentration of 2 $mg \cdot L^{-1}$. Mass spectrometry and data processing were performed using established protocols (Hu et al., 2018; Xu et al., 2019). In brief, K isotopic ratios were measured with a high-resolution mode of "cool plasma" (low RF power from 750 to 850W) to suppress interferences from residual and isobaric ($^{40}Ar^{1}H^{+}$ on $^{41}K^{+}$ and $^{38}Ar^{1}H^{+}$ on $^{39}K^{+}$) argides. We used a dry plasma introduction system involving a CETAC Aridus II desolvation nebulizer system, a Savillex™ PFA spray chamber, and a C-Flow PFA microconcentric nebulizer, to reduce argide formation and increase sensitivity. On-peak zero for K mass 41 ranges between -8×10^{-4} and -1.5×10^{-3} V, approximating -3×10^{-3} V for mass 39. These signals are negligible compared to the signal produced by samples (5 to 11 V). A standard bracketing method with over 5 cycles was adopted to correct instrumental mass bias. The K isotopic compositions were reported relative to NIST SRM 3141a

with a δ notation (δ^{41}K, ‰) (Teng et al., 2017). The precision better than 0.12‰ was achieved based on repeated analyses of geostandards over a six-month period (2 S.D., Hu et al., 2018).

$$\delta^{41}\mathrm{K}\ (‰) = \left\{\frac{(^{41}\mathrm{K}/^{39}\mathrm{K})_{\mathrm{sample}}}{(^{41}\mathrm{K}/^{39}\mathrm{K})_{\mathrm{NIST\ SRM\ 3141a}}} - 1\right\} \times 1000 \qquad (34)$$

The "S.D." denotes the standard deviation over the analytical cycle of the sample. Several samples were measured twice via two separate analytical cycles, and averaged data are listed in Table A2. Two certified USGS standards (BHVO-2 and GSP-2) were processed in the same strategy and measured alongside samples for quality control and reproducibility evaluation. Potential systematic deviations among different laboratories for K isotope measurements could be alleviated by analyzing same reference materials (BHVO-2 and GSP-2). This study reports identical K isotope ratios of terrestrial igneous rocks within the analytical uncertainties, BHVO-2 of -0.40 ± 0.06‰ (2 S.D.) (a literature compilation from -0.52 to -0.40‰) and GSP-2 of -0.46 ± 0.09‰ (2 S.D.) (a literature compilation from -0.50 to -0.45‰). Errors in the text reported as 2 S.D. are similar to or smaller than the reproducibility of in-house standards. Without direct analysis, the isotopic compositions of the bulk plant and shoot were calculated by mass balance:

$$\delta^{41}\mathrm{K}_{Bulk\ or\ shoot}\ (‰) = \frac{\sum_i mC_i\delta^{41}K_i}{\sum mC_i} \qquad (35)$$

Where *m* represents the weight of dry mass (mg), *c*: K concentration (mg·L^{-1}), and *i*: tissues of the bulk plant (root + stem + leaf + reproductive tissues) or shoot (stem + leaf).

3.4. K X-ray absorption analysis

The X-ray absorption fine structure (XAFS) spectra of K were collected for K references, powdered Hawaiian soils, and powdered plant tissues (frozen dried) at Soft X-ray Micro-Characterization Beamline (SXRMB, 06B1-1), Canadian Light Source (CLS, Saskatoon, Canada) under room temperature in the vacuum chamber to reduce beam attenuation. The beamline was equipped with Si drift fluorescence detectors and was monochromated with

diffraction from InSb (111) and Si (111) double-crystals. In the photon energy range of K *K*-edge analysis (3550 to 4000 eV), the photon flux is about 2×10^{10} photon s^{-1} (Li et al., 2020b), and the beam size at the target is ~7mm×1mm (Hu et al., 2010). The *K*-edge XAFS spectra of ionic K^+ in water (KCl solutions) were collected at the beamline 4-3 of the Stanford Synchrotron Radiation Lightsource (SSRL) using a fluorescence mode. This beamline was equipped with a 7-element fluorescence drift detector, an ionization chamber, and PIPS/Lytle detectors. Within the photon energy range of K *K*-edge analysis (3550 to 4000 eV), the photon flux is ~2×10^{10} photon s^{-1} at 100 mA, and the spot size is ~7 mm×1 mm. Powdered samples were evenly spread as a thin film on double-sided K-free C tape adhered to a Cu stick before being placed in a vacuum chamber. Radiation damage was negligible, given satisfactory reproducibility. Two to four XAFS spectra were averaged to enhance signal-to-noise ratios in Athena software (Ravel and Newville, 2005).

The XAFS spectral changes are sensitive to the coordination environment of the element of interest, so they could help with phase identification. Spectral differences in K *K*-edge XAFS spectra of two references (i.e., K-pectate and ionic K^+) and plant samples could be recognized (Fig. 44). The reason for this reference selection is that 1) pectate salts are the most well-known compounds responsible for K isotopic fractionation within plants, and 2) K is almost exclusively present in its ionic form within plant tissues (Bagard et al., 2013; Barker and Pilbeam, 2016). Fresh leaves exhibit a pronounced major peak at ~3616 eV, with slightly positive offsets in the major peak by ~1 eV, in comparison with other tissues (Fig. 44a). Such a peak shift is observed in K XAFS spectra, corresponding to the spectral features of K-pectate and ionic K^+ (Fig. 44b). Nevertheless, the variations in photo energy and the k-space spectra are potentially affected by energy calibration. Another important change is the post-edge intensity, which can be identified

by colored regions in Fig. 44 and is driven by electron gain or loss in the density of empty state in K (electron movement).

The atomic environments of K in fresh leaves and roots are very different from K phases preserved in stems, bark, and dead leaves. The differences could be explained by the mixing of two components – K-pectate and ionic K^+. According to the Natoli's rule – the energy dependence on average ligand shell radius (Natoli, 1984), variations in spectra highlights the decrease in the K-O distance in fresh leaves in comparison with remaining tissues. An absence of variations in the shape of K *K*-edge XANES spectra demonstrates that the coordination numbers of K atoms do not vary between K references. Compared to ionic K^+, fewer empty orbital states of K atoms in K-pectate ($RCOO^-$) exist with a lower electron donation capacity due to the electron reception of the O *2p*-orbital, presumably reflecting a lower coordination number of K atoms in K-pectate. Moreover, a displacement of major energy peaks in the K XANES spectra between tissues can be identified (Fig. 1).

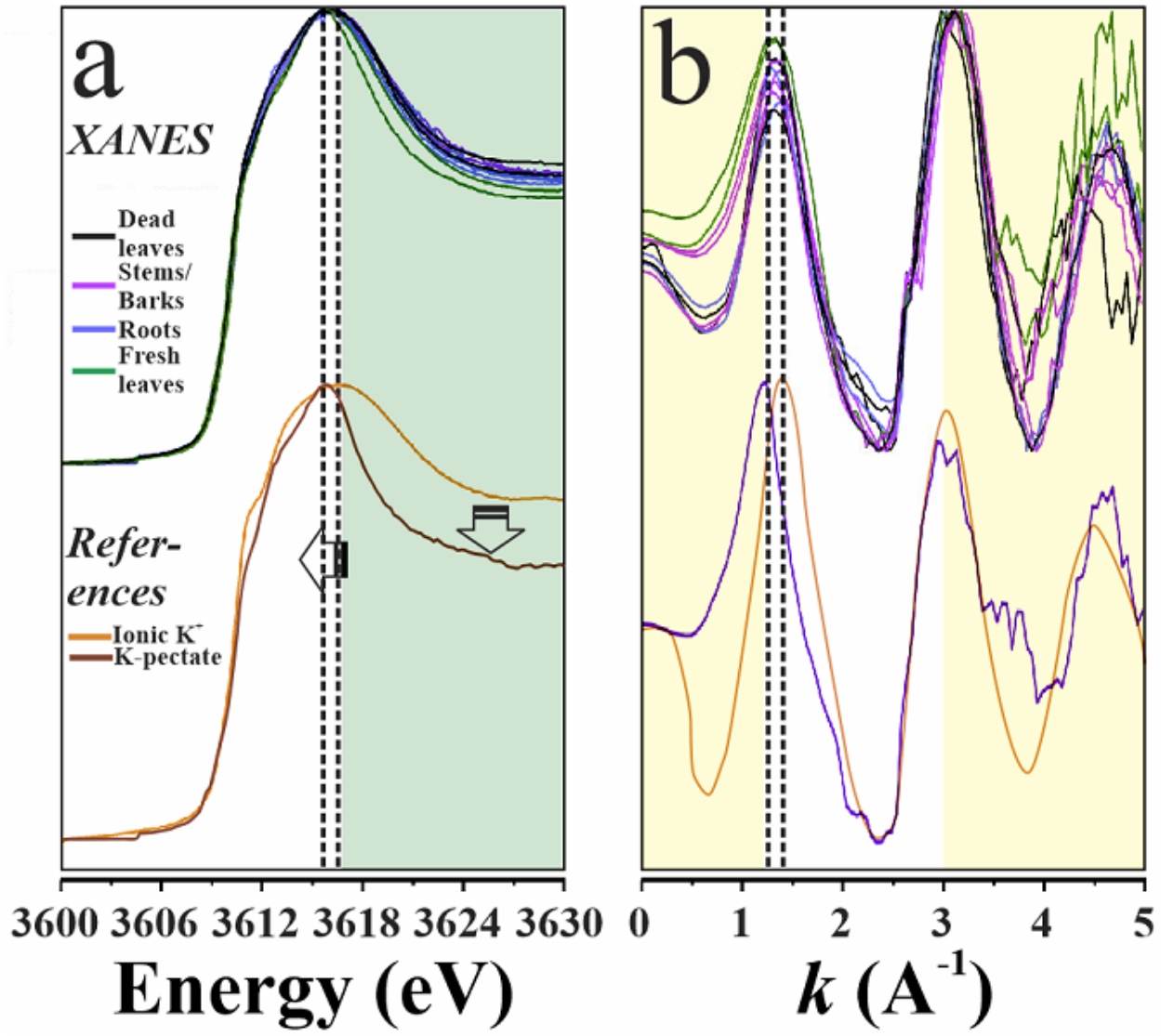

Figure 44. K *K*-edge XAFS data including (a) XANES and (b) XAFS spectra in a k space of K references and plant tissues (leaves, stems, bark, and roots).

References include K-pectate and ionic K+ (in water). The K XANES spectra of ionic K+ were collected in this study, and the XAFS spectra of ionic K+ obtained at 300 Kelvin refers to Glezakou et al. (2006). The dashed lines show slight peak shifts, the green area shows the discrepancy in the post-edge, and the yellow regions highlight changes linked to atomic coordination.

There are two common methods for quantitative identification, i.e., spectral fitting of X-ray Absorption Near-Edge Structure (XANES, a part of XAFS near the absorption edge) and full K *K*-edge XAFS spectra. In this study, fitting was performed using K-pectate and ionic K^+ spectra (Fig. 45). Only K *K*-edge XANES spectra were used for linear combination fitting since the full XAFS spectrum of ionic K was not obtained at the beamline. We used an R-factor to evaluate the goodness-of-fit. The significance between fits was determined using the Hamilton test ($p<0.05$; Calvin, 2013) with a few independent data points calculated after normalization to a sum of 100%, estimated as data range divided by the core-hole lifetime broadening. Fits were accepted when a sum of percentages reached 100±10%.

4. Results

4.1. K in plant tissues

For grass tissues, the K concentration followed a sequence of fresh leaves > stems ≈ reproductive tissues (flowers and seeds) > roots > dead leaves (Table 23). Aboveground shoots (a sum of stems and leaves) accumulated larger amounts of K than roots by ~10 $g \cdot kg^{-1}$ in the humid site and ~5 $g \cdot kg^{-1}$ in the arid site. Grasses (*P. Setaceum*) in the humid site showed higher tissue K concentrations compared with grasses (*C. Ciliaris*) in the arid site, by up to 15.3 $g \cdot kg^{-1}$ in fresh leaves (Fig. 46).

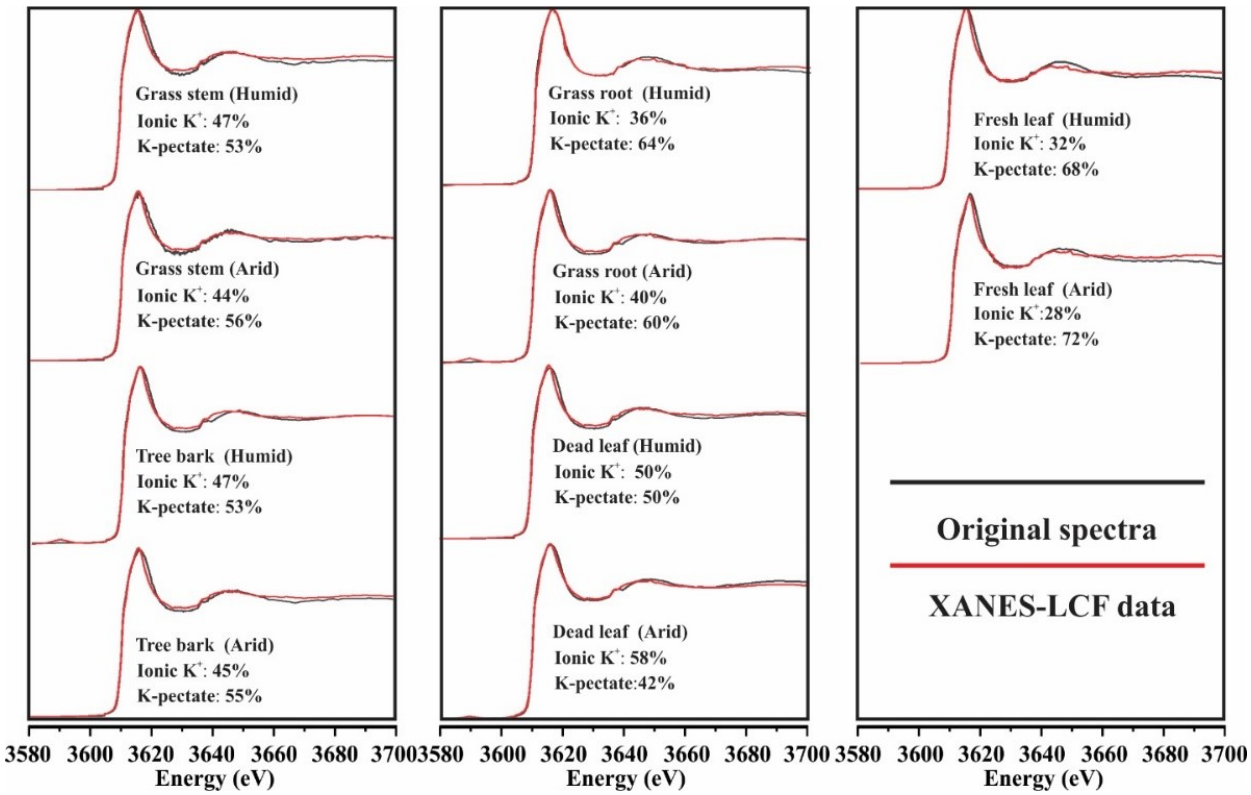

Figure 45. Potassium *K*-edge XANES spectra of plant tissues from the humid (BE) and arid (PO) sites.

The XANES spectra were subjected to linear combination fitting (XANES-LCF) based on reference compounds (i.e., ionic K^+ and K-pectate, data from Fig. 38). The original spectra and LCF curves are marked in black and red, respectively.

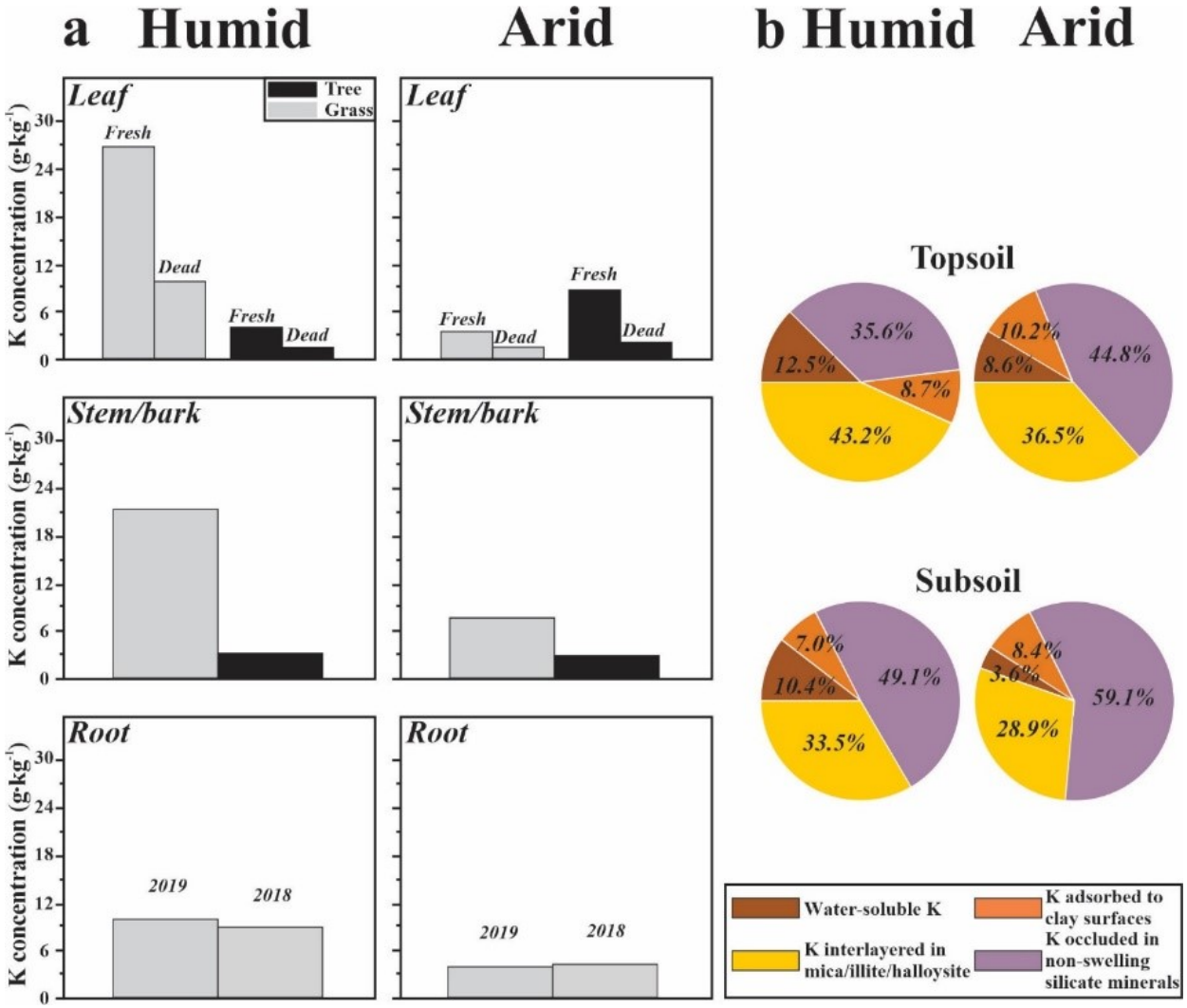

Figure 46. Potassium concentrations in plant tissues and chemically defined soil fractions in the arid and humid sites in Hawai‘i.

(a) The K concentrations in the tissues of trees and grasses (*M. integrifolia* and *P. setaceum*) at the humid site, and the tissues of trees and grasses (*P. chilensis* and *C. ciliaris*) at the arid site. (b) The fractional distribution of K in the topsoil (0-30 cm) and subsoil (30-100 cm) at the humid and arid sites, respectively.

Using averaged $\delta^{41}K$ of soil saturation extracts to approximate the $\delta^{41}K$ of soil bioavailable pools, all grass tissues showed negative isotopic shifts from soil bioavailable pools, with $\Delta^{41}K_{Plant\text{-}Source}$ of -0.89 to -0.25‰ (humid) and -0.86 to -0.04‰ (arid) Fig. 47). Isotopically light K was enriched in roots, showing $\Delta^{41}K_{Root\text{-}Source}$ from -0.40 to -0.36‰ (*P. Setaceum*, humid) and -0.29 to -0.26‰ (*C. Ciliaris*, arid). Tissue $\delta^{41}K$ data followed an order of fresh leaves > roots > stems > reproductive tissues > dead leaves (Fig. 48). Aboveground shoots (a sum of stems and leaves) were isotopically comparable to fresh leaves. The treatment of roots using HCl, which is assumed to extract K on the exterior of the roots, made up of 34% (humid) and 62% (arid) K in roots. The extraction provided $\delta^{41}K$ values of 0.29±0.07‰ (humid) and 0.61±0.07‰ (arid), higher than soil bioavailable pools.

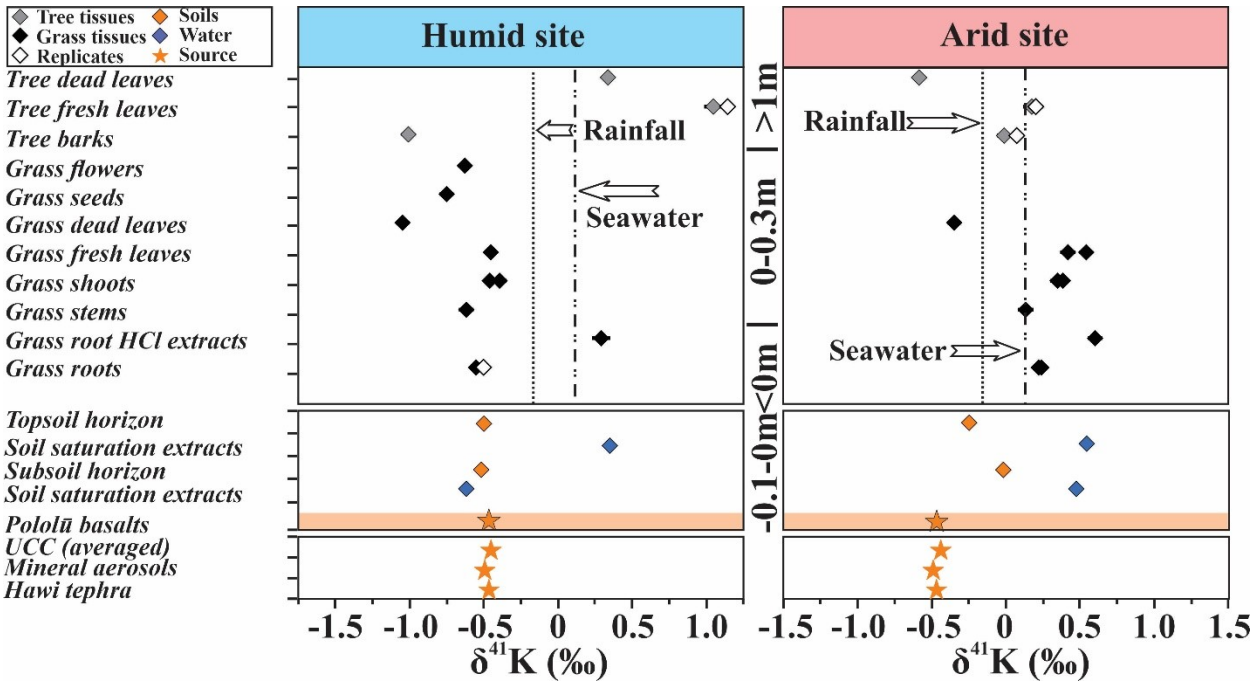

Figure 47. The K isotopic compositions of tissue in trees and grasses (*M. integrifolia* and *P. setaceum*) in the humid site, and trees and grasses (*P. chilensis* and *C. ciliaris*) in the arid site, respectively (Table 23).

Hollow diamonds represent duplicate analysis of tissue $\delta^{41}K$. Measured $\delta^{41}K$ in bulk soils are symbolized by orange diamonds. The $\delta^{41}K$ values of the basaltic substrate (Pololū basalt and Hāwī tephra), the upper continent crust (UCC, Huang et al., 2020), and dust-sourced mineral aerosols (Chinese loess JX-1, Huang et al., 2020) are plotted for comparison. The $\delta^{41}K$ values of rainwater and seawater (Hille et al., 2019; Wang et al., 2020) are marked using dashed and dotted lines, respectively. The analytical uncertainties (2 S.D.) of $\delta^{41}K$ are smaller than the symbol sizes.

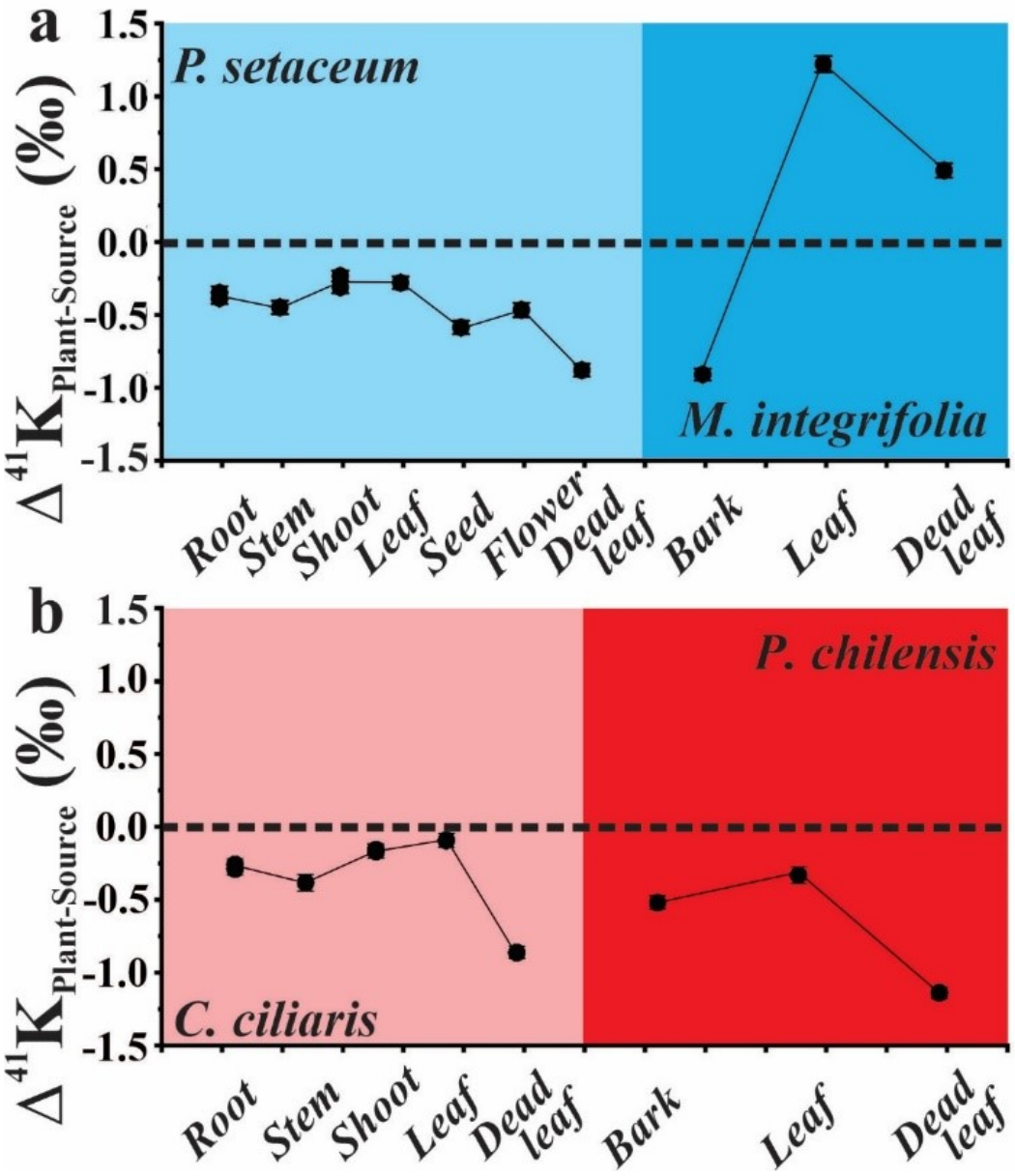

Figure 48. The K isotopic compositions of plant tissues in comparison with averaged $\delta^{41}K$ values of soil saturation extracts (taken as soil bioavailable pools and normalized to 0‰) from the (a) humid site and (b) arid site.

Isotopically light K is preferentially taken up by grassroots from soil bioavailable pools. For intra-plant K isotopic fractionation, the stem, seed, and flower of grasses are enriched in isotopically lighter K. Heavier K isotopes are preferentially accumulated in fresh leaves, while lighter K isotopes are enriched in dead leaves of trees and grasses in the study area.

Table 23. A summary of sampling information including locations, species and K chemistry.

Type	Sample locations, types, and species	No.	Height above surface (cm)	K ($g \cdot kg^{-1}$)	$\delta^{41}K$ (‰)	2S.D. (‰)	N	$\Delta^{41}K_{Plant-Source}$ (‰)
Water	Filtered rainwater (2018 October)	W-1	n.d.	n.d.	-0.21	0.11	7	n.d.
	Filtered rainwater (2019 July)	W-2	n.d.	n.d.	-0.16	0.07	71	n.d.
	Hāwī tephra	W-3	n.d.	8.4	-0.48	0.10	6	n.d.
	Pololū basalt	W-4	n.d.	8.1	-0.48	0.04	7	n.d.
Trees	Humid *M. integrifolia* fresh leaf (2019 July)	B-1	150	4.9	1.07	0.10	5	1.22
	Replicate	B-1	150	n.d.	1.15	0.09	5	1.30
	Averaged value	B-1	150	4.0	1.11	0.10	5	1.26
	Humid *M. integrifolia* dead leaf (2019 July)	B-2	150	1.6	0.34	0.07	5	0.49
	Humid *M. integrifolia* bark (2019 July)	B-3	140	3.3	-1.06	0.06	7	-0.92
Grasses	Humid *P. setaceum* seed (2018 October)	B-4	30	20.1	-0.74	0.07	5	-0.60
	Humid *P. setaceum* flower (2018 October)	B-5	30	18.3	-0.62	0.05	7	-0.48
	Humid *P. setaceum* fresh leaf (2019 July)	B-6	10 - 30	26.8	-0.43	0.06	5	-0.29
	Humid *P. setaceum* fresh shoot (2019 July)	B-7	0 - 30	25.8	-0.46	0.04	6	-0.32
	Humid *P. setaceum* fresh root (2018 October)	B-8	(-40) - 0	9.0	-0.5	0.07	7	-0.36
	Humid *P. setaceum* fresh shoot (2018 October)	B-9	0 - 30	24.3	-0.39	0.07	7	-0.25
	Humid *P. setaceum* dead leaf (2019 July)	B-10	10 - 30	2.0	-1.03	0.08	7	-0.89
	Humid *P. setaceum* stem (2019 July)	B-11	0 - 10	21.4	-0.6	0.07	5	-0.46
	Humid *P. setaceum* root (2019 July)	B-12	(-40) - 0	10.0	-0.54	0.07	7	-0.40
	Humid *P. setaceum* root HCl extracts (2019 July)	B-13	(-40) - 0	n.d.	0.29	0.07	7	n.d.
Soil and extracts	Humid topsoil	B-14	(-30) - 0	28.7	-0.49	0.06	7	n.d.
	Soil saturation extracts	B-15	(-30) - 0	n.d.	0.34	0.08	6	n.d.
	Humid subsoil	B-16	(-100) - (-30)	8.7	-0.54	0.07	6	n.d.
	Soil saturation extracts	B-17	(-100) - (-30)	n.d.	-0.63	0.08	6	n.d.
Trees	Arid *P. chilensis* fresh leaf (2019 July)	P1	150	8.9	0.22	0.05	5	-0.29
	Replicate	P1	150	n.d.	0.20	0.05	5	-0.31
	Averaged value	P1	150	8.9	0.21	0.05	5	-0.30
	Arid *P. chilensis* dead leaf (2019 July)	P2	150	2.1	-0.63	0.06	7	-1.14
	Arid *P. chilensis* bark (2019 July)	P3	140	2.9	-0.01	0.06	7	-0.52
	Replicate	P3	140	n.d.	0.07	0.05	7	-0.44
	Averaged	P3	140	n.d.	0.03	0.05	7	-0.48
Grasses	Arid *C. ciliaris* fresh leaf (2019 July)	P4	10 - 30	11.5	0.41	0.05	5	-0.10
	Replicate	P4	10 - 30	n.d.	0.53	0.04	5	0.02
	Averaged value	P4	10 - 30	11.5	0.47	0.05	5	-0.04
	Arid *C. ciliaris* fresh shoot (2019 July)	P5	0 - 30	10.7	0.35	0.05	6	-0.16
	Arid *C. ciliaris* fresh root (2018 October)	P6	(-30) - 0	4.2	0.25	0.06	7	-0.26
	Arid *C. ciliaris* fresh shoot (2018 October)	P7	0 - 30	9.5	0.34	0.07	6	-0.17
	Arid *C. ciliaris* dead leaf (2019 July)	P8	10 - 30	1.5	-0.35	0.08	8	-0.86
	Arid *C. ciliaris* stem (2019 July)	P9	0 - 10	7.7	0.13	0.08	5	-0.38
	Arid *C. ciliaris* roots (2019 July)	P10	(-30) - 0	4.0	0.22	0.06	7	-0.29
	Arid *C. ciliaris* root HCl extracts (2019 July)	P11	(-30) - 0	n.d.	0.61	0.07	7	n.d.
Soil and extracts	Arid topsoil	P12	(-30) - 0	1.7	-0.14	0.06	6	n.d.
	Soil saturation extracts	P13	(-30) - 0	n.d.	0.54	0.10	6	n.d.
	Arid subsoil	P14	(-100) - (-30)	1.8	-0.24	0.07	6	n.d.
	Soil saturation extracts	P15	(-100) - (-30)	n.d.	0.48	0.08	6	n.d.

Note 1. K is translocated from soil pools to roots, between stem and leaves and then to dead leaves for tress and grasses, respectively. Note 2. The height below surface is marked using a negative value of the height above surface. Note 3. "n.d.": not determined. 2S.D.=two standard deviation; N=the number of analytical cycles. $\Delta^{41}K_{Plant-Source}$ value is calculated from $\delta^{41}K_{Plant}$ subtracted by averaged $\delta^{41}K_{Soil\ saturation\ extracts}$, which is the mean value of $\delta^{41}K_{Soil\ saturation\ extracts}$.

For tree tissues, the K concentration followed a sequence of fresh leaves > bark > dead leaves (Table 23). Fresh leaves of *M. integrifolia* in the humid site had lower concentrations of K compared with *P. chilensis* in the arid site by 4.9 $g \cdot kg^{-1}$.

Fresh leaves were isotopically heavier than bark and dead leaves in both sites. Similar to grass tissues, the lowest $\delta^{41}K_{Plant}$ value was found in dead leaves (Figs. 47-48), and the enrichment of lighter K isotopes in dead leaves occurred in parallel with the reduction in K concentration. All tree tissues in the arid site exhibited negative $\Delta^{41}K_{Plant\text{-}Source}$ values (-1.14 to -0.30‰), while tree tissues in the humid site showed both negative and positive K isotopic shifts from soil bioavailable pools (-0.92 to 1.26‰). In addition, the K isotopes in arid trees exhibited a smaller shift in $\Delta^{41}K_{Plant\text{-}Source}$ values than in humid trees.

The K-pectate and ionic K^+ in plants were identified by K *K*-edge XAFS spectra, based on spectral features (peak shifts and amplitudes, Fig. 44). According to XANES-LCF (Fig. 45), we quantified the following groups with distinct compositions of K-pectate and ionic K^+: (i) roots, (ii) stems (and bark), (iii) fresh leaves, and (iv) dead leaves. Grassroots and fresh leaves showed the highest proportions of K-pectate of 60-64% and 68-72%, respectively. Dead leaves exhibited the least proportions of K-pectate ranging from 42 to 50%. In grass stems, 53-56% of K was associated with pectate, and 44-47% of K presented as free ions. In tree bark, 53-55% of K was linked with pectate, and 45-47% of K existed as free ions.

4.2. K in soils and waters

The K concentrations in soils and waters in the humid site were different from the arid site (Table 23 and Fig. 46). At the humid site, the K concentration (28.7 $g \cdot kg^{-1}$) in the topsoil (0-30 cm) was higher than those of the subsoil (30-100 cm) (8.7 $g \cdot kg^{-1}$) and the basaltic substrate

(8.1 $g \cdot kg^{-1}$) (Table 23). The arid soil showed a reverse pattern in depth (1.7 $g \cdot kg^{-1}$ K in the topsoil and 1.8 $g \cdot kg^{-1}$ K in the subsoil).

The topsoil and subsoil in the humid site had comparable $\delta^{41}K$ values of -0.49±0.06‰ and -0.54±0.07‰, respectively. Soil $\delta^{41}K$ values in the humid site were comparable to those of the basaltic substrate (e.g., Pololū lava, -0.48±0.04‰; Hāwī tephra, -0.48±0.10‰) and atmospherically derived mineral aerosols (e.g., Chinese loess JX-1, -0.46±0.05‰) reported in Huang et al. (2020). The $\delta^{41}K$ values of the arid soil (-0.14±0.06‰, topsoil; -0.24±0.07‰, subsoil) were higher than those of the basaltic substrate and Asian-sourced mineral aerosols.

For chemically-defined fractions in the topsoil, most soil-hosted K (~36-59%) was fixed in occluded phases, and interlayered K made up ~29–43% soil K. Soil exchangeable K (clay adsorbed) and water-soluble K were relatively less important, accounting for ~7–10% and ~4–13% soil K, respectively (Fig. 46). A marked difference in $\delta^{41}K$ existed between the soil saturation extracts at the humid site (0.34±0.08‰, the topsoil; -0.63±0.08‰, the subsoil). In comparison, the $\delta^{41}K$ values of the soil saturation extracts at the arid site were identical (0.54±0.10‰, topsoil; 0.48±0.08‰, subsoil) within the analytical uncertainties. Based on field observation, the roots of trees and grasses were able to reach the bioavailable pool of the topsoil and subsoil. To derive a rough estimate of the K isotopic composition of soil bioavailable pool (source), we averaged the $\delta^{41}K$ values of soil extracts of the topsoil and subsoil (Bullen and Chadwick, 2016). According to this assumption, $\delta^{41}K$ values in soil bioavailable pools (averaged) were -0.15±0.08‰ and 0.51±0.09‰ in humid and arid sites, respectively. Rainwater samples had $\delta^{41}K$ values from -0.21±0.11 to -0.16±0.07‰.

5. Discussion

5.1. Intra-plant K isotopic fractionation

During intra-plant circulation, the maximum isotopic fractionations between roots, leaves, and stems (bark) exhibit $\Delta^{41}K$ values ranging from 0.82 to 2.17‰ for trees and 0.60 to 0.82‰ for grasses, respectively (Fig. 47). Therefore, intra-plant K isotopic fractionation is probably associated with ion-exchange processes along the transport pathway. Given the presence of K-pectate (Figs. 44-45), we infer that intra-plant K isotopic fractionation is linked to cation-exchange processes with the $RCOO^-$ groups in the cell walls of xylem tissues. It is known that isotopic fractionation in chromatographic processes results in preferential complexation of isotopically heavier K with cation-exchange resin (rich in $RCOO^-$ groups), producing large K isotopic fractionation up to 0.3‰ (Kawada et al., 1991; Xu et al., 2019). Accordingly, we anticipate that ion-exchange process during intra-plant circulation could induce heavier K isotopic compositions in roots and fresh leaves (rich in K-pectate) than stems (and bark) (rich in K^+) (Fig. 49). This pattern is consistent with the observation that stems (and bark) are depleted in heavier K isotopes compared to the soil extraction and thus have heavier K isotopic composition in fresh leaves and roots (Fig. 48). This trend is obvious for sampled grasses while less evident for trees, probably due to a limited number (N=2) of K *K*-edge XANES analysis of tree tissues, so further study is needed.

Lacking sufficient *K*-edge XAFS data of K references, we cannot exclude the co-existence of other organic-K phases in addition to K-pectate within plants. For example, in *Medicago truncatula* Gaertn. some K may remain lodged in fresh leaves as crystalline Ca-oxalate compound (whewellite, $CaC_2O_4 \cdot H_2O$) (Punshon et al., 2013). Even though not all plant K participates in intra-plant circulation, it appears that a portion of K forms mobile organic-K

complexes such as K-pectate and this process leads to isotopically heavier K in roots and fresh leaves.

Substantial variations in tissue K concentration and its isotopic composition between litter and living biomass provide insights into K translocation within plants and into dead tissues (Fig. 47). Dead leaves exhibit lighter K isotopic composition compared to fresh leaves (Fig. 48). This difference can be better explained by K redistribution from the older leaves (poor in K-pectate) to younger tissues rich in (K-pectate). This interpretation is supported by the XANES-$\Delta^{41}K$ comparison (Fig. 49) that $\Delta^{41}K_{Plant\text{-}Source}$ is positively correlated to the percent of K-pectate. We also found that intra-plant K isotopic fractionation is comparatively large for sampled trees relative to grasses (Fig. 48). A possible explanation for this trend is that trees operate over longer time scales and transport distances than grasses, thus magnifying K isotopic fractionation by ion-exchange process during intra-plant circulation.

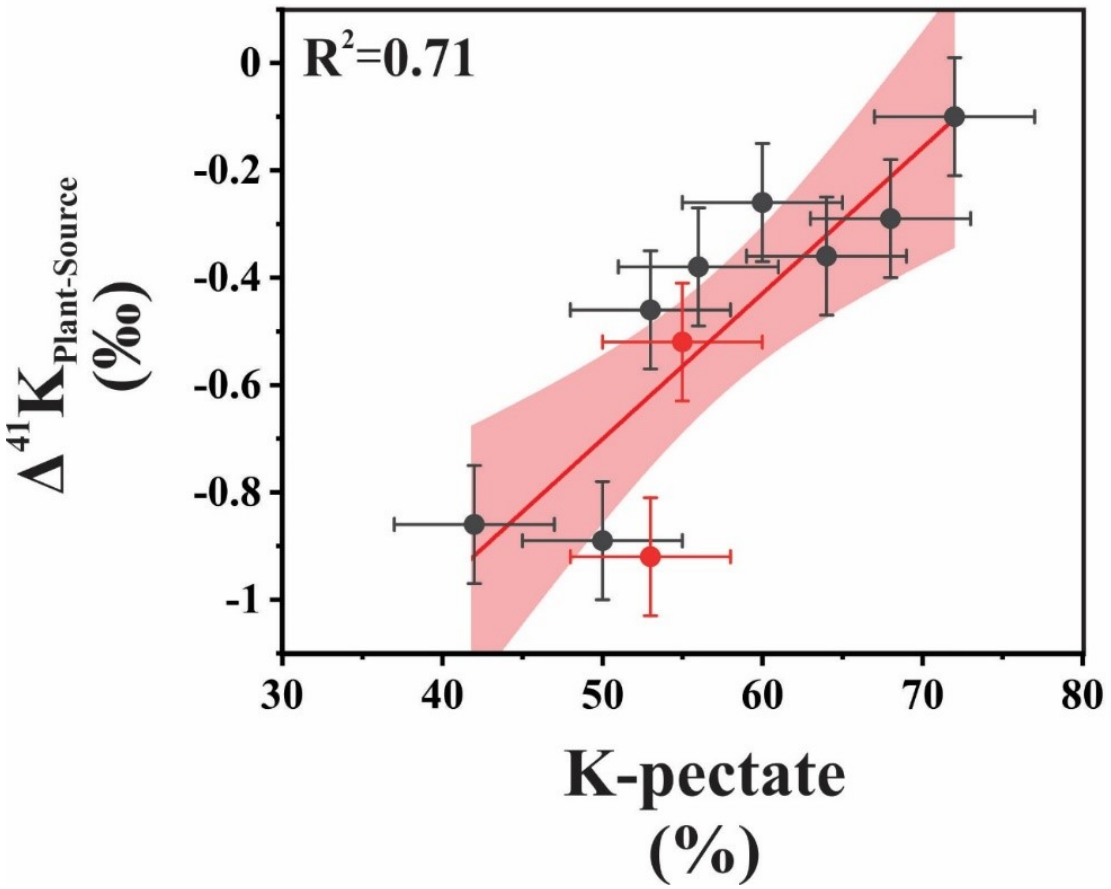

Figure 49. Potassium isotopic compositions in plant tissues versus the proportions of K-pectate based on XANES-LCF quantification (data depicted in Fig. 45).

Tissue K isotopic compositions are normalized to the K compositions of soil saturation extracts (averaged) to assess intra-plant K isotopic fractionation. Measured grasses and trees are marked by grey and red, respectively. The error bars on the Y-axis represent the uncertainties of K isotope measurements (a long-term 2 S.D. value of 0.11‰, Hu et al., 2018), and the error bars on the X-axis represent the general uncertainty of the XANES-LCF approach (5%). A positive linear correlation is found (R^2=0.71), and the red line denotes the linear fitting, and the red area covers the 95% confidence bands.

5.2. Root-soil K isotopic fractionation

Negative $\Delta^{41}K_{Root\text{-}Source}$ values demonstrate that plants preferentially take up isotopically lighter K from soil bioavailable pools in the humid and arid systems (Table 23 and Fig. 48). This interpretation is consistent with recent results obtained from hydroponic experiments of several crops (Christensen et al., 2018). We suggest two driving forces responsible for plant preference for isotopically lighter K, including adsorption on roots (and extracellular excretions of roots) and subsequent ion transport into root cells (Christensen et al., 2018).

Root adsorption is the retention of heavier K isotopes outside of root cells, leaving lighter K to be used by root cells. It could be supported by HCl leaching experiment of grassroots (Fig. 47), revealing that adsorption-driven K isotopic fractionation at the root-soil interface. The $\delta^{41}K$ values of grassroot-HCl extracts are higher than those of untreated grassroots and soil saturation extracts (averaged) (Table 23), suggesting that K isotopic fractionation occurred before K entering the root cells. Therefore, K in roots is separated into two pools, a lighter pool utilized by plants and a heavier pool remained at root surface and gelatinous material on the exterior of the roots. The $\delta^{41}K$ values of root residues after subtracting the contribution of K in root-HCl extracts based on K isotope mass balances. This calculation provides comparable $\Delta^{41}K_{Residual\ root\text{-}Source}$ values of -0.77‰ and -0.92‰ for humid and arid soils, respectively. We consider that near-constant K isotopic fractionations driven by root uptake of K probably indicate the same fractionation mechanism in both sites.

To maintain sufficient K concentration in cellular cytoplasm, K should be taken up by roots along the concentration gradient from the lower K^+ concentration external solution in soils (White and Karley, 2010). During root uptake, K isotopes can be fractionated (Christensen et al., 2018). Plant K^+ assimilation broadly involves a low-affinity (passive) transport path with ion-

specific channels plus the electrogenic pump and a high-affinity (active) transport path using ion-specific carriers and the symporter system (Ashley et al., 2006). In general, the low-affinity transport path could be activated with high extracellular K concentrations (>1 mM) and the high-affinity transport path operates at low extracellular K concentrations (<1 mM) (e.g., Schachtman and Schroeder, 1994; Britto and Kronzucker, 2008). Because we did not collect porewater, soil saturation extracts may not fully represent temporal soil solutions. Another limitation is that K concentration in soil solutions may change over time; and therefore, the sampling period and amount of antecedent moisture may also matter.

Although the K concentration in soil solution cannot be robustly constrained, several lines of evidence demonstrate the low-affinity transport path is more important. Firstly, we use the K concentration in leaves of sampled plants compared with comparable plant species reported with sufficient K supplies to evaluate the abundance of soil bioavailable K. Here we assume that the physiological properties are similar to those of drought-enduring trees (*Eucalyptus grandis* W. Hill, and *Eucalyptus urophylla* S.T. Blake) of 8-20 $g \cdot kg^{-1}$ (Rocha et al., 2019; Santos et al., 2020). Leaf K concentrations of trees (*P. chilensis*, 8.9 $g \cdot kg^{-1}$) in the arid site fall in a range with sufficient K supplies. Secondly, K is not considered as a limiting nutrient in Hawaiian soils based on fertilizer experiments using a dominant tree species (*Metrosideros polymorpha* Gaudich.) in Hawai‘i (Vitousek and Farrington, 1997). Lastly, considerable $\Delta^{41}K_{\text{Residual root-Source}}$ values for grass correspond to marked K isotopic fractionation driven by K transfer into roots. These values are comparable to an apparent K fractionation by about -1‰ produced by the size difference between ^{39}K and ^{41}K during K transport via ion channels (favored in the low-affinity path) (Christensen et al., 2018). As estimated in Christensen et al. (2018), the high-affinity transport path operated under low external K^+, which would fractionate

K isotopes much less than that of the low-affinity path. This high-affinity mechanism cannot reconcile measured $\Delta^{41}K_{\text{Residual Root-Source}}$ close to -1‰. In sum, we consider that the low-affinity, passive mechanism drives the K isotopic fractionation between soil bioavailable pools and plant roots in studied soil-plant systems.

5.3. K in soils and bioavailable pools

The isotopic variation of K in <2-mm soils and saturation extracts fed by rainfall could be principally ascribed to source mixing of basaltic substrate, dust-derived mineral aerosols, and marine aerosols (Fig. 47). Collected rainwater has averaged $\delta^{41}K$ value close to -0.18‰ (Table 23). Due to atmospheric processes, Asian-derived mineral aerosols may be partially dissolved in rain droplets, which was determined using radiogenic Sr isotopes of the same soil samples (Li et al., 2020a). The addition of mineral aerosols to the humid soil contribute substantial K to the soil pool because primary basaltic sources were depleted by leaching during weathering (Kurtz et al., 2001; Ryu et al., 2014). This argument is also supported by abundant quartz and mica (Li et al., 2020a) and interlayered K in these soils (K hosted in micaceous minerals derived from dusts, Fig. 46) (Merrill et al., 1994; Kurtz et al., 2001). Thus, despite intense weathering alteration, the humid soil shows $\delta^{41}K$ values identical to those of mineral aerosols (Chinese loess, -0.46±0.05‰, Huang et al., 2020). Overall, the input of dust-derived mineral aerosols in soils likely masks the effect of basalt weathering that preferentially leaves light K isotopes in soils/regoliths (Chen et al., 2020; Teng et al., 2020).

Since K is a macronutrient, plant cycles (i.e., plant uptake and return of inorganic nutrients from depth to near soil surface) might add biological K in surface soils. Biologically utilized K is generally isotopically lighter than the source based on field observation in this study and hydroponic experiments (Christensen et al., 2018). Despite variations in plant covers and

species in the humid and arid systems, we here provide two lines of evidence against marked plant imprints on soil K budget in both sites based on K isotopes.

First, we would expect a negative K isotopic shift in soils from the basaltic sources driven by plant cycling, which however, is not the case here (Fig. 46). An explanation is that the humid soil has ~90% K hosted in silicates and plant imprints could be masked by mineral aerosols (Fig. 46). By contrast, the arid soil shows higher $\delta^{41}K$ values compared with their potential sources – the Pololū lava and mineral aerosols, especially for the topsoil with a marked, positive isotopic offset of ~0.4‰ from the basaltic substrate. High $\delta^{41}K$ of the arid soil can be ascribed to the progressive accumulation of marine aerosols (using $\delta^{41}K_{Seawater}$ ~0.14‰, Hille et al., 2019; Wang et al., 2020) due to higher evapotranspiration relative to precipitation (Goodfellow et al., 2014; Li et al., 2020a).

Moreover, saturation extracts are used to represent bioavailable pools. The $\delta^{41}K$ values of saturation extracts differ between the topsoil and subsoil (Fig. 47). It is known that lighter K isotopes are preferentially taken by plants (Christensen et al., 2018 and this study) from bioavailable pools in the topsoil and subsoil, and then isotopically lighter K mostly returns to the topsoil pool once plants die and decay. Since plants take up K and then release again, constantly fractionating K, we expect K in the topsoil pool to be lighter than the subsoil pool over time. However, here we have not established full plant mass balance or the rate of K cycling. We did find however that $\delta^{41}K$ values in the saturation extracts of the topsoil are more isotopically heavier than those of the subsoil in both sites (Fig. 47). Heavier K in topsoil saturation extracts likely have resulted from the dominance of marine aerosols, and K in subsoil saturation extracts might be regulated by weathering leaching. In summation, the concentration of K in soils should

be much greater than the amount of K being added through plant cycling, and thus plant-cycled fraction of total K is not large enough to affect the isotopic value of soils.

6. Summary and Conclusions

In Hawai‘i, a wide variability in the K isotopic composition of plants reflects intra-plant and root-soil isotopic fractionations. Intra-plant K isotopic fractionation is regulated by cation-exchange processes. Plant tissues with higher proportions of organic-K association (i.e., K-pectate) are more enriched in heavier K isotopes, causing higher $\delta^{41}K$ values in roots and fresh leaves and lower $\delta^{41}K$ in stems (and bark) and dead leaves. Intra-plant K isotopic fractionation is larger in trees compared with that of grasses, which could be ascribed to longer transport distances, and thus magnifying K isotopic fractionation during intra-plant circulation. At root-soil interfaces, adsorption onto root surface and extracellular excretion and lateral uptake in the root cells following a low-affinity transport pathway play important roles, which promote isotopically light K entering the root cells from soil bioavailable pools in both humid and arid sites. The variability of the K isotopic composition in bulk soils and saturation extracts mainly reflects mixing between the basaltic substrate and atmospheric deposition with limited influence from plants. The K isotopic composition of the humid soil is strongly influenced by atmospherically deposited mineral aerosols, which are rich in K-bearing minerals. In contrast, the isotopic compositions of marine aerosols could be well preserved in the arid soil due to relatively weak chemical leaching. The data demonstrate that stable K isotopes are a promising tool for understanding mechanisms of K utilization by plants and biogeochemical K cycling.

CHAPTER 9: SUMMARY AND FUTURE WORK

This dissertation advances our current understandings of Li and K isotope behaviors during chemical weathering combined experimental work with field investigations. The outcomes demonstrate that Li and K isotopes could be strongly fractionated by fluid-mineral interaction and biological activity because of their large isotopic mass differences and thus have potentials to trace biogeochemical weathering. The main conclusions from this dissertation include:

1. Chapter 2 presents a new dual-column separation method for Li purification using long (8 cm) and short (4 cm) chromatographic columns loaded with AG50W-X8 resin. Compared with single-column systems, this dual-column system has two distinct advantages: (a) It enables efficient (~ 6 h, excluding evaporation time) Li elution and satisfactory recovery, with negligible matrix residues in Li collections (e.g., Na^+ and polyvalent cations as Ca^{2+}, Mg^{2+}, Al^{3+}). (b) The dual-column isolation routinely achieved a consistent elution curve for lithium cuts (7 to 16 ml), avoiding re-calibration of columns with respect to compositional variations. Therefore, this dual-column system can be widely used for chemically diverse geological samples.

2. Chapters 3 and 4 investigate Li and K isotope fractionation during clay adsorption based on batch fluid-mineral interaction experiments. I have demonstrated that Li isotope fractionation during kaolinite uptake is best described using a closed-system Rayleigh distillation model ($\alpha \sim 0.992$). These results are also consistent with the theoretical calculation of Li^+ desolvation and field observation. The enrichment of the solution in light K isotopes relative to adsorbed K on clays yields an isotopic

fractionation factor between adsorbed and aqueous phases of ~0.75‰, best described by an equilibrium fractionation mechanism with an α of ~1.00075. I reported differences in the atomic coordination of K on clay surfaces (outer-sphere complexation) and within clay structures, which might be responsible for the opposite directions of K isotopic fractionation between clay adsorption and field observations. We also highlight the difference in K isotopic fractionation between clay incorporation and surface adsorption.

3. Chapter 5 investigates Li and K isotope fractionation during silicate dissolution in closed batch systems. The isotopic and elemental behaviors of Li and K during ligand-driven and proton-driven dissolution are not the same, and the difference is reasoned by ligand-cation interactions and backward reactions. In summary, the exchange of metals and isotopes during dissolution likely occurs in multiple steps: (i) kinetic loss of ions from silicate minerals in rocks into fluids, (ii) the break-down of primary silicates, and (iii) back-reactions (adsorption and/or precipitation). The first step promotes the liberation of light isotopes, which then can be balanced by the second step (or affected by ligand- cation interaction). The third step may occur, producing different isotopic behaviors.

4. Chapter 6 investigates the processes of soil-atmosphere-biosphere exchanges for Li isotope fractionation in regolith profiles developed on same-age lavas in humid and arid climatic conditions in Hawai‘i. Li geochemistry in the shallow regolith is mainly affected by atmospheric addition, vegetation cycling, and secondary mineral formation, while it is controlled by pore fluid percolation and accumulation in the deep regolith. Dust and ash inputs from recent Hawi eruptions support the Li enrichment in the topsoil. The fidelity of biogeochemical cycling resulted in peak Li accumulations in the rhizospheric soils, and light Li upward translocation as plant growth, and return into pore fluids by vegetative decay. Secondary mineral formation is crucial for Li redistribution and its isotopic fractionation. Li isotopic compositions in the deep regolith are similar to the parent rock, and downward infiltrative fluids generate accumulation zones. The results of this study emphasize climate and long-neglected biological controls on terrestrial Li cycle.

6. Chapter 7 provides K element chemistry, phase, and isotopic composition in the regolith profiles developed at the humid and arid sides of Kohala Mountain, Hawai‘i. I conclude that K derived from eolian accretion over time is critical, especially the humid regolith receiving heavy rainfall. This conclusion is supported by increased crustal K imprint, enriched quartz and illite-K phases, and more radiogenic Nd-Sr isotopic compositions towards the surface. The light K isotopic composition in the humid regolith relative to the basaltic $\delta^{41}K$ value is principally caused by preferential incorporation of isotopically light K into kaolin minerals. In comparison, heavier K isotopic compositions in the arid regolith than the basaltic $\delta^{41}K$ reflect an interplay between clay adsorption of isotopically heavier K under more alkaline condition and better preservation of marine aerosol K imprints. Biological activities contribute to soil K enrichment, but exert negligible influences on K isotopic variations due to rapid leaching and the masking effects of exogenous sources. The outcome supports that K isotopic composition in the regolith depends on climate, which makes terrestrial K isotopic records a potential tracer of weathering processes and paleo-climate.

6. Chapter 8 investigates the K speciation and K isotopic composition in trees (*Macadamia integrifolia* Maiden & Betche; *Prosopis chilensis* (Mol.) Stuntz) and grasses (*Pennisetum setaceum* (Forssk.) Chiov; *Cenchrus ciliaris* L.) sampled from a humid and an arid soil-plant system in Hawai‘i. In Hawai‘i, wide variability in the K isotopic composition of plants reflects intra-plant and root-soil isotopic fractionations. Intra-plant K isotopic fractionation is regulated by cation-exchange processes. Plant tissues with higher proportions of organic-K association are more enriched in heavier K isotopes, causing higher $\delta^{41}K$ values in roots and fresh leaves and lower $\delta^{41}K$ in stems (and barks) and dead leaves. Intra-plant K isotopic fractionation is larger in trees compared with that of grasses, which could be ascribed to longer transport distances, and thus magnifying K isotopic fractionation during intra-plant circulation. At root-soil interfaces, adsorption onto root surface and extracellular excretion and lateral uptake in the root cells following a low-affinity transport pathway play important roles, promoting isotopically light K entering

the root cells from soil bioavailable pools in both humid and arid sites. K isotopic composition of the humid soil is substantially influenced by atmospherically deposited mineral aerosols, which are rich in K-bearing minerals. In contrast, the isotopic compositions of marine aerosols could be well preserved in the arid soil due to relatively weak chemical leaching. It demonstrated that K isotopes are a promising tool for better understanding plant K utilization and biogeochemical K cycling.

7. In addition to the work presented in the dissertation, I listed proposed future directions coupling Li and K isotope systematics with synchrotron radiation techniques. It is known that marine carbonates provide an archive of temporal seawater composition. The application of synchrotron-based techniques can help to determine and quantify atomic speciation, which could help to understand Li and K isotope fractionation in marine biogenic carbonates and reconstruct seawater isotopic composition in past oceans. The outcome potentially improves the understanding of weathering and global biogeochemical cycles over Earth's history.

APPENDIX 1: TABLE OF REFERENCE ELEMENTAL ANALYSIS BY Q-ICP-MS

SRM No.	Description	Location	[Li] (ppm)	[K] (ppm)	[Mg] (ppm)	[Al] (ppm)	[Ca] (ppm)	N
BHVO-2	Basalt, USGS	Hawaiian Volcanic Observatory	5.0[a]	4215	43150	72170	80413	20
			4.5[b]	4314	43380	71470	81428	n.d.
			4.5[c]	4256	43542	71152	81428	27
NASS-7	Seawater, CNRC	Seawater	0.21[a]	1145	2054	2770	378435	20
			n.d.[b]	1127	2040	2780	377500	n.d.
SLRS-5	River water, CNRC	Ottawa Britannia, Purification Plant	0.47[a]	0.87	2.64	0.05	10.28	20
			n.d.[b]	0.84	2.54	0.05	10.50	n.d.
			n.d.[d]	0.92	2.55	0.05	10.30	11
			0.45[e]	0.86	2.52	0.05	10.32	n.d.
JG-2	Granite, GSJ	Naegi granite	46.1[a]	38956	210	68525	4960	20
			42.2[b]	39080	220	66010	5000	20
			n.d.[f]	36000	n.d.	n.d.	4900	n.d.
GSP-2	Granite, USGS	Granodiorite, Silver Plume, Colorado	3590[a]	44510	5790	79200	15400	20
			3600[b]	44642	5760	78882	15000	n.d.
			3480[g]	44200	5900	80200	16000	n.d.
			n.d.[h]	44800	n.d.	n.d.	15000	n.d.

Note: [a]Data collected in this study; [b]Certified values; [c]Jochum et al. (2016); [d]Liu et al. (2015); [e]Yeghicheyan et al. (2013); [f]Korotev (1996); [g]Zhang et al. (2016); [h]Cotta et al. (2007). Data of selected major elements are provided. SRM: standard reference materials; N: the number of element analytical cycles for Q-ICP-MS measurement. n.d.: not determined.

APPENDIX 2: TABLE OF REFERENCE ISOTOPIC ANALYSIS BY Q/MC-ICP-MS

SRM NO.	Description	Location	$\delta^7Li_{measured}$ (‰)	2 S.D. (‰)	$\delta^{41}K_{measured}$ (‰)	2 S.D. (‰)
BHVO-2	Basalt, USGS	Hawaiian Volcanic Observatory	4.70[a]	0.60	-0.49[a]	0.08
			4.63[b]	0.16	-0.48[a]	0.04
			4.80[c]	0.30	-0.48[i]	n.d.
			4.90[d]	0.80	-0.50[j]	0.19
			4.66[e]	0.22	-0.52[k]	0.24
			4.63[f]	0.16	-0.41[l]	0.02
GSP-2	Granodiorite, USGS	Silver Plume, Colorado	-0.64[a]	0.60	-0.46[a]	0.09
			-0.46[a]	1.1	-0.43[h]	0.07
			-0.78[e]	0.25	-0.50[j]	0.12
			-0.56[b]	0.55	-0.48[k]	0.10
			-0.56[f]	0.72	-0.42[l]	0.03
KGa-2	Kaolinite, CMS	Georgia, USA	0.20[a]	1.1	-0.44[a]	0.07
SWy-2	Montmorillonite,	Wyoming, USA	-0.30[a]	1.1	-0.63[a]	0.08

Note: [a]Data collected in this study; [b]W. Li et al. (2019); [c]Elliott et al. (2006); [d]Pogge von Strandmann et al. (2010); [e]Lin et al. (2016); [f]Jeffcoate et al. (2004); [g]Huang et al. (2010); [h]Liu and Li (2019).; [ci]Chen et al. (2019); [j]W. Li et al. (2016); [k]Morgan et al. (2018); [l]X. Li et al. (2020). SRM: standard reference materials; 2 S.D.: two standard deviation corrected by a Student's *t* factor; N: number of analytical cycles. n.d.: not determined.

REFERENCES

Ai, G., Sun, T., Dong, X., 2014. Gas chromatography/isotope ratio mass spectrometry: Analysis of methanol, ethanol and acetic acid by direct injection of aqueous alcoholic and acetic acid samples. Rapid Commun. Mass Spectrom. 28, 1674–1682. https://doi.org/10.1002/rcm.6948

Amiotte Suchet, P., Probst, J.L., Ludwig, W., 2003. Worldwide distribution of continental rock lithology: Implications for the atmospheric/soil CO_2 uptake by continental weathering and alkalinity river transport to the oceans . Global Biogeochem. Cycles 17, n/a-n/a. https://doi.org/10.1029/2002gb001891

Au, P.I., Leong, Y.K., 2013. Rheological and zeta potential behaviour of kaolin and bentonite composite slurries. Colloids Surfaces A Physicochem. Eng. Asp. 436, 530–541. https://doi.org/10.1016/j.colsurfa.2013.06.039

Alexandre, A., Meunier, J.D., Colin, F., Koud, J.M., 1997. Plant impact on the biogeochemical cycle of silicon and related weathering processes. Geochim. Cosmochim. Acta 61, 677–682. https://doi.org/10.1016/S0016-7037(97)00001-X

Ashley, M.K., Grant, M., Grabov, A., 2006. Plant responses to potassium deficiencies: A role for potassium transport proteins. J. Exp. Bot. 57(2), 425-436. https://doi.org/10.1093/jxb/erj034

Aucour, A.M., Bedell, J.P., Queyron, M., Magnin, V., Testemale, D., Sarret, G., 2015. Dynamics of Zn in an urban wetland soil-plant system: Coupling isotopic and EXAFS approaches. Geochim. Cosmochim. Acta 160, 55–69. https://doi.org/10.1016/j.gca.2015.03.040

An, Z., Liu, T., Lu, Y., Porter, S.C., Kukla, G. Wu, X., Hua, Y., 1990. The long-term paleomonsoon variation recorded by the loess-paleosol sequence in central China. Quat. Int. 7, 91-95. https://doi.org/10.1016/1040-6182(90)90042-3

Anbar, A.D., Rouxel, O., 2007. Metal stable isotopes in paleoceanography. Annu. Rev. Earth Planet. Sci. 35, 717-746. https://doi.org/10.1146/annurev.earth.34.031405.125029

Arendt, C.A., Aciego, S.M., Hetland, E.A., 2015. An open-source Bayesian Monte Carlo isotope mixing model with applications in Earth surface processes. Geochem. Geophys. Greosys. 16(5), 1274-1292. https://doi.org/10.1002/2014GC005683

Bagard, M.L., Schmitt, A.D., Chabaux, F., Pokrovsky, O.S., Viers, J., Stille, P., Labolle, F., Prokushkin, A.S., 2013. Biogeochemistry of stable Ca and radiogenic Sr isotopes in a larch-covered permafrost-dominated watershed of Central Siberia. Geochim. Cosmochim. Acta 114, 169–187. https://doi.org/10.1016/j.gca.2013.03.038

Bagard, M.L., West, A.J., Newman, K., Basu, A.R., 2015. Lithium isotope fractionation in the Ganges-Brahmaputra floodplain and implications for groundwater impact on seawater isotopic composition. Earth Planet. Sci. Lett. 432, 404–414. https://doi.org/10.1016/j.epsl.2015.08.036

Balistrieri, L.S., Borrok, D.M., Wanty, R.B., Ridley, W.I., 2008. Fractionation of Cu and Zn isotopes during adsorption onto amorphous Fe(III) oxyhydroxide: Experimental mixing of acid rock drainage and ambient river water. Geochim. Cosmochim. Acta 72, 311–328. https://doi.org/10.1016/j.gca.2007.11.013

Balland-Bolou-Bi, C., Bolou-Bi, E.B., Vigier, N., Mustin, C., Poszwa, A., 2019. Increased Mg release rates and related Mg isotopic signatures during bacteria-phlogopite interactions. Chem. Geol. 506, 17–28. https://doi.org/10.1016/j.chemgeo.2018.12.020

Barker, A.V., Pilbeam, D.J., 2016. Handbook of plant nutrition, Handbook of Plant Nutrition. CRC Press.

https://doi.org/10.21273/hortsci.42.2.422b

Bataille, C.P., Willis, A., Yang, X., Liu, X.M., 2017. Continental igneous rock composition: A major control of past global chemical weathering. Sci. Adv. 3. https://doi.org/10.1126/sciadv.1602183

Bayon, G., Burton, K.W., Soulet, G., Vigier, N., Dennielou, B., Etoubleau, J., Ponzevera, E., German, C.R., Nesbitt, R.W., 2009. Hf and Nd isotopes in marine sediments: Constraints on global silicate weathering. Earth Planet. Sci. Lett. 277, 318–326. https://doi.org/10.1016/j.epsl.2008.10.028

Beaulieu, E., Goddëris, Y., Donnadieu, Y., Labat, D., Roelandt, C., 2012. High sensitivity of the continental-weathering carbon dioxide sink to future climate change. Nat. Clim. Chang. https://doi.org/10.1038/nclimate1419

Beig, M.S., Lüttge, A., 2006. Albite dissolution kinetics as a function of distance from equilibrium: Implications for natural feldspar weathering. Geochim. Cosmochim. Acta 70, 1402–1420. https://doi.org/10.1016/j.gca.2005.10.035

Bencala, K.E., McKnight, D.M., Zellweger, G.W., 1990. Characterization of transport in an acidic and metal-rich mountain stream based on a lithium tracer injection and simulations of transient storage. Water Resour. Res. 26, 989–1000. https://doi.org/10.1029/WR026i005p00989

Berner, K., Berner, R.A., 2012. Global environment: Water, air, and geochemical cycles, Global Environment: Water, Air, and Geochemical Cycles (Second Edition). Princeton University Press. https://doi.org/10.1080/00207233.2012.753739

Blättler, C.L., Jenkyns, H.C., Reynard, L.M., Henderson, G.M., 2011. Significant increases in global weathering during Oceanic Anoxic Events 1a and 2 indicated by calcium isotopes. Earth Planet. Sci. Lett. 309, 77–88. https://doi.org/10.1016/j.epsl.2011.06.029

Bogatko, S., Claeys, P., De Proft, F., Geerlings, P., 2013. Li^+ speciation and the use of 7Li/6Li isotope ratios for ancient climate monitoring. Chem. Geol. 357, 1–7. https://doi.org/10.1016/j.chemgeo.2013.08.019

Bohlin, M.S., Bickle, M.J., 2019. The reactive transport of Li as a monitor of weathering processes in kinetically limited weathering regimes. Earth Planet. Sci. Lett. 511, 233–243. https://doi.org/10.1016/j.epsl.2019.01.034

Bohlin, M.S., Misra, S., Lloyd, N., Elderfield, H., Bickle, M.J., 2018. High-precision determination of lithium and magnesium isotopes utilising single column separation and multi-collector inductively coupled plasma mass spectrometry. Rapid Commun. Mass Spectrom. 32, 93–104. https://doi.org/10.1002/rcm.8020

Bouchez, J., Von Blanckenburg, F., Schuessler, J.A., 2013. Modeling novel stable isotope ratios in the weathering zone. Am. J. Sci. 313, 267–308. https://doi.org/10.2475/04.2013.01

Bourg, I.C., Richter, F.M., Christensen, J.N., Sposito, G., 2010. Isotopic mass dependence of metal cation diffusion coefficients in liquid water. Geochim. Cosmochim. Acta 74, 2249–2256. https://doi.org/10.1016/j.gca.2010.01.024

Brant, C., Coogan, L.A., Gillis, K.M., Seyfried, W.E., Pester, N.J., Spence, J., 2012. Lithium and Li-isotopes in young altered upper oceanic crust from the East Pacific Rise. Geochim. Cosmochim. Acta 96, 272–293. https://doi.org/10.1016/j.gca.2012.08.025

Brantley, S.L., Liermann, L.J., Guynn, R.L., Anbar, A., Icopini, G.A., Barling, J., 2004. Fe isotopic fractionation during mineral dissolution with and without bacteria. Geochim. Cosmochim. Acta 68, 3189–3204. https://doi.org/10.1016/j.gca.2004.01.023

Brantley, S.L., White, A.F., 2009. Approaches to modeling weathered regolith, in: Reviews in Mineralogy and Geochemistry. pp. 435–484. https://doi.org/10.2138/rmg.2009.70.10

Brazier, J.M., Schmitt, A.D., Gangloff, S., Pelt, E., Chabaux, F., Tertre, E., 2019. Calcium isotopic fractionation during adsorption onto and desorption from soil phyllosilicates (kaolinite, montmorillonite and muscovite). Geochim. Cosmochim. Acta 250, 324–347. https://doi.org/10.1016/j.gca.2019.02.017

Bryan, A.L., Dong, S., Wilkes, E.B., Wasylenki, L.E., 2015. Zinc isotope fractionation during adsorption onto Mn oxyhydroxide at low and high ionic strength. Geochim. Cosmochim. Acta 157, 182–197. https://doi.org/10.1016/j.gca.2015.01.026

Bryant, C.J., McCulloch, M.T., Bennett, V.C., 2003. Impact of matrix effects on the accurate measurement of Li isotope ratios by inductively coupled plasma mass spectrometry (MC-ICP-MS) under "cold" plasma conditions. J. Anal. At. Spectrom. 18, 734–737. https://doi.org/10.1039/b212083f

Bullen, T., Chadwick, O., 2016. Ca, Sr and Ba stable isotopes reveal the fate of soil nutrients along a tropical climosequence in Hawaii. Chem. Geol. 422, 25–45. https://doi.org/10.1016/j.chemgeo.2015.12.008

Burt, R., 1995. Soil Survey Laboratory Information Manual. Soil Survey Investigations Report No. 45, USDA Soil Survey Laboratory.

Becker, J.S., Füllner, K., Seeling, U.D., Fornalczyk, G., Kuhn, A.J., 2008. Measuring magnesium, calcium and potassium isotope ratios using ICP-QMS with an octopole collision cell in tracer studies of nutrient uptake and translocation in plants. Anal. Bioanal. Chem. 390, 571–578. https://doi.org/10.1007/s00216-007-1603-6

Bolou-Bi, E.B., Poszwa, A., Leyval, C., Vigier, N., 2010. Experimental determination of magnesium isotope fractionation during higher plant growth. Geochim. Cosmochim. Acta 74, 2523–2537. https://doi.org/10.1016/j.gca.2010.02.010

Brewer, A.K., Kueck ,P.D., 1934. The relative abundance of the isotopes of lithium, potassium and rubidium. Phys. Rev. 46, 894–897.

Britto, D.T., Kronzucker, H.J., 2008. Cellular mechanisms of potassium transport in plants. Physiol. Plant. 133(4), 637–650. https://doi.org/10.1111/j.1399-3054.2008.01067.x

Brimhall, G.H., Dietrich, W.E., 1987. Constitutive mass balance relations between chemical composition, volume, density, porosity, and strain in metasomatic hydrochemical systems: results on weathering and pedogenesis. Geochim. Cosmochim. Acta 51(3), 567-587. https://doi.org/10.1016/0016-7037(87)90070-6

Calvin, S., 2013. XAFS for Everyone, XAFS for Everyone. CRC Press. https://doi.org/10.1201/b14843

Casey, W.H., Westrich, H.R., Banfield, J.F., Ferruzzi, G., Arnold, G.W., 1993. Leaching and reconstruction at the surfaces of dissolving chain-silicate minerals. Nature 366, 253–256. https://doi.org/10.1038/366253a0

Chadwick, O.A., Chorover, J., 2001. The chemistry of pedogenic thresholds. Geoderma 100, 321–353. https://doi.org/10.1016/S0016-7061(01)00027-1

Chadwick, O.A., Derry, L.A., Vitousek, P.M., Huebert, B.J., Hedin, L.O., 1999. Changing sources of nutrients during four million years of ecosystem development. Nature. https://doi.org/10.1038/17276

Chadwick, O.A., Gavenda, R.T., Kelly, E.F., Ziegler, K., Olson, C.G., Crawford Elliott, W., Hendricks, D.M., 2003. The impact of climate on the biogeochemical functioning of volcanic soils. Chem. Geol. 202, 195–223. https://doi.org/10.1016/j.chemgeo.2002.09.001

Chan, L.H., Leeman, W.P., You, C.F., 2002. Lithium isotopic composition of Central American volcanic arc lavas: Implications for modification of subarc mantle by slab-derived fluids: Correction. Chem. Geol. 182, 293–300. https://doi.org/10.1016/S0009-2541(01)00298-4

Chan, L.H., Leeman, W.P., You, C.F., 1999. Lithium isotopic composition of Central American Volcanic Arc lavas: Implications for modification of subarc mantle by slab-derived fluids. Chem. Geol. 160, 255–280. https://doi.org/10.1016/S0009-2541(99)00101-1

Chao, L.I., Yang, S., 2010. Is chemical index of alteration (cia) a reliable proxy for chemical weathering in global drainage basins? Am. J. Sci. 310, 111–127. https://doi.org/10.2475/02.2010.03

Chapela Lara, M., Buss, H.L., Pogge von Strandmann, P.A.E., Schuessler, J.A., Moore, O.W., 2017. The influence of critical zone processes on the Mg isotope budget in a tropical, highly weathered andesitic catchment. Geochim. Cosmochim. Acta 202, 77–100. https://doi.org/10.1016/j.gca.2016.12.032

Chapman, J.B., Weiss, D.J., Shan, Y., Lemburger, M., 2009. Iron isotope fractionation during leaching of granite and basalt by hydrochloric and oxalic acids. Geochim. Cosmochim. Acta 73, 1312–1324. https://doi.org/10.1016/j.gca.2008.11.037

Chaudhuri, S., Clauer, N., Semhi, K., 2007. Plant decay as a major control of river dissolved potassium: A first estimate. Chem. Geol. 243, 178–190. https://doi.org/10.1016/j.chemgeo.2007.05.023

Chen, H., Liu, X.M., Wang, K., 2020. Potassium isotope fractionation during chemical weathering of basalts. Earth Planet. Sci. Lett. 539. https://doi.org/10.1016/j.epsl.2020.116192

Chen, H., Tian, Z., Tuller-Ross, B., Korotev, R.L., Wang, K., 2019. High-precision potassium isotopic analysis by MC-ICP-MS: An inter-laboratory comparison and refined K atomic weight. J. Anal. At. Spectrom. 34, 160–171. https://doi.org/10.1039/c8ja00303c

Chernonozhkin, S.M., Goderis, S., Lobo, L., Claeys, P., Vanhaecke, F., 2015. Development of an isolation procedure and MC-ICP-MS measurement protocol for the study of stable isotope ratio variations of nickel. J. Anal. At. Spectrom. 30, 1518–1530. https://doi.org/10.1039/c5ja00080g

Choi, M.S., Ryu, J.S., Park, H.Y., Lee, K.S., Kil, Y., Shin, H.S., 2013. Precise determination of the lithium isotope ratio in geological samples using MC-ICP-MS with cool plasma. J. Anal. At. Spectrom. 28, 505–509. https://doi.org/10.1039/c2ja30293d

Chorom, M., Rengasamy, P., 1995. Dispersion and zeta potential of pure clays as related to net particle charge under varying pH, electrolyte concentration and cation type. Eur. J. Soil Sci. 46, 657–665. https://doi.org/10.1111/j.1365-2389.1995.tb01362.x

Chorover, J., Amistadi, M.K., Chadwick, O.A., 2004. Surface charge evolution of mineral-organic complexes during pedogenesis in Hawaiian basalt. Geochim. Cosmochim. Acta 68, 4859–4876. https://doi.org/10.1016/j.gca.2004.06.005

Chorover, J., DiChiaro, M.J., Chadwick, O.A., 1999. Structural Charge and Cesium Retention in a Chronosequence of Tephritic Soils. Soil Sci. Soc. Am. J. 63, 169–177. https://doi.org/10.2136/sssaj1999.03615995006300010024x

Christensen, J.N., Qin, L., Brown, S.T., Depaolo, D.J., 2018. Potassium and Calcium Isotopic Fractionation by Plants (Soybean [Glycine max], Rice [Oryza sativa], and Wheat [Triticum

aestivum]). ACS Earth Sp. Chem. 2, 745–752. https://doi.org/10.1021/acsearthspacechem.8b00035

Cibin, G., Mottana, A., Marcelli, A., Brigatti, M.F., 2005. Potassium coordination in trioctahedral micas investigated by K-edge XANES spectroscopy. Mineral. Petrol. 85, 67–87. https://doi.org/10.1007/s00710-005-0099-z

Clergue, C., Dellinger, M., Buss, H.L., Gaillardet, J., Benedetti, M.F., Dessert, C., 2015. Influence of atmospheric deposits and secondary minerals on Li isotopes budget in a highly weathered catchment, Guadeloupe (Lesser Antilles). Chem. Geol. 414, 28–41. https://doi.org/10.1016/j.chemgeo.2015.08.015

Cox, A.E., Joern, B.C., Brouder, S.M., Gao, D., 1999. Plant-available potassium assessment with a modified sodium tetraphenylboron method. Soil Sci. Soc. Am. J. 63, 902–911. https://doi.org/10.2136/sssaj1999.634902x

Crews, T.E., Kitayama, K., Fownes, J.H., Riley, R.H., Herbert, D.A., Mueller-Dombois, D., Vitousek, P.M., 1995. Changes in soil phosphorus fractions and ecosystem dynamics across a long chronosequence in Hawaii. Ecology 76, 1407–1424. https://doi.org/10.2307/1938144

Caldelas, C., Dong, S., Araus, J.L., Jakob Weiss, D., 2011. Zinc isotopic fractionation in Phragmites australis in response to toxic levels of zinc. J. Exp. Bot. 62, 2169–2178. https://doi.org/10.1093/jxb/erq414

Capo, R.C., Whipkey, C.E., Blachère, J.R., Chadwick, O.A., 2000. Pedogenic origin of dolomite in a basaltic weathering profile, Kohala peninsula, Hawaii. Geology 28, 271–274. https://doi.org/10.1130/0091-7613(2000)28%3C271:POODIA%3E2.0.CO;2

Chaignon, V., Bedin, F., Hinsinger, P., 2002. Copper bioavailability and rhizosphere pH changes as affected by nitrogen supply for tomato and oilseed rape cropped on an acidic and a calcareous soil. Plant Soil 243, 219–228. https://doi.org/10.1023/A:1019942924985

Cobert, F., Schmitt, A.D., Bourgeade, P., Labolle, F., Badot, P.M., Chabaux, F., Stille, P., 2011. Experimental identification of Ca isotopic fractionations in higher plants. Geochim. Cosmochim. Acta 75, 5467–5482. https://doi.org/10.1016/j.gca.2011.06.032

Cuadros, J., Andrade, G., Ferreira, T. O., de Moya Partiti, C. S., Cohen, R., Vidal-Torrado, P., 2017. The mangrove reactor: fast clay transformation and potassium sink. Appl. Clay Sci. 140, 50-58. https://doi.org/10.1016/j.clay.2017.01.022

Chauvel, C., Garçon, M., Bureau, S., Besnault, A., Jahn, B. M., Ding, Z., 2014. Constraints from loess on the Hf–Nd isotopic composition of the upper continental crust. Earth Planet. Sci. Lett. 388, 48-58. https://doi.org/10.1016/j.epsl.2013.11.045

De La Rocha, C.L., DePaolo, D.J., 2000. Isotopic evidence for variations in the marine calcium cycle over the cenozoic. Science 289, 1176–1178. https://doi.org/10.1126/science.289.5482.1176

Dellinger, M., Bouchez, J., Gaillardet, J., Faure, L., Moureau, J., 2017. Tracing weathering regimes using the lithium isotope composition of detrital sediments. Geology 45, 411–414. https://doi.org/10.1130/G38671.1

Dellinger, M., Gaillardet, J., Bouchez, J., Calmels, D., Louvat, P., Dosseto, A., Gorge, C., Alanoca, L., Maurice, L., 2015. Riverine Li isotope fractionation in the Amazon River basin controlled by the weathering regimes. Geochim. Cosmochim. Acta 164, 71–93. https://doi.org/10.1016/j.gca.2015.04.042

DePaolo, D.J., 2011. Surface kinetic model for isotopic and trace element fractionation during

precipitation of calcite from aqueous solutions. Geochim. Cosmochim. Acta 75, 1039–1056. https://doi.org/10.1016/j.gca.2010.11.020

Dixon, J.L., Chadwick, O.A., Pavich, M.J., 2018. Climatically controlled delivery and retention of meteoric 10Be in soils. Geology 46, 899–902. https://doi.org/10.1130/G45176.1

Dong, S., Wasylenki, L.E., 2016. Zinc isotope fractionation during adsorption to calcite at high and low ionic strength. Chem. Geol. 447, 70–78. https://doi.org/10.1016/j.chemgeo.2016.10.031

Dosseto, A., Vigier, N., Joannes-Boyau, R., Moffat, I., Singh, T., Srivastava, P., 2015. Rapid response of silicate weathering rates to climate change in the Himalaya. Geochemical Perspect. Lett. 1, 10–19. https://doi.org/10.7185/geochemlet.1502

Dultz, S., Behrens, H., Helsch, G., Deubener, J., 2016. Electrolyte effects on surface chemistry of basaltic glass in the initial stages of dissolution. Chem. Geol. 426, 71–84. https://doi.org/10.1016/j.chemgeo.2016.01.027

Durrant, C.B., Begg, J.D., Kersting, A.B., Zavarin, M., 2018. Cesium sorption reversibility and kinetics on illite, montmorillonite, and kaolinite. Sci. Total Environ. 610–611, 511–520. https://doi.org/10.1016/j.scitotenv.2017.08.122

Edmond, J.M., 1992. Himalayan tectonics, weathering processes, and the strontium isotope record in marine limestones. Science 258, 1594–1597. https://doi.org/10.1126/science.258.5088.1594

Eiriksdottir, E.S., Gislason, S.R., Oelkers, E.H., 2015. Direct evidence of the feedback between climate and nutrient, major, and trace element transport to the oceans. Geochim. Cosmochim. Acta 166, 249–266. https://doi.org/10.1016/j.gca.2015.06.005

Freundlich, H., 1922. Colloid & capillary chemistry. EP Dutton & Company.

Fang, Q., Hong, H., Furnes, H., Chorover, J., Luo, Q., Zhao, L., Algeo, T.J., 2019. Surficial weathering of kaolin regolith in a subtropical climate: Implications for supergene pedogenesis and bedrock argillization. Geoderma 337, 225–237. https://doi.org/10.1016/j.geoderma.2018.09.020

Fernandez, A., Borrok, D.M., 2009. Fractionation of Cu, Fe, and Zn isotopes during the oxidative weathering of sulfide-rich rocks. Chem. Geol. 264, 1–12. https://doi.org/10.1016/j.chemgeo.2009.01.024

Gaillardet, J., Dupré, B., Louvat, P., Allègre, C.J., 1999. Global silicate weathering and CO2 consumption rates deduced from the chemistry of large rivers. Chem. Geol. 159, 3–30. https://doi.org/10.1016/S0009-2541(99)00031-5

Gao, Y., Casey, J.F., 2012. Lithium Isotope Composition of Ultramafic Geological Reference Materials JP-1 and DTS-2. Geostand. Geoanalytical Res. 36, 75–81. https://doi.org/10.1111/j.1751-908X.2011.00117.x

Geilert, S., Vroon, P.Z., Roerdink, D.L., Van Cappellen, P., van Bergen, M.J., 2014. Silicon isotope fractionation during abiotic silica precipitation at low temperatures: Inferences from flow-through experiments. Geochim. Cosmochim. Acta 142, 95–114. https://doi.org/10.1016/j.gca.2014.07.003

Geng, G., Shi, Z., Leemann, A., Borca, C., Huthwelker, T., Glazyrin, K., Pekov, I. V., Churakov, S., Lothenbach, B., Dähn, R., Wieland, E., 2020. Atomistic structure of alkali-silica reaction products refined from X-ray diffraction and micro X-ray absorption data. Cem. Concr. Res. 129. https://doi.org/10.1016/j.cemconres.2019.105958

Georg, R.B., Reynolds, B.C., West, A.J., Burton, K.W., Halliday, A.N., 2007. Silicon isotope variations

accompanying basalt weathering in Iceland. Earth Planet. Sci. Lett. 261, 476–490. https://doi.org/10.1016/j.epsl.2007.07.004

Giambelluca, T.W., Chen, Q., Frazier, A.G., Price, J.P., Chen, Y.L., Chu, P.S., Eischeid, J.K., Delparte, D.M., 2013. Online rainfall atlas of Hawai'i. Bull. Am. Meteorol. Soc. 94, 313–316. https://doi.org/10.1175/BAMS-D-11-00228.1

Gillaspy, G.E., Keddie, J.S., Oda, K., Gruissem, W., 1995. Plant inositol monophosphatase is a lithium-sensitive enzyme encoded by a multigene family. Plant Cell 7, 2175–2185. https://doi.org/10.1105/tpc.7.12.2175

Glezakou, V.A., Chen, Y., Fulton, J.L., Schenter, G.K., Dang, L.X., 2006. Electronic structure, statistical mechanical simulations, and EXAFS spectroscopy of aqueous potassium. Theor. Chem. Acc. 115, 86–99. https://doi.org/10.1007/s00214-005-0054-4

Goldich, S.S., 1938. A Study in Rock-Weathering. J. Geol. 46, 17–58. https://doi.org/10.1086/624619

Goodfellow, B.W., Chadwick, O.A., Hilley, G.E., 2014. Depth and character of rock weathering across a basaltic-hosted climosequence on Hawai'i. Earth Surf. Process. Landforms 39, 381–398. https://doi.org/10.1002/esp.3505

Gou, L.F., Jin, Z., Pogge von Strandmann, P.A.E., Li, G., Qu, Y.X., Xiao, J., Deng, L., Galy, A., 2019. Li isotopes in the middle Yellow River: Seasonal variability, sources and fractionation. Geochim. Cosmochim. Acta 248, 88–108. https://doi.org/10.1016/j.gca.2019.01.007

Gou, W., Li, J., Li, W, 2018. Zinc Isotope Fractionation during Sorption onto Al Oxides: Atomic Level Understanding from EXAFS. Environ. Sci. Technol. 52, 9087–9096. https://doi.org/10.1021/acs.est.8b01414

Greaves, G.N., Gurman, S.J., Catlow, C.R.A., Chadwick, A. V., Houde-Walter, S., Henderson, C.M.B., Dobson, B.R., 1991. A structural basis for ionic diffusion in oxide glasses. Philos. Mag. A Phys. Condens. Matter, Struct. Defects Mech. Prop. 64, 1059–1072. https://doi.org/10.1080/01418619108204878

Griffioen, J., 2001. Potassium adsorption ratios as an indicator for the fate of agricultural potassium in groundwater. J. Hydrol. 254, 244–254. https://doi.org/10.1016/S0022-1694(01)00503-0

Gu, C., Hart, S.C., Turner, B.L., Hu, Y., Meng, Y., Zhu, M., 2019. Aeolian dust deposition and the perturbation of phosphorus transformations during long-term ecosystem development in a cool, semi-arid environment. Geochim. Cosmochim. Acta 246, 498–514. https://doi.org/10.1016/j.gca.2018.12.017

Guinoiseau, D., Gélabert, A., Moureau, J., Louvat, P., Benedetti, M.F., 2016. Zn Isotope Fractionation during Sorption onto Kaolinite. Environ. Sci. Technol. 50, 1844–1852. https://doi.org/10.1021/acs.est.5b05347

Gupta, N., Yadav, K.K., Kumar, V., Kumar, S., Chadd, R.P., Kumar, A., 2019. Trace elements in soil-vegetables interface: Translocation, bioaccumulation, toxicity and amelioration - A review. Sci. Total Environ. https://doi.org/10.1016/j.scitotenv.2018.10.047

Guelke, M., Von Blanckenburg, F., 2007. Fractionation of stable iron isotopes in higher plants. Environ. Sci. Technol. 41, 1896–1901. https://doi.org/10.1021/es062288j

Giambelluca, T. W., Chen, Q., Frazier, A. G., Price, J. P., Chen, Y. L., Chu, P. S., Eischied, J. K., Delparte, D. M., 2013. Online rainfall atlas of Hawai'i. Bull. Am. Meteor. Soc. 94(3), 313-316. https://doi.org/10.1175/BAMS-D-11-00228.1

Gaschnig, R. M., Rudnick, R. L., McDonough, W. F., Kaufman, A. J., Hu, Z. and Gao, S., 2014. Onset of oxidative weathering of continents recorded in the geochemistry of ancient glacial diamictites. Earth Planet. Sci. Lett. 408, 87-99. https://doi.org/10.1016/j.epsl.2014.10.002

Hänggi, P., Talkner, P., Borkovec, M., 1990. Reaction-rate theory: Fifty years after Kramers. Rev. Mod. Phys. 62, 251–341. https://doi.org/10.1103/RevModPhys.62.251

Hannon, A.C., Vessal, B., Parker, J.M., 1992. The structure of alkali silicate glasses. J. Non. Cryst. Solids 150, 97–102. https://doi.org/10.1016/0022-3093(92)90102-P

Hartmann, J., West, A.J., Renforth, P., Köhler, P., De La Rocha, C.L., Wolf-Gladrow, D.A., Dürr, H.H., Scheffran, J., 2013. Enhanced chemical weathering as a geoengineering strategy to reduce atmospheric carbon dioxide, supply nutrients, and mitigate ocean acidification. Rev. Geophys. 51, 113–149. https://doi.org/10.1002/rog.20004

Hastwell, G., 2005. Nutrient cycling and limitation: Hawaii as a model system. Austral Ecol. 30, 609–610. https://doi.org/10.1111/j.1442-9993.2005.01458.x

Hathorne, E.C., James, R.H., 2006. Temporal record of lithium in seawater: A tracer for silicate weathering? Earth Planet. Sci. Lett. 246, 393–406. https://doi.org/10.1016/j.epsl.2006.04.020

Hausrath, E.M., Navarre-Sitchler, A.K., Sak, P.B., Williams, J.Z., Brantley, S.L., 2011. Soil profiles as indicators of mineral weathering rates and organic interactions for a Pennsylvania diabase. Chem. Geol. 290, 89–100. https://doi.org/10.1016/j.chemgeo.2011.08.014

Heidmann, I., Christl, I., Kretzschmar, R., 2005. Sorption of Cu and Pb to kaolinite-fulvic acid colloids: Assessment of sorbent interactions. Geochim. Cosmochim. Acta 69, 1675–1686. https://doi.org/10.1016/j.gca.2004.10.002

Heimsath, A.M., DiBiase, R.A., Whipple, K.X., 2012. Soil production limits and the transition to bedrock-dominated landscapes. Nat. Geosci. 5, 210–214. https://doi.org/10.1038/ngeo1380

Henchiri, S., Gaillardet, J., Dellinger, M., Bouchez, J., Spencer, R.G.M., 2016. Riverine dissolved lithium isotopic signatures in low-relief central Africa and their link to weathering regimes. Geophys. Res. Lett. 43, 4391–4399. https://doi.org/10.1002/2016GL067711

Henderson, G.M., 2002. New oceanic proxies for paleoclimate. Earth Planet. Sci. Lett. 203, 1–13. https://doi.org/10.1016/S0012-821X(02)00809-9

Hess, J., Bender, M.L., Schilling, J.G., 1986. Evolution of the ratio of strontium-87 to strontium-86 in seawater from cretaceous to present. Science 231, 979–984. https://doi.org/10.1126/science.231.4741.979

Hille, M., Hu, Y., Huang, T.Y., Teng, F.Z., 2019. Homogeneous and heavy potassium isotopic composition of global oceans. Sci. Bull. 64, 1740–1742. https://doi.org/10.1016/j.scib.2019.09.024

Hindshaw, R.S., Tosca, R., Goût, T.L., Farnan, I., Tosca, N.J., Tipper, E.T., 2019. Experimental constraints on Li isotope fractionation during clay formation. Geochim. Cosmochim. Acta 250, 219–237. https://doi.org/10.1016/j.gca.2019.02.015

Ho, Y.S., McKay, G., 1999. Pseudo-second order model for sorption processes. Process Biochem. 34, 451–465. https://doi.org/10.1016/S0032-9592(98)00112-5

Hofmann, A.E., Bourg, I.C., DePaolo, D.J., 2012. Ion desolvation as a mechanism for kinetic isotope fractionation in aqueous systems. Proc. Natl. Acad. Sci. U. S. A. 109, 18689–18694. https://doi.org/10.1073/pnas.1208184109

Holland, H.D., 2005. Sea level, sediments and the composition of seawater. Am. J. Sci. 305, 220–239. https://doi.org/10.2475/ajs.305.3.220

Hotchkiss, S., Vitousek, P.M., Chadwick, O.A., Price, J., 2000. Climate cycles, geomorphological change, and the interpretation of soil and ecosystem development. Ecosystems 3, 522–533. https://doi.org/10.1007/s100210000046

Howard, J.L., Clawson, C.R., Daniels, W.L., 2012. A comparison of mineralogical techniques and potassium adsorption isotherm analysis for relative dating and correlation of Late Quaternary soil chronosequences. Geoderma 179–180, 81–95. https://doi.org/10.1016/j.geoderma.2012.02.020

Hsieh, J.C.C., Chadwick, O.A., Kelly, E.F., Savin, S.M., 1998. Oxygen isotopic composition of soil water: Quantifying evaporation and transpiration. Geoderma 82, 269–293. https://doi.org/10.1016/S0016-7061(97)00105-5

Hanano, D., Weis, D., Scoates, J. S., Aciego, S., DePaolo, D. J., 2010. Horizontal and vertical zoning of heterogeneities in the Hawaiian mantle plume from the geochemistry of consecutive postshield volcano pairs: Kohala-Mahukona and Mauna Kea–Hualalai. Geochem. Geophy. Geosys. 11(1). Q01004. https://doi.org/10.1029/2009GC002782

Hu, Y., Chen, X.Y., Xu, Y.K., Teng, F.Z., 2018. High-precision analysis of potassium isotopes by HR-MC-ICPMS. Chem. Geol. 493, 100–108. https://doi.org/10.1016/j.chemgeo.2018.05.033

Hu, Y.F., Coulthard, I., Chevrier, D., Wright, G., Igarashi, R., Sitnikov, A., Yates, B.W., Hallin, E.L., Sham, T.K., Reininger, R., 2010. Preliminary commissioning and performance of the soft x-ray micro-characterization beamline at the Canadian light source, in: AIP Conference Proceedings. pp. 343–346. https://doi.org/10.1063/1.3463208

Huang, K.F., You, C.F., Liu, Y.H., Wang, R.M., Lin, P.Y., Chung, C.H., 2010. Low-memory, small sample size, accurate and high-precision determinations of lithium isotopic ratios in natural materials by MC-ICP-MS. J. Anal. At. Spectrom. 25, 1019–1024. https://doi.org/10.1039/b926327f

Huang, T.Y., Teng, F.Z., Rudnick, R.L., Chen, X.Y., Hu, Y., Liu, Y.S., Wu, F.Y., 2020. Heterogeneous potassium isotopic composition of the upper continental crust. Geochim. Cosmochim. Acta 278, 122–136. https://doi.org/10.1016/j.gca.2019.05.022

Huffman, G.P., Huggins, F.E., Shoenberger, R.W., Walker, J.S., Lytle, F.W., Greegor, R.B., 1986. Investigation of the structural forms of potassium in coke by electron microscopy and X-ray absorption spectroscopy. Fuel 65, 621–632. https://doi.org/10.1016/0016-2361(86)90354-6

Huh, Y., Chan, L.H., Chadwick, O.A., 2004. Behavior of lithium and its isotopes during weathering of Hawaiian basalt. Geochem. Geophys. Geosys. 5. https://doi.org/10.1029/2004GC000729

Huh, Y., Chan, L.H., Edmond, J.M., 2001. Lithium isotopes as a probe of weathering processes: Orinoco River. Earth Planet. Sci. Lett. 194, 189–199. https://doi.org/10.1016/S0012-821X(01)00523-4

Huh, Y., Chan, L.H., Zhang, L., Edmond, J.M., 1998. Lithium and its isotopes in major world rivers: implications for weathering and the oceanic budget. Geochim. Cosmochim. Acta 62, 2039–2051. https://doi.org/10.1016/S0016-7037(98)00126-4

Holmqvist J., Øgaard A.F., Öborn I., Edwards A.C., Mattsson L., Sverdrup H., 2003. Application of the profile model to estimate potassium release from mineral weathering in Northern European agricultural soils. Eur. J. Agron. 20(1-2),149–163. https://doi.org/10.1016/S1161-0301(03)00064-9

Humayun, M., Koeberl, C., 2004. Potassium isotopic composition of Australasian tektites. Meteorit. Planet. Sci. 39, 1509–1516. https://doi.org/10.1111/j.1945-5100.2004.tb00125.x

Humayun, M., Clayton, R.N., 1995. Precise determination of the isotopic composition of potassium: Application to terrestrial rocks and lunar soils. Geochim. Cosmochim. Acta 59(10), 2115–2130. https://doi.org/10.1016/0016-7037(95)00131-X

Iler, R.K., 1979. The chemistry of silica. https://doi.org/10.1016/0160-9327(80)90074-5

Imseng, M., Wiggenhauser, M., Keller, A., Müller, M., Rehkämper, M., Murphy, K., Kreissig, K., Frossard, E., Wilcke, W., Bigalke, M., 2018. Fate of Cd in Agricultural Soils: A Stable Isotope Approach to Anthropogenic Impact, Soil Formation, and Soil-Plant Cycling. Environ. Sci. Technol. 52, 1919–1928. https://doi.org/10.1021/acs.est.7b05439

Jabraoui, H., Achhal, E.M., Hasnaoui, A., Garden, J.L., Vaills, Y., Ouaskit, S., 2016. Molecular dynamics simulation of thermodynamic and structural properties of silicate glass: Effect of the alkali oxide modifiers. J. Non. Cryst. Solids 448, 16–26. https://doi.org/10.1016/j.jnoncrysol.2016.06.030

Jackson, M.L., Levelt, T.W.M., Syers, J.K., Rex, R.W., Clayton, R.N., Sherman, G.D., Uehara, G., 1971. Geomorphological relationships of tropospherically derived quartz in the soils of the Hawaiian Islands. pp. 515–525. https://doi.org/10.2136/sssaj1971.03615995003500040051x

Jackson, W.E., Brown, G.E., Ponader, C.W., 1987. X-ray absorption study of the potassium coordination environment in glasses from the NaAlSi3O8-KAlSi3O8 binary. Structural implications for the mixed-alkali effect. J. Non. Cryst. Solids 93, 311–322. https://doi.org/10.1016/S0022-3093(87)80177-1

James, R.H., Palmer, M.R., 2000. The lithium isotope composition of international rock standards. Chem. Geol. 166, 319–326. https://doi.org/10.1016/S0009-2541(99)00217-X

Jeffcoate, A.B., Elliott, T., Thomas, A., Bouman, C., 2004. Precise, small sample size determinations of lithium isotopic compositions of geological reference materials and modern seawater by MC-ICP-MS. Geostand. Geoanalytical Res. 28, 161–172. https://doi.org/10.1111/j.1751-908X.2004.tb01053.x

Jobbágy, E.G., Jackson, R.B., 2001. The distribution of soil nutrients with depth: Global patterns and the imprint of plants. Biogeochemistry 53, 51–77. https://doi.org/10.1023/A:1010760720215

John, C.M., Mutti, M., Adatte, T., 2003. Mixed carbonate-siliciclastic record on the North African margin (Malta) - Coupling of weathering processes and mid Miocene climate. Bull. Geol. Soc. Am. 115, 217–229. https://doi.org/10.1130/0016-7606(2003)115<0217:MCSROT>2.0.CO;2

Jouvin, D., Weiss, D.J., Mason, T.F.M., Bravin, M.N., Louvat, P., Zhao, F., Ferec, F., Hinsinger, P., Benedetti, M.F., 2012. Stable isotopes of Cu and Zn in higher plants: Evidence for Cu reduction at the root surface and two conceptual models for isotopic fractionation processes. Environ. Sci. Technol. 46, 2652–2660. https://doi.org/10.1021/es202587m

Kalinowska, M., Hawrylak-Nowak, B., Szymańska, M., 2013. The influence of two lithium forms on the growth, L-ascorbic acid content and lithium accumulation in lettuce plants. Biol. Trace Elem. Res. 152, 251–257. https://doi.org/10.1007/s12011-013-9606-y

Kamber, B.S., Greig, A., Collerson, K.D., 2005. A new estimate for the composition of weathered young upper continental crust from alluvial sediments, Queensland, Australia. Geochim. Cosmochim. Acta 69, 1041–1058. https://doi.org/10.1016/j.gca.2004.08.020

Kamijo, N., Handa, K., Umesaki, N., 1996. Soft x-ray xafs studies on the local structure of k2o-sio2 glasses. Mater. Trans. JIM 37, 927–931. https://doi.org/10.2320/matertrans1989.37.927

Kasting, J.F., Catling, D., 2003. Evolution of a Habitable Planet. Annu. Rev. Astron. Astrophys. 41, 429–

463. https://doi.org/10.1146/annurev.astro.41.071601.170049

Kennedy, M.J., Chadwick, O.A., Vitousek, P.M., Derry, L.A., Hendricks, D.M., 1998. Changing sources of base cations during ecosystem development, Hawaiian Islands. Geology 26, 1015–1018. https://doi.org/10.1130/0091-7613(1998)026<1015:CSOBCD>2.3.CO;2

Kiczka, M., Wiederhold, J.G., Frommer, J., Kraemer, S.M., Bourdon, B., Kretzschmar, R., 2010a. Iron isotope fractionation during proton- and ligand-promoted dissolution of primary phyllosilicates. Geochim. Cosmochim. Acta 74, 3112–3128. https://doi.org/10.1016/j.gca.2010.02.018

Kiczka, M., Wiederhold, J.G., Kraemer, S.M., Bourdon, B., Kretzschmar, R., 2010b. Iron isotope fractionation during Fe uptake and translocation in alpine plants. Environ. Sci. Technol. 44, 6144–6150. https://doi.org/10.1021/es100863b

Kimball, B.E., Rimstidt, J.D., Brantley, S.L., 2010. Chalcopyrite dissolution rate laws. Appl. Geochemistry 25, 972–983. https://doi.org/10.1016/j.apgeochem.2010.03.010

Kimmig, S.R., Holmden, C., Bélanger, N., 2018. Biogeochemical cycling of Mg and its isotopes in a sugar maple forest in Québec. Geochim. Cosmochim. Acta 230, 60–82. https://doi.org/10.1016/j.gca.2018.03.020

Kisakurek, B., James, R.H., Harris, N.B.W., 2005. Li and δ7Li in Himalayan rivers: Proxies for silicate weathering? Earth Planet. Sci. Lett. 237, 387–401. https://doi.org/10.1016/j.epsl.2005.07.019

Kisakürek, B., Widdowson, M., James, R.H., 2004. Behaviour of Li isotopes during continental weathering: The Bidar laterite profile, India. Chem. Geol. 212, 27–44. https://doi.org/10.1016/j.chemgeo.2004.08.027

Korkisch, J., Feik, F., Ahluwalia, S.S., 1967. Cation-exchange behaviour of several elements in nitric acid-organic solvent media. Talanta 14, 1069–1081. https://doi.org/10.1016/0039-9140(67)80145-0

Košler, J., Kučera, M., Sylvester, P., 2001. Precise measurement of Li isotopes in planktonic foraminiferal tests by quadrupole ICPMS. Chem. Geol. 181, 169–179. https://doi.org/10.1016/S0009-2541(01)00280-7

Kosmulski, M., 2006. pH-dependent surface charging and points of zero charge: III. Update. J. Colloid Interface Sci. 298(2), 730-741. https://doi.org/10.1016/j.jcis.2006.01.003

Kosmulski, M., 2011. The pH-dependent surface charging and points of zero charge. V. Update. J. Colloid Interface Sci. 353, 1–15. https://doi.org/10.1016/j.jcis.2010.08.023

Kump, L.R., Brantley, S.L., Arthur, M.A., 2000. Chemical Weathering, Atmospheric CO2 , and Climate . Annu. Rev. Earth Planet. Sci. 28, 611–667. https://doi.org/10.1146/annurev.earth.28.1.611

Kurtz, A.C., Derry, L.A., Chadwick, O.A., 2001. Accretion of Asian dust to Hawaiian soils: Isotopic, elemental, and mineral mass balances. Geochim. Cosmochim. Acta 65, 1971–1983. https://doi.org/10.1016/S0016-7037(01)00575-0

Kawada, K., Ol, T., Hosoe, M., Kakihana, H., 1991. Fractionation of potassium isotopes in cation-exchange chromatography. J. Chromatogr. A 538, 355–364. https://doi.org/10.1016/S0021-9673(01)88856-7

Kopáček, J., Turek, J., Hejzlar, J., Šantrůčková, H., 2009. Canopy leaching of nutrients and metals in a mountain spruce forest. Atmos. Environ. 43, 5443–5453. https://doi.org/10.1016/j.atmosenv.2009.07.031

Lagergren, S.K., 1898. About the theory of so-called adsorption of soluble substances. Sven.

Vetenskapsakad. Handingarl 24, 1–39.

Lam, P.J., Robinson, L.F., Blusztajn, J., Li, C., Cook, M.S., McManus, J.F., Keigwin, L.D., 2013. Transient stratification as the cause of the North Pacific productivity spike during deglaciation. Nat. Geosci. 6, 622–626. https://doi.org/10.1038/ngeo1873

Langmuir, I., 1918. The adsorption of gases on plane surfaces of glass, mica and platinum. J. Am. Chem. Soc. 40, 1361–1403. https://doi.org/10.1021/ja02242a004

Lechler, M., Pogge von Strandmann, P.A.E., Jenkyns, H.C., Prosser, G., Parente, M., 2015. Lithium-isotope evidence for enhanced silicate weathering during OAE 1a (Early Aptian Selli event). Earth Planet. Sci. Lett. 432, 210–222. https://doi.org/10.1016/j.epsl.2015.09.052

Lee, S., Anderson, P.R., Bunker, G.B., Karanfil, C., 2004. EXAFS study of Zn sorption mechanisms on montmorillonite. Environ. Sci. Technol. 38, 5426–5432. https://doi.org/10.1021/es0350076

Lemarchand, E., Chabaux, F., Vigier, N., Millot, R., Pierret, M.C., 2010. Lithium isotope systematics in a forested granitic catchment (Strengbach, Vosges Mountains, France). Geochim. Cosmochim. Acta 74, 4612–4628. https://doi.org/10.1016/j.gca.2010.04.057

Lenton, T.M., Von Bloh, W., 2001. Biotic feedback extends the life span of the biosphere. Geophys. Res. Lett. 28, 1715–1718. https://doi.org/10.1029/2000GL012198

Li, D., Liu, S.A., Li, S., 2015. Copper isotope fractionation during adsorption onto kaolinite: Experimental approach and applications. Chem. Geol. 396, 74–82. https://doi.org/10.1016/j.chemgeo.2014.12.020

Li, G., West, A.J., 2014. Evolution of Cenozoic seawater lithium isotopes: Coupling of global denudation regime and shifting seawater sinks. Earth Planet. Sci. Lett. 401, 284–293. https://doi.org/10.1016/j.epsl.2014.06.011

Li, J., Huang, X.L., Wei, G.J., Liu, Y., Ma, J.L., Han, L., He, P.L., 2018. Lithium isotope fractionation during magmatic differentiation and hydrothermal processes in rare-metal granites. Geochim. Cosmochim. Acta 240, 64–79. https://doi.org/10.1016/j.gca.2018.08.021

Li, S., Li, W., Beard, B.L., Raymo, M.E., Wang, X., Chen, Y., Chen, J., 2019. K isotopes as a tracer for continental weathering and geological K cycling. Proc. Natl. Acad. Sci. U. S. A. 116, 8740–8745. https://doi.org/10.1073/pnas.1811282116

Li, W., Beard, B.L., Li, S., 2016. Precise measurement of stable potassium isotope ratios using a single focusing collision cell multi-collector ICP-MS. J. Anal. At. Spectrom. 31, 1023–1029. https://doi.org/10.1039/c5ja00487j

Li, W., Kwon, K.D., Li, S., Beard, B.L., 2017. Potassium isotope fractionation between K-salts and saturated aqueous solutions at room temperature: Laboratory experiments and theoretical calculations. Geochim. Cosmochim. Acta 214, 1–13. https://doi.org/10.1016/j.gca.2017.07.037

Li, W., Liu, X.M., Godfrey, L. V., 2019. Optimisation of Lithium Chromatography for Isotopic Analysis in Geological Reference Materials by MC-ICP-MS. Geostand. Geoanalytical Res. 43, 261–276. https://doi.org/10.1111/ggr.12254

Li, W., Liu, X.M., 2020a. Mobilization and partitioning of rare earth elements in the presence of humic acids and siderophores. Chemosphere 254. https://doi.org/10.1016/j.chemosphere.2020.126801

Li, W., Liu, X. M., 2020b. Experimental investigation of lithium isotope fractionation during kaolinite adsorption: Implications for chemical weathering. Geochim. Cosmochim. Acta 284, 156-172.

https://doi.org/10.1016/j.gca.2020.06.025

Li, W., Liu, X.M., Chadwick, O.A., 2020a, Lithium isotope behavior in Hawaiian regoliths: Soil-atmosphere-biosphere exchanges. Geochim. Cosmochim. Acta 285, 175–192. https://doi.org/10.1016/j.gca.2020.07.012

Li, W., Liu, X.M., Hu, Y.F., 2020b, Potassium and calcium K-edge XANES in chemical compounds and minerals: Implications for geological phase identification. Geostand. Geoanalytical Res. 44(4), 805-819. https://doi.org/10.1111/ggr.12351

Li, W., Liu, X.M., Wang, K., Koefoed, P., 2021a. Lithium and potassium isotope fractionation during silicate rock dissolution: An experimental approach. Chem. Geol. 568, 120142. https://doi.org/10.1016/j.chemgeo.2021.120142

Li, W., Liu, X.M., Hu, Y., Teng, F.Z., Hu, Y.F., 2021b. Potassium isotopic fractionation during clay adsorption. Geochim. Cosmochim. Acta 304, 160-177. https://doi.org/10.1016/j.gca.2021.04.027

Li, W., Liu, X.M., Hu, Y., Teng, F.Z., Hu, Y.F., Chadwick, O.A., 2021c. Potassium isotopic fractionation in a humid and an arid soil–plant system in Hawai ‘i. Geoderma 400, 115219. https://doi.org/10.1016/j.geoderma.2021.115219

Li, Y., Wang, W., Huang, S., Wang, K., Wu, Z., 2019a. First-principles investigation of the concentration effect on equilibrium fractionation of K isotopes in feldspars. Geochim. Cosmochim. Acta 245, 374–384. https://doi.org/10.1016/j.gca.2018.11.006

Li, Y., Wang, W., Wu, Z., Huang, S., 2019b. First-principles investigation of equilibrium K isotope fractionation among K-bearing minerals. Geochim. Cosmochim. Acta 264, 30–42. https://doi.org/10.1016/j.gca.2019.07.038

Liao, Y., Zheng, S, Nie, J., Xie, J., Lu, Y., Qin, X., 2013. Long-term effect of fertilizer and rice straw on mineral composition and potassium adsorption in a reddish paddy Ssil. J. Integr. Agric. 12, 694–710. https://doi.org/10.1016/S2095-3119(13)60288-9

Lin, J., Liu, Y., Hu, Z., Yang, L., Chen, K., Chen, H., Zong, K., Gao, S., 2016. Accurate determination of lithium isotope ratios by MC-ICP-MS without strict matrix-matching by using a novel washing method. J. Anal. At. Spectrom. 31, 390–397. https://doi.org/10.1039/c5ja00231a

Liu, H.C., You, C.F., Huang, K.F., Chung, C.H., 2012. Precise determination of triple Sr isotopes (δ87Sr and δ88Sr) using MC-ICP-MS. Talanta 88, 338–344. https://doi.org/10.1016/j.talanta.2011.10.050

Liu, S., Li, Y., Liu, Jie, Ju, Y., Liu, Jianming, Yang, Z., Shi, Y., 2018. Equilibrium lithium isotope fractionation in Li-bearing minerals. Geochim. Cosmochim. Acta 235, 360–375. https://doi.org/10.1016/j.gca.2018.05.029

Liu, X.M., Li, W., 2019. Optimization of lithium isotope analysis in geological materials by quadrupole ICP-MS. J. Anal. At. Spectrom. 34, 1708–1717. https://doi.org/10.1039/c9ja00175a

Liu, X.M., Rudnick, R.L., 2011. Constraints on continental crustal mass loss via chemical weathering using lithium and its isotopes. Proc. Natl. Acad. Sci. U. S. A. 108, 20873–20880. https://doi.org/10.1073/pnas.1115671108

Liu, X.M., Rudnick, R.L., McDonough, W.F., Cummings, M.L., 2013. Influence of chemical weathering on the composition of the continental crust: Insights from Li and Nd isotopes in bauxite profiles developed on Columbia River Basalts. Geochim. Cosmochim. Acta 115, 73–91. https://doi.org/10.1016/j.gca.2013.03.043

Liu, X.M., Teng, F.Z., Rudnick, R.L., McDonough, W.F., Cummings, M.L., 2014. Massive magnesium depletion and isotope fractionation in weathered basalts. Geochim. Cosmochim. Acta 135, 336–349. https://doi.org/10.1016/j.gca.2014.03.028

Liu, X.M., Wanner, C., Rudnick, R.L., McDonough, W.F., 2015. Processes controlling δ7Li in rivers illuminated by study of streams and groundwaters draining basalts. Earth Planet. Sci. Lett. 409, 212–224. https://doi.org/10.1016/j.epsl.2014.10.032

Liu, Y., Lu, H., Wu, Y., Hu, T., Li, Q., 2010. Hydration and coordination of K^+ solvation in water from ab initio molecular-dynamics simulation. J. Chem. Phys. 132. https://doi.org/10.1063/1.3369624

Low, M.J.D., 1960. Kinetics of chemisorption of gases on solids. Chem. Rev. 60, 267–312. https://doi.org/10.1021/cr60205a003

Lucas, Y., 2001. The role of plants in controlling rates and products of weathering: Importance of biological pumping. Annu. Rev. Earth Planet. Sci. 29, 135–163. https://doi.org/10.1146/annurev.earth.29.1.135

Li, X., Han, G., Zhang, Q., Miao, Z., 2020. Optimal separation method for high-precision K isotope analysis by using MC-ICP-MS with a dummy bucket. J. Anal. At. Spectrom. 35(7), 1330-1339. https://doi.org/10.1039/D0JA00127A

Lützenkirchen, J., 1997. Ionic strength effects on cation sorption to oxides: Macroscopic observations and their significance in microscopic interpretation. J. Colloid Interface Sci. 195, 149–155. https://doi.org/10.1006/jcis.1997.5160

Lerman, A., Meybeck, M., 2012. Physical and Chemical Weathering in Geochemical Cycles. Nato Science Series C. 251. Springer Science & Business Media.

Lacan, F., Tachikawa, K., Jeandel, C., 2012. Neodymium isotopic composition of the oceans: A compilation of seawater data. Chem. Geol. 300, 177-184. https://doi.org/10.1016/j.chemgeo.2012.01.019

Ma, T., Weynell, M., Li, S.L., Liu, Y., Chetelat, B., Zhong, J., Xu, S., Liu, C.Q., 2020. Lithium isotope compositions of the Yangtze River headwaters: Weathering in high-relief catchments. Geochim. Cosmochim. Acta 280, 46–65. https://doi.org/10.1016/j.gca.2020.03.029

Magna, T., Wiechert, U.H., Halliday, A.N., 2004. Low-blank isotope ratio measurement of small samples of lithium using multiple-collector ICPMS. Int. J. Mass Spectrom. 239, 67–76. https://doi.org/10.1016/j.ijms.2004.09.008

Marschall, H.R., Pogge von Strandmann, P.A.E., Seitz, H.M., Elliott, T., Niu, Y., 2007. The lithium isotopic composition of orogenic eclogites and deep subducted slabs. Earth Planet. Sci. Lett. 262, 563–580. https://doi.org/10.1016/j.epsl.2007.08.005

Mavromatis, V., Harrison, A.L., Eisenhauer, A., Dietzel, M., 2017. Strontium isotope fractionation during strontianite (SrCO3) dissolution, precipitation and at equilibrium. Geochim. Cosmochim. Acta 218, 201–214. https://doi.org/10.1016/j.gca.2017.08.039

Mavromatis, V., van Zuilen, K., Purgstaller, B., Baldermann, A., Nägler, T.F., Dietzel, M., 2016. Barium isotope fractionation during witherite (BaCO3) dissolution, precipitation and at equilibrium. Geochim. Cosmochim. Acta 190, 72–84. https://doi.org/10.1016/j.gca.2016.06.024

Mazzi, F., Galli, E., Gottardi, G., 1976. The crystal structure of tetragonal leucite. Am. Mineral. 61, 108–115.

Miller, D.G., Ting, A.W., Rard, J.A., Eppstein, L.B., 1986. Ternary diffusion coefficients of the brine systems NaCl (0.5 M)-Na2SO4 (0.5 M)-H2O and NaCl (0.489 M)-MgCl2 (0.051 M)-H2O (seawater composition) at 25°C. Geochim. Cosmochim. Acta 50, 2397–2403. https://doi.org/10.1016/0016-7037(86)90021-9

Millot, R., Girard, J.P., 2007. Lithium isotope fractionation during adsorption onto mineral surfaces. Clays Nat. Eng. Barriers Radioact. Waste Confin. 3rd Int. Meet. 307–308.

Millot, R., Guerrot, C., Vigier, N., 2004. Accurate and high-precision measurement of lithium isotopes in two reference materials by MC-ICP-MS. Geostand. Geoanalytical Res. 28, 153–159. https://doi.org/10.1111/j.1751-908X.2004.tb01052.x

Millot, R., Petelet-Giraud, E., Guerrot, C., Négrel, P., 2010a. Multi-isotopic composition (δ7Li-δ11B-δD-δ18O) of rainwaters in France: Origin and spatio-temporal characterization. Appl. Geochemistry 25, 1510–1524. https://doi.org/10.1016/j.apgeochem.2010.08.002

Millot, R., Vigier, N., Gaillardet, J., 2010b. Behaviour of lithium and its isotopes during weathering in the Mackenzie Basin, Canada. Geochim. Cosmochim. Acta 74, 3897–3912. https://doi.org/10.1016/j.gca.2010.04.025

Misra, S., Froelich, P.N., 2012. Lithium isotope history of cenozoic seawater: Changes in silicate weathering and reverse weathering. Science 335, 818–823. https://doi.org/10.1126/science.1214697

Misra, S., Froelich, P.N., 2009. Measurement of lithium isotope ratios by quadrupole-ICP-MS: Application to seawater and natural carbonates. J. Anal. At. Spectrom. 24, 1524–1533. https://doi.org/10.1039/b907122a

Morgan, L.E., Santiago Ramos, D.P., Davidheiser-Kroll, B., Faithfull, J., Lloyd, N.S., Ellam, R.M., Higgins, J.A., 2018. High-precision 41K/39K measurements by MC-ICP-MS indicate terrestrial variability of: δ 41K. J. Anal. At. Spectrom. 33, 175–186. https://doi.org/10.1039/c7ja00257b

Moriguti, T., Nakamura, E., 1998. High-yield lithium separation and the precise isotopic analysis for natural rock and aqueous samples. Chem. Geol. 145, 91–104. https://doi.org/10.1016/S0009-2541(97)00163-0

Murphy, M.J., Porcelli, D., Pogge von Strandmann, P.A.E., Hirst, C.A., Kutscher, L., Katchinoff, J.A., Mörth, C.M., Maximov, T., Andersson, P.S., 2019. Tracing silicate weathering processes in the permafrost-dominated Lena River watershed using lithium isotopes. Geochim. Cosmochim. Acta 245, 154–171. https://doi.org/10.1016/j.gca.2018.10.024

Moynier, F., Hu, Y., Wang, K., Zhao, Y., Gérard, Y., Deng ,Z., Moureau, J., Li, W.Q., Simon, J.I., Teng, F.Z., 2021. Potassium isotopic composition of various samples using a dual-path collision cell-capable multiple-collector inductively coupled plasma mass spectrometer, Nu instruments Sapphire. Chem. Geol. 571, 120144. https://doi.org/10.1016/j.chemgeo.2021.120144

McDougall, I., 1964. Potassium-argon ages from lavas of the Hawaiian Islands. Geol. Soc. Am. Bull. 75(2), 107-128. https://doi.org/10.1130/0016-7606(1964)75[107:PAFLOT]2.0.CO;2

Merrill, J., Arnold, E., Leinen, M., Weaver, C., 1994. Mineralogy of aerolian dust reaching the North Pacific Ocean 2. Relationship of mineral assemblages to atmospheric transport patterns. J. Geophys. Res. 99, 21025-21032. https://doi.org/10.1029/94JD01734

Nielsen, L.C., DePaolo, D.J., De Yoreo, J.J., 2012. Self-consistent ion-by-ion growth model for kinetic isotopic fractionation during calcite precipitation. Geochim. Cosmochim. Acta 86, 166–181. https://doi.org/10.1016/j.gca.2012.02.009

Nishi, K., Shimizu, K.I., Takamatsu, M., Yoshida, H., Satsuma, A., Tanaka, T., Yoshida, S., Hattori, T., 1998. Deconvolution analysis of Ga K-Edge XANES for quantification of gallium coordinations in oxide environments. J. Phys. Chem. B 102, 10190–10195. https://doi.org/10.1021/jp982704p

Nishio, Y., Nakai, S., 2002. Accurate and precise lithium isotopic determinations of igneous rock samples using multi-collector inductively coupled plasma mass spectrometry. Anal. Chim. Acta 456, 271–281. https://doi.org/10.1016/S0003-2670(02)00042-9

Nesbitt, H., Young, G. M., 1982. Early Proterozoic climates and plate motions inferred from major element chemistry of lutites. Nature 299(5885), 715-717. https://doi.org/10.1038/299715a0

Ockert, C., Gussone, N., Kaufhold, S., Teichert, B.M.A., 2013. Isotope fractionation during Ca exchange on clay minerals in a marine environment. Geochim. Cosmochim. Acta 112, 374–388. https://doi.org/10.1016/j.gca.2012.09.041

Olasolo, P., Juárez, M.C., Morales, M.P., Damico, S., Liarte, I.A., 2016. Enhanced geothermal systems (EGS): A review. Renew. Sustain. Energy Rev. https://doi.org/10.1016/j.rser.2015.11.031

Opfergelt, S., Burton, K.W., Georg, R.B., West, A.J., Guicharnaud, R.A., Sigfusson, B., Siebert, C., Gislason, S.R., Halliday, A.N., 2014. Magnesium retention on the soil exchange complex controlling Mg isotope variations in soils, soil solutions and vegetation in volcanic soils, Iceland. Geochim. Cosmochim. Acta 125, 110–130. https://doi.org/10.1016/j.gca.2013.09.036

Pal, Y., Wong, M.T.F., Gilkes, R.J., 1999. The forms of potassium and potassium adsorption in some virgin soils from south-western Australia. Aust. J. Soil Res. 37, 695–709. https://doi.org/10.1071/sr98083

Palumbo, B., Angelone, M., Bellanca, A., Dazzi, C., Hauser, S., Neri, R., Wilson, J., 2000. Influence of inheritance and pedogenesis on heavy metal distribution in soils of Sicily, Italy. Geoderma 95, 247–266. https://doi.org/10.1016/S0016-7061(99)00090-7

Parendo, C.A., Jacobsen, S.B., Wang, K., 2017. K isotopes as a tracer of seafloor hydrothermal alteration. Proc. Natl. Acad. Sci. U. S. A. 114, 1827–1831. https://doi.org/10.1073/pnas.1609228114

Parkhurst, D.L., Appelo, C.A.J., 2013. Description of Input and Examples for PHREEQC Version 3 — A Computer Program for Speciation , Batch-Reaction , One-Dimensional Transport , and Inverse Geochemical Calculations. U.S. Geol. Surv. Tech. Methods, B. 6, chapter A43. https://doi.org/10.1016/0029-6554(94)90020-5

Parrington, J.R., Zoller, W.H., Aras, N.K., 1983. Asian dust: Seasonal transport to the Hawaiian Islands. Science 220, 195–197. https://doi.org/10.1126/science.220.4593.195

Peacock, C.L., Sherman, D.M., 2004. Copper(II) sorption onto goethite, hematite and lepidocrocite: A surface complexation model based on ab initio molecular geometries and EXAFS spectroscopy. Geochim. Cosmochim. Acta 68, 2623–2637. https://doi.org/10.1016/j.gca.2003.11.030

Pearce, C.R., Saldi, G.D., Schott, J., Oelkers, E.H., 2012. Isotopic fractionation during congruent dissolution, precipitation and at equilibrium: Evidence from Mg isotopes. Geochim. Cosmochim. Acta 92, 170–183. https://doi.org/10.1016/j.gca.2012.05.045

Penniston-Dorland, S., Liu, X.M., Rudnick, R.L., 2017. Lithium isotope geochemistry, in: Non-Traditional Stable Isotopes. Walter de Gruyter GmbH, pp. 165–218. https://doi.org/10.2138/rmg.2017.82.6

Pfister, S., Capo, R.C., Stewart, B.W., Macpherson, G.L., Phan, T.T., Gardiner, J.B., Diehl, J.R., Lopano, C.L., Hakala, J.A., 2017. Geochemical and lithium isotope tracking of dissolved solid sources in

Permian Basin carbonate reservoir and overlying aquifer waters at an enhanced oil recovery site, northwest Texas, USA. Appl. Geochem. 87, 122–135. https://doi.org/10.1016/j.apgeochem.2017.10.013

Phan, T.T., Capo, R.C., Stewart, B.W., Macpherson, G.L., Rowan, E.L., Hammack, R.W., 2016. Factors controlling Li concentration and isotopic composition in formation waters and host rocks of Marcellus Shale, Appalachian Basin. Chem. Geol. 420, 162–179. https://doi.org/10.1016/j.chemgeo.2015.11.003

Pistiner, J.S., Henderson, G.M., 2003. Lithium-isotope fractionation during continental weathering processes. Earth Planet. Sci. Lett. 214, 327–339. https://doi.org/10.1016/S0012-821X(03)00348-0

Pogge von Strandmann, P.A.E., Burton, K.W., James, R.H., van Calsteren, P., Gíslason, S.R., Mokadem, F., 2006. Riverine behaviour of uranium and lithium isotopes in an actively glaciated basaltic terrain. Earth Planet. Sci. Lett. 251, 134–147. https://doi.org/10.1016/j.epsl.2006.09.001

Pogge von Strandmann, P.A.E., Fraser, W.T., Hammond, S.J., Tarbuck, G., Wood, I.G., Oelkers, E.H., Murphy, M.J., 2019. Experimental determination of Li isotope behaviour during basalt weathering. Chem. Geol. 517, 34–43. https://doi.org/10.1016/j.chemgeo.2019.04.020

Pogge von Strandmann, P.A.E., Frings, P.J., Murphy, M.J., 2017. Lithium isotope behaviour during weathering in the Ganges Alluvial Plain. Geochim. Cosmochim. Acta 198, 17–31. https://doi.org/10.1016/j.gca.2016.11.017

Pogge von Strandmann, P.A.E., Henderson, G.M., 2015. The Li isotope response to mountain uplift. Geology 43, 67–70. https://doi.org/10.1130/G36162.1

Pogge von Strandmann, P.A.E., James, R.H., van Calsteren, P., Gíslason, S.R., Burton, K.W., 2008. Lithium, magnesium and uranium isotope behaviour in the estuarine environment of basaltic islands. Earth Planet. Sci. Lett. 274, 462–471. https://doi.org/10.1016/j.epsl.2008.07.041

Pogge Von Strandmann, P.A.E., Jenkyns, H.C., Woodfine, R.G., 2013. Lithium isotope evidence for enhanced weathering during Oceanic Anoxic Event 2. Nat. Geosci. 6, 668–672. https://doi.org/10.1038/ngeo1875

Pogge von Strandmann, P.A.E., Opfergelt, S., Lai, Y.J., Sigfússon, B., Gislason, S.R., Burton, K.W., 2012. Lithium, magnesium and silicon isotope behaviour accompanying weathering in a basaltic soil and pore water profile in Iceland. Earth Planet. Sci. Lett. 339–340, 11–23. https://doi.org/10.1016/j.epsl.2012.05.035

Pogge von Strandmann, P.A.E., Burton, K.W., James, R.H., van Calsteren, P., Gislason, S.R., 2010. Assessing the role of climate on uranium and lithium isotope behaviour in rivers draining a basaltic terrain. Chem. Geol. 270, 227–239. https://doi.org/10.1016/j.chemgeo.2009.12.002

Pogge von Strandmann, P.A.E., Desrochers, A., Murphy, M.J., Finlay, A.J., Selby, D., Lenton, T.M., 2017. Global climate stabilisation by chemical weathering during the Hirnantian glaciation. Geochemical Perspect. Lett. 3, 230–237. https://doi.org/10.7185/geochemlet.1726

Pokrovsky, O.S., Galy, A., Schott, J., Pokrovski, G.S., Mantoura, S., 2014. Germanium isotope fractionation during Ge adsorption on goethite and its coprecipitation with Fe oxy(hydr)oxides. Geochim. Cosmochim. Acta 131, 138–149. https://doi.org/10.1016/j.gca.2014.01.023

Porder, S., Hilley, G.E., Chadwick, O.A., 2007. Chemical weathering, mass loss, and dust inputs across a climate by time matrix in the Hawaiian Islands. Earth Planet. Sci. Lett. 258, 414–427. https://doi.org/10.1016/j.epsl.2007.03.047

Putra, A.R., Tachibana, Y., Tanaka, M., Suzuki, T., 2018. Lithium isotope separation using displacement chromatography by cation exchange resin with high degree of cross-linkage. Fusion Eng. Des. 136, 377–380. https://doi.org/10.1016/j.fusengdes.2018.02.045

Punshon, T., Tappero, R., Ricachenevsky, F.K., Hirschi, K., Nakata, P.A., 2013. Contrasting calcium localization and speciation in leaves of the Medicago truncatula mutant cod5 analyzed via synchrotron X-ray techniques. Plant J. 76, 627–633. https://doi.org/10.1111/tpj.12322

Qafoku, N.P., 2015. Climate-change effects on soils: accelerated weathering, soil carbon, and elemental cycling. In Advances in Agronomy. Academic Press. pp. 111-172. https://doi.org/10.1016/bs.agron.2014.12.002

Raczek, I., Jochum, K.P., Hofmann, A.W., 2001. Neodymium and strontium isotope data for USGS reference GSP-1 , GSP-2 and eight MPI-DING reference glasses. Geostand. Newsletterthe J. Geostand. Geoanalysis 27, 173–179. https://doi.org/10.1111/j.1751-908X.2003.tb00644.x

Ravel, B., Newville, M., 2005. ATHENA, ARTEMIS, HEPHAESTUS: Data analysis for X-ray absorption spectroscopy using IFEFFIT. J. Synchrotron Radiation 12, 537–541. https://doi.org/10.1107/S0909049505012719

Reimann, C., Englmaier, P., Flem, B., Gough, L., Lamothe, P., Nordgulen, Smith, D., 2009. Geochemical gradients in soil O-horizon samples from southern Norway: Natural or anthropogenic? Appl. Geochemistry 24, 62–76. https://doi.org/10.1016/j.apgeochem.2008.11.021

Reinholdt, M.X., Hubert, F., Faurel, M., Tertre, E., Razafitianamaharavo, A., Francius, G., Prêt, D., Petit, S., Béré, E., Pelletier, M., Ferrage, E., 2013. Morphological properties of vermiculite particles in size-selected fractions obtained by sonication. Appl. Clay Sci. 77–78, 18–32. https://doi.org/10.1016/j.clay.2013.03.013

Rex, R.W., Syers, J.K., Jackson, M.L., Clayton, R.N., 1969. Eolian origin of quartz in soils of Hawaiian Islands and in Pacific pelagic sediments. Science 163, 277–279. https://doi.org/10.1126/science.163.3864.277

Richter, F.M., Bruce Watson, E., Chaussidon, M., Mendybaev, R., Christensen, J.N., Qiu, L., 2014. Isotope fractionation of Li and K in silicate liquids by Soret diffusion. Geochim. Cosmochim. Acta 138, 136–145. https://doi.org/10.1016/j.gca.2014.04.012

Richter, F.M., Mendybaev, R.A., Christensen, J.N., Hutcheon, I.D., Williams, R.W., Sturchio, N.C., Beloso, A.D., 2006. Kinetic isotopic fractionation during diffusion of ionic species in water. Geochim. Cosmochim. Acta 70, 277–289. https://doi.org/10.1016/j.gca.2005.09.016

Roberts, J., Kaczmarek, K., Langer, G., Skinner, L.C., Bijma, J., Bradbury, H., Turchyn, A. V., Lamy, F., Misra, S., 2018. Lithium isotopic composition of benthic foraminifera: A new proxy for paleo-pH reconstruction. Geochim. Cosmochim. Acta 236, 336–350. https://doi.org/10.1016/j.gca.2018.02.038

Robinson, B.H., Yalamanchali, R., Reiser, R., Dickinson, N.M., 2018. Lithium as an emerging environmental contaminant: Mobility in the soil-plant system. Chemosphere 197, 1–6. https://doi.org/10.1016/j.chemosphere.2018.01.012

Rosner, M., Ball, L., Peucker-Ehrenbrink, B., Blusztajn, J., Bach, W., Erzinger, J., 2007. A simplified, accurate and fast method for lithium isotope analysis of rocks and fluids, and δ7Li values of seawater and rock reference materials. Geostand. Geoanalytical Res. 31, 77–88. https://doi.org/10.1111/j.1751-908X.2007.00843.x

Rudnick, R.L., Gao, S., 2013. Composition of the Continental Crust, in: Treatise on Geochemistry:

Second Edition. Elsevier Inc., pp. 1–51. https://doi.org/10.1016/B978-0-08-095975-7.00301-6

Rudnick, R.L., Tomascak, P.B., Njo, H.B., Gardner, L.R., 2004. Extreme lithium isotopic fractionation during continental weathering revealed in saprolites from South Carolina. Chem. Geol. 212, 45–57. https://doi.org/10.1016/j.chemgeo.2004.08.008

Rudolph, W., Brooker, M.H., Pye, C.C., 1995. Hydration of lithium ion in aqueous solution. J. Phys. Chem. 99, 3793–3797. https://doi.org/10.1002/chin.199530002

Ryu, J.S., Jacobson, A.D., Holmden, C., Lundstrom, C., Zhang, Z., 2011. The major ion, δ44/40Ca, δ44/42Ca, and δ26/24Mg geochemistry of granite weathering at pH=1 and T=25°C: Power-law processes and the relative reactivity of minerals. Geochim. Cosmochim. Acta 75, 6004–6026. https://doi.org/10.1016/j.gca.2011.07.025

Ryu, J.S., Vigier, N., Lee, S.W., Lee, K.S., Chadwick, O.A., 2014. Variation of lithium isotope geochemistry during basalt weathering and secondary mineral transformations in Hawaii. Geochim. Cosmochim. Acta 145, 103–115. https://doi.org/10.1016/j.gca.2014.08.030

Rocha, J.H.T., Gonçalves, J.L., de, M., Ferraz, A., de, V., Poiati, D.A., Arthur Junior, J.C., Hubner, A. 2019. Growth dynamics and productivity of an Eucalyptus grandis plantation under omission of N, P, K Ca and Mg over two crop rotation. For. Ecol. Manage. 447, 158–168. https://doi.org/10.1016/j.foreco.2019.05.060

Santiago Ramos, D.P., Morgan, L.E., Lloyd, N.S., Higgins, J.A., 2018. Reverse weathering in marine sediments and the geochemical cycle of potassium in seawater: Insights from the K isotopic composition (41K/39K) of deep-sea pore-fluids. Geochim. Cosmochim. Acta 236, 99–120. https://doi.org/10.1016/j.gca.2018.02.035

Sardans, J., Peñuelas, J., 2015. Potassium: A neglected nutrient in global change. Glob. Ecol. Biogeogr. https://doi.org/10.1111/geb.12259

Sauzéat, L., Rudnick, R.L., Chauvel, C., Garçon, M., Tang, M., 2015. New perspectives on the Li isotopic composition of the upper continental crust and its weathering signature. Earth Planet. Sci. Lett. 428, 181–192. https://doi.org/10.1016/j.epsl.2015.07.032

Schauble, E.A., 2004. Applying stable isotope fractionation theory to new systems. Rev. Mineral. Geochemistry. https://doi.org/10.2138/gsrmg.55.1.65

Schoonheydt, R.A., Johnston, C.T., 2006. Chapter 3 Surface and Interface Chemistry of Clay Minerals. Dev. Clay Sci. https://doi.org/10.1016/S1572-4352(05)01003-2

Schweinsberg, H., Liebau, F., 1974. Die Kristallstruktur des K4[Si8O19]: ein neuer Silikat-Schichttyp . Acta Crystallogr. Sect. B Struct. Crystallogr. Cryst. Chem. 30, 2206–2213. https://doi.org/10.1107/s0567740874006753

Sen, A., Ganguly, B., 2010. What is the minimum number of water molecules required to dissolve a potassium chloride molecule? J. Comput. Chem. 31, 2948–2954. https://doi.org/10.1002/jcc.21590

Shahzad, B., Tanveer, M., Hassan, W., Shah, A.N., Anjum, S.A., Cheema, S.A., Ali, I., 2016. Lithium toxicity in plants: Reasons, mechanisms and remediation possibilities – A review. Plant Physiol. Biochem. https://doi.org/10.1016/j.plaphy.2016.05.034

Simmons, W.B.J., Peacor, D.R., 1972. Refinement of the crystal structure of a volcanic nepheline. Am. Miner. 57, 1711–1719.

Smith, D.L., Milford, M.H., Zuckerman, J.J., 1966. Mechanism for intercalation of kaolinite by alkali

acetates. Science 153, 741–743. https://doi.org/10.1126/science.153.3737.741

Soil Survey Staff, 2017. Soil Survey Manual Agriculture. Handbook 18. USDA, Nat. Resour. Conserv. Serv. https://doi.org/10.1097/00010694-195112000-00022

Sossi, P.A., Halverson, G.P., Nebel, O., Eggins, S.M., 2015. Combined separation of Cu, Fe and Zn from rock matrices and improved analytical protocols for stable isotope determination. Geostand. Geoanalytical Res. 39, 129–149. https://doi.org/10.1111/j.1751-908X.2014.00298.x

Spengler, S.R., Garcia, M.O., 1988. Geochemistry of the Hawi lavas, Kohala Volcano, Hawaii. Contrib. to Mineral. Petrol. 99, 90–104. https://doi.org/10.1007/BF00399369

Spiro, C.L., Wong, J., Lytle, F.W., Greegor, R.B., Maylotte, D.H., Lamson, S.H., 1986. Forms of potassium in coal and its combustion products. Fuel 65, 327–336. https://doi.org/10.1016/0016-2361(86)90291-7

Sposito, G., Skipper, N.T., Sutton, R., Park, S.H., Soper, A.K., Greathouse, J.A., 1999. Surface geochemistry of the clay minerals. Proc. Natl. Acad. Sci. U. S. A. 96, 3358–3364. https://doi.org/10.1073/pnas.96.7.3358

Srihari, V., Das, A., 2008. The kinetic and thermodynamic studies of phenol-sorption onto three agro-based carbons. Desalination 225, 220–234. https://doi.org/10.1016/j.desal.2007.07.008

Stallard, R., 1995. Tectonic, environmental, and Human aspects of weathering and erosion: A global review from a steady-state perspective. Annu. Rev. Earth Planet. Sci. 23, 11–39. https://doi.org/10.1146/annurev.earth.23.1.11

Stewart, B.W., Capo, R.C., Chadwick, O.A., 2001. Effects of rainfall on weathering rate, base cation provenance, and Sr isotope composition of Hawaiian soils. Geochim. Cosmochim. Acta 65, 1087–1099. https://doi.org/10.1016/S0016-7037(00)00614-1

Stille, P., Pierret, M.C., Steinmann, M., Chabaux, F., Boutin, R., Aubert, D., Pourcelot, L., Morvan, G., 2009. Impact of atmospheric deposition, biogeochemical cycling and water-mineral interaction on REE fractionation in acidic surface soils and soil water (the Strengbach case). Chem. Geol. 264, 173–186. https://doi.org/10.1016/j.chemgeo.2009.03.005

Strawn, D.G., Sparks, D.L., 1999. The use of XAFS to distinguish between inner- and outer-sphere lead adsorption complexes on montmorillonite. J. Colloid Interface Sci. 216, 257–269. https://doi.org/10.1006/jcis.1999.6330

Sun, Y., Teng, F.Z., Hu, Y., Chen, X.Y., Pang, K.N., 2020. Tracing subducted oceanic slabs in the mantle by using potassium isotopes. Geochim. Cosmochim. Acta 278, 353–360. https://doi.org/10.1016/j.gca.2019.05.013

Sutherland, D.G.J., Bancroft, G.M., Tan, K.H., 1992. Vibrational splitting in Si2p core-level photoelectron spectra of silicon molecules. J. Chem. Phys. 97, 7918–7931. https://doi.org/10.1063/1.463467

Swann, R.L., Laskowski, D.A., McCall, P.J., 1983. A rapid method of the estimation of the environmental parameters octanol/water partition coeffient, soil sorption constant, water to air ratio, and water solubility. Residue Rev. Vol. 85, 17–28. https://doi.org/10.1007/978-1-4612-5462-1_3

Song Z., Wang H., Strong P. J., Li Z., Jiang P., 2012. Plant impact on the coupled terrestrial biogeochemical cycles of silicon and carbon: Implications for biogeochemical carbon sequestration. Earth-Science Rev. 115, 319–331. https://doi.org/10.1016/j.earscirev.2012.09.006

Shabala, S., 2003. Regulation of potassium transport in leaves: from molecular to tissue level. Ann. Bot. 92(5), 627-634. https://doi.org/10.1093/aob/mcg191

Santos, E.F., Mateus, N.S., Rosário, M.O., Garcez, T.B., Mazzafera, P., Lavres, J., 2020. Enhancing potassium content in leaves and stems improves drought tolerance of eucalyptus clones. Physiol. Plant. 1-12. https://doi.org/10.1111/ppl.13228

Schachtman, D.P., Schroeder, J.I., 1994. Structure and transport mechanism of a high-affinity potassium uptake transporter from higher plants. Nature 370, 655–658. https://doi.org/10.1038/370655a0

Schmitt, A.D., Cobert, F., Bourgeade, P., Ertlen, D., Labolle, F., Gangloff, S., Badot, P.M., Chabaux, F., Stille, P., 2013. Calcium isotope fractionation during plant growth under a limited nutrient supply. Geochim. Cosmochim. Acta 110, 70–83. https://doi.org/10.1016/j.gca.2013.02.002

Soil Survey Laboratory Staff. 1992. Soil survey laboratory methods manual. Soil Survey Investigations Report. No.42. USDA-SCS, National Soil Survey Center, Lincoln, NE.

Tabor, N.J., Montanez, I.P., Southard, R.J., 2002. Paleoenvironmental reconstruction from chemical and isotopic compositions of Permo-Pennsylvanian pedogenic minerals. Geochim. Cosmochim. Acta 66, 3093–3107. https://doi.org/10.1016/S0016-7037(02)00879-7

Takahashi, Y., Dahlgren, R.A., Kanno, H., Nanzyo, M., Takahashi, T., 2018. Mechanisms for high potassium selectivity of soils dominated by halloysite from northern California, USA. Soil Sci. Plant Nutr. 64, 90–99. https://doi.org/10.1080/00380768.2017.1411167

Teng, F.Z., Hu, Y., Ma, J.L., Wei, G.J., Rudnick, R.L., 2020. Potassium isotope fractionation during continental weathering and implications for global K isotopic balance. Geochim. Cosmochim. Acta 278, 261–271. https://doi.org/10.1016/j.gca.2020.02.029

Teng, F.Z., Li, W.Y., Rudnick, R.L., Gardner, L.R., 2010. Contrasting lithium and magnesium isotope fractionation during continental weathering. Earth Planet. Sci. Lett. 300, 63–71. https://doi.org/10.1016/j.epsl.2010.09.036

Teng, F., Wang, S., Moynier, F., 2019. Tracing the formation and differentiation of the Earth by non-traditional stable isotopes. Sci. China Earth Sci. 62(11), 1702-1715. https://doi.org/10.1007/s11430-019-9520-6

Teng, F.Z., Mcdonough, W.F., Rudnick, R.L., Walker, R.J., Sirbescu, M.L.C., 2006. Lithium isotopic systematics of granites and pegmatites from the Black Hills, South Dakota. Am. Mineral. 91, 1488–1498. https://doi.org/10.2138/am.2006.2083

Thanh, L.D., Sprik, R., 2016. Zeta potential in porous rocks in contact with monovalent and divalent electrolyte aqueous solutions. Geophysics 81, D303–D314. https://doi.org/10.1190/GEO2015-0571.1

Tomascak, P.B., 2004. Developments in the understanding and application of lithium isotopes in the earth and planetary sciences. Rev. Mineral. Geochem. https://doi.org/10.2138/gsrmg.55.1.153

Tomascak, P.B., Magna, T., Dohmen, R., 2016. Advances in Lithium Isotope Geochemistry, Springer. https://doi.org/10.1007/978-3-319-01430-2

Tomascak, P.B., Tera, F., Helz, R.T., Walker, R.J., 1999. The absence of lithium isotope fractionation during basalt differentiation: New measurements by multicollector sector ICP-MS. Geochim. Cosmochim. Acta 63, 907–910. https://doi.org/10.1016/S0016-7037(98)00318-4

Tombácz, E., Szekeres, M., 2006. Surface charge heterogeneity of kaolinite in aqueous suspension in

comparison with montmorillonite. Appl. Clay Sci. 34, 105–124. https://doi.org/10.1016/j.clay.2006.05.009

Torn, M.S., Trumbore, S.E., Chadwick, O.A., Vitousek, P.M., Hendricks, D.M., 1997. Mineral control of soil organic carbon storage and turnover. Nature 389, 170–173. https://doi.org/10.1038/38260

Tripler, C.E., Kaushal, S.S., Likens, G.E., Todd Walter, M., 2006. Patterns in potassium dynamics in forest ecosystems. Ecol. Lett. https://doi.org/10.1111/j.1461-0248.2006.00891.x

Tsai, P.H., You, C.F., Huang, K.F., Chung, C.H., Sun, Y. Bin, 2014. Lithium distribution and isotopic fractionation during chemical weathering and soil formation in a loess profile. J. Asian Earth Sci. 87, 1–10. https://doi.org/10.1016/j.jseaes.2014.02.001

Tuller-Ross, B., Savage, P.S., Chen, H., Wang, K., 2019. Potassium isotope fractionation during magmatic differentiation of basalt to rhyolite. Chem. Geol. 525, 37–45. https://doi.org/10.1016/j.chemgeo.2019.07.017

Tang, Y.T., Cloquet, C., Deng, T.H.B., Sterckeman, T., Echevarria, G., Yang, W.J., Morel, J.L., Qiu, R.L., 2016. Zinc isotope fractionation in the hyperaccumulator noccaea caerulescens and the nonaccumulating plant Thlaspi arvense at Low and High Zn Supply. Environ. Sci. Technol. 50, 8020–8027. https://doi.org/10.1021/acs.est.6b00167

Tipper, E.T., Stevenson, E.I., Alcock, V., Knight, A.C., Baronas, J.J., Hilton, R.G., Bickle, M.J., Larkin, C.S., Feng, L., Relph, K.E., Hughes, G., 2021. Global silicate weathering flux overestimated because of sediment–water cation exchange. Proc. Natl. Acad. Sci. U. S. A. 118(1). e2016430118 https://doi.org/10.1073/pnas.2016430118

Taubaso, C., Afonso, M. D. S., Sánchez, R. T., 2004. Modelling soil surface charge density using mineral composition. Geoderma 121(1-2), 123-133. https://doi.org/10.1016/j.geoderma.2003.11.005

Takahashi, Y., Dahlgren, R. A., Kanno, H., Nanzyo, M., Takahashi, T., 2018. Mechanisms for high potassium selectivity of soils dominated by halloysite from northern California, USA. J. Soil Sci. Plant Nutr. 64(1), 90-99. https://doi.org/10.1080/00380768.2017.1411167

Uhlig, D., Amelung, W., Von Blanckenburg, F., 2020. Mineral nutrients sourced in deep regolith sustain long-term nutrition of mountainous temperate forest ecosystems. Global Biogeochem. Cycles 34(9), e2019GB006513. https://doi.org/10.1029/2019GB006513

Van Hoecke, K., Belza, J., Croymans, T., Misra, S., Claeys, P., Vanhaecke, F., 2015. Single-step chromatographic isolation of lithium from whole-rock carbonate and clay for isotopic analysis with multi-collector ICP-mass spectrometry. J. Anal. At. Spectrom. 30, 2533–2540. https://doi.org/10.1039/c5ja00165j

Varma, S., Rempe, S.B., 2006. Coordination numbers of alkali metal ions in aqueous solutions. Biophys. Chem. 124, 192–199. https://doi.org/10.1016/j.bpc.2006.07.002

Vasconcelos, I.F., Haack, E.A., Maurice, P.A., Bunker, B.A., 2008. EXAFS analysis of cadmium(II) adsorption to kaolinite. Chem. Geol. 249, 237–249. https://doi.org/10.1016/j.chemgeo.2008.01.001

Verney-Carron, A., Vigier, N., Millot, R., 2011. Experimental determination of the role of diffusion on Li isotope fractionation during basaltic glass weathering. Geochim. Cosmochim. Acta 75, 3452–3468. https://doi.org/10.1016/j.gca.2011.03.019

Vigier, N., Decarreau, A., Millot, R., Carignan, J., Petit, S., France-Lanord, C., 2008. Quantifying Li isotope fractionation during smectite formation and implications for the Li cycle. Geochim. Cosmochim. Acta 72, 780–792. https://doi.org/10.1016/j.gca.2007.11.011

Vigier, N., Gislason, S.R., Burton, K.W., Millot, R., Mokadem, F., 2009. The relationship between riverine lithium isotope composition and silicate weathering rates in Iceland. Earth Planet. Sci. Lett. 287, 434–441. https://doi.org/10.1016/j.epsl.2009.08.026

Vigier, N., Goddéris, Y., 2015. A new approach for modeling Cenozoic oceanic lithium isotope paleo-variations: The key role of climate. Clim. Past 11, 635–645. https://doi.org/10.5194/cp-11-635-2015

Vitousek, P.M., Chadwick, O.A., Crews, T.E., Fownes, J.H., Hendricks, D.M., Herbert, D., 1997. Soil and ecosystem development across the Hawaiian Islands. GSA Today 7.

Vitousek, P.M., Ladefoged, T.N., Kirch, P. V., Hartshorn, A.S., Graves, M.W., Hotchkiss, S.C., Tutjapurkar, S., Chadwick, O.A., 2004. Soils, agriculture, and society in precontact Hawai'i. Science 304, 1665–1669. https://doi.org/10.1126/science.1099619

Voegelin, A.R., Nägler, T.F., Pettke, T., Neubert, N., Steinmann, M., Pourret, O., Villa, I.M., 2012. The impact of igneous bedrock weathering on the Mo isotopic composition of stream waters: Natural samples and laboratory experiments. Geochim. Cosmochim. Acta 86, 150–165. https://doi.org/10.1016/j.gca.2012.02.029

Vogel, C., Helfenstein, J., Massey, M.S., Sekine, R., Kretzschmar, R., Beiping, L., Peter, T., Chadwick ,O.A., Tamburini, F., Rivard, C., Herzel, H., Adam, C., Pradas del Real, A.E., Castillo-Michel, H., Zuin, L., Wang, D., Felix, R., Lasalle-Kaiser, B., Frossard, E., 2021. Microspectroscopy reveals dust-derived apatite grains in acidic, highly weathered Hawaiian soils. Geoderma 381, 114681. https://doi.org/10.1016/j.geoderma.2020.114681

Wall, A.J., Mathur, R., Post, J.E., Heaney, P.J., 2011. Cu isotope fractionation during bornite dissolution: An in situ X-ray diffraction analysis. Ore Geol. Rev. 42, 62–70. https://doi.org/10.1016/j.oregeorev.2011.01.001

Wang, K., Jacobsen, S.B., 2016. An estimate of the Bulk Silicate Earth potassium isotopic composition based on MC-ICPMS measurements of basalts. Geochim. Cosmochim. Acta 178, 223–232. https://doi.org/10.1016/j.gca.2015.12.039

Wang, K., Close, H.G., Tuller-Ross, B., Chen, H., 2020. Global average potassium isotope composition of modern seawater. ACS Earth Space Chem. 4(7), 1010-1017. https://doi.org/10.1021/acsearthspacechem.0c00047

Wang, K., Peucker-Ehrenbrink, B., Chen, H., Lee, H., Hasenmueller, E.A., 2021. Dissolved potassium isotopic composition of major world rivers. Geochim. Cosmochim. Acta 294, 145-159. https://doi.org/10.1016/j.gca.2020.11.012

Wang, Q.L., Chetelat, B., Zhao, Z.Q., Ding, H., Li, S.L., Wang, B.L., Li, J., Liu, X.L., 2015. Behavior of lithium isotopes in the Changjiang River system: Sources effects and response to weathering and erosion. Geochim. Cosmochim. Acta 151, 117–132. https://doi.org/10.1016/j.gca.2014.12.015

Wanner, C., Sonnenthal, E.L., Liu, X.M., 2014. Seawater δ^7Li: A direct proxy for global CO2 consumption by continental silicate weathering? Chem. Geol. 381, 154–167. https://doi.org/10.1016/j.chemgeo.2014.05.005

Wardle, D.A., Walker, L.R., Bardgett, R.D., 2004. Ecosystem properties and forest decline in contrasting long-term chronosequences. Science 305, 509–513. https://doi.org/10.1126/science.1098778

Wasylenki, L.E., Swihart, J.W., Romaniello, S.J., 2014. Cadmium isotope fractionation during adsorption to Mn oxyhydroxide at low and high ionic strength. Geochim. Cosmochim. Acta 140, 212–226. https://doi.org/10.1016/j.gca.2014.05.007

Wasylenki, L.E., Schaefer, A.T., Chanda, P., Farmer, J.C., 2020. Differential behavior of tungsten stable isotopes during sorption to Fe versus Mn oxyhydroxides at low ionic strength. Chemical Geology, 558, 119836. https://doi.org/10.1016/j.chemgeo.2020.119836

Watkins, J.M., DePaolo, D.J., Watson, E.B., 2017. Kinetic fractionation of non-traditional stable isotopes by diffusion and crystal growth reactions, in: Non-Traditional Stable Isotopes. Walter de Gruyter GmbH, pp. 85–126. https://doi.org/10.2138/rmg.2017.82.4

Weiss, D.J., Boye, K., Caldelas, C., Fendorf, S., 2014. Zinc Isotope Fractionation during Early Dissolution of Biotite Granite. Soil Sci. Soc. Am. J. 78, 171–179. https://doi.org/10.2136/sssaj2012.0426

Weiss, D.J., Mason, T.F.D., Zhao, F.J., Kirk, G.J.D., Coles, B.J., Horstwood, M.S.A., 2005. Isotopic discrimination of zinc in higher plants. New Phytol. 165, 703–710. https://doi.org/10.1111/j.1469-8137.2004.01307.x

Weissbart, E.J., Rimstidt, J.D., 2000. Wollastonite: Incongruent dissolution and leached layer formation. Geochim. Cosmochim. Acta 64, 4007–4016. https://doi.org/10.1016/S0016-7037(00)00475-0

Wetzel, F., de Souza, G.F., Reynolds, B.C., 2014. What controls silicon isotope fractionation during dissolution of diatom opal? Geochim. Cosmochim. Acta 131, 128–137. https://doi.org/10.1016/j.gca.2014.01.028

Weynell, M., Wiechert, U., Schuessler, J.A., 2017. Lithium isotopes and implications on chemical weathering in the catchment of Lake Donggi Cona, northeastern Tibetan Plateau. Geochim. Cosmochim. Acta 213, 155–177. https://doi.org/10.1016/j.gca.2017.06.026

Whipkey, C.E., Capo, R.C., Chadwick, O.A., Stewart, B.W., 2000. The importance of sea spray to the cation budget of a coastal Hawaiian soil: A strontium isotope approach. Chem. Geol. 168, 37–48. https://doi.org/10.1016/S0009-2541(00)00187-X

White, A.F., Schulz, M.S., Stonestrom, D.A., Vivit, D. V., Fitzpatrick, J., Bullen, T.D., Maher, K., Blum, A.E., 2009. Chemical weathering of a marine terrace chronosequence, Santa Cruz, California. Part II: Solute profiles, gradients and the comparisons of contemporary and long-term weathering rates. Geochim. Cosmochim. Acta 73, 2769–2803. https://doi.org/10.1016/j.gca.2009.01.029

Wiederhold, J.G., Kraemer, S.M., Teutsch, N., Borer, P.M., Halliday, A.N., Kretzschmar, R., 2006. Iron isotope fractionation during proton-promoted, ligand-controlled, and reductive dissolution of goethite. Environ. Sci. Technol. 40, 3787–3793. https://doi.org/10.1021/es052228y

Wiegand, B.A., Chadwick, O.A., Vitousek, P.M., Wooden, J.L., 2005. Ca cycling and isotopic fluxes in forested ecosystems in Hawaii. Geophys. Res. Lett. 32, 1–4. https://doi.org/10.1029/2005GL022746

Wilke, M., Farges, F., Petit, P.E., Brown, G.E., Martin, F., 2001. Oxidation state and coordination of Fe in minerals: An Fe K-XANES spectroscopic study. Am. Mineral. 86, 714–730. https://doi.org/10.2138/am-2001-5-612

Wilke, R.J., Dayal, R., 1982. The behavior of iron, manganese and silicon in the Peconic River estuary, New York. Estuar. Coast. Shelf Sci. 15, 577–586. https://doi.org/10.1016/0272-7714(82)90009-9

Willenbring, J.K., Von Blanckenburg, F., 2010. Long-term stability of global erosion rates and weathering during late-Cenozoic cooling. Nature 465, 211–214. https://doi.org/10.1038/nature09044

Williams, L.B., Hervig, R.L., 2005. Lithium and boron isotopes in illite-smectite: The importance of crystal size. Geochim. Cosmochim. Acta 69, 5705–5716. https://doi.org/10.1016/j.gca.2005.08.005

Wimpenny, J., Colla, C.A., Yu, P., Yin, Q.Z., Rustad, J.R., Casey, W.H., 2015. Lithium isotope fractionation during uptake by gibbsite. Geochim. Cosmochim. Acta 168, 133–150. https://doi.org/10.1016/j.gca.2015.07.011

Wimpenny, J., Gíslason, S.R., James, R.H., Gannoun, A., Pogge Von Strandmann, P.A.E., Burton, K.W., 2010. The behaviour of Li and Mg isotopes during primary phase dissolution and secondary mineral formation in basalt. Geochim. Cosmochim. Acta 74, 5259–5279. https://doi.org/10.1016/j.gca.2010.06.028

Wunder, B., Meixner, A., Romer, R.L., Feenstra, A., Schettler, G., Heinrich, W., 2007. Lithium isotope fractionation between Li-bearing staurolite, Li-mica and aqueous fluids: An experimental study. Chem. Geol. 238, 277–290. https://doi.org/10.1016/j.chemgeo.2006.12.001

White P., Karley A., 2010. Cell biology of metals and nutrients. in Plant Cell Monographs, Springer, Berlin. pp. 199-224. https://doi.org/10.1007/978-3-642-10613-2

Weis, J.S., Weis, P., 2004. Metal uptake, transport and release by wetland plants: Implications for phytoremediation and restoration. Environ. Int. 30, 685–700. https://doi.org/10.1016/j.envint.2003.11.002

Xu, W., Chen, D., Chu, W., Wu, Z., Marcelli, A., Mottana, A., Soldatov, A., Brigatti, M.F., 2011. Quantitative local structure determination in mica crystals: Ab initio simulations of polarization XANES at the potassium K-edge. J. Synchrotron Radiat. 18, 418–426. https://doi.org/10.1107/S0909049511002949

Xu, W., Zhu, J.M., Johnson, T.M., Wang, X., Lin, Z.Q., Tan, D., Qin, H., 2020. Selenium isotope fractionation during adsorption by Fe, Mn and Al oxides. Geochim. Cosmochim. Acta 272, 121–136. https://doi.org/10.1016/j.gca.2020.01.001

Xu, Y.K., Hu, Y., Chen, X.Y., Huang, T.Y., Sletten, R.S., Zhu, D., Teng, F.Z., 2019. Potassium isotopic compositions of international geological reference materials. Chem. Geol. 513, 101–107. https://doi.org/10.1016/j.chemgeo.2019.03.010

Yamaguchi, T., Ohzono, H., Yamagami, M., Yamanaka, K., Yoshida, K., Wakita, H., 2010. Ion hydration in aqueous solutions of lithium chloride, nickel chloride, and caesium chloride in ambient to supercritical water. J. Mol. Liq. 153, 2–8. https://doi.org/10.1016/j.molliq.2009.10.012

Yamaji, K., Makita, Y., Watanabe, H., Sonoda, A., Kanoh, H., Hirotsu, T., Ooi, K., 2001. Theoretical estimation of lithium isotopic reduced partition function ratio for lithium ions in aqueous solution. J. Phys. Chem. A 105, 602–613. https://doi.org/10.1021/jp001303i

Yasui, I., Hasegawa, H., Imaoka, M., 1983. X-ray diffraction study of the structure of silicate glasses. Part 1. alkali metasilicate glasses. Phys. Chem. Glas. 24, 65–71.

Yin, Z., Ding, Z., Hu, H., Liu, K., Chen, Q., 2010. Dissolution of zinc silicate (hemimorphite) with ammonia-ammonium chloride solution. Hydrometallurgy 103, 215–220. https://doi.org/10.1016/j.hydromet.2010.03.006

Yuan, W., Saldi, G.D., Chen, J. Bin, Vetuschi Zuccolini, M., Birck, J.L., Liu, Y., Schott, J., 2018. Gallium isotope fractionation during Ga adsorption on calcite and goethite. Geochim. Cosmochim. Acta 223, 350–363. https://doi.org/10.1016/j.gca.2017.12.008

Zeng, H., Rozsa, V.F., Nie, N.X., Zhang, Z., Pham, T.A., Galli, G., Dauphas, N., 2019. Ab initio calculation of equilibrium isotopic fractionations of potassium and rubidium in minerals and water. ACS Earth Sp. Chem. 3, 2601–2612. https://doi.org/10.1021/acsearthspacechem.9b00180

Zhang, L., Chan, L.H., Gieskes, J.M., 1998. Lithium isotope geochemistry of pore waters from Ocean Drilling Program Sites 918 and 919, Irminger Basin. Geochim. Cosmochim. Acta 62, 2437–2450. https://doi.org/10.1016/S0016-7037(98)00178-1

Zhang, S., Yuan, L., Li, W., Lin, Z., Li, Y., Hu, S., Zhao, B., 2017. Characterization of pH-fractionated humic acids derived from Chinese weathered coal. Chemosphere 166, 334–342. https://doi.org/10.1016/j.chemosphere.2016.09.095

Zheng, C., Chen, C., Chen, Y., Ong, S.P., 2020. Random forest models for accurate identification of coordination environments from X-ray absorption near-edge structure. Patterns 1, 100013. https://doi.org/10.1016/j.patter.2020.100013

Ziegler, K., Chadwick, O.A., Brzezinski, M.A., Kelly, E.F., 2005. Natural variations of δ30Si ratios during progressive basalt weathering, Hawaiian Islands. Geochim. Cosmochim. Acta 69, 4597–4610. https://doi.org/10.1016/j.gca.2005.05.008

Ziegler, K., Hsieh, J.C.C., Chadwick, O.A., Kelly, E.F., Hendricks, D.M., Savine, S.M., 2003. Halloysite as a kinetically controlled end product of arid-zone basalt weathering. Chem. Geol. 202, 461–478. https://doi.org/10.1016/j.chemgeo.2002.06.001

Zhao, M.Y., Zheng, Y.F., 2015. The intensity of chemical weathering: Geochemical constraints from marine detrital sediments of Triassic age in South China. Chem. Geol. 391, 111-122. https://doi.org/10.1016/j.chemgeo.2014.11.004

Zhang, W., Qi, L., Hu, Z., Zheng, C., Liu, Y., Chen, H., Gao, S., Hu, S., 2016. An Investigation of digestion methods for trace elements in bauxite and their determination in ten bauxite reference materials using inductively coupled plasma-mass spectrometry. Geostand. Geoanalytical Res. 40(2), 195-216. https://doi.org/10.1111/j.1751-908X.2015.00356.x